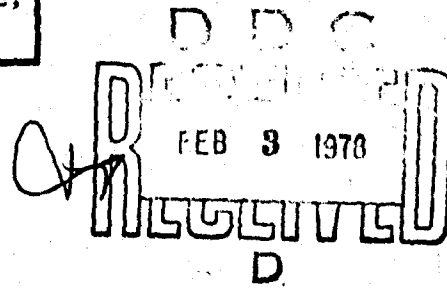AD A049579

USAAMRDL-TR-76-16

BEARINGLESS TAIL ROTOR LOADS AND STABILITY

Boeing Vertol Company
Box 16858
Philadelphia, Penn. 19142

November 1977

Final Report for Period March 1975 - January 1976

DDC
RECEIVED
FEB 3 1978
D

Prepared for

APPLIED TECHNOLOGY LABORATORY
RESEARCH AND TECHNOLOGY LABORATORIES (AVRADCOM)
Fort Eustis, Va. 23604

APPLIED TECHNOLOGY LABORATORY POSITION STATEMENT

This report provides the physical and aerodynamic properties of a bearingless tail rotor and its dynamic response to define the effects of configuration changes on loads and stability characteristics. The report is considered to be technically sound and within the originally intended scope of effort.

Mr. Donald J. Merkley of the Technology Applications Division served as project engineer for this work.

REPORT DOCUMENTATION PAGE		READ INSTRUCTIONS BEFORE COMPLETING FORM
1. REPORT NUMBER USAAMRDL-TR-76-16	2. GOVT ACCESSION NO.	3. RECIPIENT'S CATALOG NUMBER
4. TITLE (and Subtitle) BEARINGLESS TAIL ROTOR LOADS AND STABILITY.		5. TYPE OF REPORT & PERIOD COVERED Final Report. Mar 75 - Jan 1976.
		6. PERFORMING ORG. REPORT NUMBER D210-11025-1
7. AUTHOR(s) W. T. Edwards W. Miao		8. CONTRACT OR GRANT NUMBER(s) DAAJ02-75-C-0017
9. PERFORMING ORGANIZATION NAME AND ADDRESS Boeing Vertol Company Box 16858 Philadelphia, Pa. 19142		10. PROGRAM ELEMENT, PROJECT, TASK AREA & WORK UNIT NUMBERS 62209A 1F262209AH7600 044EK
11. CONTROLLING OFFICE NAME AND ADDRESS Applied Technology Laboratory, U.S. Army Research and Technology Laboratories Fort Eustis, Virginia 23604		12. REPORT DATE November 1977
		13. NUMBER OF PAGES 287
14. MONITORING AGENCY NAME & ADDRESS(if different from Controlling Office)		15. SECURITY CLASS. (of this report) Unclassified
		15a. DECLASSIFICATION/DOWNGRADING SCHEDULE

16. DISTRIBUTION STATEMENT (of this Report)

Approved for public release; distribution unlimited.

17. DISTRIBUTION STATEMENT (of the abstract entered in Block 20, if different from Report)

18. SUPPLEMENTARY NOTES

19. KEY WORDS (Continue on reverse side if necessary and identify by block number)

Flex-Strap Tail Rotor
Stability Boundary
Scissors Mode
"C" Mode
Strap Loads

Blade Sweep
Configuration Parameters
Strap Shear Center
Stall Flutter
Bearingless Rotor

20. ABSTRACT (Continue on reverse side if necessary and identify by block number)

During the period from July 1973 through December 1973, four wind tunnel model tests were conducted at the Boeing Vertol Wind Tunnel. In these four tests, a model flex-strap bearingless tail rotor was studied for aeroelastic stability characteristics and loads. In all, 12 individual rotor parameters were investigated to determine their effect on aeroelastic stability.

DD FORM 1473 EDITION OF 1 NOV 65 IS OBSOLETE

403 682

20.   Abstract

All data required to define the structural and aerodynamic
characteristics of the basic model and structural data required
to define the test stand and drive system are presented.   In
addition, the physical properties required to describe the
various parameters are documented, thus providing a complete
description of each configuration tested.

The effect of each test parameter on the aeroelastic stability
boundaries is indicated through plots of actual measured bound-
aries.   Where available, the alternating strap loads for these
configurations are presented.   A limited amount of analysis was
conducted and seemed to correlate with the test results.

ACCESSION for

RTIS	White Section	X
DDC	Buff Section	☐
UNANNOUNCED		☐
JUSTIFICATION		

BY
DISTRIBUTION/AVAILABILITY CODES

| Dist. | AVAIL. and, or SPECIAL | |
| A | | |

D D C

FEB 3 1978

D

SUMMARY

This report documents data collected by the Boeing Vertol Company during testing of an 8-foot-diameter bearingless tail rotor. This tail rotor model uses a fiberglass flex-strap blade retention system designed to provide inplane frequencies above the rotor speed. The results and conclusions which appear in the report are therefore directed to a stiff-inplane rotor system.

The flex-strap retention system uses a single, continuous fiberglass flex-strap member to join and retain opposing rotor blades. This lightweight member provides very low resistance to blade flap motions, while reacting inplane shear due to rotor torque and vertical shear due to rotor thrust. Centrifugal force is reacted directly between the opposing blades through the strap.

The 8-foot-diameter model was tested at the Boeing Vertol Wind Tunnel facility in four test phases between July 1973 and December 1973. The four test phases, designated BVWT 124, BVTC 009, BVWT 129, and BVTC 011, contain over 150 data runs.

The information presented in this report is the result of work in four aspects of the model testing and analysis.

1)   A detailed description of the model rotor blade, retention strap, control system, drive system, and test stand is presented. Sufficient information on physical and aerodynamic properties are provided to enable analytical determination of the elastic fully coupled flap-lag-torsion characteristics of the baseline rotor system and subsequently the stability and loads characteristics.

2)   The details of 12 different configuration parameters, which were varied throughout the testing of the model, are presented. In particular, any change in basic radial properties such as weight, inertia, or stiffness due to a parameter variation is recorded.

3)   Test data is selected and plotted to indicate the effects of the parametric variations on model aeroelastic stability, modal frequency, and flex-strap loads. The effects of these parameters thus documented provide a data base for future exploratory or developmental tests.

4)   A limited amount of analytical work is performed and the results are summarized. Through this effort it was discovered that the dynamic characteristics of the flex strap are dependent upon the reactions of the centrifugal force along the strap. These dynamic effects require more extensive study. However, using a simplified

representation of these complex characteristics, pre-
dictions were obtained using the Boeing Vertol Company's
Y-69 analysis which indicate reasonable correlation
with test stability data.

4

PREFACE

This program was conducted for the Eustis Directorate, U.S. Army Air Mobility Research and Development Laboratory, * under contract DAAJ02-75-C-0017. Technical Monitor for the Eustis Directorate was D.J. Merkley. W. Miao was project manager and W.T. Edwards was project engineer at the Boeing Vertol Company.

The program documented all the relevant test data and physical properties for a bearingless flex-strap tail rotor wind tunnel model that was tested during the period from July 1973 to December 1973 at Boeing Vertol. A limited amount of analysis was conducted to correlate and to validate the test results.

---

* On 1 September 1977, the Eustis Directorate, U.S. Army Air Mobility Research and Development Laboratory was redesignated the Applied Technology Laboratory, U.S. Army Research and Technology Laboratories (AVRADCOM).

5

TABLE OF CONTENTS

TABLE OF CONTENTS
(Continued)

7

TABLE OF CONTENTS
(Continued)

LIST OF ILLUSTRATIONS

9

LIST OF ILLUSTRATIONS
(Continued)

LIST OF ILLUSTRATIONS
(Continued)

LIST OF ILLUSTRATIONS
(Continued)

LIST OF ILLUSTRATIONS
(Continued)

13

LIST OF ILLUSTRATIONS
(Continued)

LIST OF ILLUSTRATIONS
(Continued)

LIST OF ILLUSTRATIONS
(Continued)

LIST OF ILLUSTRATIONS
(Continued)

LIST OF ILLUSTRATIONS
(Continued)

LIST OF TABLES

1.0 INTRODUCTION

1.1 Flex-strap Tail Rotor

Over the past several years there has been a trend toward the increased usage of bearingless helicopter rotors for both main and tail rotors. This form of rotor system offers many advantages over more conventional hinged systems. Among these advantages are fewer parts, reduced maintenance requirements, and improved tolerance to ballistic damage.

The bearingless rotor detailed in this document is an 8-foot-diameter stiff-inplane model flex-strap tail rotor design, Figure 1. In the "flex-strap" design, the opposing rotor blades are retained by a single continuous fiberglass strap that is centered at and passes directly through the hub. An exploded view of this assembly is shown in Figure 2. Torque from the rotor blades is reacted through two cruciform torsion flexures, as shown in Figure 3. The hub of the model is constructed in such a way that two such flex straps, each with one pair of rotor blades, are mounted one above the other (oriented perpendicular to each other) for a four-bladed configuration.

1.2 Test Program

The entire test program being reported was conducted at the Boeing Vertol Wind Tunnel facility. The test results and model configurations are taken from four test phases designated: BVWT 124, BVTC 007, BVWT 129, and BVTC 011, which were conducted between July 1973 and December 1973.

The objectives of these test programs were to:

(1) Determine the effects of 12 different configuration parameters on aeroelastic stability characteristics of the bearingless model.

(2) Determine the effects of these parameters on the strap loads.

(3) Gain a more complete understanding of the dynamic behavior and characteristics of the model in terms of observed modal frequencies.

To satisfy these objectives, over 150 data runs were conducted. These data runs were designed to explore a wide range of rotor speeds, thrust, shaft angle, and forward speed, well beyond the requirements expected in current production aircraft.

The test program revealed several forms of instability and provided a significant amount of data on the operating limits and characteristics of these phenomena. Two major types of
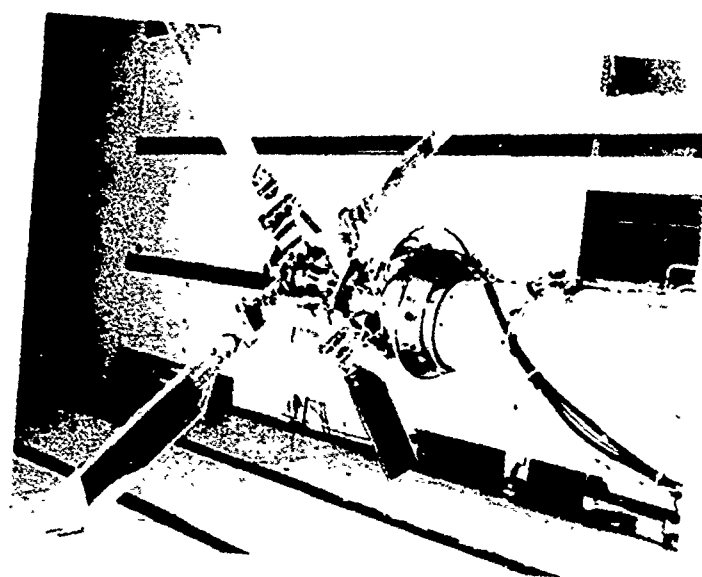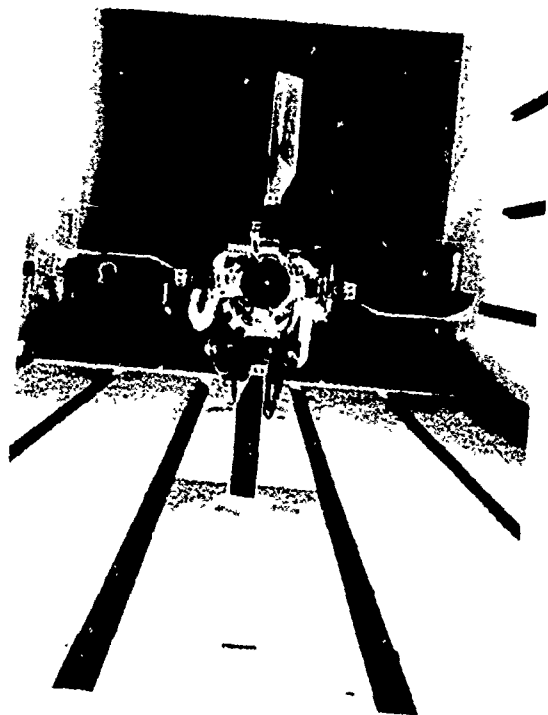
FIGURE 1   FLEX-STRAP MODEL IN TUNNEL
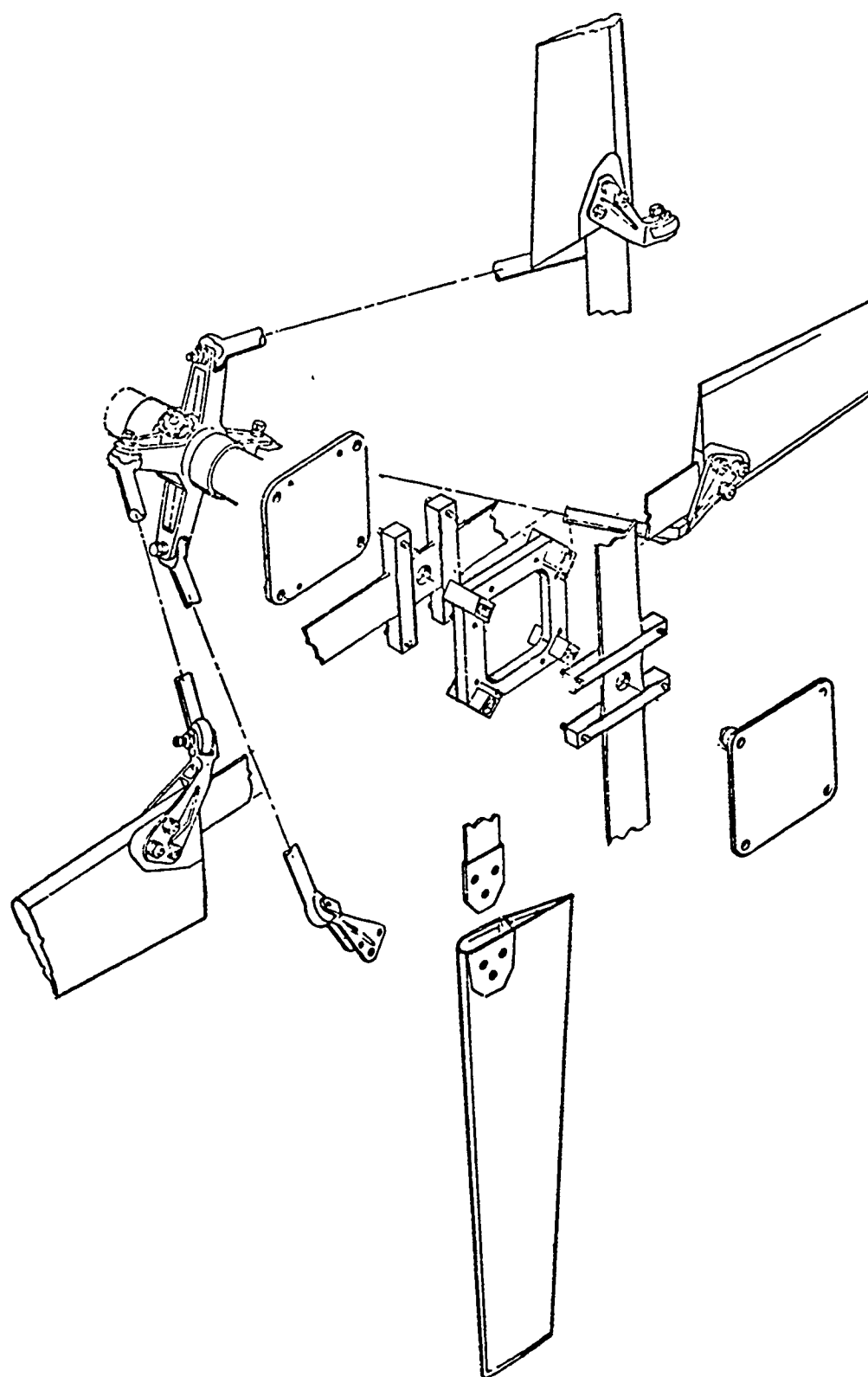
FIGURE 2   FLEX-STRAP TAIL ROTOR ASSEMBLY

MOMENT LIMITING
ATTACHMENT

FLEX STRAP

CRUCIFORM TORSION
FLEXURES

BLADE MOUNTING
DOUBLER

VIEW A-A

SECT B-B
5 X SIZE

SECT C-C
5 X SIZE
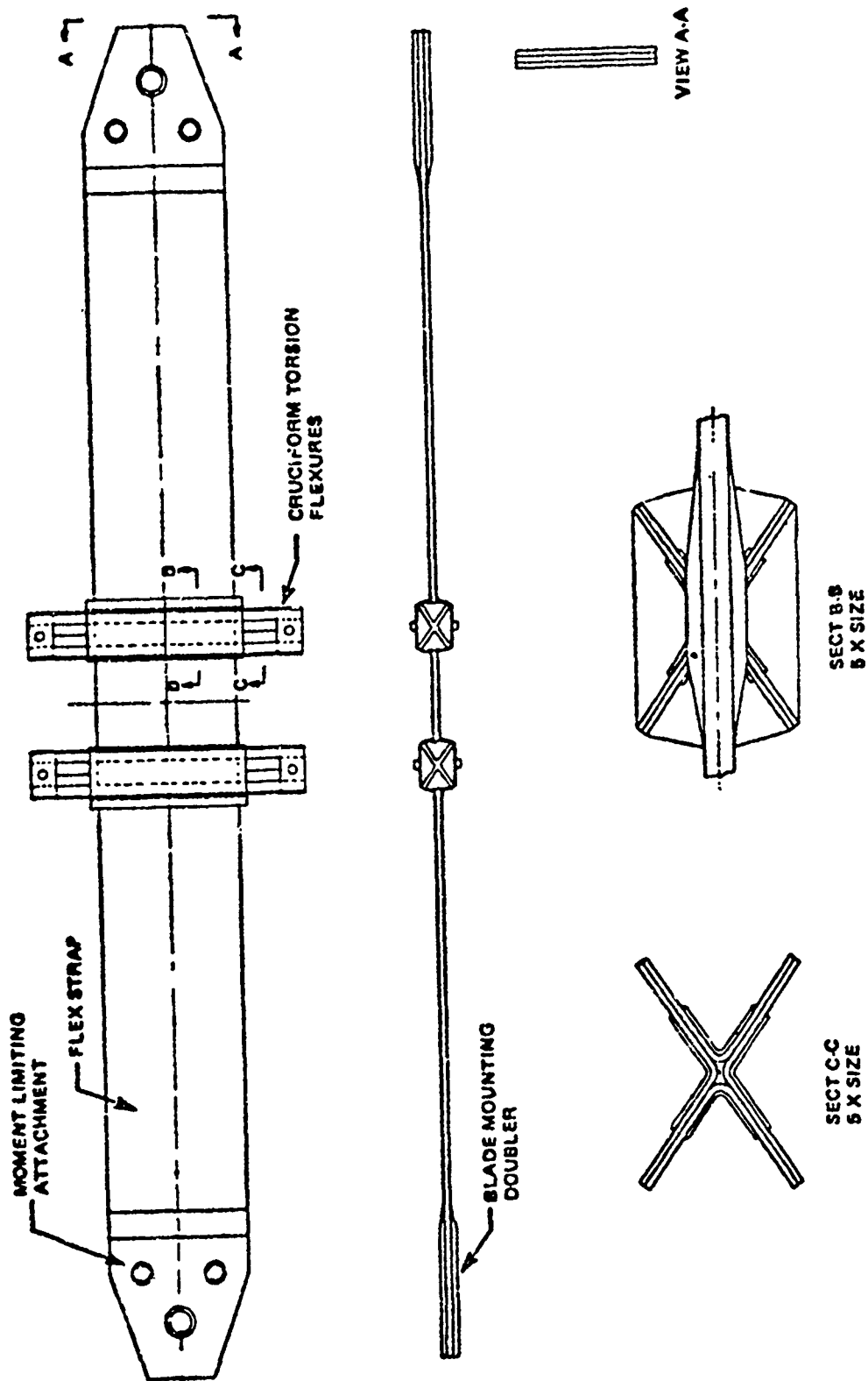
FIGURE 3   FLEX-STRAP CONSTRUCTION

24

instabilities were encountered: a flap-lag type of instability
of the first flap and first chord modes, and a flap-torsion
type of instability involving the first torsion and second flap
modes. Details of these instabilities are presented in Section
5.0.

1.3 Contract Objectives

The objective of this contract as listed in Reference 1 is to
document the comprehensive test data available so that it can
be used in the future, either to further develop the design
concept, or to correlate with the indispensible mathematical
analysis. As new computing methods are developed, they can be
exercised against test data, using the properties and configu-
rations documented herein to check out programs and to build
confidence in them.

2.0 DESCRIPTION OF TEST SETUP

The testing of the 8-foot-diameter tail rotor model was conducted in four test phases. The tests BVWT 124 and BVWT 129 were performed in the 20-foot by 20-foot test section of the Boeing Vertol V/STOL Wind Tunnel. A photograph of the model installed in the tunnel is shown in Figure 4. The slotted wall test section configuration shown in the picture was used in forward flight testing. For hover testing, the ceiling of the test section was removed (Figure 5).

The tests BVTC 009 and BVTC 011 were conducted in the 20-by 20.5-by 36-foot hover test cell. A photograph of the model installed in the test cell is shown in Figure 6. Recirculation in the test cell is minimized by testing with the large 6-by 16-foot window, shown in the background of Figure 6, open, and the 10-by 10-foot cell doors, not shown, open.

In the sections that follow, a complete description of the structural and aerodynamic properties of this tail rotor model are presented. In addition, the structural properties of the model control system, drive system, and test stand are given. All components of the basic model are identical for both the wind tunnel and the test cell portions of the test program.

For reference, the spanwise locations of the structural components which comprise one rotor blade and flex-strap retention system are summarized in Table 1. Detailed descriptions of these components are contained in Sections 2.1 and 2.2. Because the rotor blade flex-strap retention system is continuous from the center of rotation to the blade tip, the contributions of the various components to the physical properties in Sections 2.1 and 2.2 are shown in the same figures with labels indicating each component's contribution to the particular property.

2.1 Tail Rotor Blade Data

The tail rotor blades used in this testing are composite blades manufactured by Messerschmitt-Boelkow-Blohm. They are like those of the BO-105 tail rotor (7.08-inch chord with zero twist) except a nominal VR-7 (12-percent thick) series airfoil section is used in the tests.

The behavior of three different airfoil sections was observed during the tests. These airfoils differ only in the curvature of the leading edge. They are designated VR-6.9, VR-7.2, and VR-7.4 from the smallest curvature to the largest. The characteristics of these airfoils appear in Section 3.12.

2.1.1 Blade Spanwise Structural Data

The blade most used during the four phases is the blade with

26
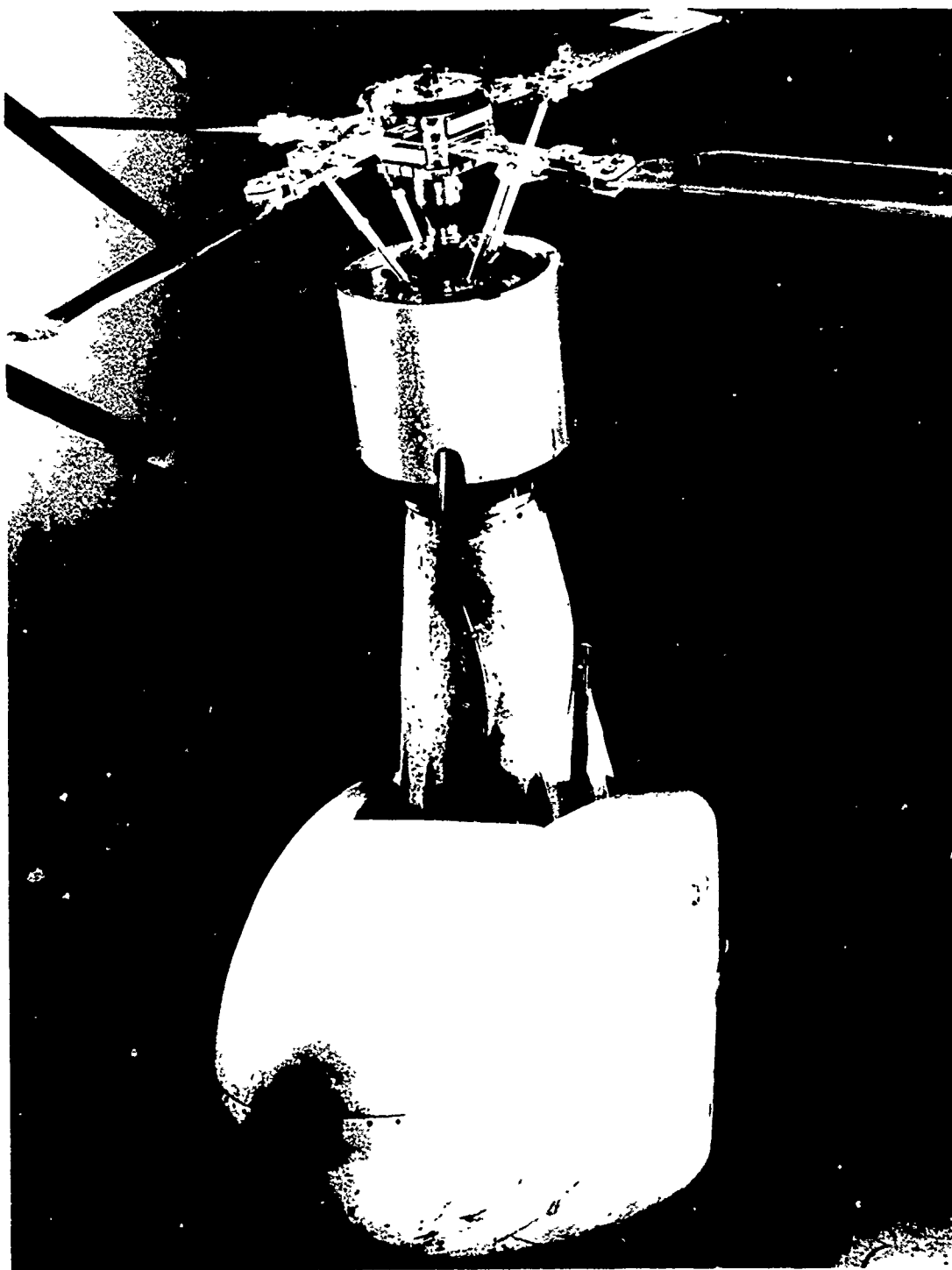
FIGURE 4   BOEING VERTOL WIND TUNNEL INSTALLATION,
FORWARD FLIGHT TEST CONFIGURATION

FIGURE 5   BOEING VERTOL WIND TUNNEL INSTALLATION,
            HOVER TEST CONFIGURATION

28

FIGURE 6 TEST CELL INSTALLATION

TABLE 1   SPANWISE LOCATION OF STRUCTURAL COMPONENTS

| COMPONENT | STATION | | ITEM |
	IN.	x/R	
BLADE	48.	1.0	TIP
	18.875	.3932	INBRD END OF BLADE
CLEVIS	20.5	.4271	OUTBRD END OF CLEVIS
	19.5	.4063	BLADE ATTACHMENT POINT
	16.95	.3531	OUTBRD SIDE OF CLEVIS TAPER
	16.15	.3365	INBRD SWEEP POINT
	15.5	.323	INBRD END OF CLEVIS
PITCH ARM	13.9	.2896	OUTBRD END OF PITCH ARM
	12.9	.2479	INBRD END OF PITCH ARM
STRAP	18.35	.3823	OUTBRD END OF STRAP
	11.6	.2417	INBRD SIDE PAD
	2.47	.0514	OUTBRD SIDE FLEXURE
	1.25	.0260	INBRD SIDE FLEXURE
	0	0	CENTER OF ROTATION

the VR-7.2 airfoil section. This blade, balanced to the quarter chord, will serve as the baseline for reporting blade spanwise properties. The other blades with the airfoil sections VR-6.9 to VR-7.4 have essentially identical structural properties. However, these blades have significantly different aerodynamic characteristics, which is covered in Section 3.12.

The spanwise blade properties extend from the radial station $x/R = .392$ to $x/R = 1.0$ ($R = 48$ inches). The blade structural properties, documented in Figures 7 to 14, are:

- the radial distribution of weight (Figure 7)
- the radial distribution of pitch inertia (Figure 8)
- the radial location of neutral axis and shear center (Figure 9)
- the undeformed radial twist distribution (Figure 10)
- the radial distribution of chord length (Figure 11)
- the radial distributions of torsional, flapwise, and chordwise stiffnesses (Figures 12, 13, and 14, respectively)

All of the blade structural data presented is taken directly from information supplied by the manufacturer with the exception of the spanwise weight and pitch inertia distributions. These properties have been corrected to account for additional nose balance weight of 0.027 lb/in. from station $x/R = .3917$ to $x/R = 1.0$ ($R = 48$ in.), which was added to bring the mass balance of the blade to the quarter chord along the entire span.

The flapwise and chordwise mass moments of inertia were not determined for the blade and therefore must be approximated from mass and pitch inertia distributions, if desired. For most analytical work, it is reasonable to assume that the magnitude of flapwise inertia distribution is between 0 and 15% of the value of the distributed pitch inertia and that the magnitude of chordwise inertia distribution is equal to the difference of the distributed pitch inertia and the flapwise inertia.

2.1.2 Blade Aerodynamic Data

During the tail rotor stability testing, the VR-7.2 blade airfoil section with a 7.08-inch chord was considered to be the reference configuration. Therefore, for the purpose of this report this is the baseline blade.

The blade is untwisted along its span; however, it is mounted at a prepitch angle of 9° noseup relative to the strap, as shown in Figure 10. The blade has a trailing-edge tab that extends from $x/R = .543$ to $x/R = 1.0$ ($R = 48$ in). The tab is set to an angle of 4.5° up ($\delta_c = 4.5°$).

31
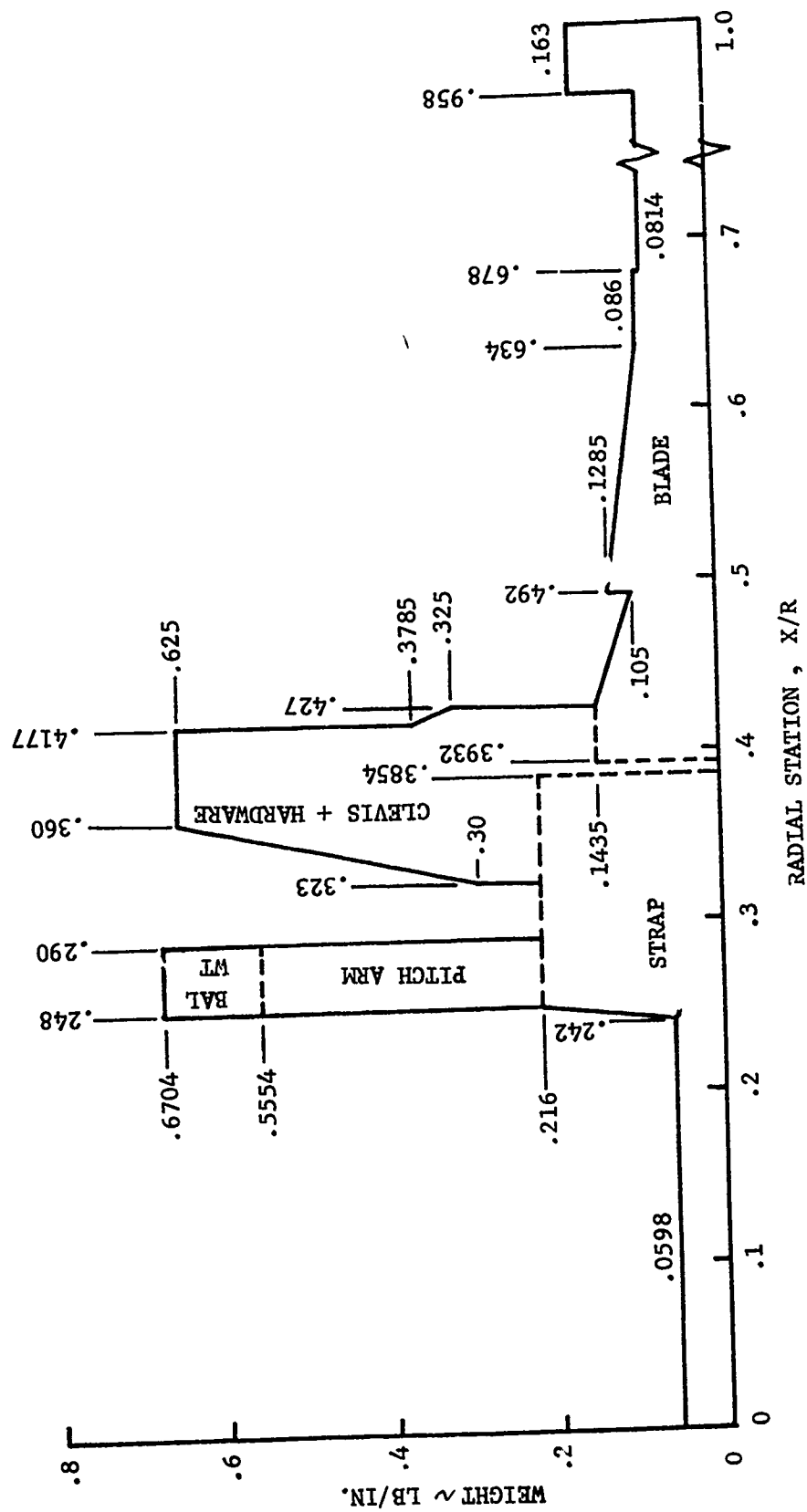
FIGURE 7 RADIAL WEIGHT DISTRIBUTION – BASELINE
CONFIGURATION

32
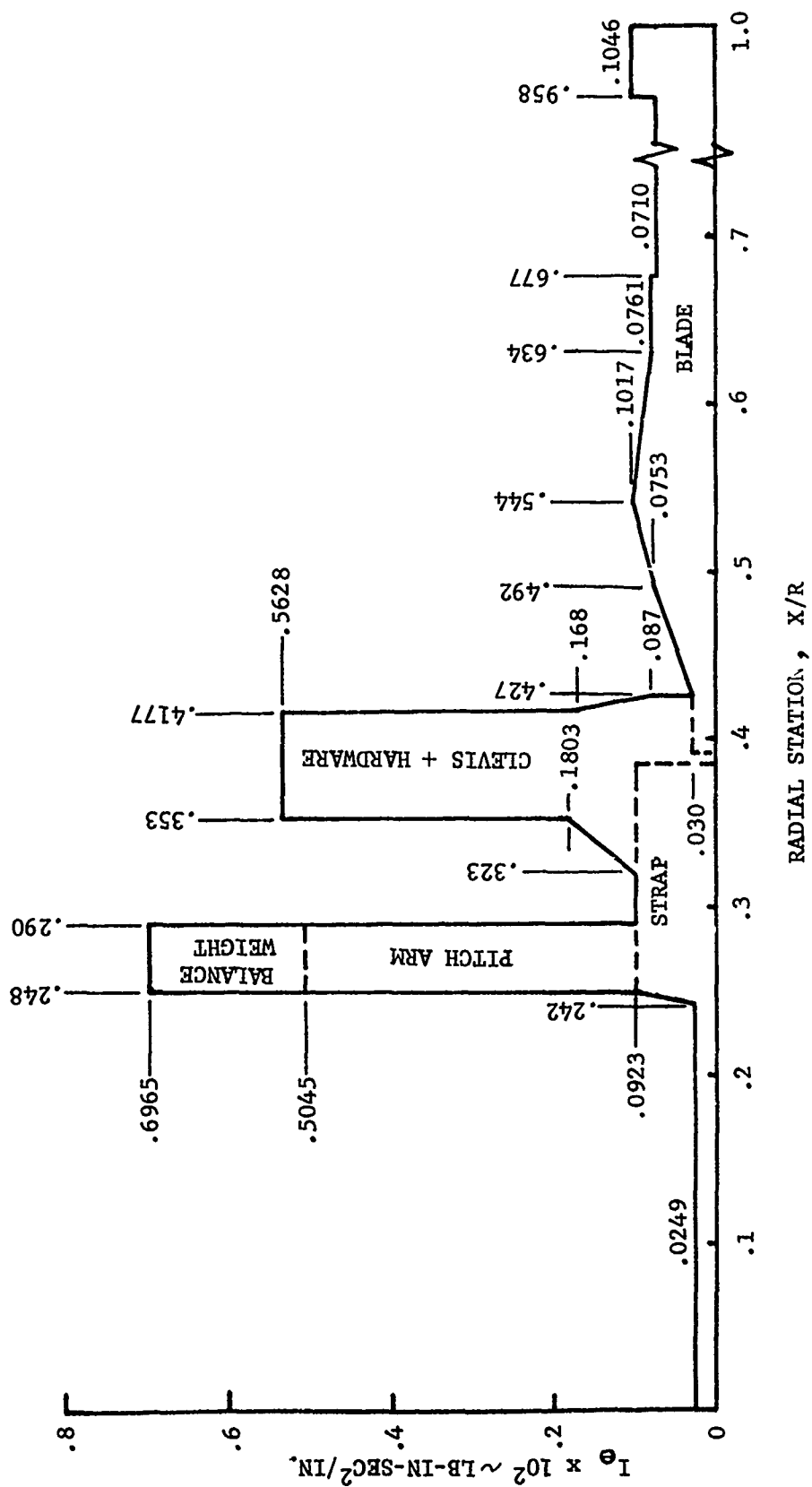
FIGURE 8 RADIAL PITCH INERTIA DISTRIBUTION –
BASELINE CONFIGURATION

33
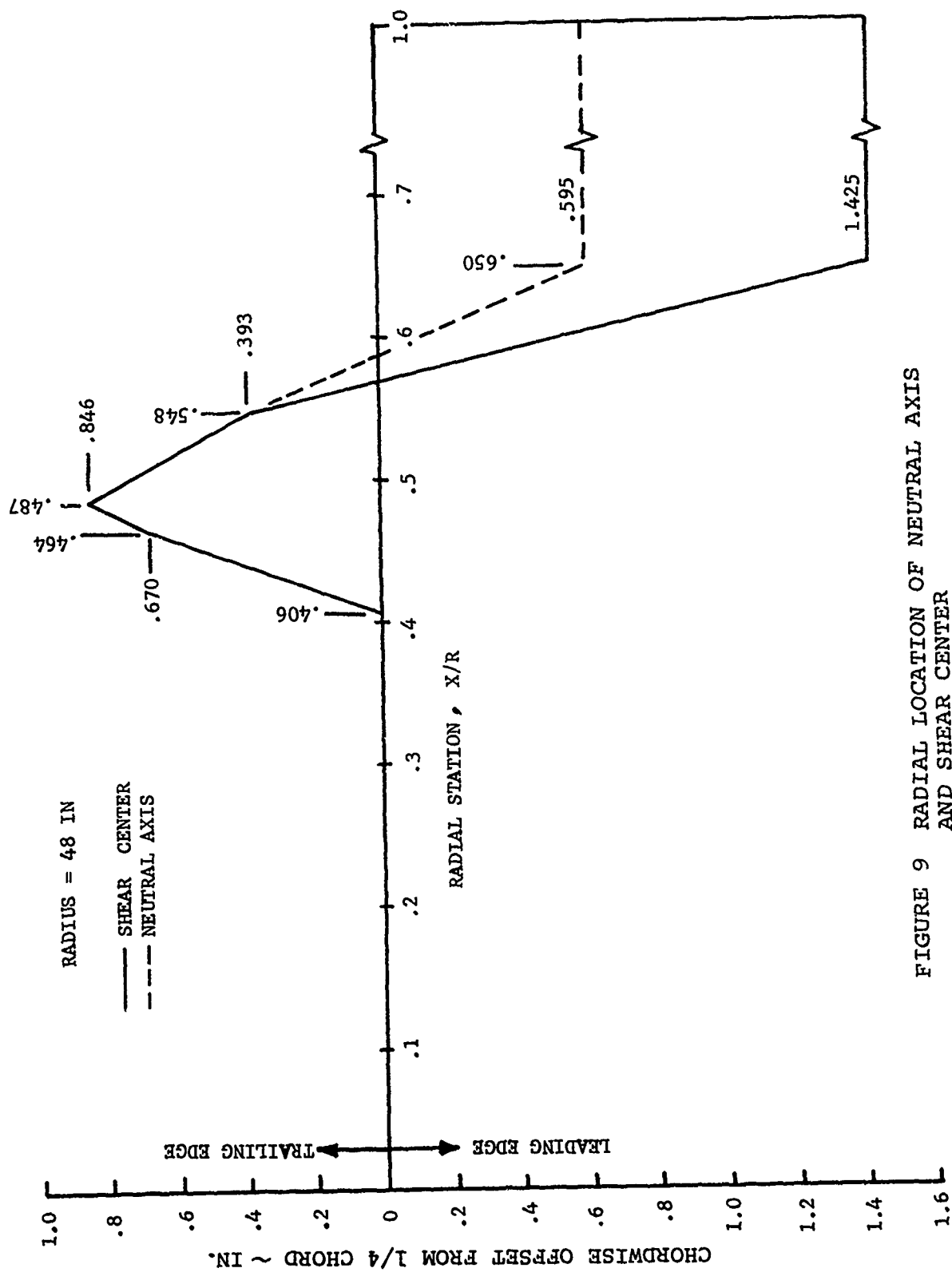
FIGURE 9   RADIAL LOCATION OF NEUTRAL AXIS
AND SHEAR CENTER

RADIUS = 48 IN

——— SHEAR CENTER
– – – NEUTRAL AXIS

RADIAL STATION, X/R

CHORDWISE OFFSET FROM 1/4 CHORD ~ IN.

LEADING EDGE

TRAILING EDGE

34
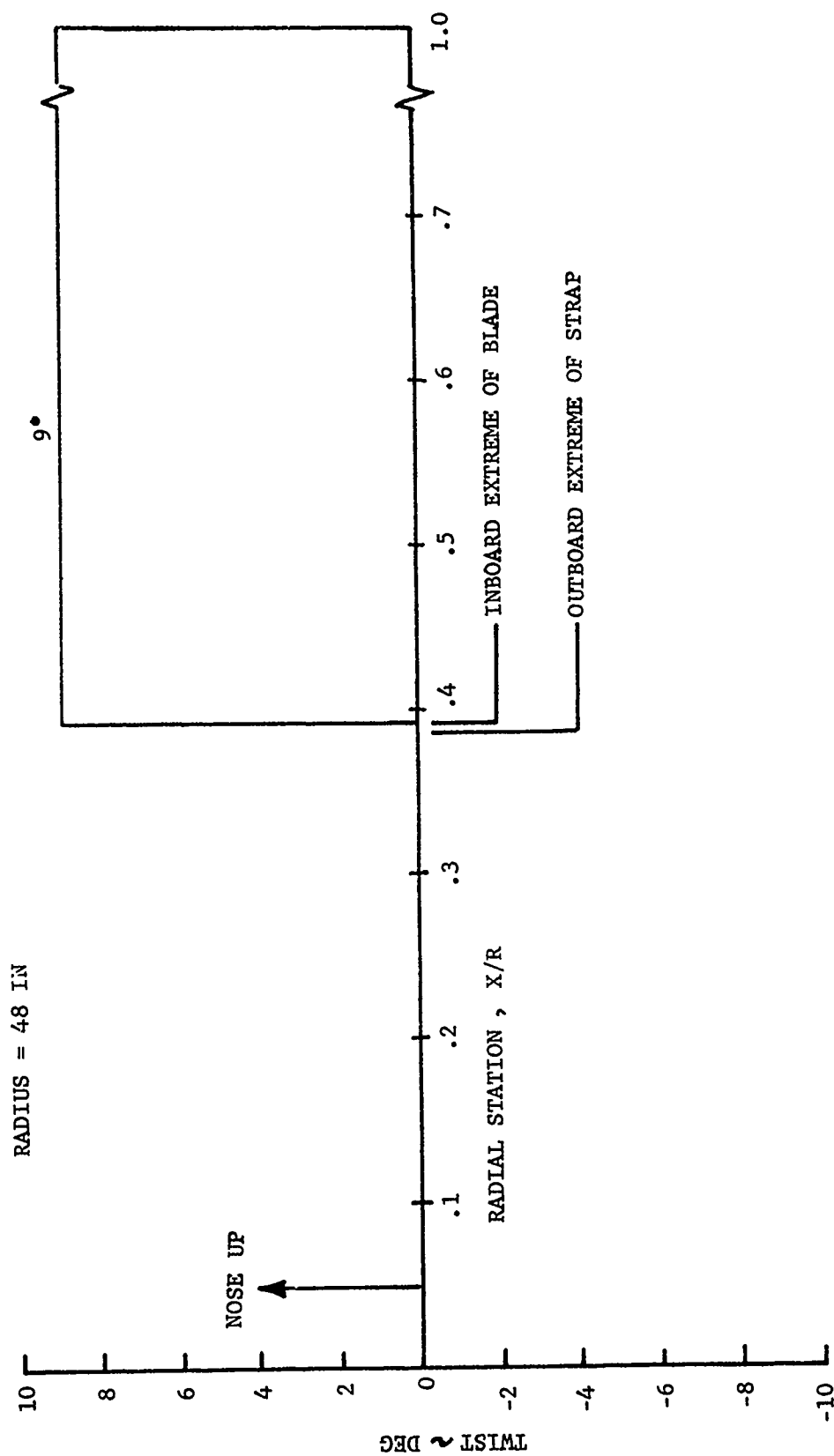
FIGURE 10   UNDEFORMED RADIAL TWIST DISTRIBUTION

35
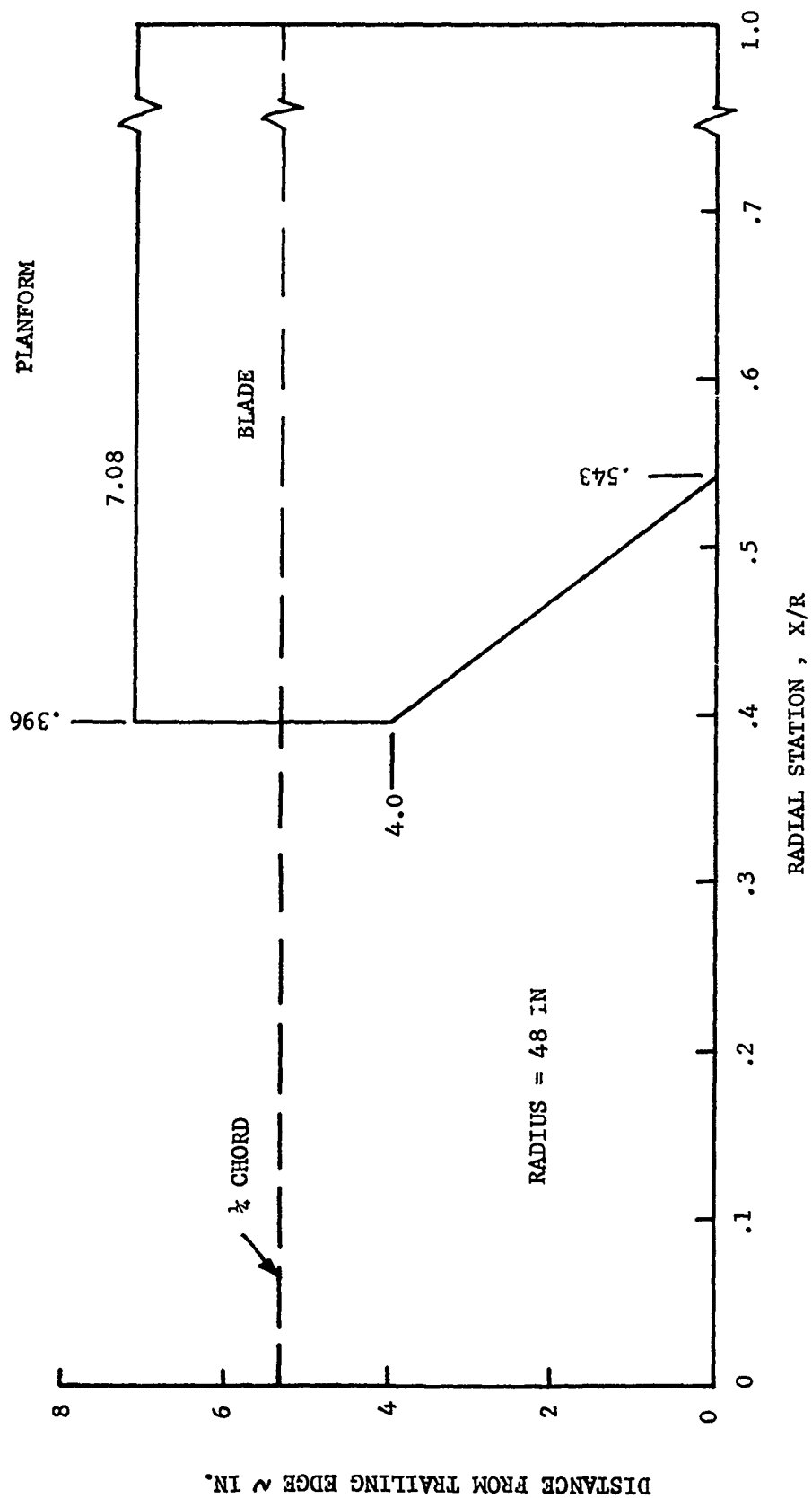
FIGURE 11 RADIAL DISTRIBUTION OF CHORD LENGTH
(PLANFORM)

FIGURE 12   RADIAL DISTRIBUTION OF TORSIONAL STIFFNESS

* CF AND SEVERAL OTHER FACTORS INCREASE
THE EFFECTIVE GJ OF THE STRAP
(SEE SECTION 7.3.3)

37
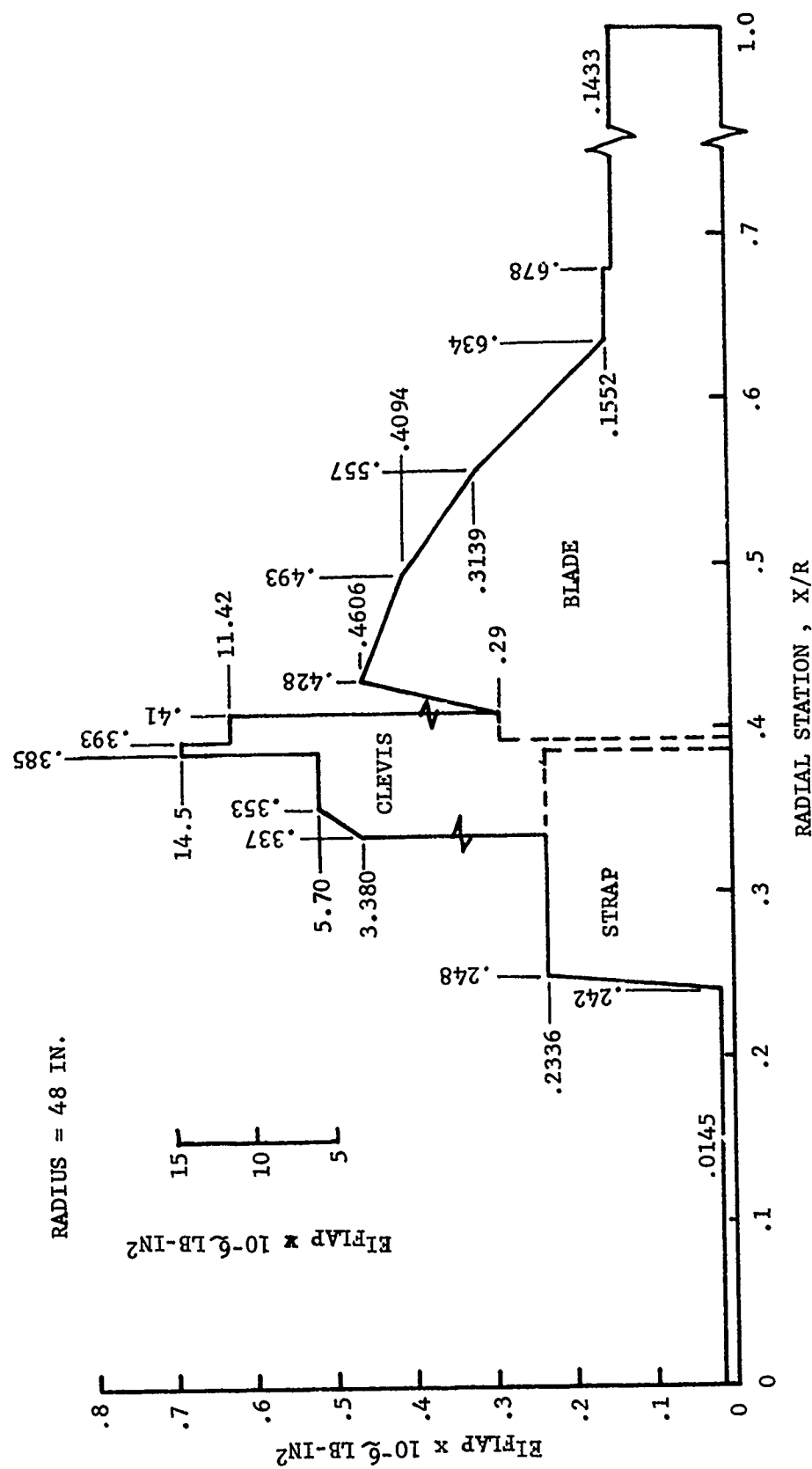
FIGURE 13   RADIAL DISTRIBUTION OF FLAPWISE STIFFNESS
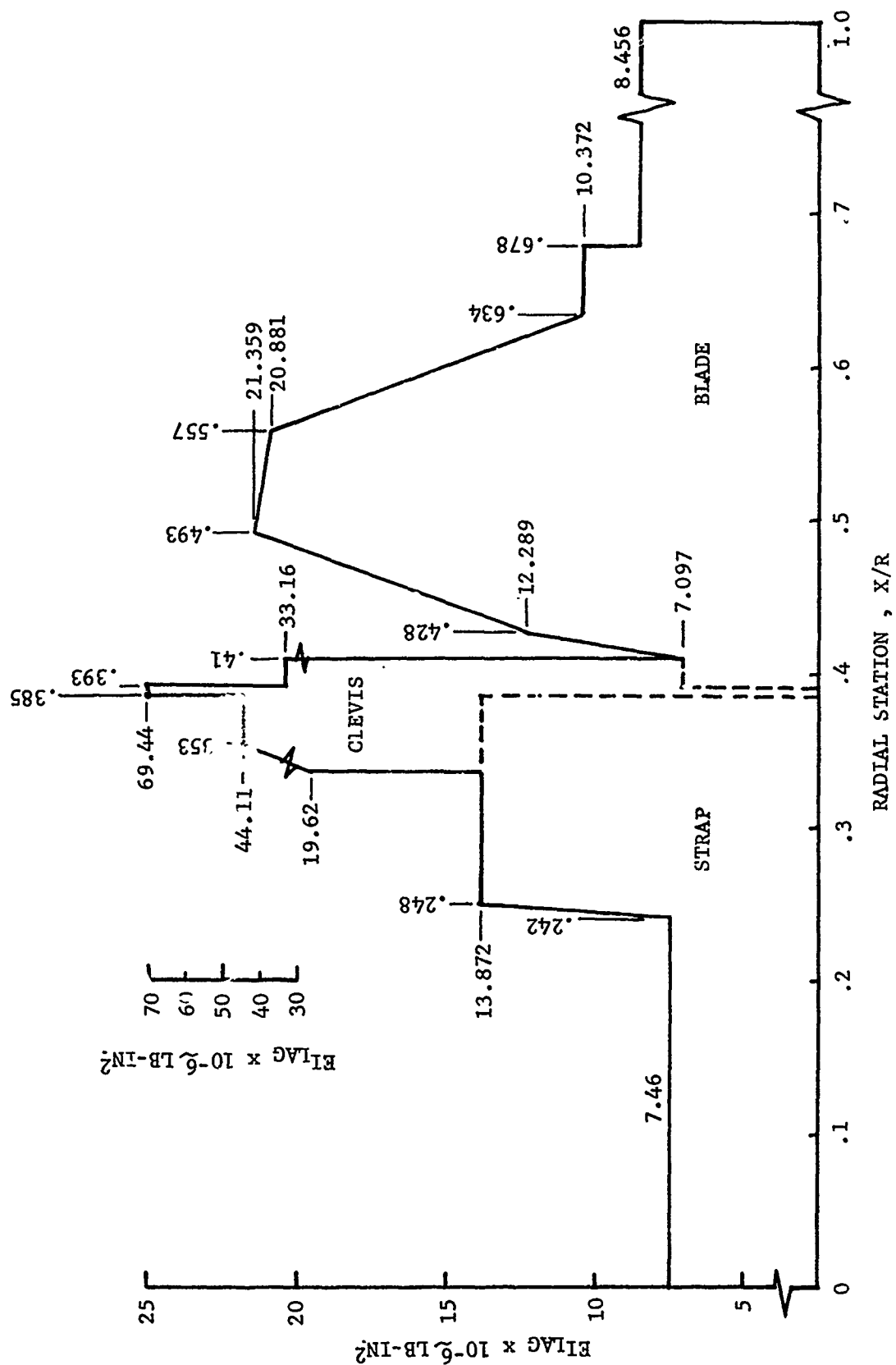
FIGURE 14   RADIAL DISTRIBUTION OF CHORDWISE STIFFNESS
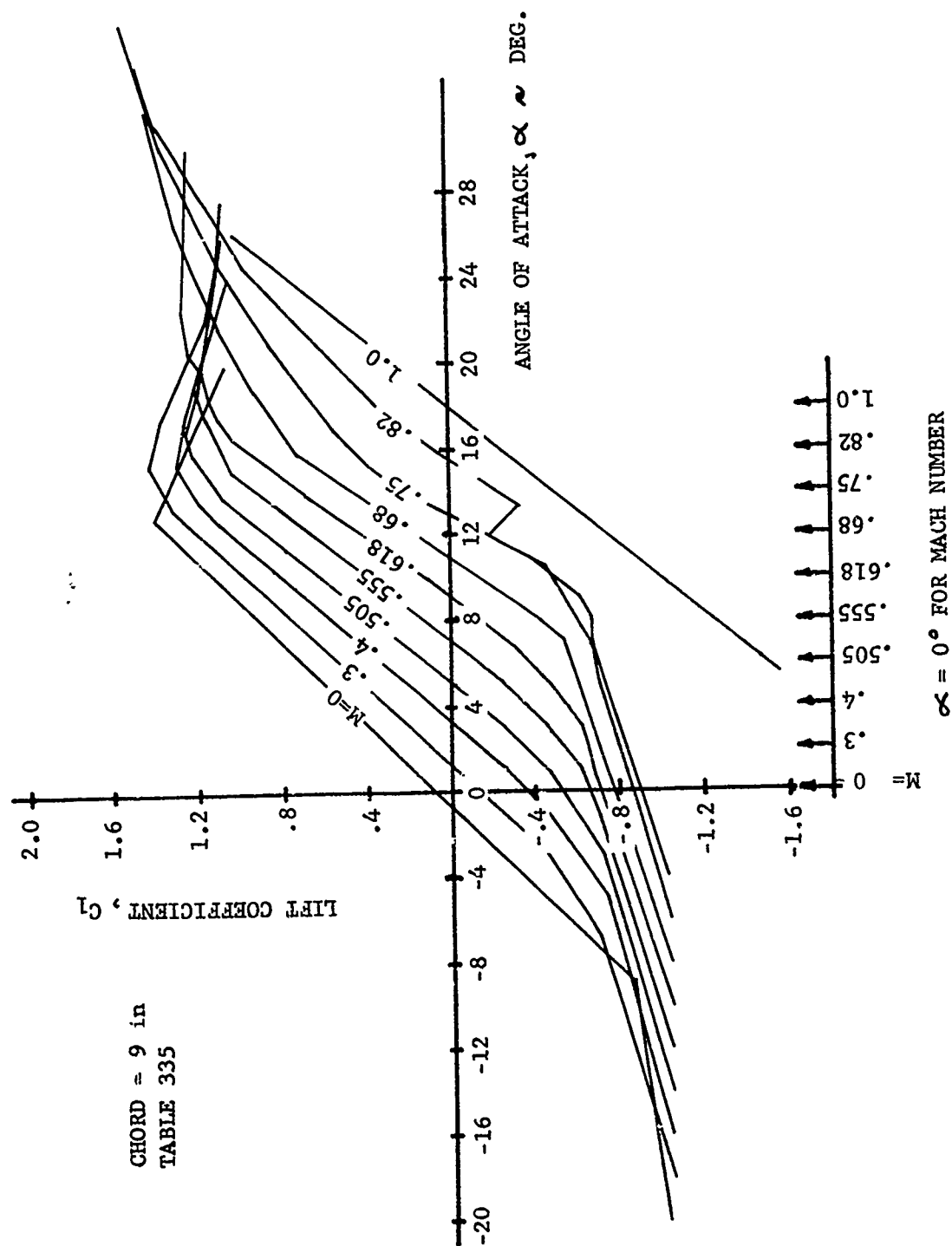
FIGURE 15   VR-7.2 AIRFOIL LIFT COEFFICIENT VERSUS ANGLE OF ATTACK

CHORD = 9 in
TABLE 335

40
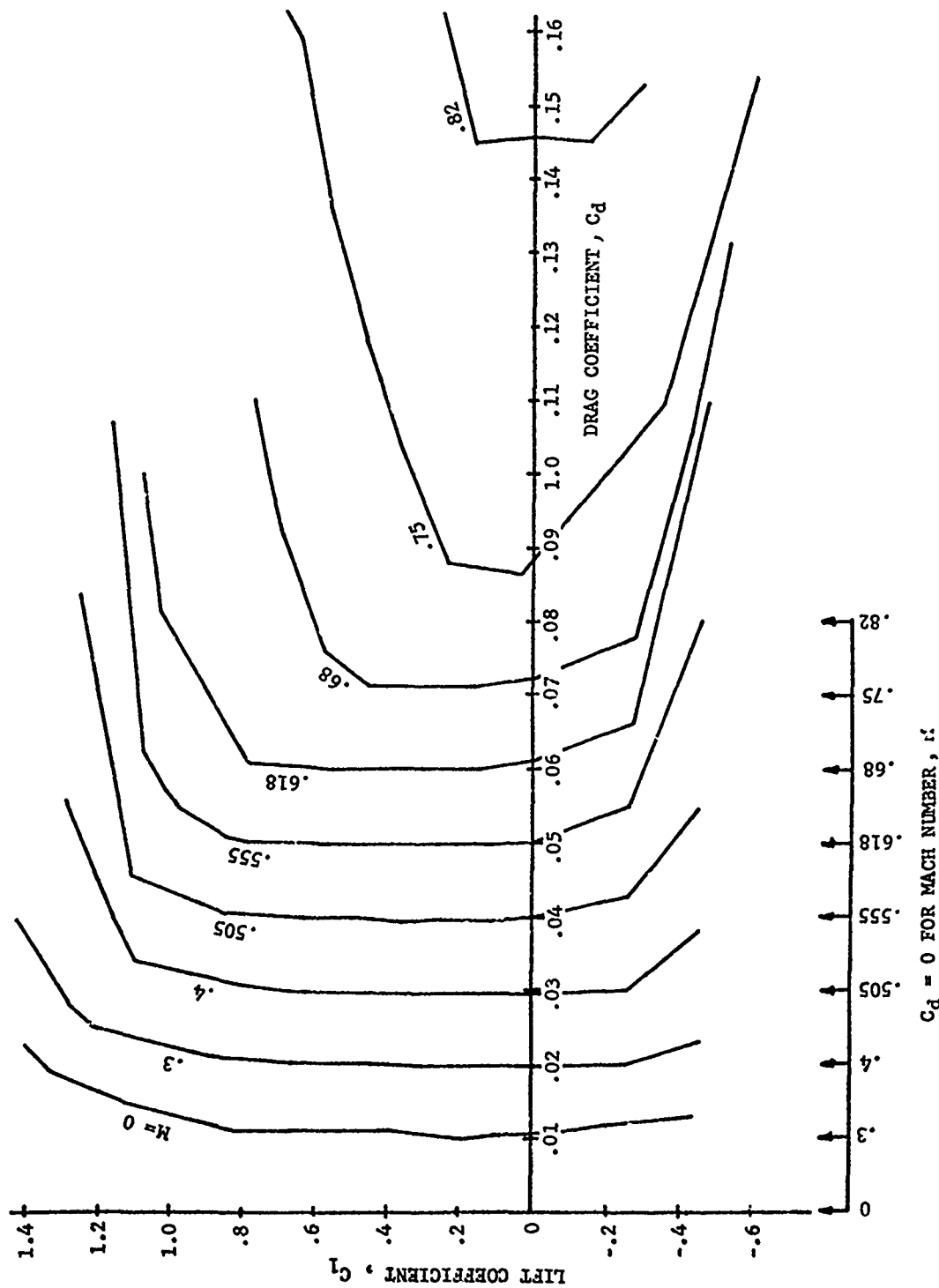
FIGURE 16   VR-7.2 AIRFOIL "LINEARIZED" DRAG POLARS
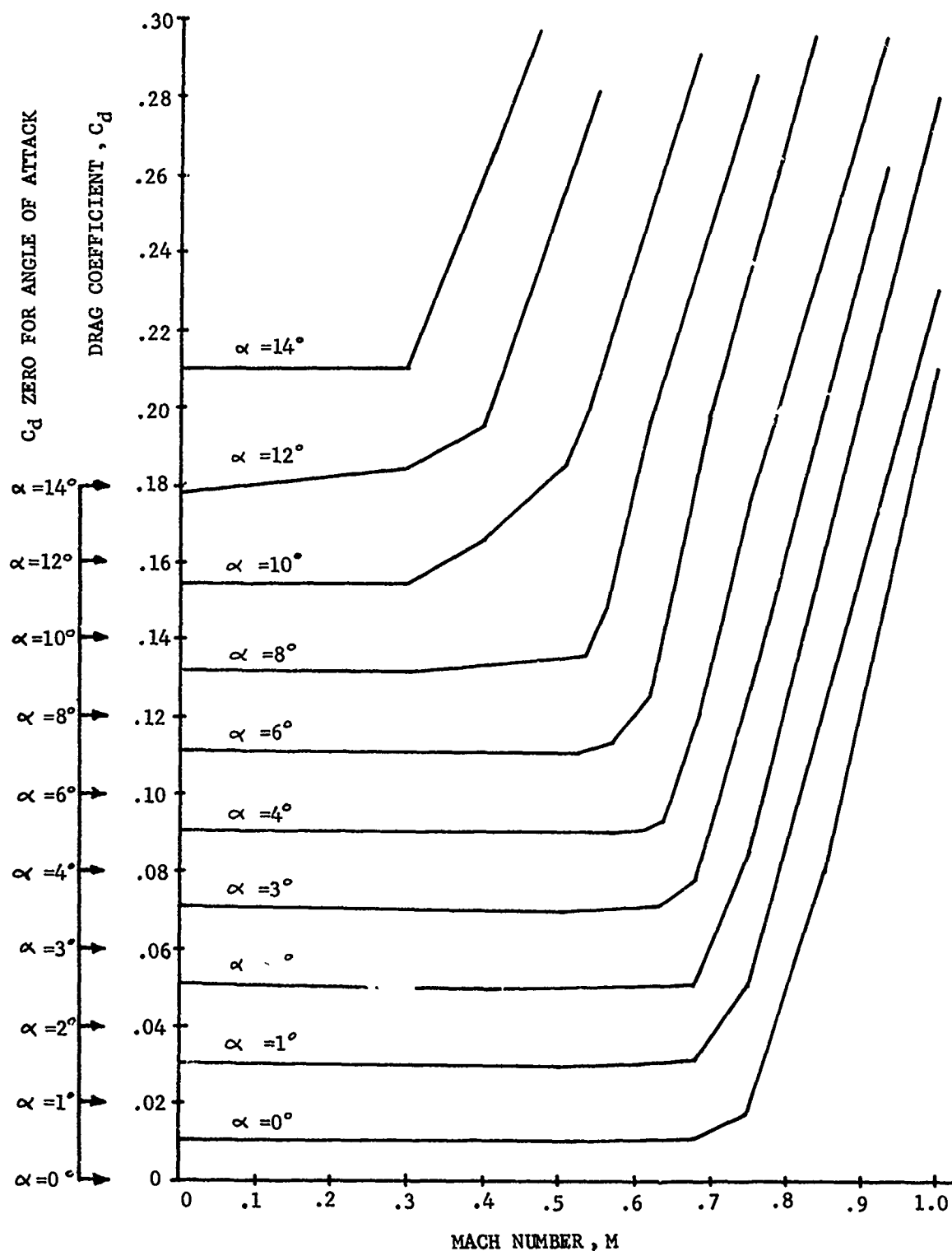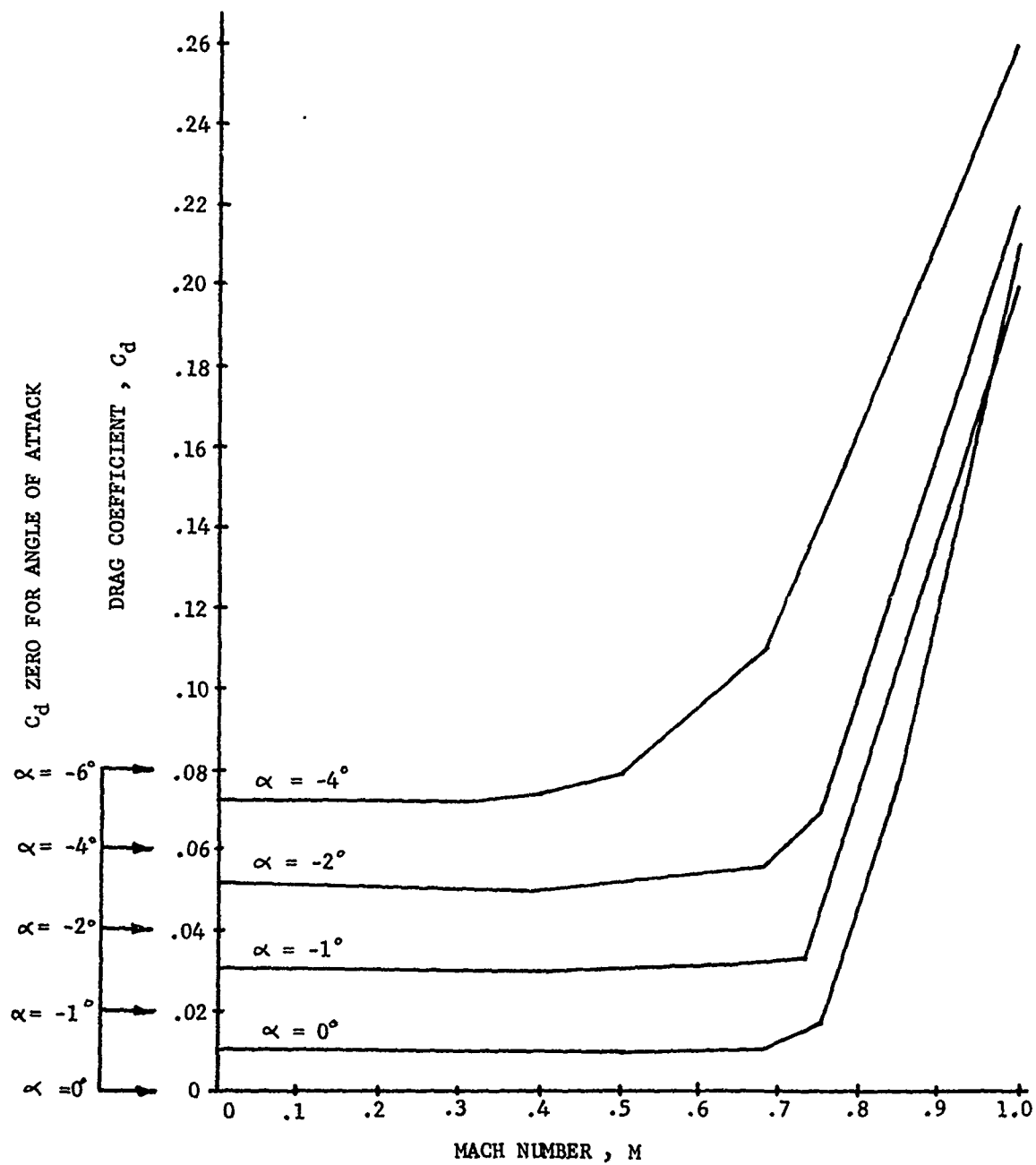
FIGURE 17   VR-7.2 AIRFOIL DRAG COEFFICIENT VERSUS
MACH NUMBER (PART I)

FIGURE 17 VR-7.2 AIRFOIL DRAG COEFFICIENT VERSUS
MACH NUMBER (PART II)

43

FIGURE 18   VR-7.2 AIRFOIL MOMENT COEFFICIENT
            VERSUS MACH NUMBER (PART I)

44

FIGURE 18   VR-7.2 AIRFOIL MOMENT COEFFICIENT
VERSUS MACH NUMBER (PART II)

45
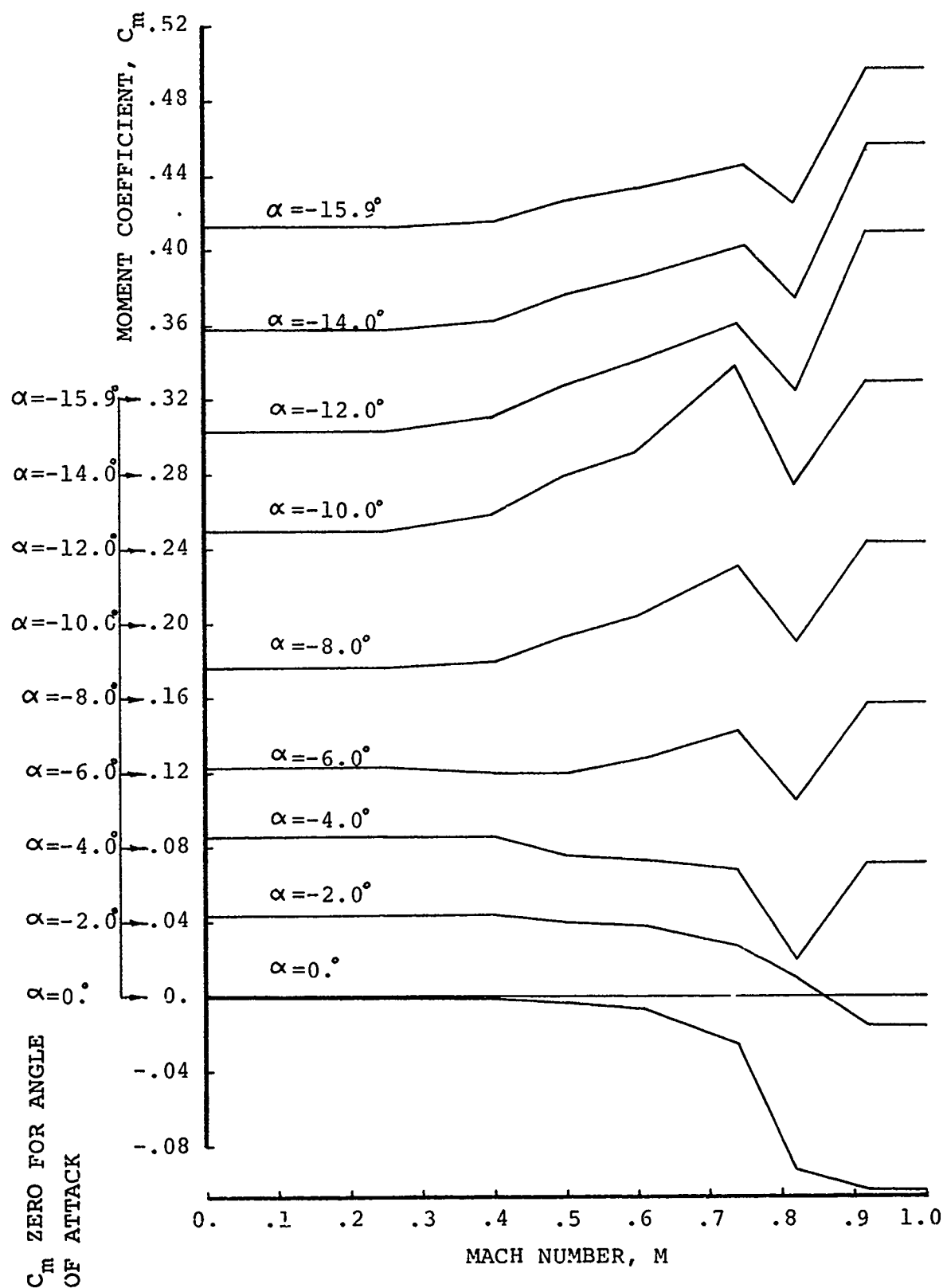
The aerodynamic characteristics for the VR-7.2 airfoil with the 4.5° tab are plotted in Figures 15 through 18. These characteristics are also tabulated as Appendix A of this report.

2.2 Strap and Control System Attachment

The flex-strap retention system is a relatively new method of providing lightweight, bearingless blade retention. The major components of the flex-strap are shown in Figure 19.

These components are, from outboard to inboard:

(1) Blade Clevis - This piece of hardware is an aluminum fitting that is bolted to the strap on the inboard end and bolted to the blade on the outboard end, thus joining the blade to the strap. The clevis is also used to introduce a prepitch angle between the strap and the blade.

(2) Pitch Arm - The pitch arm provides the means of direct control of the blade angle of attack. It is bolted directly to the flex-strap pad area and is oriented by the pitch link.

(3) Flex strap - The flex strap is an all fiberglass member that extends between opposite rotor blades. One clevis and one pitch arm are bolted to each end of the strap along the pad (built up area).

As shown in Figure 19, there are two fiberglass flexure cross-members at the 2-inch span, which are an integral part of the strap assembly. The flexures are designed to provide low resistance to blade flapping, but at the same time react the shear loads resulting from thrust and torque. The model flexures are held in steel tie bars, as shown in Figure 19, which are bolted to the rotor hub.

The geometry of the flex-strap retention system is detailed below. However, it should be noted that this retention system introduces no blade precone or blade droop except as noted in Section 3.4.

The spanwise properties for the components follow.

2.2.1 Flex Strap

The dimensions of the strap and pad are shown in Figure 20. The straps are made of SP250-SF1 fiberglass with a +5° fiber orientation. The pad material is SP250-SF1 fiberglass with a +45° fiber orientation. The details of the basic flex strap and pad configuration are presented in Table 2.

46
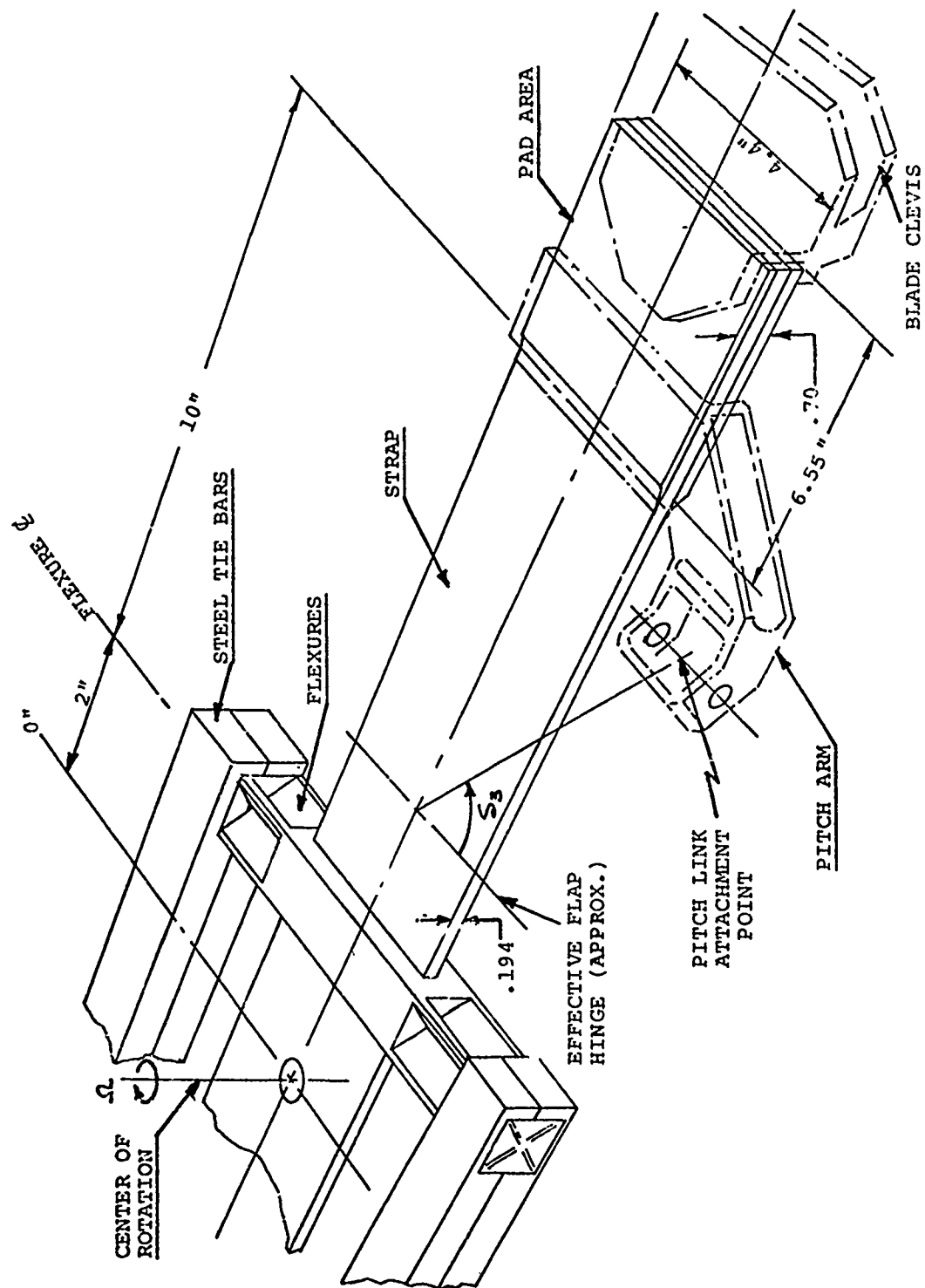
FIGURE 19   TYPICAL CONSTANT WIDTH FLEX STRAP
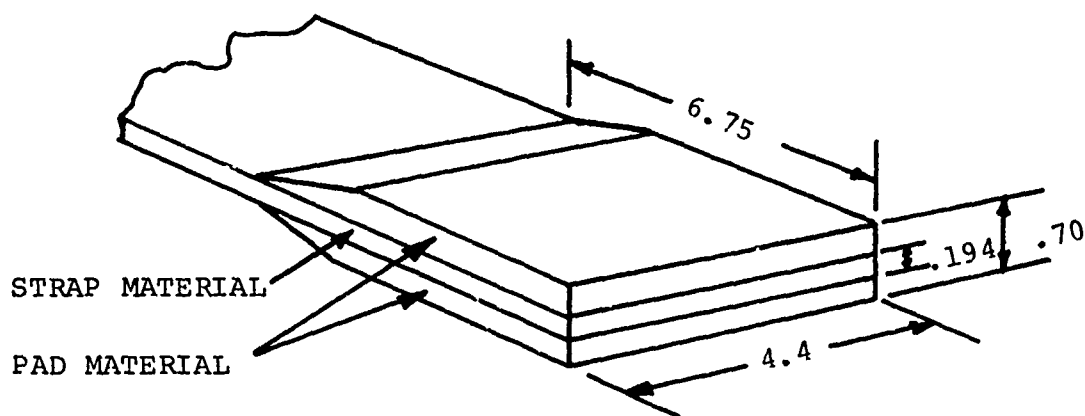
FIGURE 20   DETAIL OF FLEX-STRAP PAD AREA

TABLE 2   BASIC PROPERTIES OF FLEX STRAP
AND PAD

Flex Strap

Width	4.4 in.
Thickness	.194 in.
Effective Length [1]	9.0 in.
Modulus of Elasticity	5.43×10^6 lb-in^2
Density	.079 lb/in^3

(1) The effective length of the strap is the distance
between the outboard side of the flexure to the
inboard side of the pad.

Flex Strap Pad

Width	4.4 in.
Thickness at Pad	.70 in.
Length	6.75 in.
Modulus of Elasticity	1.78×10^6 lb-in^2
"G"	1.76×10^6 lb-in^2

The modulus of elasticity ($E = 5.43 \times 10^6$ lb/in^2), presented in the table for the strap, was measured experimentally. This was accomplished by applying a bending moment to straps 335 and 336 (4.4-inch width) and measuring the strain due to bending. Data from this experiment appears in Figure 21.

The radial distributions for the strap properties are calculated directly from the data in Table 2. These distributions are presented in Figures 7 through 14. In these figures the combined strap and pad are identified as "strap", which extends from the center of rotation to $x/R = 0.385$. Note the pad is the builtup segment between $x/R = 0.242$ and $x/R = 0.385$.

In all of the test configurations, the centerline of the strap passes through the center of rotation and aligns exactly with the blade quarter chord at the junction of the blade and the clevis, $x/R = 0.406$. The only exception is when the blade chordwise position relative to the strap is varied as a parameter. This is detailed in Section 3.6.

2.2.2 Pitch Arm

The baseline pitch arm (P/N CR037H246) is designed to provide $-65°$ of δ_3 coupling. The δ_3 coupling is a flap-pitch coupling (flapup-noseup positive), which results primarily from the location of the attachment point of the pitch arm to the pitch link relative to the effective flapping hinge. This is indicated in Figure 19.

The pitch arm is bolted across the pad area over a relatively short span section, as shown in Figure 22. This piece of hardware has a negligible influence on the radial stiffness distributions. The weight and inertia of the pitch arm, however, are not negligible. These properties, measured from an existing pitch arm, are presented in Table 3.

The stiffness of this pitch arm, between the point of attachment of the pitch arm to the pitch link and the attachment point of the pitch arm to the flex strap, was determined in the out-of-plane direction. This stiffness is 76,923 lb/in. The stiffness in the inplane direction was not determined but may be considered to be at least as stiff.

For several periods of testing, a pitch arm balance weight was used to move the chordwise center of gravity of the pitch arm to the strap centerline. This weight was bolted to the pitch arm on the side opposite to the pitch link attachment point. Although this weight is not one of the specific parameters studied in this report, its spanwise weight and inertia distributions have been included in Figures 7 and 8 for reference.
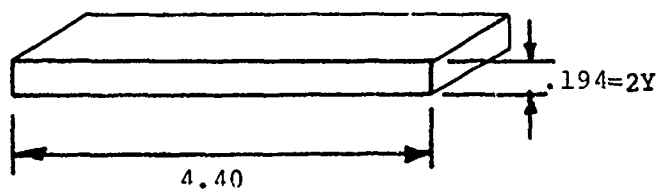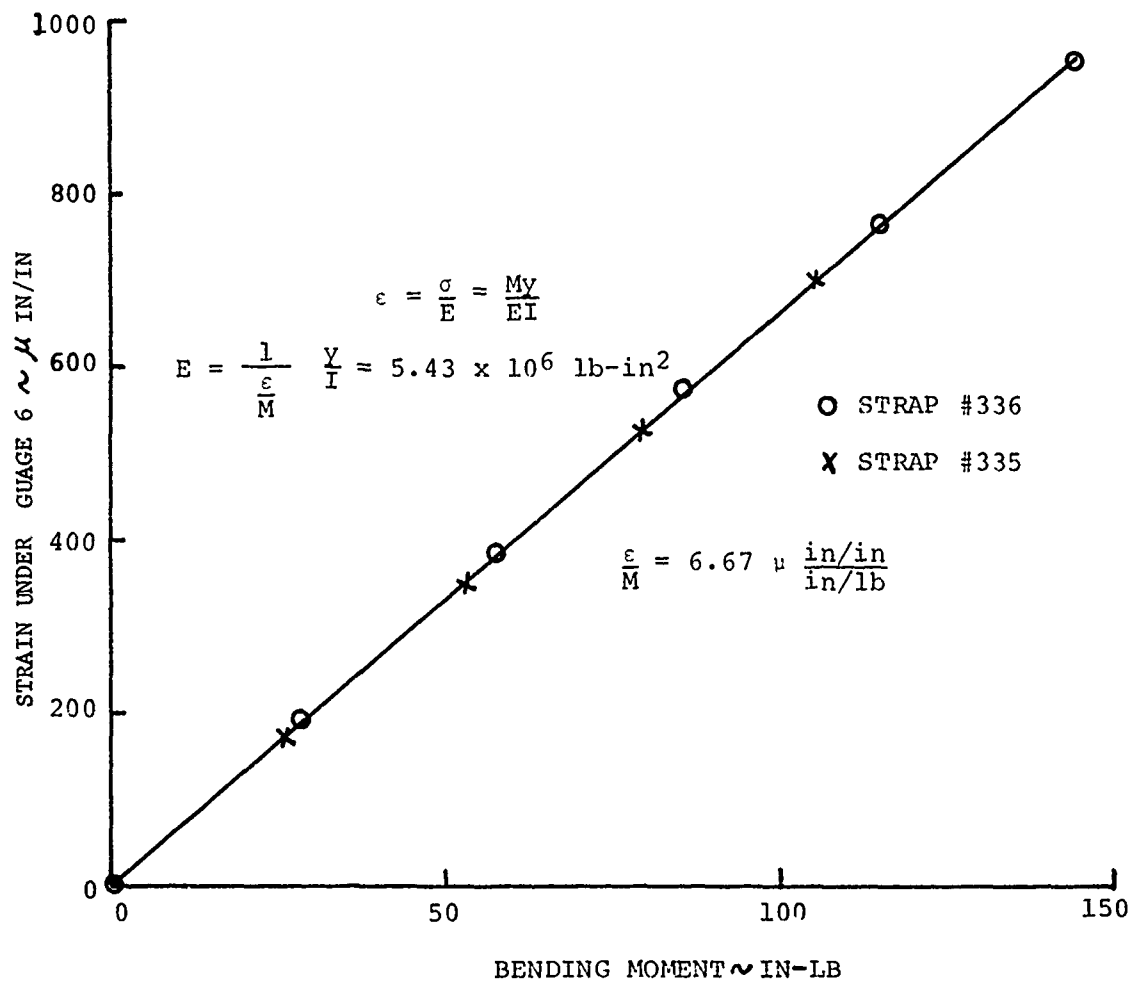
FIGURE 21   MODULUS OF ELASTICITY (E) – CALIBRATION
FOR 4.4-INCH STRAP

2.2.3 Blade Clevis

The clevis is used primarily for two purposes--to retain the blade and to orient the blade relative to the strap. Blade sweep is introduced by using eccentric bushings at the blade-to-strap attachment point or at the strap-to-clevis attachment. The clevis also prepitches the blade relative to the strap at span station $x/R = 0.387$. Information on the range of these parameters is presented in Sections 3.1 and 3.4.

The blade clevis designated part CR037H251-1 is considered to be the baseline clevis for the 8-foot tail rotor model tests. This clevis, shown in Figure 22, provides 9° of prepitch (for a flat strap, the $\theta_{.75R} = 9°$) with a blade sweep of 11° aft and a predroop of 1.76°. These angular rotations are explained in more detail in Section 3.4.

The measured basic properties for the clevis are shown in Table 4. These properties were used to determine the distributed clevis properties presented in Figures 7 through 14. The weight and inertia of the clevis in these distributions are assumed to extend over the entire length of the clevis, $x/R = .323$ to $x/R = .427$. The clevis sitffnesses, however, contribute to the total distributed stiffnesses only between the blade attachment point $x/R = 0.406$ and the most inboard connection of the clevis to the strap, $x/R = 0.337$.

2.3 Control System

The control system is the complete mechanism for the introduction of collective or cyclic pitch for the 8-foot tail rotor model. A photograph of the model control system appears in Figure 23. The component parts of the control system from the hub down, as the model was mounted on the test stand, are:

- the model hub
- the pitch arms
- the pitch links
- the swashplate
- three hydraulic control actuators
- a spacer
- the test stand (Section 2.5)

A feedback control system is used to remotely position the control actuators for collective and cyclic pitch. This system operated Moog hydraulic valves on the test stand. Valve control voltages which position the actuators were determined by subtracting the command voltage generated from the position selected in the control room from the true swashplate position voltage measured by three position potentiometers, one on each of the actuator rods.

ROTATION

3.5

11.35
11.6
11.85
12.35

13.35
13.9

PITCH ARM
CRO37H246-1

16.15

CLEVIS
CRO37H251

17.55

19.5
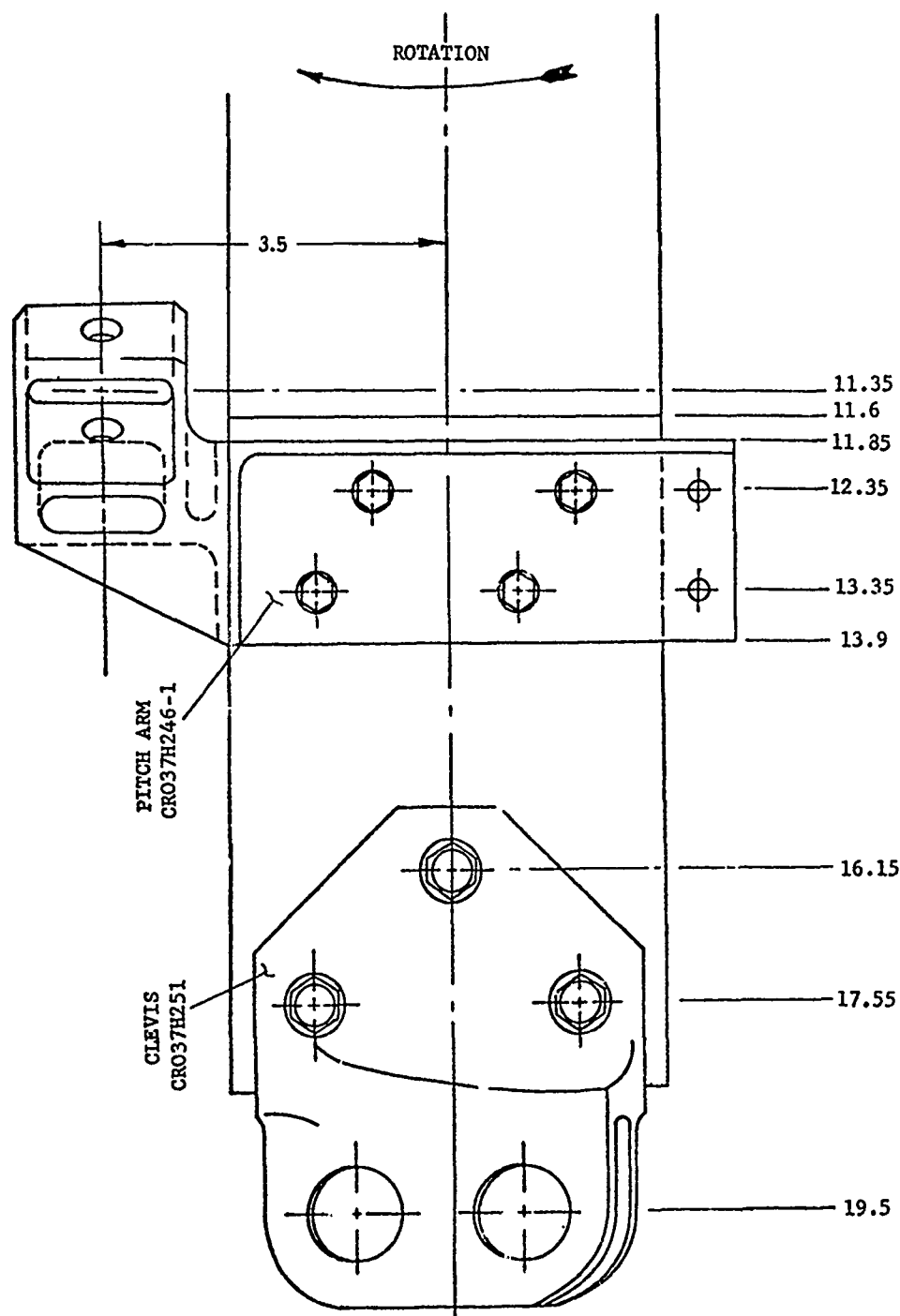
FIGURE 22   DRAWING OF $\delta_3 = -65°$ PITCH ARM AND 9°
CLEVIS MOUNTED ON STRAP PAD

52

TABLE 3   BASIC PROPERTIES OF PITCH ARM

PITCH ARM (P/N CR037H246)

($\delta_3 = -65°$ Configuration)

Weight	.6017 lb
I_{xx}	.0079 lb-in-sec^2
I_{yy}	.0050 lb-in-sec^2
I_{zz}	.0160 lb-in-sec^2

Note: Measured from a test pitch arm, excluding bolts.

TABLE 4   BASIC PROPERTIES OF BLADE CLEVIS

CLEVIS (P/N CR037H25101)

(9° Clevis Angle)

Weight	.9913 lb
I_{xx}	.00935 lb-in-sec^2
I_{yy}	.0218 lb-in-sec^2
Modulus of Elasticity	10.5×10^6 lb-in^2
"G"	6×10^6 lb-in^2

Note: Measured from a test clevis, excluding bolts.
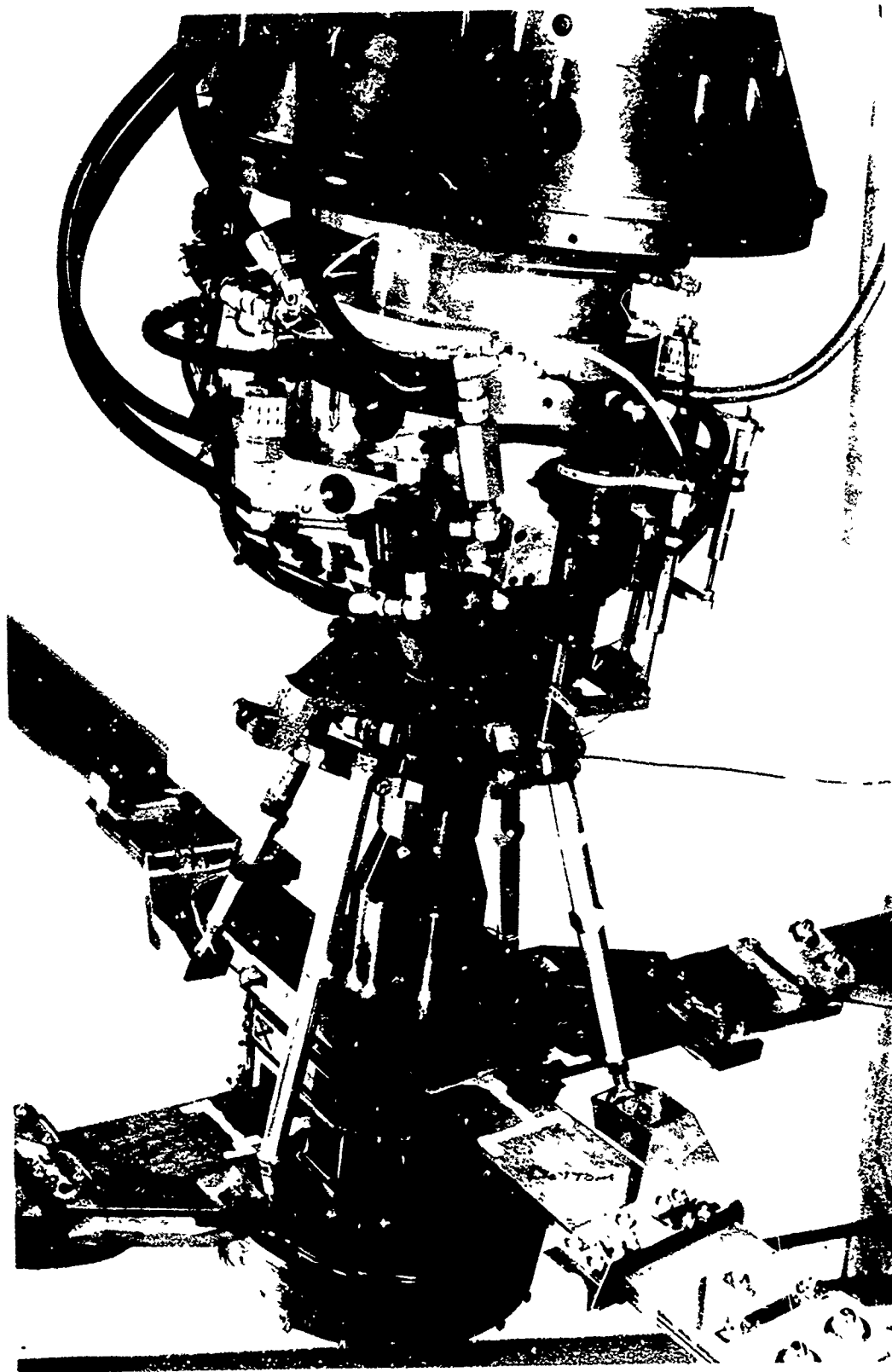
FIGURE 23 MODEL UPPER ASSEMBLY - CONTROL SYSTEM

54

Two actuators are diametrically opposed on the swashplate, providing one cyclic component by differential motion. The third actuator is positioned 90° away from the other two and provides the other cyclic input by moving independent of them. Collective pitch control is gained by moving all three actuators simultaneously.

The control system properties for the baseline $\delta_3 = -65°$ rotor configuration were determined. A schematic drawing of the components considered in this configuration is shown in Figure 24. As indicated in this figure, the total control system stiffness is determined by the stiffnesses of the pitch arm, the pitch link, the stationary swashplate, and the actuator. (The actuator is mounted to the rigid stand.) The flexibilities for these components are presented in Table 5. The total control system stiffness determined from this data is 12,308 lb/in.

The swashplate used during the model testing was weighed to determine its mass. It was found that the rotating swashplate weighs 4.5 lb and the stationary swashplate weighs 16.4 lb, for a total of 20.9 lb.

Some consideration was given to the damping present in the total model control system. While no data or measurements have been taken which directly indicate the damping inherent in this system, from experience, a value of 0.01 to 0.02 critical effective viscous damping may be reasonably assumed to exist.

2.4 Model Drive System

The 8-foot-diameter tail rotor model drive system and motor are mounted in the Dynamic Rotor Test Stand (DRTS). The orientation of the DRTS as it was mounted in the wind tunnel for test phases BVWT 124 and 129 is detailed in Section 2.5. Figure 25 shows the position of the major components of the drive system in the DRTS and their inertias. As shown, the motor and drive shafts lie immediately below the model and are directly aligned with it.

The electric motor in the figure is a 400-hp, variable frequency motor that drives the model through a speed-reducing transmission. The motor is limited to a maximum speed of 9500 rpm. The reducing transmission is a 5:1 planetary gearbox that gives the model a maximum speed of 1900 rpm. The inertia of the motor is 14.61 lb-in-sec^2.

Directly above the electric motor and transmission is a steel shaft section with an inertia of 0.030 lb-in-sec^2. The torsional stiffness and length for this shaft and the upper shaft sections are shown in Figure 26. The length of the steel shaft is 14.33 inches and its stiffness is 1.551×10^6 in-lb/rad.

PITCH ARM
$\delta_3 = -45°$ P/N CR037H274
$\delta_3 = -65°$ P/N CR037H246

Ω

Z

Y

UPPER FLEX STRAP

LOWER FLEX STRAP

X

LOWER FLEX STRAP
PITCH LINK

UPPER FLEX STRAP
PITCH LINK

$\delta_3 = -45°$ P/N CR037H249-4
$\delta_3 = -65°$ P/N CR037H249-1

NOMINAL LENGTHS OF PITCH
LINKS
$\ell(\delta_3 = -45°) = 13.18$ IN
$\ell(\delta_3 = -65°) = 14.88$ IN

$\delta_3 = -45°$ P/N CR037H249-5
$\delta_3 = -65°$ P/N CR037H249-4

NOMINAL LENGTHS OF PITCH
LINKS
$\ell(\delta_3 = -45°) = 13.77$ IN
$\ell(\delta_3 = -65°) = 13.68$ IN

HYD. ACTUATORS

OFFSET OF LOWER PITCH LINK
ATTACHMENT PT. FROM
$\mathcal{L}$ =3.783 in.

$\mathcal{L}$

FIGURE 24 COMPONENTS OF $\delta_3 = -65°$ CONTROL SYSTEM

56

TABLE 5   STIFFNESS CHARACTERISTICS OF THE CONTROL
          SYSTEM, $\delta_3 = -65°$

	Axial Deflection
Pitch arm - upper flex strap	.00001300
Pitch link - upper flex strap	.00000435
Stationary swashplate	.0003067
Actuator	.0000010005
Total Deflection	.00032505 in

$$\text{Axial spring constant} = \frac{1}{.00032505} = 3076 \text{ lb/in}$$

	Axial Deflection
Pitch arm - lower flex strap	.00001300
Pitch link - lower flex strap	.00000430
Stationary swashplate	.0003067
Actuator	.0000010005
Total Deflection	.00032500 in

Axial spring constant = 3077 lb/in

TOTAL CONTROL SYSTEM STIFFNESS = 4 x 3077 = 12,308 LB/IN

STRAPS ARE LOCATED 1.0 IN.
ABOVE AND BELOW HUB CENTER

ROTOR HUB SECTION
WITHOUT BLADE

I_Z=.141 lb-in-sec^2
W =30. lb

ALUM. TUBE WITH
FLEX COUPLING
I_Z=.075 lb-in-sec^2
I_Y=.928 lb-in-sec^2
W =10. lb

STEEL SHAFT
I_Z=.030 lb-in-sec
I_Y=.6073 lb-in-sec
W =11. lb

5:1 REDUCTION

ELECTRIC MOTOR
I_Z=14.61 lb-in-sec^2
W =300 lbs

SHAFT PIVOT POINT
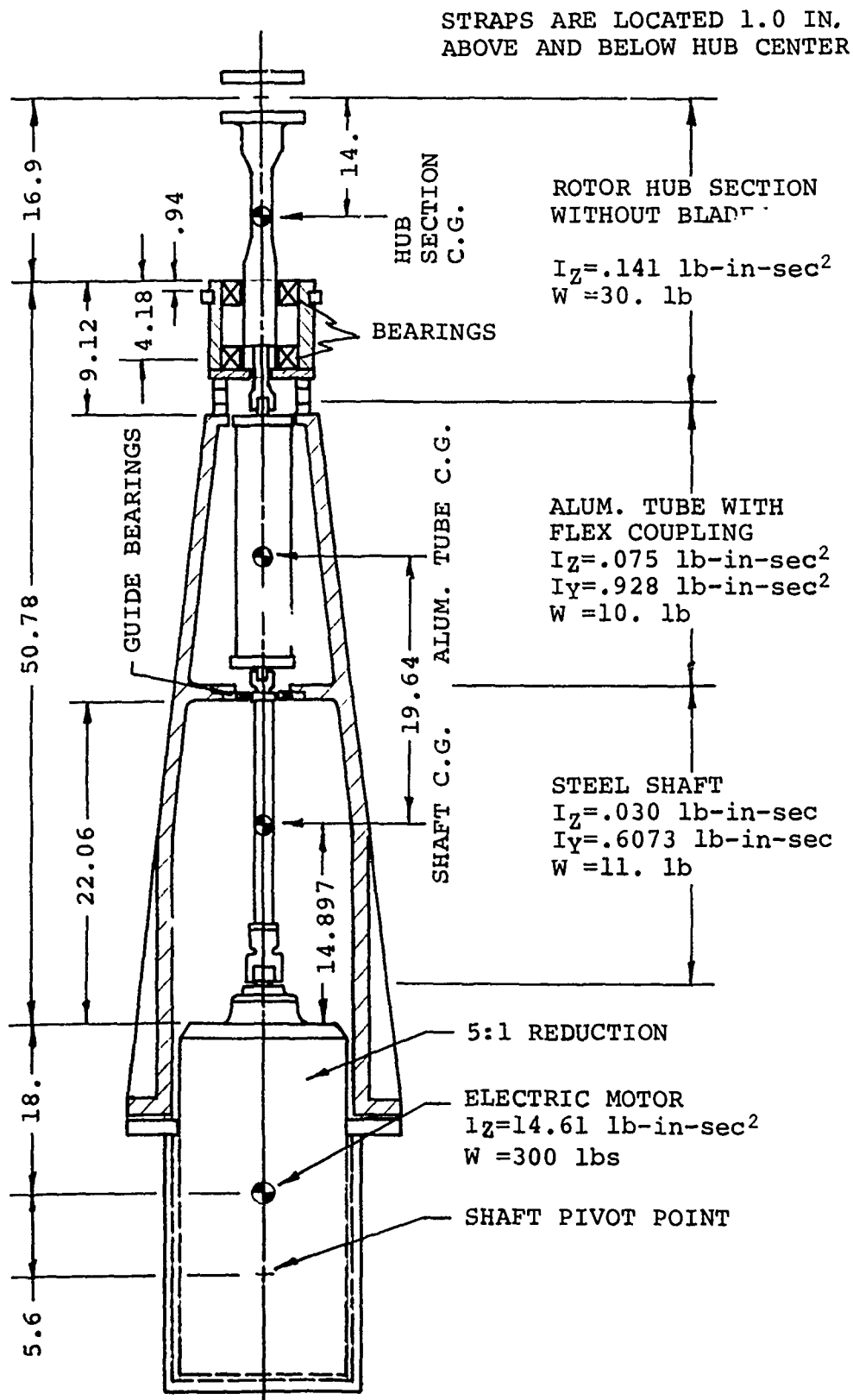
FIGURE 25   DRIVE SYSTEM INERTIA PROPERTIES

58

$K_{HUB} = 17.36 \times 10^6$ in-lb/rad
$\ell = 10.775$ in.

K_1, ℓ_1
K_2, ℓ_2
K_3, ℓ_3
K_4, ℓ_4
K_5, ℓ_5

$.61787 \times 10^6 \dfrac{\text{in-lb}}{\text{rad}}$

$K_6 = .8458 \times 10^6$ in-lb/rad
$\ell_6 = 14.25$ in.

$.43088 \times 10^6$ in.-lb/rad

$K_7 = 1.551 \times 10^6$ in-lb/rad
$\ell_7 = 14.326$ in.

5:1 REDUCTION

SHAFT PIVOT POINT

$K_1 = 5.9975 \times 10^6$ in-lb/rad
$K_2 = 4.9609 \times 10^6$ in-lb/rad
$K_3 = 146.37 \times 10^6$ in-lb/rad
$K_4 = 64.224 \times 10^6$ in-lb/rad
$K_5 = 22.010 \times 10^6$ in-lb/rad

$\ell_1 = 1.875$ in.
$\ell_2 = 4.25$ in.
$\ell_3 = 2.56$ in.
$\ell_4 = 2.56$ in.
$\ell_5 = 4.00$ in.
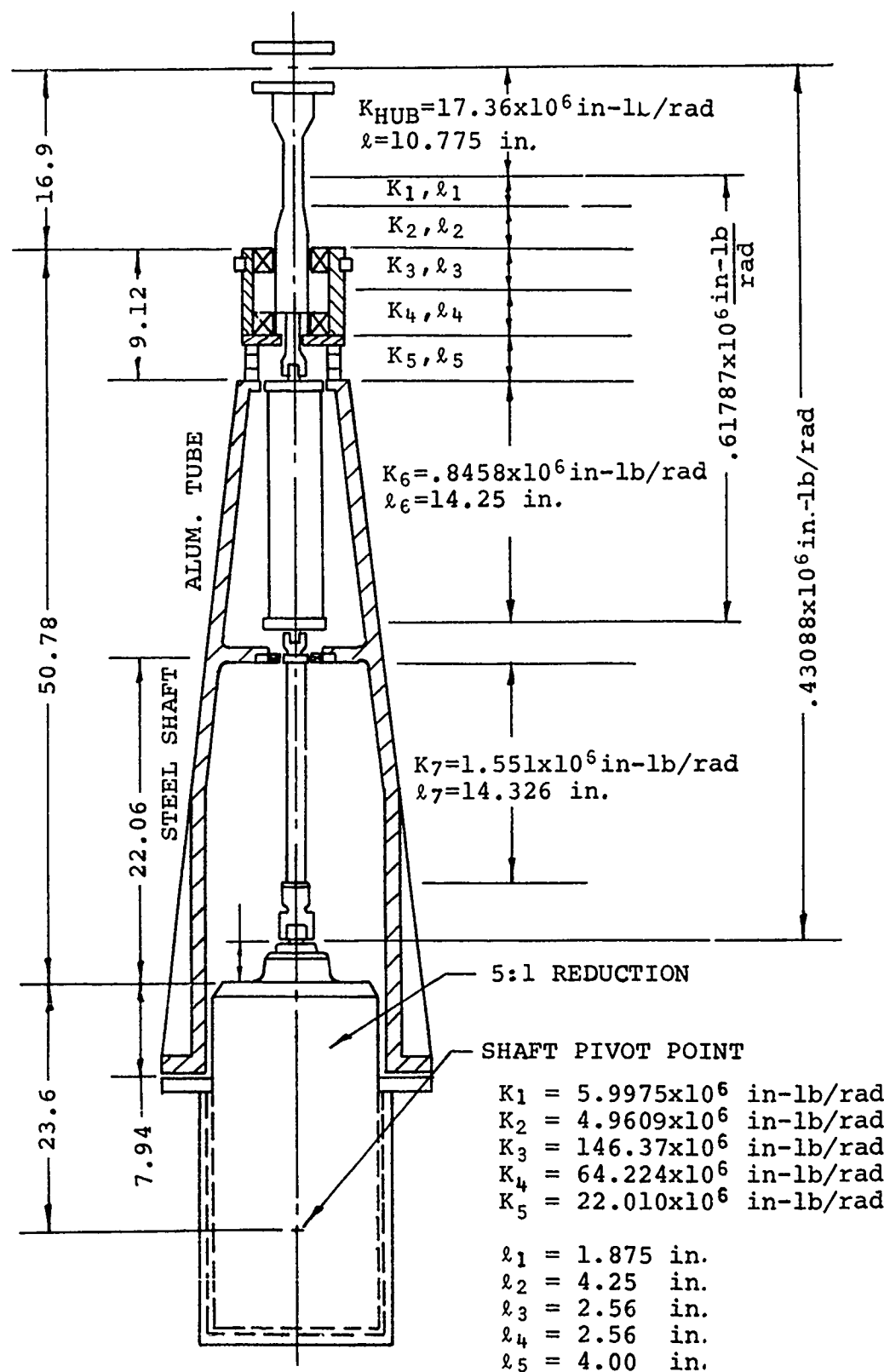
FIGURE 26   DRIVE SYSTEM PYSICAL DIMENSIONS AND STIFFNESS PROPERTIES

59

Between the steel shaft and the hub section is an aluminum tube section with flex couplings. The inertia of this section is 0.075 lb-in-sec^2; the stiffness is 0.8458 x 10^6 in-lb/rad; and the length is 14.25 inches.

Above the aluminum shaft section there are several shorter sections that have negligible inertia compared to the major shaft components. The lengths and stiffness of these components are indicated on Figure 26. The inertia of the rotor hub is 0.141 lb-in-sec^2 with blades removed.

2.5 Test Stand

The 8-foot-diameter tail rotor model was mounted on the Dynamic Rotor Test Stand (DRTS), which incorporates the 400-hp variable frequency motor, Section 2.4. A sketch of the DRTS as it was installed in the wind tunnel test section is shown in Figure 27. The principal portion of the DRTS, which contains all of the dynamic components of the test stand detailed in Section 2.4, is positioned between the test section stations 1000 and 1055 in this drawing. The pivot of the motor, shown in Figure 25, corresponds to the test section station 1055.

As shown in the figure, the major components of the test stand are:

- the model
- the DRTS-containing motor
- a short cannon
- the Gilmore strut, which is cantilevered to the tunnel floor structure

For the two test phases BVTC 009 and BVTC 011, the model was disconnected from the short cannon at station 1157.5 and joined to a rigid floor mount. A photograph of this arrangement with the model installed in the hover test cell was presented in Figure 6.

In the two sections which follow, information providing the dynamic and additional static characteristics of the stand is provided.

2.5.1 Test Stand Shake Test

A shake test to determine the natural frequencies and mode shapes of the test stand was conducted at the range of frequencies which may influence the dynamics of the rotor. Excitations were input to the shaft immediately below the rotor hub in both the lateral and longitudinal directions (each direction excited separately). The frequency of excitation was varied from 10 cps to over 200 cps.
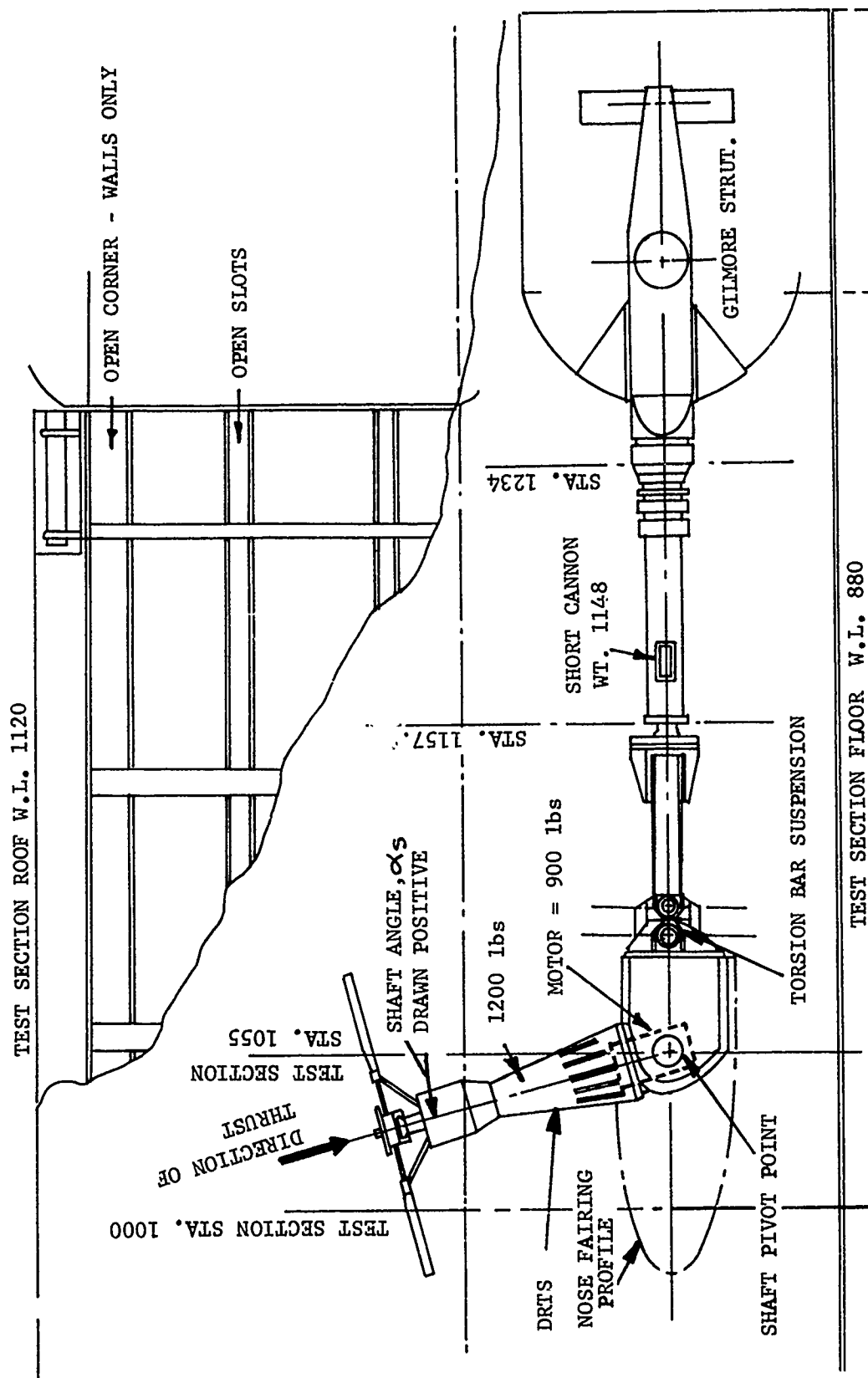
FIGURE 27   INSTALLATION DETAILS – DRTS
IN TEST SECTION

TEST SECTION ROOF W.L. 1120

OPEN CORNER – WALLS ONLY

OPEN SLOTS

GILMORE STRUT.

STA. 1234

SHORT CANNON
WT. 1148

STA. 1157.

TORSION BAR SUSPENSION

TEST SECTION FLOOR W.L. 880

SHAFT ANGLE, α_s
DRAWN POSITIVE

1200 lbs

MOTOR = 900 lbs

TEST SECTION
STA. 1055

DIRECTION OF
THRUST

TEST SECTION STA. 1000

DRTS

NOSE FAIRING
PROFILE

SHAFT PIVOT POINT

61

With the mo⁝ ⁝ hub, adapter hardware, and blades removed, as
the longitu ⁝al excitation was applied, a single mode of re-
sponse was observed at 210 cps, as shown in Figure 28. No
additional mode was observed using lateral excitation. The
frequency of the mode dropped as the adapter hardware, hub,
and blades were replaced. The recorded frequency of this mode
in the baseline configuration was 46 cps. The further addition
of several available hub weights provided a sensitivity of the
mode to hub weight. No other mode was observed throughout the
shake test using either longitudinal or lateral excitation.

The shape of the mode was determined. This was accomplished
by reading the accelerations at several stations along the
upper portion of the test stand, using a "roving" accelerometer
while shaking the test stand at the resonant frequency. These
results appear in Figure 29. As shown in the figure, the
motion of the hub is due primarily to deflection of the shaft.
The motion of the DRTS appeared to be small and may therefore
be neglected.

2.5.2 Detail of Test Stand Components and Dimensions

The components of the complete test stand installation were
listed above and are shown in Figure 27. As shown in the
figure, the entire motor drive system detailed in Section 2.4
is contained in the DRTS above the shaft pivot point (near motor
c.g.), at test section station 1055. The other dimensions of
the installation are shown in the figure.

The model shake test results of Section 2.5.1 indicate that the
only significant flexibility, relative to the model, is in the
shaft of the drive system. Therefore, the static lateral stiff-
ness at the rotor hub in the plane of the blades was deter-
mined. This stiffness is 0.2193×10^{-6} in/lb-in for moments
applied at the rotor hub. For inplane hub shears the hub
section is effectively rigid, therefore the reference distances
of 20.5 and 18.5 inches should be used to convert to moments
for the two straps (see Figure 25).

The orientation of the model relative to the flow of air, which
is from left to right in Figure 27, was determined by the
Gilmore Strut and by the angle at the shaft pivot point. For
the four test phases considered in this report, pivoting at the
shaft pivot point was exclusively used to orient the model.
The resulting shaft angle, α_S, as indicated in the figure, is
positive when the DRTS is rotated into the wind-producing flow
up through the rotor.
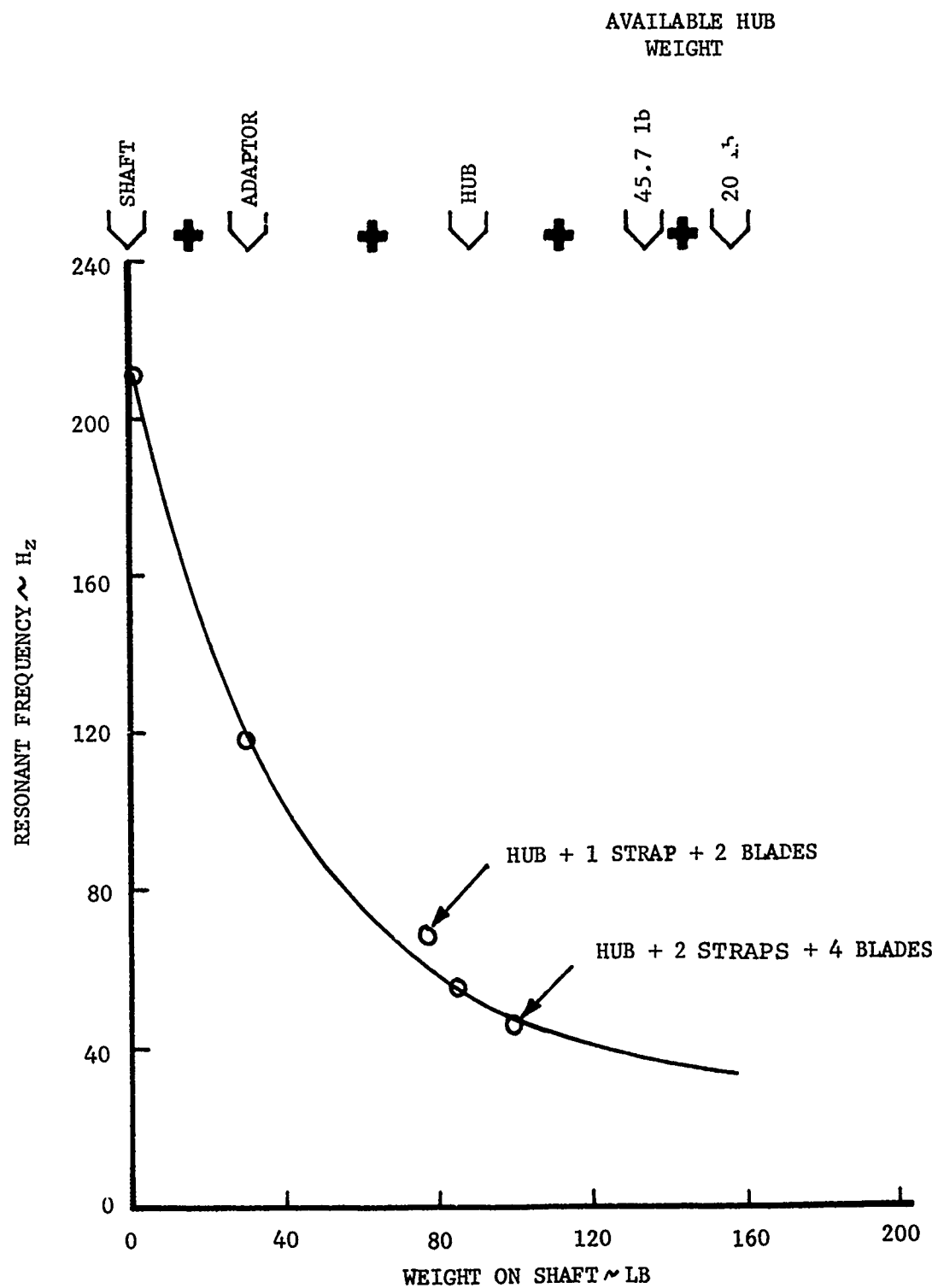
FIGURE 28   EFFECT OF WEIGHT ON TEST
                   STAND NATURAL FREQUENCY

HUB WEIGHTS ON SHAKER FREQUENCY = 29.5 H_z
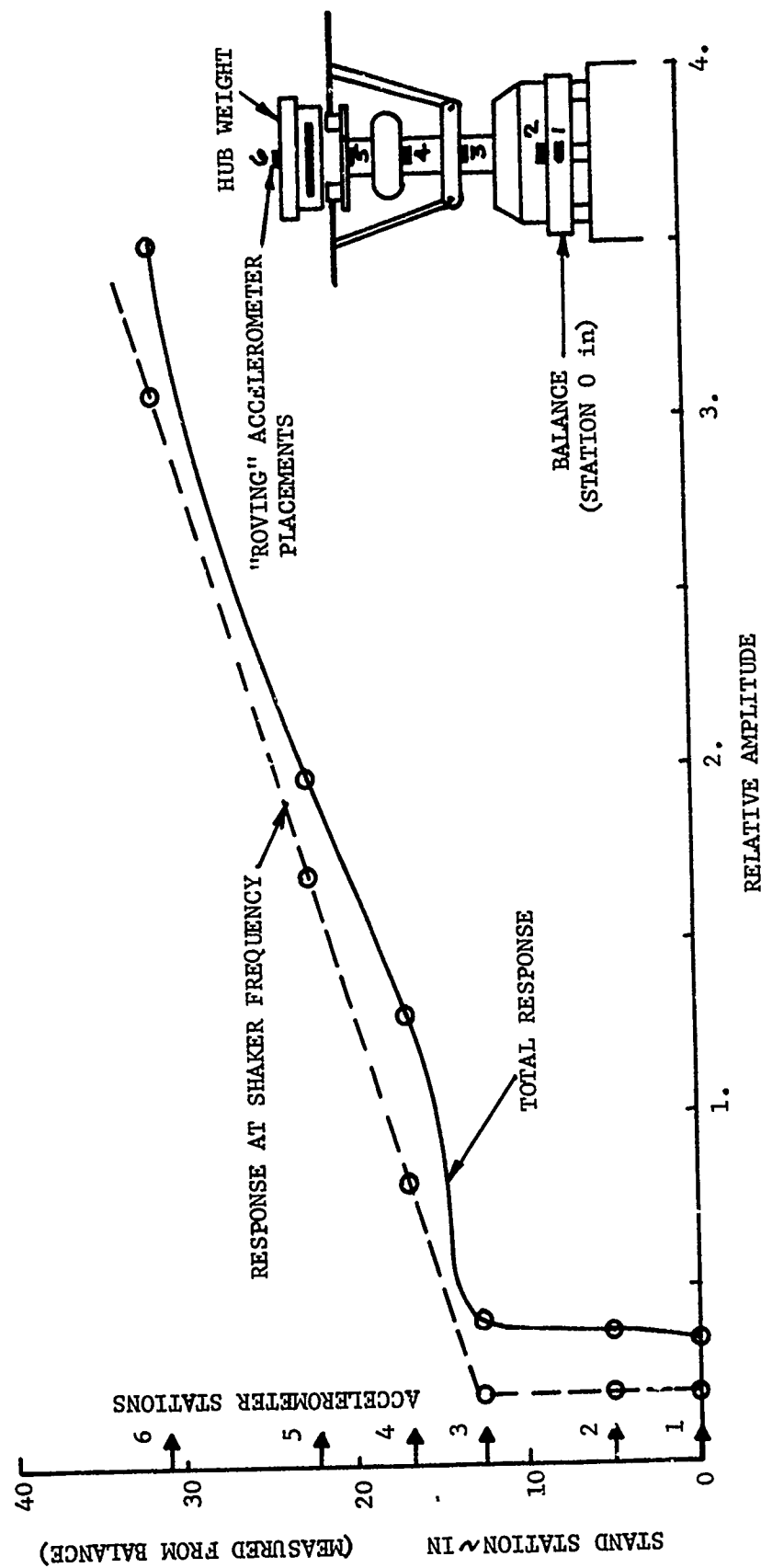
FIGURE 29   MODE SHAPE OF MODEL ASSEMBLY WITHOUT BLADES

3.0 DESCRIPTION OF TEST CONFIGURATION PARAMETERS

During the course of the aeroelastic stability and loads testing of the 8-foot-diameter bearingless tail rotor model, variations of critical configuration parameters were made and the resulting effects on stability observed. It is the purpose of this section to accurately describe the parameter changes listed in Table 6.

When considered, singly or in combination with other parameters, the parameters may be added to the basic configuration presented in Section 2.0 to provide a complete model representation. The effect of the parameters on stability and model frequencies follows in Section 5.0 and the corresponding load data in Section 6.0. Photographs of several parameters are in Appendix C.

3.1 Clevis Angle

The baseline blade clevis was described in Section 2.2.3. An option to the 9° baseline clevis, P/N CR037H-251, is the 26° clevis, P/N CR037H-250. Figure 30 is a drawing of this clevis and the $\delta_3 = -45°$ pitch arm, which is detailed in Section 3.3. The radial property distributions for the 26° clevis is identical to the baseline distributions with the following exceptions:

(1) Pretwist - This should reflect a 26° noseup rotation at station 0.385 x/R (in place of the 9° baseline rotation of Figure 10).

(2) Weight - The weight of the 26° clevis is on the average of 1.070 lb for the clevis, 0.33 lb for inboard bolts, and 0.800 lb for the outboard bolts, totaling 2.280 lb. This is 0.054 lb heavier than the baseline configuration. Therefore, the weight distribution, Figure 7, should be increased between x/R = 0.036 and x/R = 0.4177 by 0.0190 lb/in. or from 0.625 lb/in. to 0.643 lb/in, to represent the 26° configuration.

(3) Pitch Inertia - The inertia increases approximately proportional to the mass. Therefore, between x/R = 0.353 and x/R = 0.4177, the pitch inertia should be 0.00579 lb-in-sec^2/in. for the 26° clevis configuration.

These are the only properties influenced by blade clevis. All others remain as indicated in Figures 7 through 14.

TABLE 6 PARAMETERS VARIED AND STRAPS USED

PARAMETER VARIED	TEST			
	BVWT 124	BVTC 009	BVWT 129	BVTC 011
Clevis Angle (blade pitch at flat strap)	x	x		
Pitch-Link Tilt (α_1: pitch-lag coupling	x	x	x	
δ_3 (pitch-flap coupling)	x		x	
Blade Sweep	x	x	x	x
Radius of Sweep Point				x
Blade Chordwise Position Relative to Strap				x
Tip Weight	x	x	x	x
Inboard Weight and Lag Damping		x		
Strap Width		x		
Elastomeric Hub Inserts		x	x	x
Cruciform Strap Attachments	x	x	x	x
Airfoil Nose Bluntness	x	x		
Straps Used	334 335 336	335 336	334 335 336 337 338	334 337 338
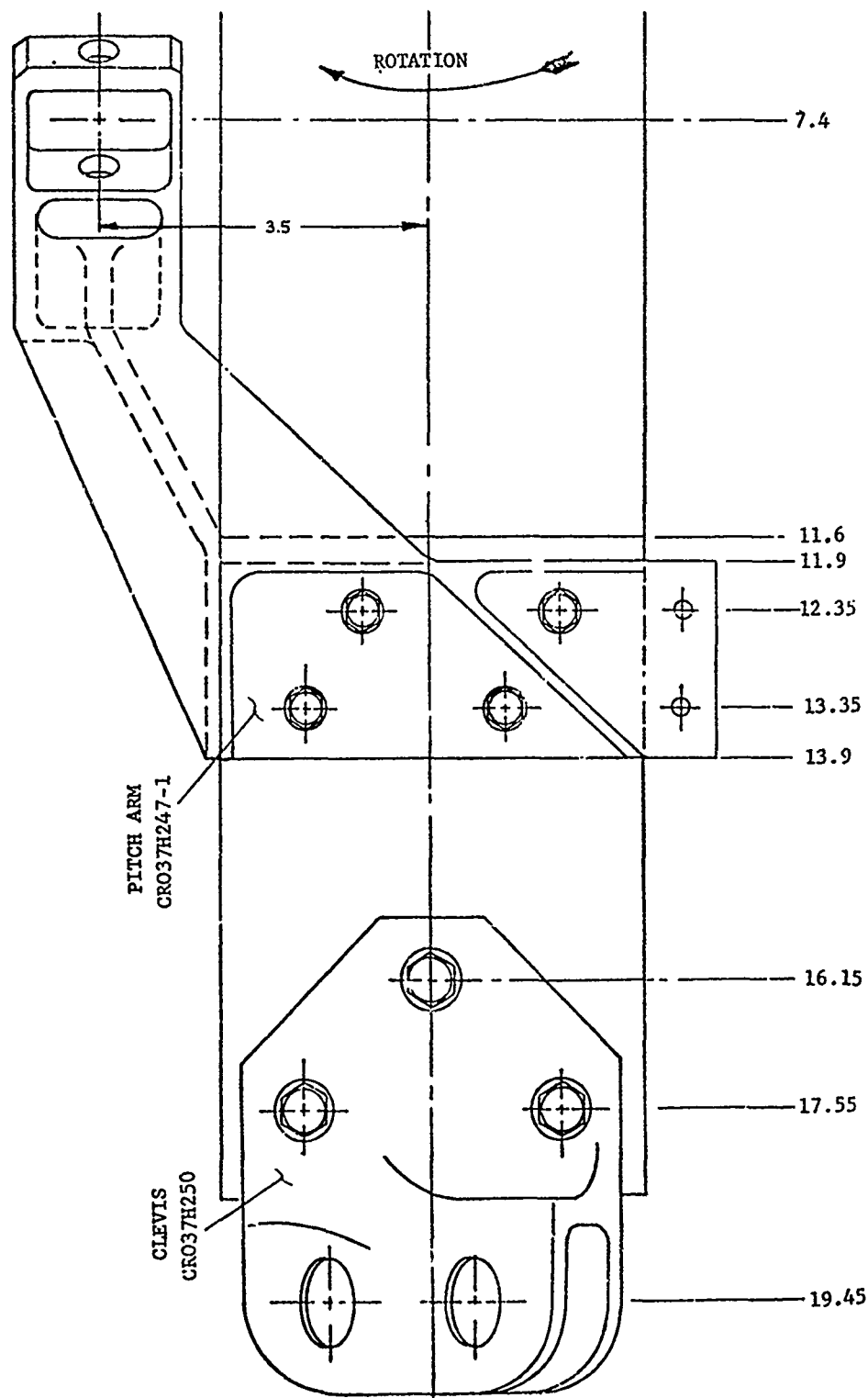
FIGURE 30   DETAIL OF δ_3 = -45° PITCH ARM AND
              26° CLEVIS

67

3.2 Pitch Link Tilt

During a portion of the test program, pitch link tilt was considered as a configuration parameter. This was accomplished by effectively lagging the rotating swashplate 36.5° relative to the rotor hub. For additional clarity, this is shown in Figure 31.

For this parameter variation there is no change in the blade parts or radial properties.

3.3 Delta-3 - Pitch-Flap Coupling

Two different δ_3 configurations were considered, the baseline $\delta_3 = -65°$ and an optional $\delta_3 = -45°$ (negative δ_3 denotes flap up/pitch nosedown). To convert from the baseline configuration to the $\delta_3 = -45°$ configuration, the baseline pitch arm, P/N CR037H246, is removed and the $\delta_3 = -45°$ pitch arm, P/N CR037H247, is substituted.

The $\delta_3 = -45°$ pitch arm is shown in Figure 30. Comparison of this pitch arm to the $\delta_3 = -65°$ presented in Figure 22 indicates that the primary difference between the two is the span-wise attachment poin: of the particular pitch arm to the pitch link. With the equivalent flap hinge unchanged, this radial variation of the attachment point varies the δ_3 angle as shown schematically in Figure 19.

There are three main differences between the optional $\delta_3 = -45°$ configuration and the $\delta_3 = -65°$ baseline configurations. These are:

(1) Weight - The weight of $\delta_3 = -45°$ pitch arm with bolts (attaching pitch arm to strap) is 0.9472 lb. Therefore, when considering this pitch arm, the weight per length between x/R = 0.290 and x/R = 0.248 is 0.4698 lb/in. Consequently, the weight distribution cver this span (see Figure 7) is 0.6858 lb/in. This corresponds to the value given for baseline $\delta_3 = -65°$

(2) Inertias - Because of the geometry and greater weight of the $\delta_3 = -45°$ pitch arm, the inertias, in pitch (I_x) and the other two directions (I_y, I_z), are higher than the baseline values. The inertias in the three directions are 0.0131 lb-in-sec^2 (I_x), 0.0154 lb-in-sec^2 (I_y flapwise), and 0.025 lb-in-sec^2 (I_z chordwise). These properties are distributed over a span of 2.016 inches between x/R = 0.290 and x/R = 0.248. This gives a distributed pitch inertia of
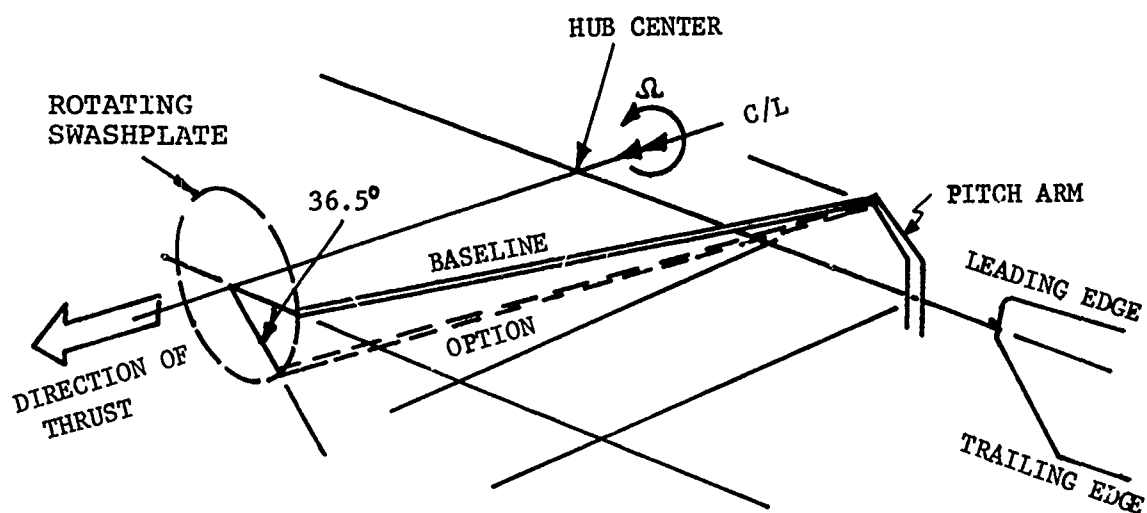
FIGURE 31   DETAIL OF PITCH LINK TILT

0.0070 lb-in-sec^2/in. The I_X for this pitch
arm plus the strap is therefore 0.00942
lb-in-sec^2/in between x/R = 0.248 and
x/R = 0.290 in Figure 8.

(3) Control System Stiffness - The flexibilities
and stiffnesses of the components of the δ_3
= -45° configuration with the associated pitch
links and pitch arms are shown in Table 7.

As shown in the table, the axial spring constant
for this control system is 955 lb/in. This
gives a total control system collective stiff-
ness of 3820 lb/in for the four-bladed configura-
tion. The effective out-of-plane inplane stiff-
nesses for this pitch arm, between the attachment
point of the pitch link and the point of attach-
ment of the pitch arm to the flex strap, were
determined. The vertical stiffness, used in cal-
culating the stiffness characteristics of the
control system, is 1360 lb/in. The horizontal
stiffness is 65,790 lb/in.

No other change in the baseline properties is noted when com-
paring the baseline pitch arm to the δ_3 = -45° pitch arm.

3.4 Blade Sweep

Blade sweep was generally introduced in the model by use of
eccentric bushings at the blade attachment point to the clevis;
unless noted otherwise, the sweep angle (Λ) will refer to this
form of sweep. (For an alternate method of sweeping the blade,
see Section 3.5.)

A schematic representation of this blade sweep is shown in
Figure 32. In this diagram the blade sweep is shown to occur
at x/R = 0.4063 (19.5 inches) within the outboard half of the
blade clevis. By sweeping the blade in this way, a small amount
of predroop is also introduced which is proportional to the
blade clevis angle, as shown in the view A-A of Figure 32. An
equation relating the three angles is

$$\tan \beta_O = \tan \Lambda \tan \theta_O$$

where β_O is the droop angle and θ_O is the prepitch or clevis
angle. This means that for the baseline configuration, with
$\Lambda = 11°$ and $\theta_O = 9°$, then $\beta_O = 1.76°$.

The range of Λ investigated during test varied from 0° to 11°
aft. There is no change in the spanwise structural properties
due to sweep.

70

TABLE 7   STIFFNESS CHARACTERISTICS OF THE CONTROL
SYSTEM, $\delta_3 = -45°$

	Axial Deflection
Pitch Arm - Upper Flex Strap	.00073557
Pitch Link - Upper Flex Strap	.0000042426
Stationary Swashplate	.0003067
Actuator	.0000010005
Total Deflection	.0010475 Inches

Axial Spring Constant = $\dfrac{1\#}{.0010475}$ = 955 lb/in.

	Axial Deflection
Pitch Arm - Lower Flex Strap	.00073557
Pitch Link - Lower Flex Strap	.000004103
Stationary Swashplate	.0003067
Actuator	.0000010005
Total Deflection	.0010473 Inches

Axial Spring Constant = $\dfrac{1\#}{.0010473}$ = 955 lb/in.

Total Control System Stiffness = 4 x 955 $\dfrac{\#}{In}$ = 3,820 lb/in.

for 4-bladed tail rotor.

1910 lb/in. for 2-bladed tail rotor.
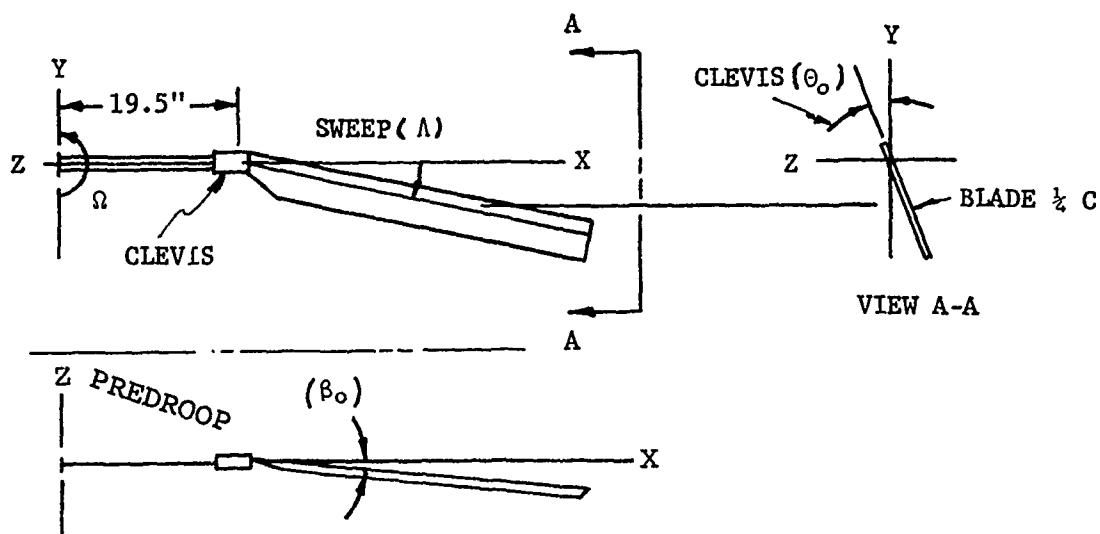
FIGURE 32   BLADE SWEEP   AT BLADE ATTACHMENT POINT
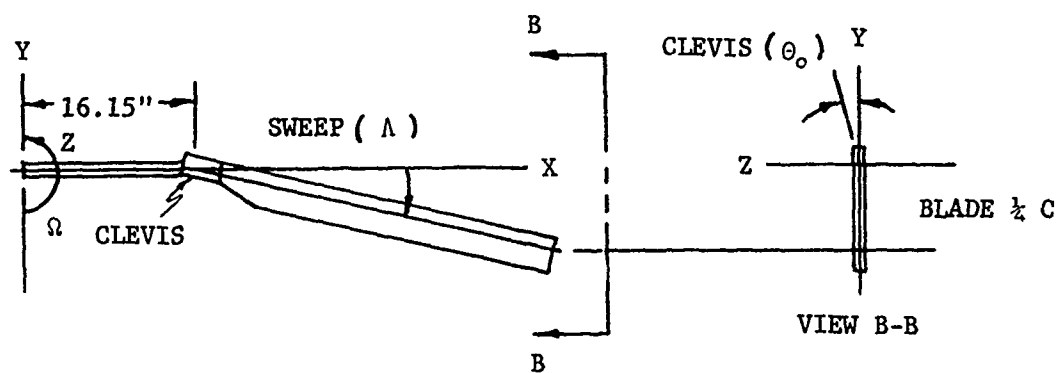
FIGURE 33   BLADE SWEEP   AT INBOARD SWEEP POINT

3.5 Radius of Sweep Point

As an alternative to the method of sweeping the blade presented
in Section 3.4, the blade was also swept at the strap to clevis
attachment or inboard sweep point, $x/R = 0.3365$ (16.15 inches).

Figure 33 indicates the orientation of the blade when swept at
the inboard sweep point. As shown, there is no blade predroop
accompanying the sweep. Compared to the baseline configura-
tion of $\theta_0 = 9°$ and $\Lambda = 11°$, which had an accompanying β_0 of
1.76°, sweep at the inboard sweep point would introduce the
sweep 3.35 inches further inboard and no predroop would be
present.

3.6 Blade Chordwise Position Relative to Strap

The variation of the blade chordwise position relative to the
strap is accomplished by combining both methods of blade sweep
detailed in Sections 3.4 and 3.5. For a blade aft offset, an
aft sweep angle is used at the inboard sweep point and forward
sweep is used at the blade attachment point. At zero sweep
angle, the blade may be offset from the centerline of the strap
of 0.61 inch.

The effect of the offset on aeroelastic stability was also ex-
plored with a sweep angle, $\Lambda = 6°$. This configuration permitted
an offset of 0.25 inch forward or 0.25 inch aft. This repre-
sents the total range of offset investigated.

3.7 Tip Weights

The tips of the blades are fitted with two thread inserts for
tip weights at 7% and 42.5% chord. The mass added at these
points, in all cases, includes the mass of the tip weight plus
the mass of the retention bolts.

In the configuration descriptions that accompany the stability
data and load data, the presence of tip weights will be noted
"TIP WEIGHT = aa/bb". "aa" denotes the mass in grams placed
on each blade's leading edge, 7% chord; and "bb" denotes the
mass in grams placed on trailing-edge locations, 42.5% chord.

3.8 Inboard Weight and Lag Damping

This configuration was designed to provide inplane blade damp-
ing. Blade clevis and strap modifications allowed the blade
and clevis freedom to pivot about the strap in a lead-lag plane
at the inboard sweep point ($x/R = .3365$). Two elastomeric
dampers were attached between the blade clevis and the strap,
one on each side of the strap. These elastomeric dampers,
manufactured by Lord Kinematics (Part No. J15456-1), comprised
two aluminum plates and sandwiching a 4 x 4 in elastomer pad,

0.4-in thick. Inplane blade loads were absorbed in combined
shear and torsional loading of the elastomer. Only one strap
(Serial No. 334) was modified to fit the elastomeric dampers.

Inboard weights were made to simulate the weight of the Lord
elastomeric damper so that the effect of the weight of the
damper device on stability could be determined independent of
the damping. These weights were fitted to strap 337 and bolted
over the clevis and pitch arm between $x/R = 0.25$ and $x/R = 0.38$.
The weights were uniform and added 7.4 lb per blade.

3.9 Strap Width

The width of the strap was varied to adjust primarily the first
inplane frequency. This was accomplished by making cutouts
along either side of the strap between span stations x/R
$= 0.116$ and $x/R = 0.224$. The details of these reductions in
width are shown in Figure 34.

The strap width that is cited in the configuration definitions
that follow will, in all cases, refer to the width of the strap
across the cutout at the narrowest part. A summary of the
strap properties between $x/R = 0.116$ and 0.224 as a function of
the strap widths is presented in Table 8.

3.10 Elastomeric Hub Inserts

The flex-strap "rubber" hub mounts two straps with flexures
and tie bars mutually perpendicular between elastomeric shear
bearings. A photograph of the breakdown of the hub with elas-
tomeric inserts is shown in Figure 35.

These inserts provide a torsional stiffness at the center of
rotation of the rotor. Three insert stiffnesses were consider-
ed. These are 700,000 in-lb/rad, 350,000 in-lb/rad, and
174,000 in-lb/rad. The inserts have no effect on the strap or
blade properties.

3.11 Cruciform Strap Attachments

For many of the test configurations, the basic flap bending
stiffness of the outboard portion of the strap is increased by
bolting one or more combinations of cruciform stiffners along
each side of the strap along the axial centerline. A descrip-
tion of each of the configurations appears in subsections
3.11.1 through 3.11.6. A sketch showing some cruciform arrange-
ment is shown in Figure 36. A summary of the effect of these
attachments on the physical properties--weight, flapwise stiff-
ness, chordwise stiffness, and torsional stiffness--is pre-
sented in Table 9 for the reduced EI configuration.

AREA OF CUTOUTS

FLEX STRAP

x/R= .224

5 3/16"

x/R= .116

3 1/8"
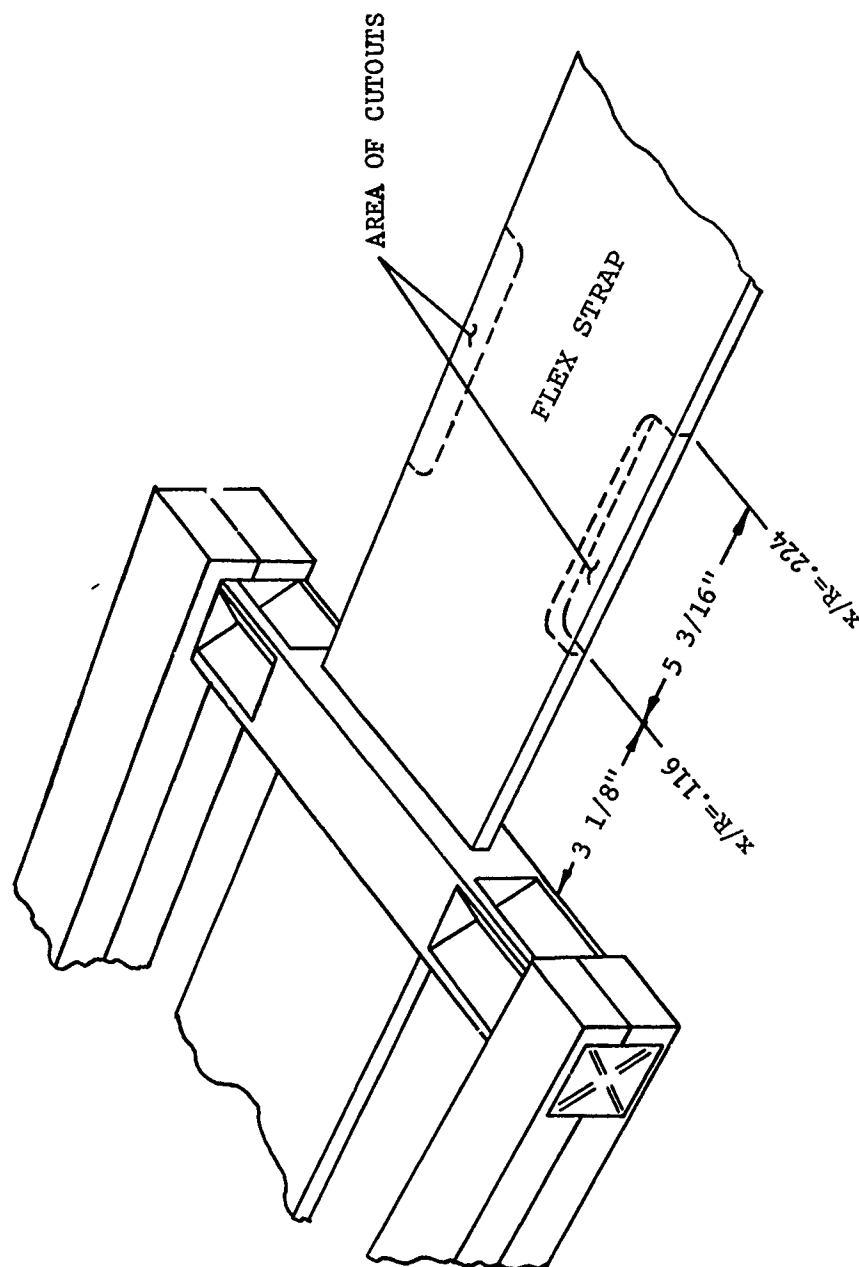
FIGURE 34   DETAIL OF REDUCTION IN WIDTH
              OF FLEX STRAP

75

TABLE 8   STRAP PROPERTIES FOR SELECT STRAP CUTOUT WIDTHS

STRAP WIDTH, in	x/R = .116 → .224				
	4.4	4.0	3.8	3.6	3.3
Weight, lb/in	.0598	.0544	.0516	.0489	.0449
Inertia, lb-S^2-in	.000249	.000226	.000215	.000204	.000187
EI_{flap}, lb-in^2	.01454	.01322	.01256	.01190	.01091
EI_{lag}, lb-in^2	7.460	5.605	4.805	4.086	3.147
GJ, lb-in^2	.006	.00545	.00518	.00491	.00450
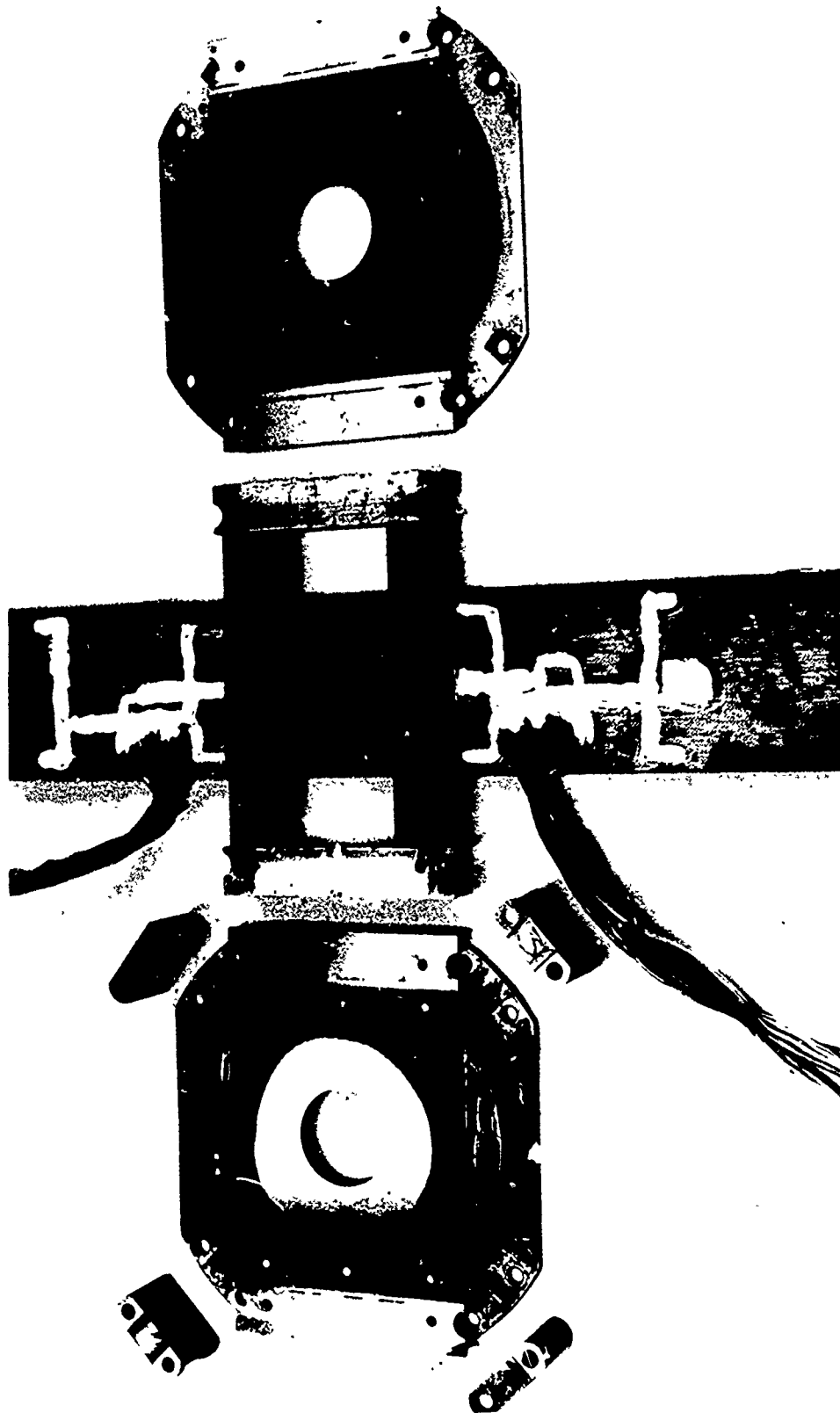
FIGURE 35 BREAKDOWN OF HUB WITH ELASTOMERIC INSERTS
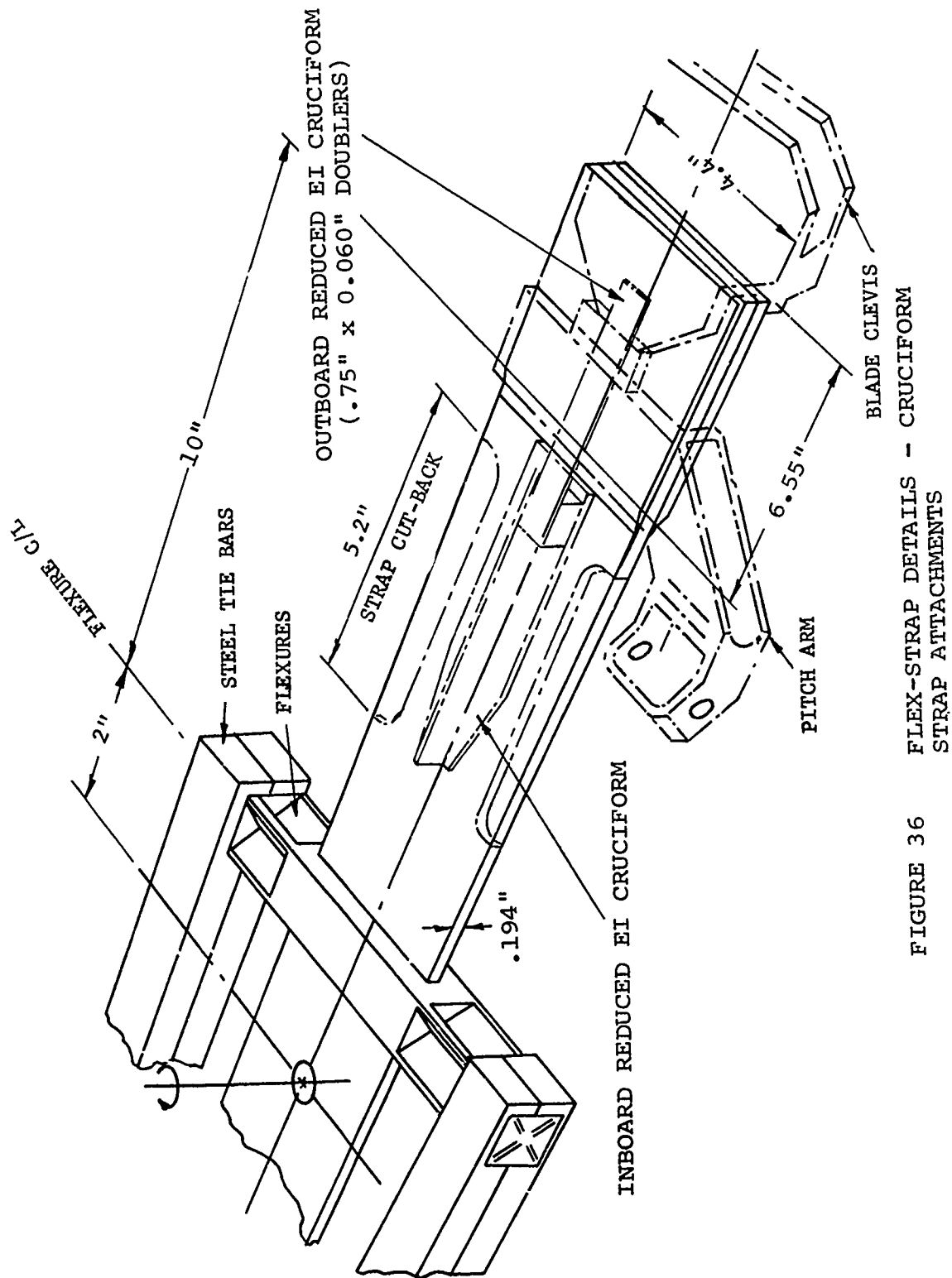
FIGURE 36   FLEX-STRAP DETAILS — CRUCIFORM
STRAP ATTACHMENTS

3.11.1 Inboard Cruciform

Two 5.2-inch-long T-sections with 2-inch-wide base and 1.75-inch web are bolted on each side of each strap arm. This arrangement spans the "flex" portion of the strap from x/R = 0.125 to 0.243, the outboard end of the cruciform butting against the blade retention pad. The sections were originally through bolted and bonded to the strap. But the bonding was omitted after the first configuration change since no significant change in physical properties was observed due to the bonding.

3.11.2 Outboard Cruciform

Two pieces of aluminum angle of 1-inch base and 1-1/2-inch web are bolted back-to-back to form an inverted T-section on each side of the blade retention pad. This cruciform spans the blade clevis and the pitch arm (x/R = 0.201 to 0.36) and is bolted through them. The outboard cruciform overlaps the inboard cruciform and they are bolted together to form a continuous rigid full cruciform.

3.11.3 Reduced EI Inboard Cruciform

Inboard cruciform as described in Section 3.11.1 with the 1.75-inch web reduced to 0.65 inch web.

3.11.4 Reduced EI Outboard Cruciform

The four L-sections described in Section 3.11.2 were replaced by two 0.060-inch-thick by 0.75-inch-wide aluminum doublers per strap arm, bridging the blade clevis and the pitch arm, overlapping the inboard cruciform as shown in Figure 36.

3.11.5 Full Cruciform

Inboard and outboard cruciform sections as described above, either full stiffness or with reduced EI, are bolted rigidly together. A photograph of the tail rotor model with this cruciform arrangement is shown in Figure 37.

3.11.6 Full Cruciform - Halves Disconnected

The inboard and outboard sections are used as described above with no interconnections at the cruciform overlap.

3.12 Airfoil Nose Bluntness

For the test of the 8-foot-diameter tail rotor, several airfoil sections were used. These sections represent a series of airfoils, designated VR-7, which differ in the airfoil nose bluntness. The contour modifications, indicating the difference in

TABLE 9 PHYSICAL PROPERTIES OF THE CRUCIFORM STRAP ATTACHMENTS

PROPERTY*	INBOARD CRUCIFORM		OUTBOARD CRUCIFORM		FULL CRUCIFORM		
X/R =	.125→.201	.201→.243	.201→.243	.243→.36	.125→.201	.201→.243	.243→.36
WEIGHT/LENGTH (LB/IN)	0.0402	0.0402	0.088	0.012	0.0402	0.121	0.012
FLAP STIFFNESS (EI$_{FLAP}$ X 10^{-6} lb-in^2)	0.5	0.5	3.09	0.450	0.5	3.59	0.450
CHORD STIFFNESS (EI$_{CHORD}$ X 10^{-6} lb-in^2)	0.80	0.8u	5.73	0.70	0.80	6.53	0.70
TORSION STIFFNESS (GJ X 10^{-6} lb-in^2)	0.0642	0.0642	0.67	0.67	0.0642	0.7342	0.67

* Values shown above are to be added to the baseline configuration properties when cruciforms are considered.
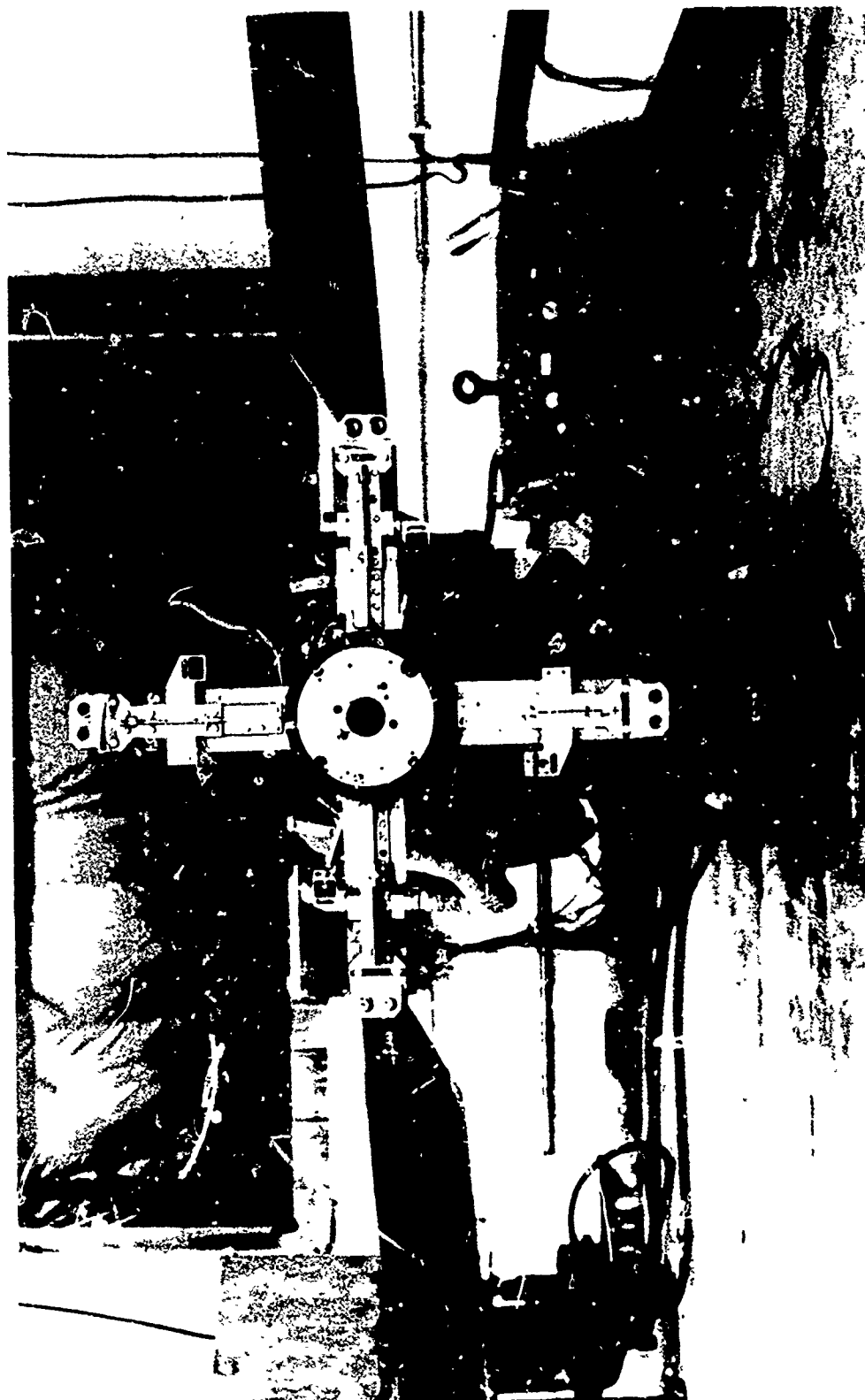
FIGURE 37   TWO-BLADED MODEL WITH FULL CRUCIFORM
STRAP ATTACHMENTS

81

the leading-edge curvature, are shown in Figure 38. As shown in this figure, the VR-6.9 airfoil has the sharpest curvature while the VR-7.4 has the fullest. The baseline airfoil for this report, VR-7.2, therefore has an intermediate curvature.

In the stability and loads testing detailed in this report, only the VR-6.9, VR-7.2, and VR-7.4 airfoils were studied. However, in the discussion of aerodynamic characteristics below, data for several of the other airfoil sections are used to make more clear certain aspects of the performance of this family of airfoils.

3.12.1 Lift Characteristics

An extensive amount of analytical and experimental work has been conducted to determine the performance characteristics of the VR-7 airfoils. The theoretical data of the maximum lift boundaries at $M = 0.4$ and $M = 0.5$ was obtained at Boeing Seattle by means of the TEA 267 potential flow-boundary layer interaction analysis.

At $M = 0.4$ the maximum lift of the VR-7 airfoil sections is limited by trailing-edge separation and is, therefore, predictable by means of boundary layer theory to a good degree of accuracy (Figure 39). The analysis shows that the leading-edge modifications do not cause a deterioration in the maximum lift boundary at $M = 0.4$. As a matter of fact, the modifications seem to improve the maximum lift by a small amount $\Delta C_{L_{MAX}} = .02$.

At $M = 0.5$ the VR-7 airfoil benefits by a favorable shock-boundary layer interaction effect, which is not predictable by any present analysis. Figure 40 compares test and theory levels for the VR-7 and VR-7.1 and shows the spread of estimated test levels for the VR-7.2 and VR-7.4. With respect to the VR-7, the VR-7.2 will lose as much as $\Delta C_{L_{MAX}} = -.2$. The VR-7.4 can cause a further reduction in maximum lift level of as much as $\Delta C_{L_{MAX}} = -0.05$ with respect to the VR-7.2.

The effect of losses in maximum lift on tail rotor performance is illustrated in Figure 41. The data shown was obtained by means of the B-92 hover analysis employing at first the standard VR-7 tables and then two table modifications in which the maximum lift at $M = 0.5$ was changed by $\Delta C_{L_{MAX}} = -.05$ and $\Delta C_{L_{MAX}} = -0.10$, respectively. By using the data in Figure 41 on an incremental basis, we can deduce that the loss in performance from the VR-7 to the VR-7.2 amounts to about 2%, and that the additional loss associated with building up the VR-7.2 to a VR-7.4 would be less than 1%.

82

THIS CONTOUR IS AN ESTIMATE
OF THE ACTUAL VR-6.9 SECTION.
THE TRUE COORDINATES FOR THIS
SECTION ARE NOT AVAILABLE.
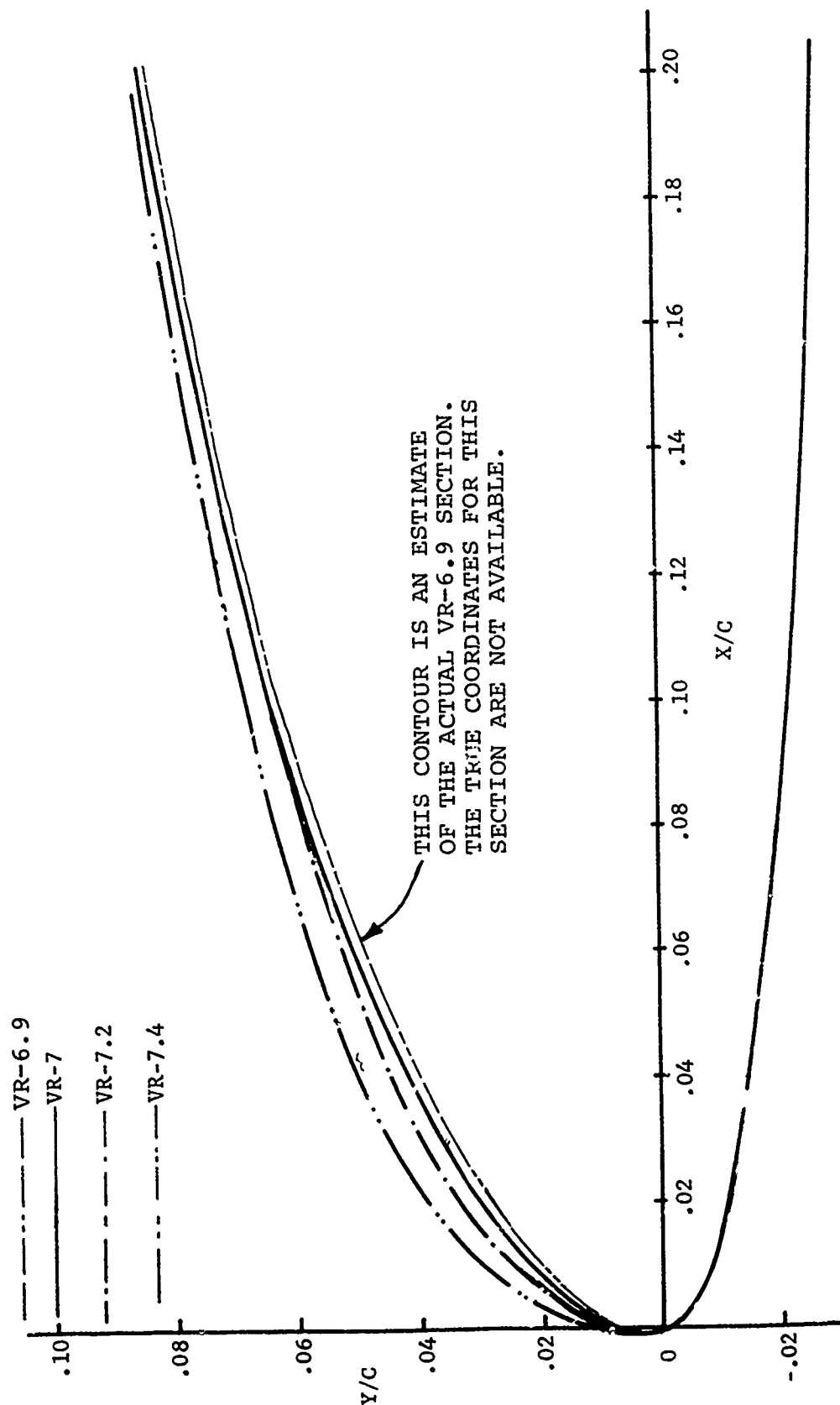
FIGURE 38   CONTOUR MODIFICATIONS OF THE VR-7 AIRFOIL
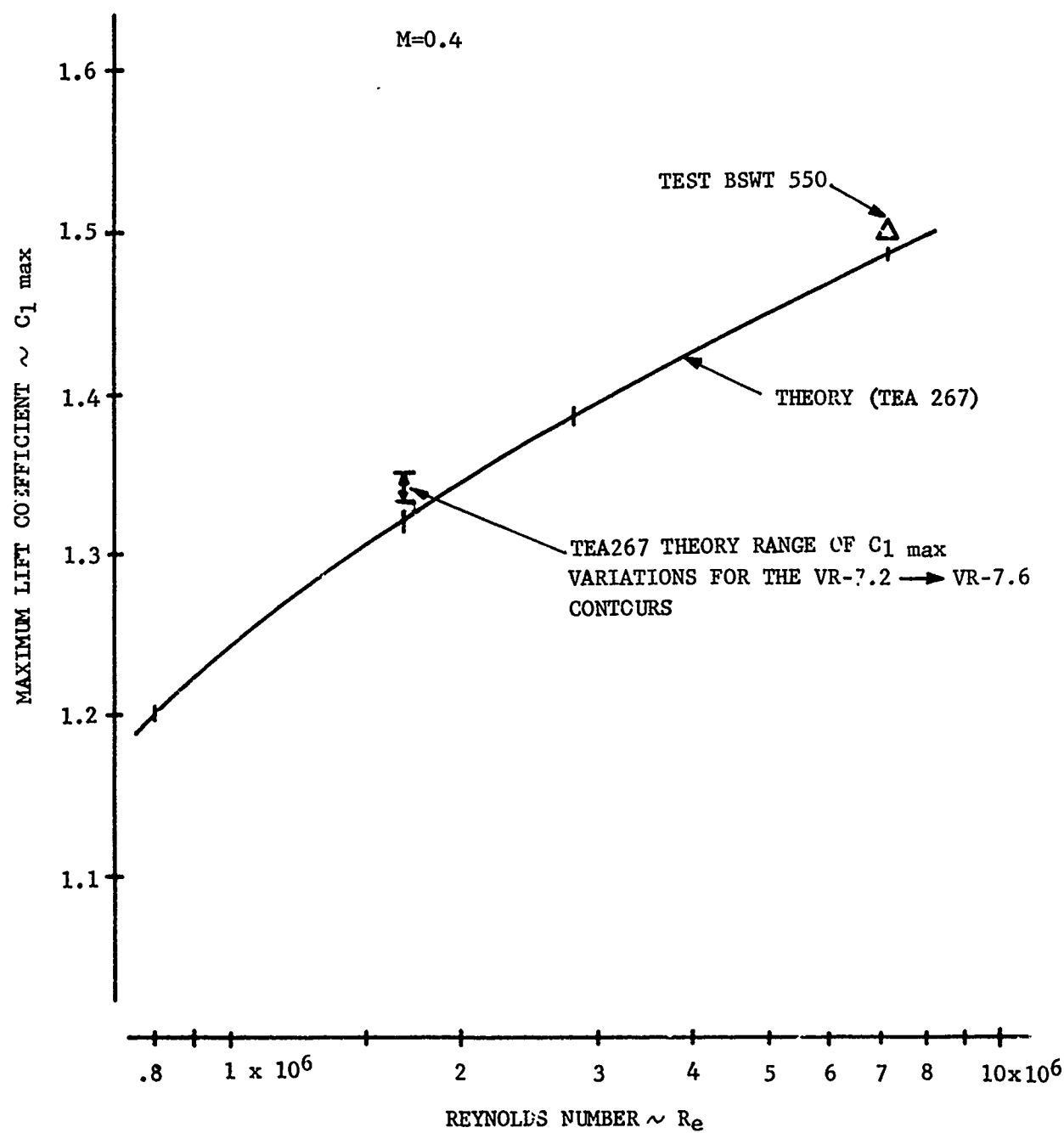
FIGURE 39   MAXIMUM LIFT COEFFICIENT OF THE VR-7
AIRFOIL M = 0.4
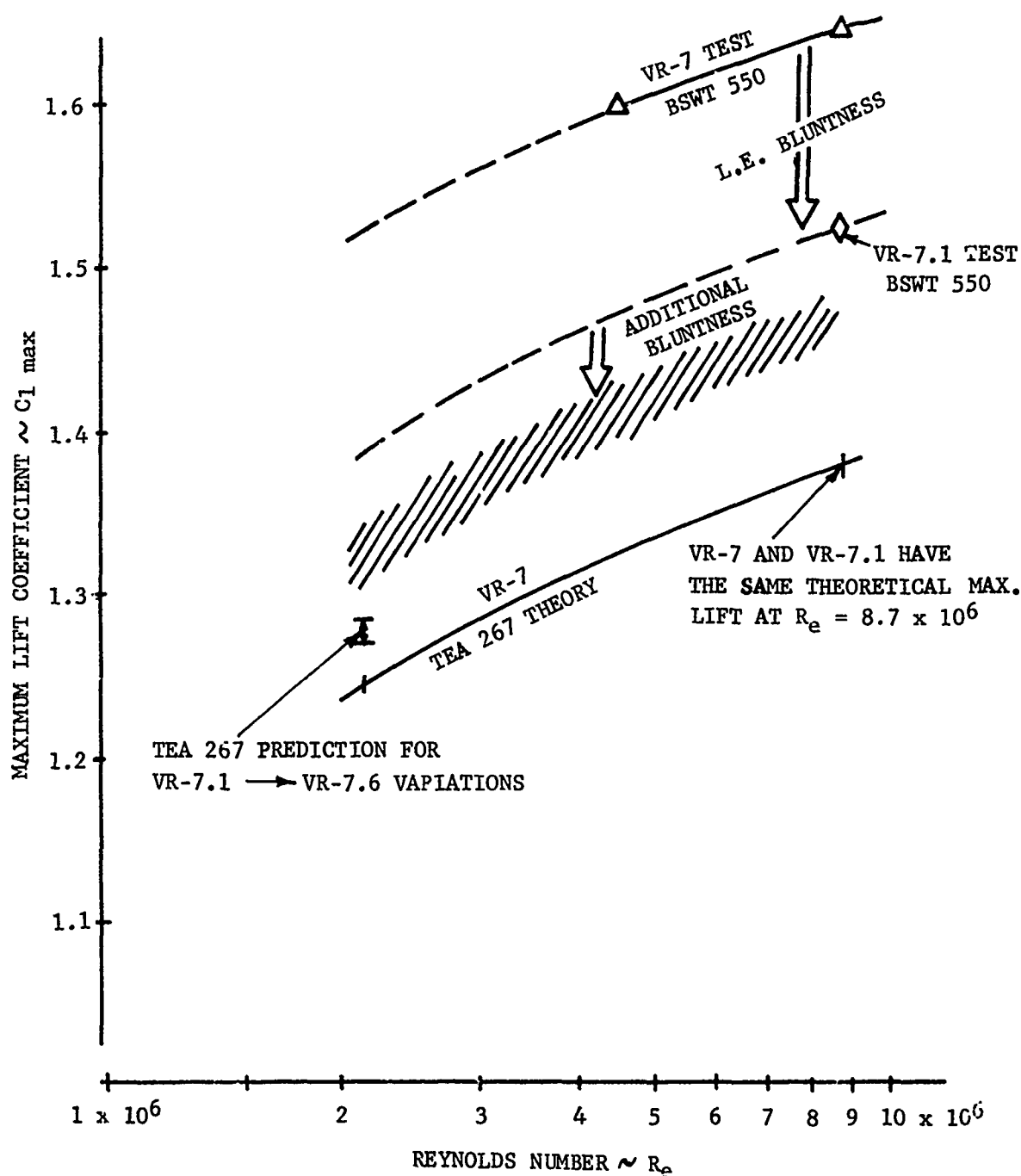
FIGURE 40   MAXIMUM LIFT COEFFICIENT OF THE VR-7
             AIRFOIL M = 0.5

85
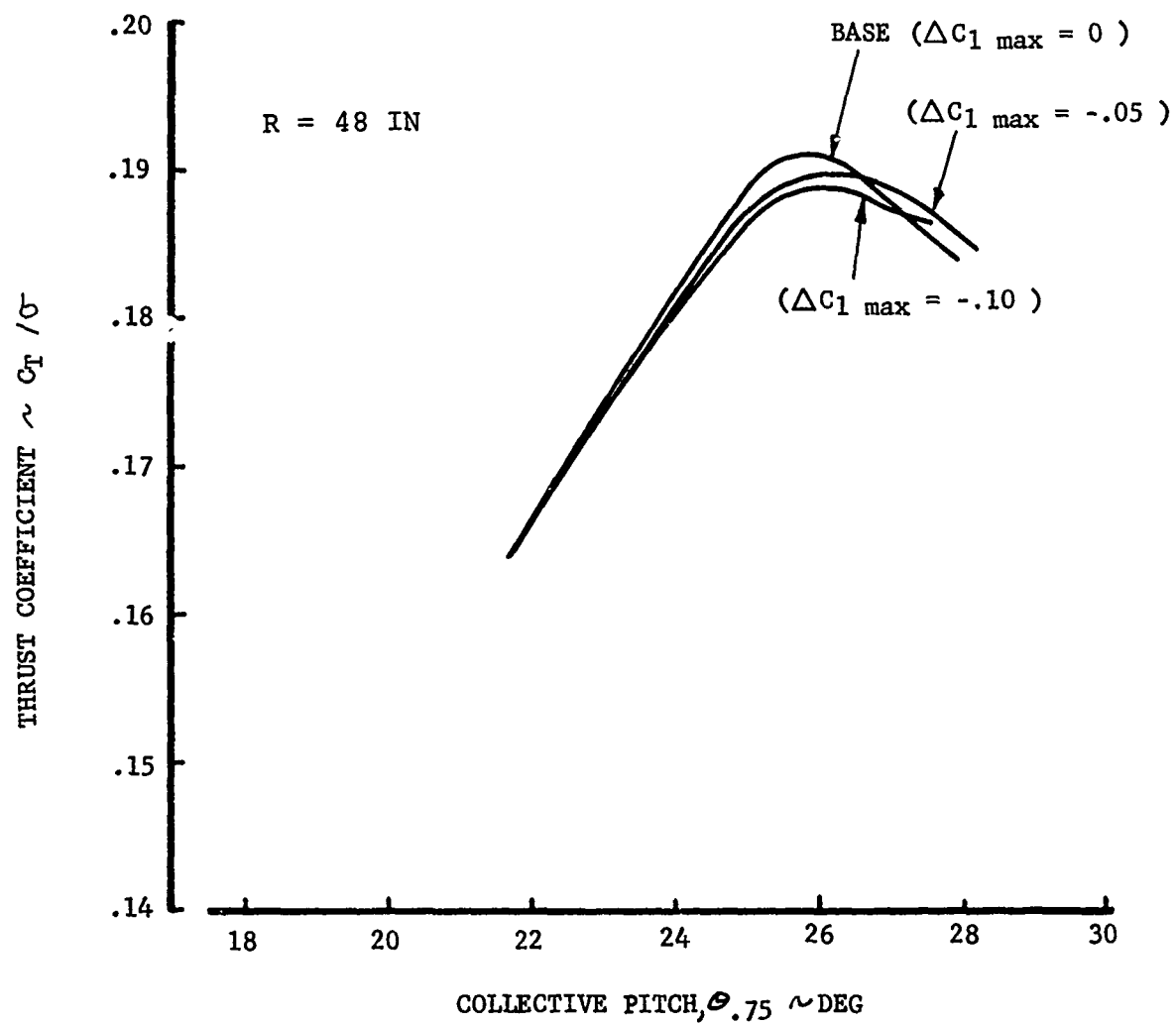
FIGURE 41   EFFECT OF VR-7 LEADING-EDGE MODIFICATIONS
ON TAIL ROTOR THRUST CAPABILITY

86

3.12.2 Some Comments on Stall Effects

Figures 42 and 43 show test data illustrating various stall regimes. The data was obtained in the Subsonic Insert of the Supersonic Wind Tunnel at Boeing Seattle during several Vertol airfoil tests, References 4 and 5.

Figure 42 shows the effect of a leading-edge contour modification on the lift stall characteristics of the VR-7 airfoil at $M = 0.5$. This data is the basis for suggesting that a leading-edge contour modification could be employed to change the stall from leading edge to trailing edge.

For reference, the effect of leading-edge stall versus trailing-edge stall on lift coefficient has been demonstrated for a fixed airfoil section using leading-edge blowing. This technique provides control of the boundary layer at the leading edge and prevents abrupt separation at the leading-edge characteristic of leading-edge stall. The airfoil considered for this experiment is the V23010-1.58. By application of leading-edge blowing, the stall at $M = 0.4$ was changed from leading-edge to trailing-edge types shown in Figure 43.

All the data shown was obtained by means of rigidly mounted two-dimensional airfoil models. Therefore, all the fluctuations shown can be assumed to be strictly related to flow separation with very little feedback from model motions in response to airloads.
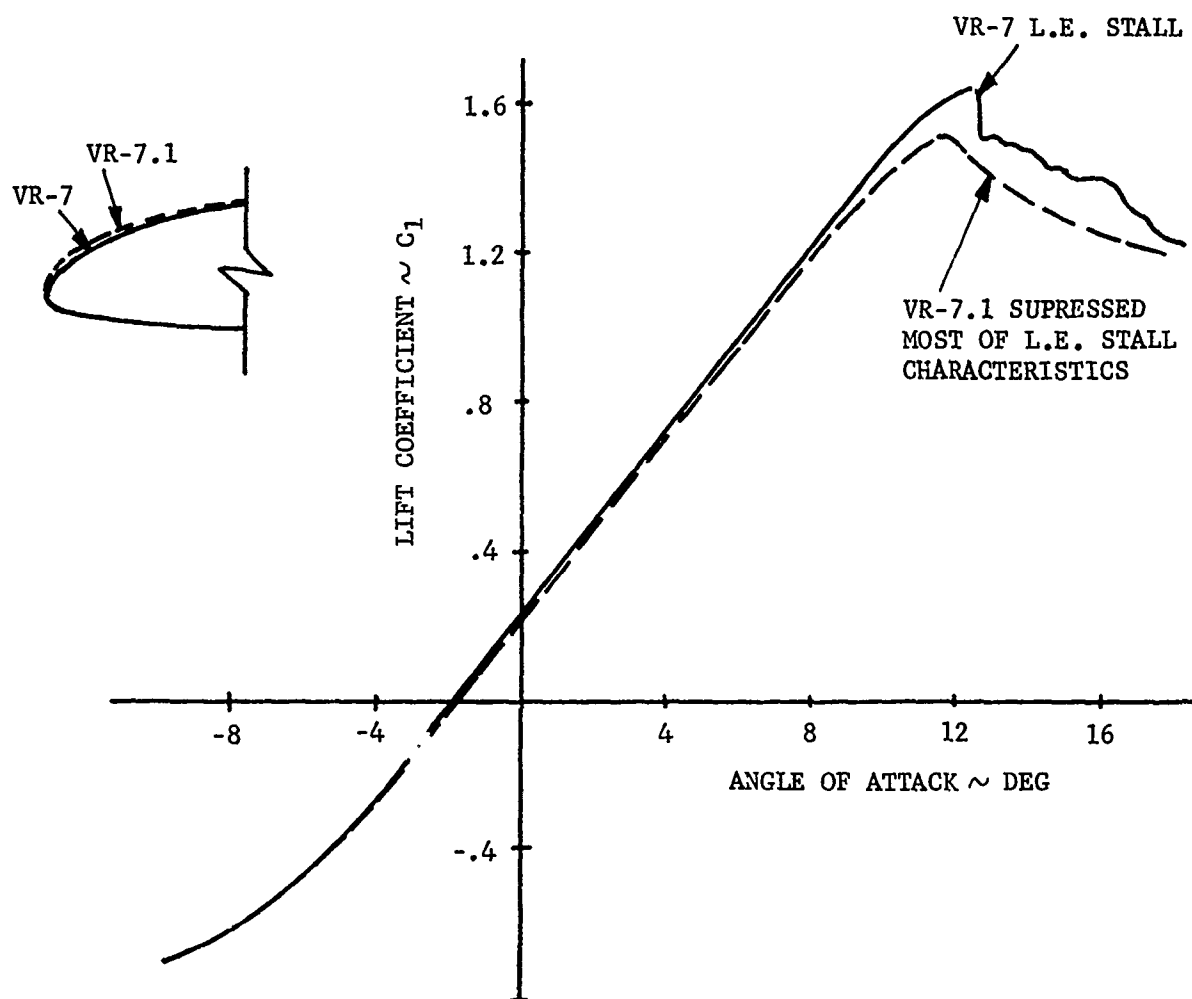
FIGURE 42   EFFECT OF L.E. BLUNTNESS ON STALL
CHARACTERISTICS OF VR-7 AIRFOIL

AIRFOIL V23010-1.58 WITH L.E. BLC   M = 0.4

$C_{1 \text{ max}} = 1.4$

LEADING-EDGE STALL
$C_M = 0.0$

$C_1 = 1.1$

LIFT COEFFICIENT ~ C_1

ANGLE OF ATTACK ~ DEG

TRAILING-EDGE STALL
$C_M = 0.015$

$C_{1 \text{ max}} = 1.4$

$C_1 = 1.25$

LIFT COEFFICIENT ~ C_1

ANGLE OF ATTACK ~ DEG
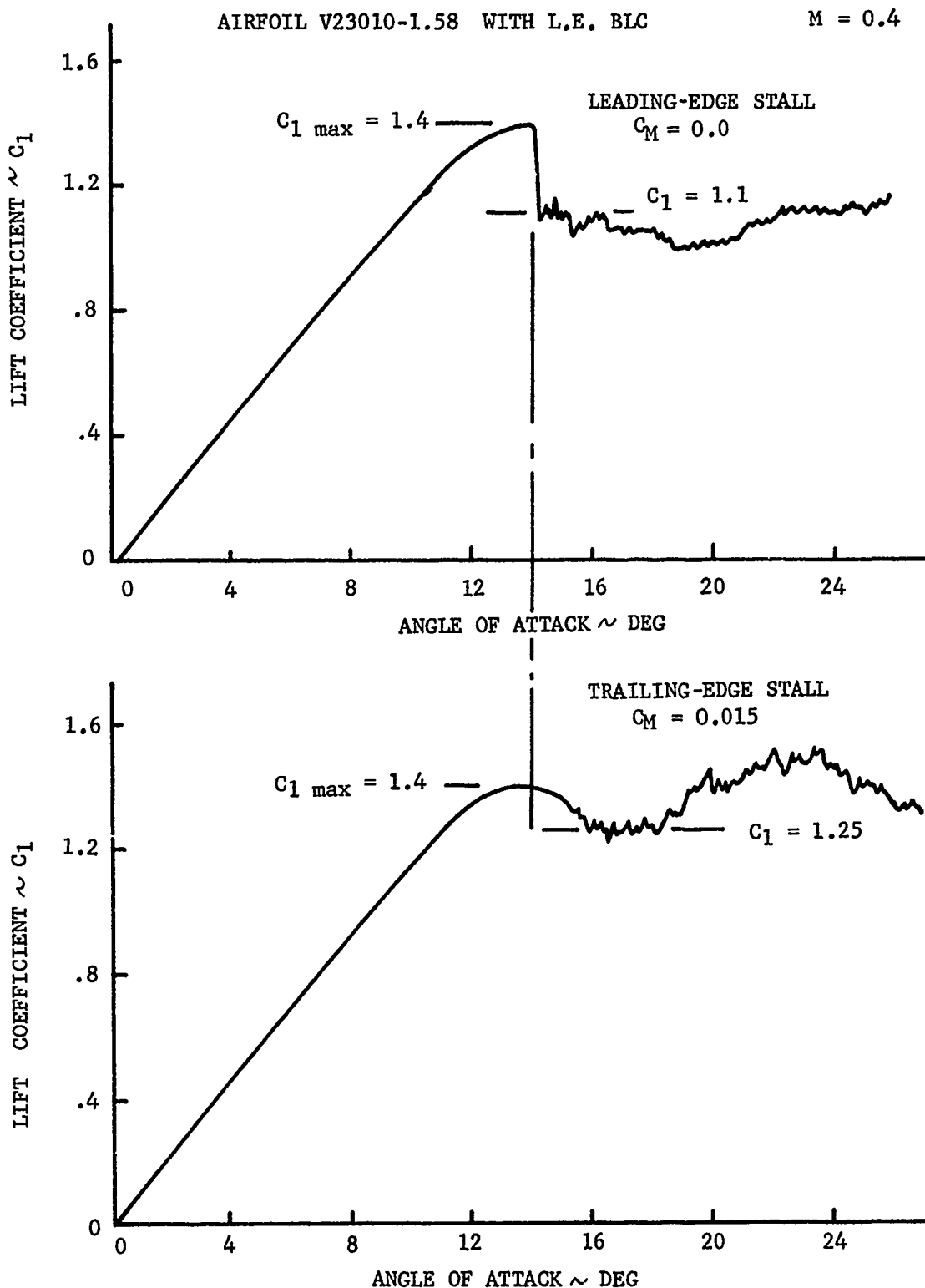
FIGURE 43   EFFECT OF CHANGE IN STALL CHARACTERISTICS
ON LIFT AFTER STALL

89

4.0 DATA ACQUISITION

4.1 Instrumentation

4.1.1 Model

The model was instrumented to measure strains in the straps and flexures but not the blades, since strains in the relatively stiff blades are not a concern in the flex-strap design. Strain gage bridges were calibrated to indicate flap bending, chord bending, and torsional moments in the root area; leading-edge and trailing-edge tension on the strap in the root area; tension on the upper and lower sides of a flexure; and tension in the pitch link. Figures 44 and 45 show gage locations in detail for the flex straps used in the four test phases.

4.1.2 Stand

Steady hub forces and moments were measured in BVWT 129 only by a four-post strain gage balance between the stand and the model assembly.

This steel balance (BV 6007) resolved the forces and moments into six components along three mutually orthogonal axes. In this way, the thrust, two inplane forces (side force and "normal" force), pitching moment, rolling moment, and torque were determined.

The following additional instrumentation was used:

- a strain-gaged torque tube in the test stand drive train to measure shaft torque

- a pendulum potentiometer in the stand to measure shaft angle

- thermocouples to measure gearbox, motor, and bearing temperatures

- lubricating oil flow meters

- 1/rev signal at a fixed azimuth

- rpm indicator

- accelerometers mounted on the stand for hub and blade balancing

4.2 Data Systems

Signals from the model and stand instrumentation described in Section 4.1 were routed through the wind tunnel data processing
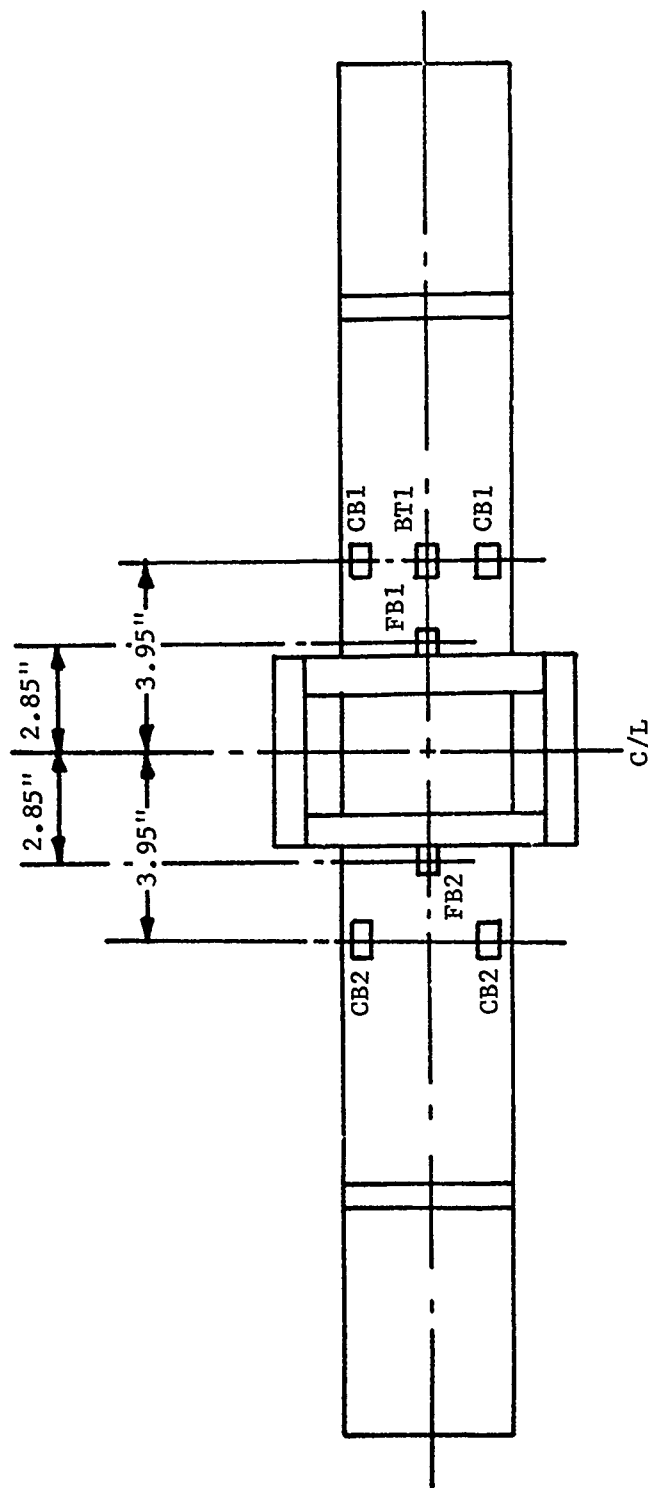
STRAP	TEST PHASE USED
334	BVWT 124, BVWT 129
335	BVWT 124, BVTC 009, BVWT 129
336	BVWT 124, BVTC 009, BVWT 129

FB - FLAP BENDING
CB - CHORD BENDING
BT - BLADE TORSION

FIGURE 4: STRAIN GAGE LOCATIONS ON STRAPS 334-336

	X		
T1	T2	T3	T4
2.68	3.18	3.68	4.18

FB - FLAP BENDING
CB - CHORD BENDING
BT - BLADE TORSION
T - ABSOLUTE TENSION

STRAP 337-1

STRAP 338-1
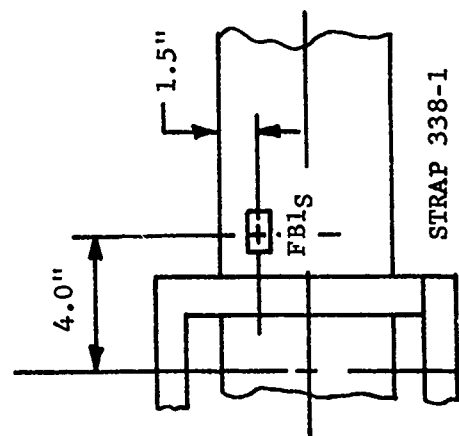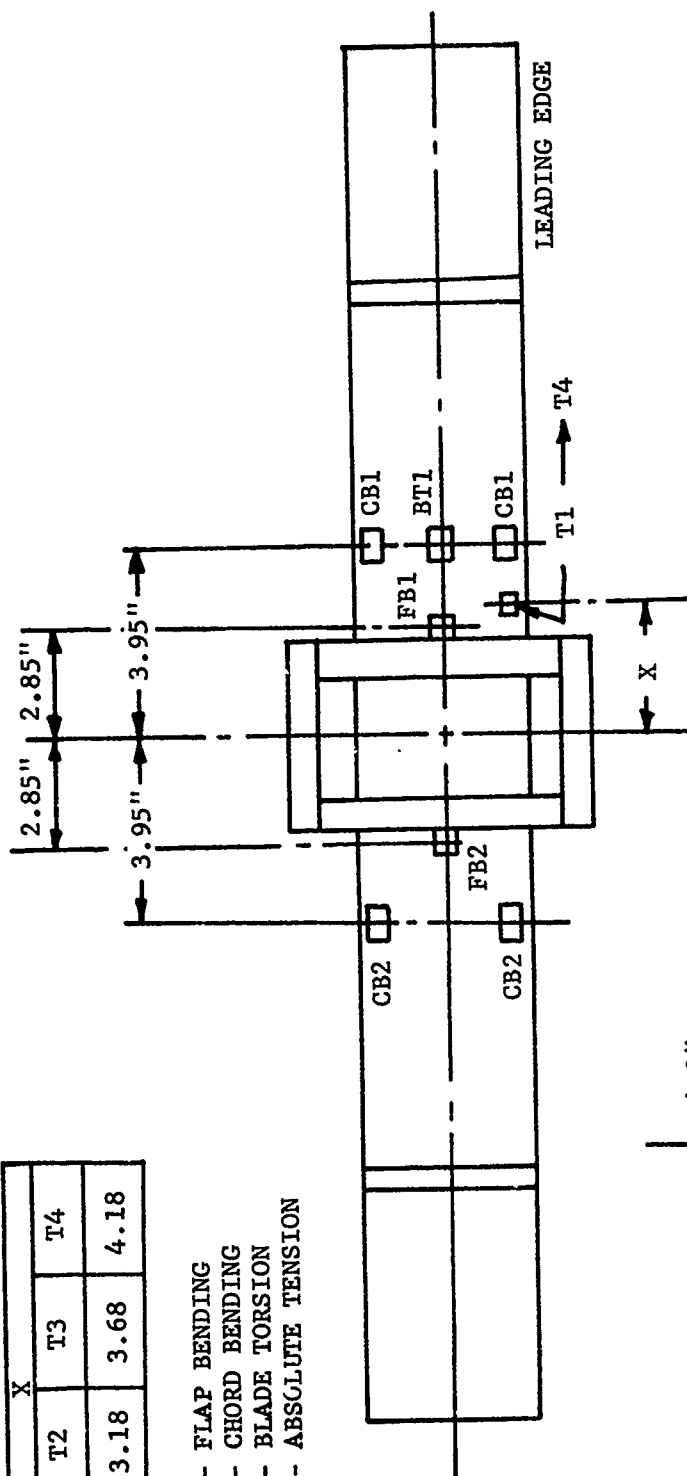
RESPLACEMENT FLAP
BENDING GAGES

S-SUBSTITUTE
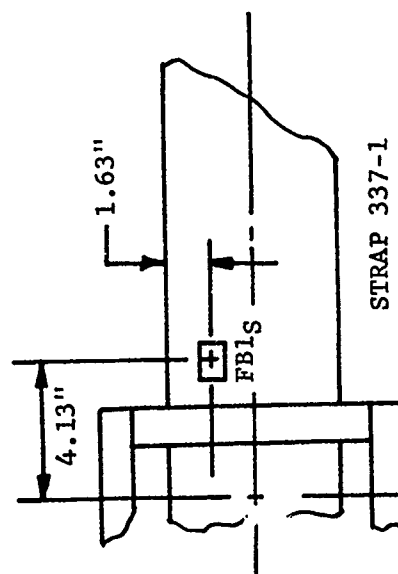
FIGURE 45   STRAIN GAGE LOCATIONS ON STRAPS 337-338

system. The system includes an IBM 1800 digital computer, an analog processor, and peripheral equipment. Three processing paths were used: the safety-of-flight monitor, the static data system, and the dynamic data system.

4.2.1 Safety-of-Flight Monitor

The safety-of-flight monitor is an analog system which provides a continuous display of critical loads. Loads are observed in three forms: as standing waves on oscilloscopes triggered by a 1/rev pulse, as patterns generated by pairs of loads on the X and Y axes of oscilloscopes (useful when the fatigue allowable for one load depends on the magnitude of another load), and on meters that show alternating loads as percentages of their fatigue allowable values. In this test, balance forces and moments were displayed on 100 percent meters and representative strap loads were displayed on oscilloscopes. An X-Y oscilloscope was used to display alternating flap versus alternating chord bending moment at the same point on one strap because the fatigue allowable for each of these bending moments depended on the size of the other. The allowables were used to draw a diamond-shaped boundary on the face of the scope within which the pattern should be kept. A second X-Y oscilloscope was similarly used at some times to display the steady level versus the alternating level of absolute fiber tension at a point on one of the straps. (See Figures 44 and 45 for the locations of absolute tension gages.) Three time-sweep oscilloscopes were used to show representative flap bending, chord bending, and torsional moments. A fourth time-sweep oscilloscope was used in some runs to display a pitch link load. Calculated fatigue allowable amplitudes were marked on the torsional moment and pitch link load oscilloscopes as horizontal bands within which the time traces should be kept.

The safety-of-flight monitor also provided signals to oscillographs on which permanent waveform records were taken at frequent intervals.

4.2.2 Static Data System

The static data system is an analog-digital processor. This system determines, at intervals of several seconds, steady levels of selected data channels (balance forces and moments, actuator positions, rpm, tunnel velocity, etc.) from which the current test conditions can be calculated. The system calculates the test conditions (force and moment coefficients, advance ratio, collective, cyclic, etc.) from each set of channel averages and updates a digital display of nine selected values. In addition to updating the display, the system routes the test conditions to a printer and a set of X-Y plotters when a "data point" is signaled by pressing a button at the control console.

Two corrections were applied to the steady balance data in the process of calculating nondimensional test conditions. First, a correction was made for balance in...ractions. Strain gage bridges are mounted on the balance in locations designed for sensitivity to single forces or moments. In prac';ce, however, each bridge has a small sensitivity to every force and moment. The axis interaction sensitivities are accounted for by forming a vector of the measured forces and moments and multiplying by an experimentally determined interaction matrix. Second, model weight tare effects were included in the calculation. Aerodynamic hub tare corrections were not made because forward flight performance data was not a test objective. Tunnel wall effect corrections were unnecessary because the slotted wall configuration was used.

4.2.3 Dynamic Data System

The dynamic data system, like the static data system, is an analog-digital processor. This system performs detailed waveform analysis on selected data channels. It operates only when the "data point" button is pressed. For each data point, a train of samples is taken from each specified data channel, permanently recorded on magnetic tape, and analyzed as desired. The results are displayed on the printer below the test conditions determined by the static data system. Data analysis includes determination of mean and alternating amplitudes and harmonic analysis of some channels.

This data system was used primarily during test BVWT 129. The loads data presented in Section 6.0 was gathered through this system.

4.2.4 Spectral Analyzer

An on-line spectral analyzer was used for continuous display of the frequency content of a chord bending gage. Random aerodynamic excitation was sufficient to make every blade bending mode except the first flap evident in the spectral display, except at very low thrust levels. This had two benefits. First, proximity to an instability boundary could be judged accurately by watching the growth in amplitude of an unstable mode as the boundary was approached. Second, the variation of modal frequencies with collective could be determined.

All modal frequencies shown in Section 5.0 were read from the spectral analyzer. An example of modal frequency dependence on collective, as determined by the spectral analyzer for one model configuration, is shown in Figure 178.

4.3 Test Technique

4.3.1 Test Technique for Stability Boundaries

During each of the four phases of testing, a uniform method of approaching and recording a stability boundary was employed. This method, as shown through wide test experience, provides the most accurate, repeatable data with the least risk of damage to the model.

A typical stability test sequence is as follows. The model was first configured with the parameters to be observed and the configuration was checked and secured. The test stand was inspected and secured; in general, this was done at least once every 20 to 30 minutes of model run time. The tunnel or test section was then secured and the model running commenced.

Hover test boundaries were approached by setting collective pitch to zero degrees (or to the lowest possible setting if the pitch links were adjusted to a higher minimum value than zero degrees) and then increasing rotor speed up to the test condition. Because no form of instability appeared at zero collective, no data was generally taken during this "run-up".

After the model rotor speed had been stabilized at the selected value (between 1200 and 1800 rpm where 1670 rpm was the nominal operating value), the collective pitch was then increased in increments. The increments in collective pitch were reduced from approximately 3° at low collectives to 1° or less in the proximity of a stability boundary. Oscillograph data was taken at each increment of collective pitch. Spectral analyzer data indicating the frequency content and component amplitude was recorded when a stability boundary or operating limit was reached.

The proximity of a stability boundary reached in this fashion was observed in several ways. On the safety-of-flight oscilloscope monitors, standing waves of rotor harmonic loads appear to intermittently "gallop" as the amplitude of natural modes, potential modes of instability, at nonharmonic frequencies, become significant. This was most readily observable in the blade chord bending gage monitor. On the spectral analyzer, analysis of the chord bending gage output indicated fluctuations in the amplitude of the noninteger frequency components.

At the collective pitch setting corresponding to an instability, the amplitude of a frequency component of a natural mode exceeds 100% of the allowable load. For the flap-lag stability boundaries this was recorded in the chordwise bending gage. In most cases the total alternating load was considerably higher than 100% due to the contributions of harmonic and other

95

loads, but for short periods of time this was not destructive
to the model. Upon reaching a boundary condition, frequency
data from the spectral analyzer was recorded and oscillograph
data taken. The collective pitch was rapidly descreased to
return the model to a stable operating condition. The
severity of the model behavior at the stability boundary de-
pended on model configuration. In cases where a stability
boundary was not reached due to some operation limit, data was
recorded at the highest collective attained.

4.3.2   Test Technique for Loads Data

The operation methods for acquiring loads data in hover are
identical to the methods applied for stability boundaries.
However, the time spent at each test condition was dictated by
the length of the data sample required by the digital data sys-
tem, and this as a rule was considerably longer than in the
stability runs. Therefore, a stability check was generally
performed for each model configuration first, so that the sus-
tained high load conditions associated with the boundary points
and beyond were not tested.

The operation method for taking data at forward flight condi-
tions was similar to that outlined above. The model was first
set at the desired rotor speed at zero collective pitch. The
tunnel speed was then selected and finally the collective or
other desired variable was input. The recording of loads data
was the same in forward flight and hover.

4.3.3   Test Operational Limitations

Throughout the stability and loads testing of the 8-foot-dia-
meter tail rotor model, several operational limitations were
observed to protect the model and test stand from damage. The
hover test envelope was defined by three limits in addition to
the various forms of stability boundaries: a power limit set
by test stand motor capability; a pitch link load limit set by
actuator capability; and a swashplate travel limit also set by
actuator capability. Some of the figures (Figure 51, for ex-
ample) include data points obtained at the edge of the test-
ing envelope. These points are labeled "model testing limit".

The swashplate travel limit was usually avoided by changing the
length of the pitch links. This permitted testing up to the
power limit, which for the normal four-bladed model was always
encountered before the limit on pitch link loads. Thus, the
power limit was the most constraining of the three limits.
Two blades were therefore removed to test configurations which
were stable up to the four-bladed power limit. Testing in the
two-bladed condition was then limited by either the two-bladed
power limit or the limit in pitch link loads.

96

5.0 TEST RESULTS - STABILITY BOUNDARIES AND FREQUENCIES

The test results which follow reflect the data collected during the four test phases (BVWT 124, BVTC 009, BVWT 129, and BVWT 011) of the 8-foot-diameter bearingless tail rotor model. These results, gathered from over 150 data points, indicate the effect of 12 configuration parameters, detailed in Section 3, on several forms of instability.

It is important to note that this particular model is a stiff inplane design (having a first inplane blade bending natural frequency greater than one per rev at operating rotor speed). The observations and conclusions drawn from them are valid for only this type of rotor. However, it is likely that the configuration parameters that were found to be influential on this model will have a significant effect over a wide range of bearingless designs, including soft inplane rotor systems.

5.1 Types of Instability

Four types of aeroelastic instability occurred as the twelve configuration parameters (Section 3.0) were varied. These instabilities occurring with negative δ_3 (flap up/pitch down coupling) are: flap-lag instability in inplane scissors and "C" modes; stall flutter in the third flexible mode (torsion); and stall flutter in the fourth flexible mode (second flap).

The flap-lag instability was produced by the proximity of the first flap and first inplane modes in this "stiff inplane" design (see Section 7.1 for plots of the natural frequencies in a vacuum). The instability appeared as a limit cycle in flap, lag, and pitch, whose amplitude grew steadily as collective was raised through a range of several degrees up to a critical value, or "stability boundary", which depended on rpm and model configuration. Above the boundary, limit cycle amplitude grew extremely rapid with collective, to the point that collectives more than about 0.5 degree beyond the boundary could not be explored without damaging the model. The limit cycle lag motion occurred in either the scissors, "S", or "C" mode (see Figure 46), depending on the relative stability of these two modes (a function of model configuration) and on which of the two modal frequencies was closer to the first flap frequency (a function of rpm). The limit cycle occurred at rotor speeds within 200-300 rpm of a crossing of the flap frequency and either of the first inplane modes (scissors or "C"). The closer the rotor speed was to an exact flap-lag crossing rpm, the lower was the critical collective for the limit cycle. Thus, on a plot of collective versus rpm, the flap-lag stability boundary was found to be a pair of valleys whose deepest points were at the exact crossing rpm's of the first flap frequency and the first inplane scissors and "C" modes. The "C" mode valley, at higher rpm, was always found to be deeper than the scissors mode

97

4-BLADED ISOLATED ROTOR - INPLANE MODES

COLLECTIVE LAG

CYCLIC LAG - "C" MODE

REACTIONLESS SCISSORS - "S" MODE
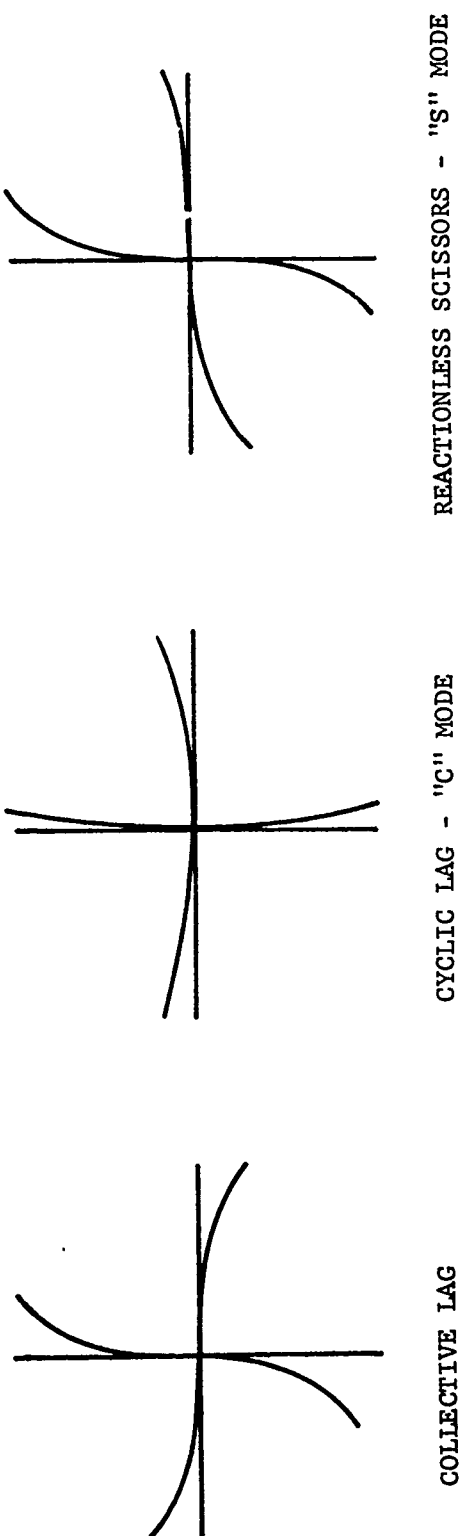
FIGURE 46   SCHEMATIC OF INPLANE MODES

valley. The depth of both valleys was strongly dependent on configuration parameters, as will be described in Section 5.2. The rpm's of the valleys were shifted as expected by configuration parameters which changed either the first flap or first inplane frequencies.

A typical flap-lag stability boundary obtained with unfavorable configuration parameters is shown in Figure 47. The boundary could have been plotted in terms of true collective, thrust coefficient, or power coefficient. Power coefficient was chosen--the practice followed throughout the test--because it was available, on-line, during all test phases, whereas true collective and thrust coefficient were not.

Strap bending and strap torsion time history waveforms recorded by oscillograph during scissors and "C" mode flap-lag instabilities are shown in Figure 48.

Stall flutter appeared as a limit cycle at high collective at either of two modal frequencies, depending on rpm. The boundary of stall flutter onset in the rpm-collective plane and the amplitude of the limit cycle depended strongly on configuration parameters that influence the intermodal coupling, as will be described in Section 5.2. Therefore, although this form of instability will be referred to as stall flutter, it should be noted that this phenomenon is most likely not flutter in the classical sense. A typical stall flutter boundary obtained with unfavorable configuration parameters is shown in Figure 49. Strap bending and torsion waveforms recorded by oscillograph during a stall flutter limit cycle are shown in Figure 50.

In the plots of the stability boundaries, the type of instability recorded is always the least stable mode. For this reason, there will be only one boundary point plotted at each rotor speed tested. This means that, if, for example, a flap-lag instability is encountered at some value of C_p/σ and Ω in a configuration that has displayed stall flutter boundaries at other rotor speeds, then the flap-lag mode has become less stable than the stall flutter mode through the change in test condition. The boundary of the stall flutter mode would still be present at some higher C_p/σ but cannot be explored further. The typical flap-lag stability boundary presented above, Figure 47, is an example of overlapping "S" mode and "C" mode boundaries. On that plot the boundaries have been extrapolated to indicate where a particular type of instability would be expected.

With respect to recording the modal frequencies, the situation is not as limited as recording boundaries. By using the spectral analyzer, the frequency of the various modes can be observed before a stability boundary is reached. Therefore, in all

99

BVWT 129 - RUN 10

3.3" Straps (335, 336)
VR-7.2/7.4 Airfoils
No Hub Inserts
9° Clevis
$\delta_3 = -65°$
$\Lambda = 6°$
Outboard Cruciform, Low EI
No Tip Weights
Canted Pitch Links

UNSTABLE
"S" MODE

STABLE
"C" MODE

UNSTABLE
"C" & "S"
MODES

UNSTABLE
"C" MODE

STABLE
"S" MODE

STABLE

○ "S" MODE ⎫
● "C" MODE ⎬ FLAP-LAG LIMIT CYCLE
             BOUNDARY

− − − − − EXTRAPOLATION OF STABILITY
           BOUNDARY

MAX. STABLE POWER COEFFICIENT , C_P/σ

RPM
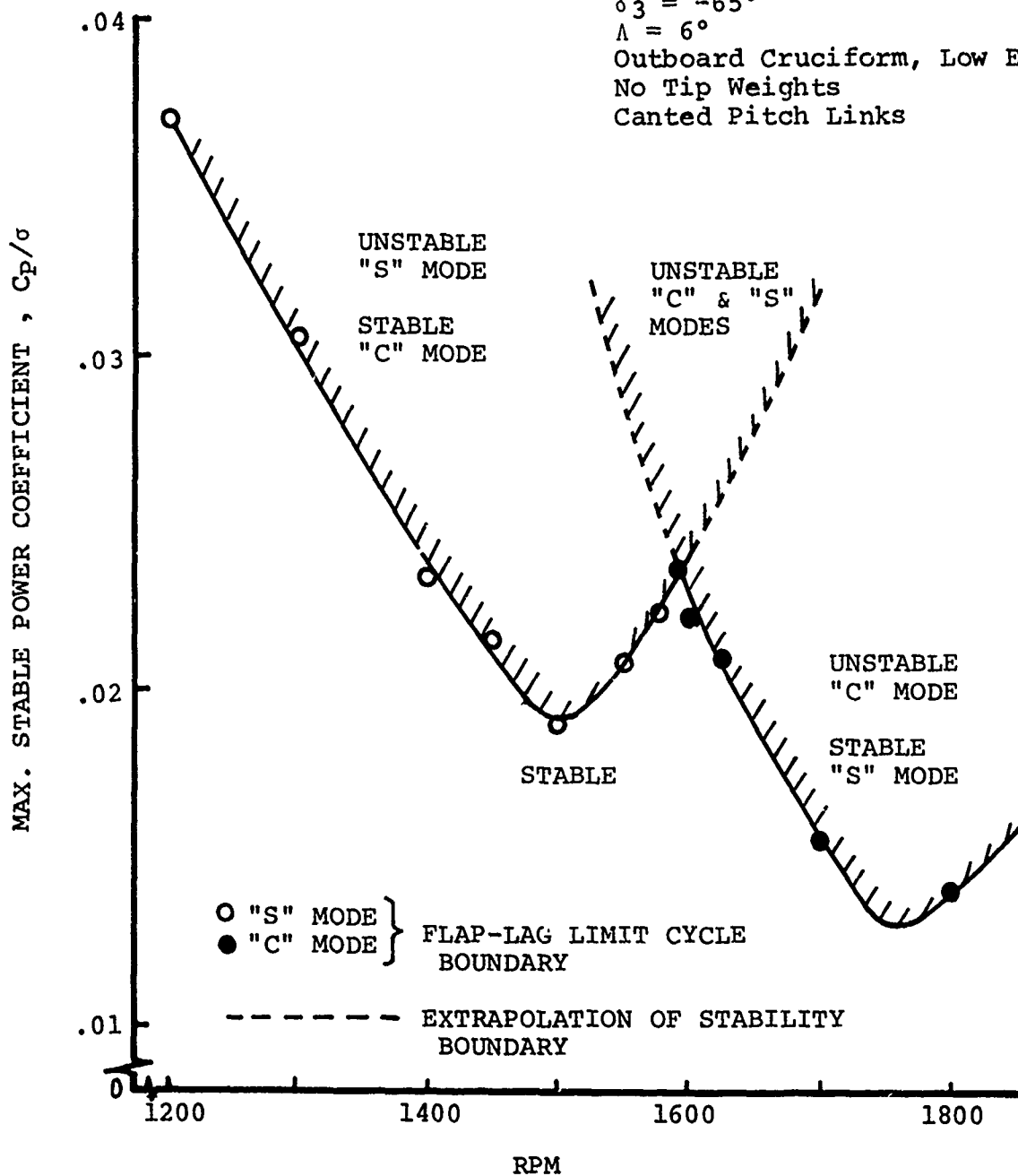
FIGURE 47   TYPICAL FLAP-LAG STABILITY BOUNDARY OBTAINED
            WITH UNFAVORABLE CONFIGURATION PARAMETER

100

FLAP BENDING
98.5 IN-LB/IN

FLAP UP

(1/REV WITH BEATS
SHOWING 1.24/REV
COMPONENT.)

(RAN OFF PAPER)

CHORD BENDING
1650 IN-LB/IN

LAG

(1.24/REV WITH BEATS
SHOWING 1/REV
COMPONENT.)

TORSION
174 IN-LB/IN

NOSEUP

(1/REV WITH BEATS
SHOWING 1.24/REV
COMPONENT.)

1/REV MARKER
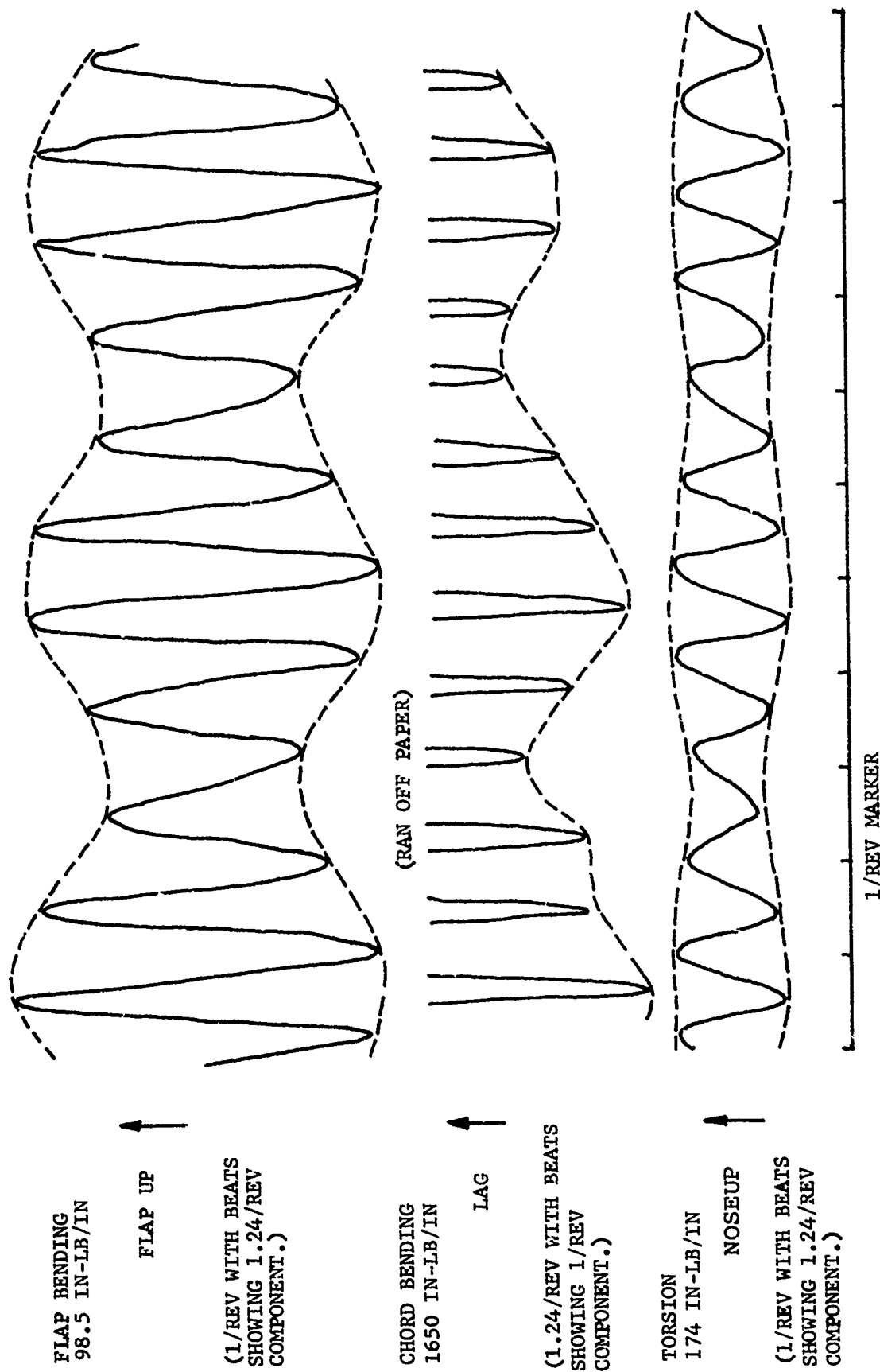
FIGURE 48   TYPICAL FLAP-LAG INSTABILITY TIME HISTORY

101

BVTC 009 - RUN 21

4.4" Straps (335, 336)
VR-6.9 Airfoil
Elastomeric Hub Inserts
$K_\zeta = 350,000$ In-Lb/Rad
$9°$ Clevis
$\delta_3 = -65°$
$\Lambda = 0°$
Inboard Cruciform
Tip Weight, 88 Fwd/0 Aft
Radial Pitch Links

□ STALL FLUTTER LIMIT CYCLE
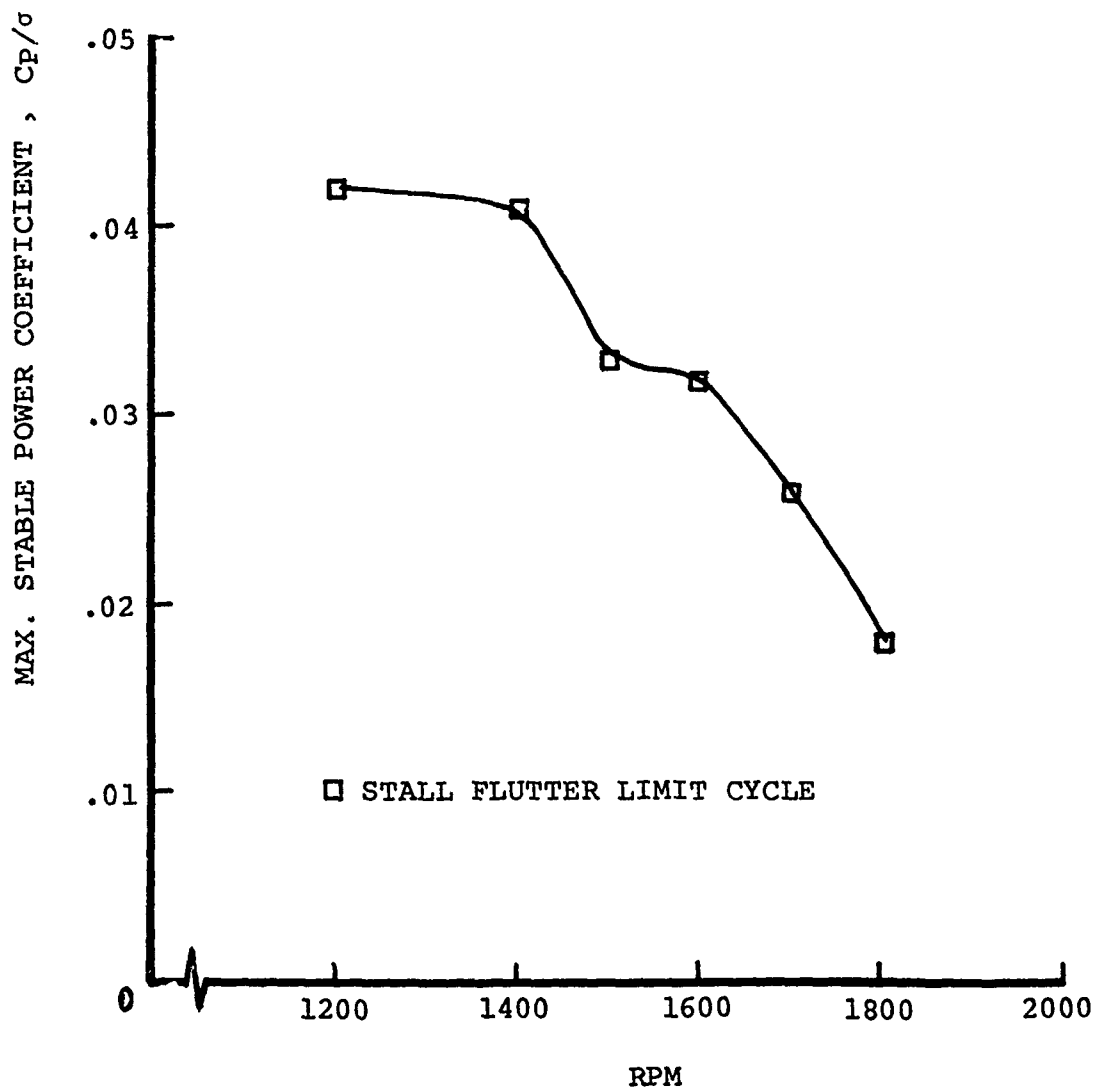
FIGURE 49   TYPICAL STALL FLUTTER BOUNDARY OBTAINED
WITH UNFAVORABLE CONFIGURATION PARAMETERS

BVWT 124, RUN 36   STRAP 335 MOMENTS

1700RPM, $\Theta_{.75}$ = 32.7   IND.

FLAP BENDING
.059R
145 in-lb/in

FLAP UP ↓
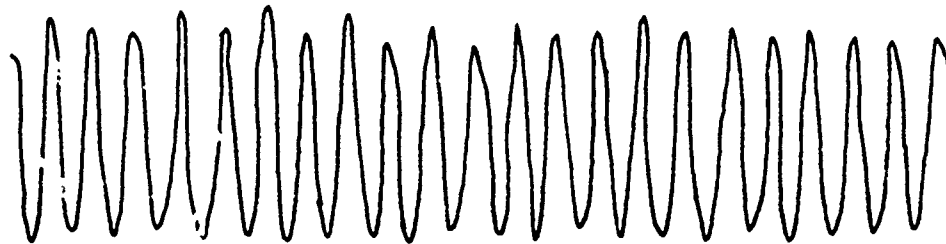
(RAN OFF PAPER)

CHORD BENDING
.082R
577 in-lb/in

LAG ↑
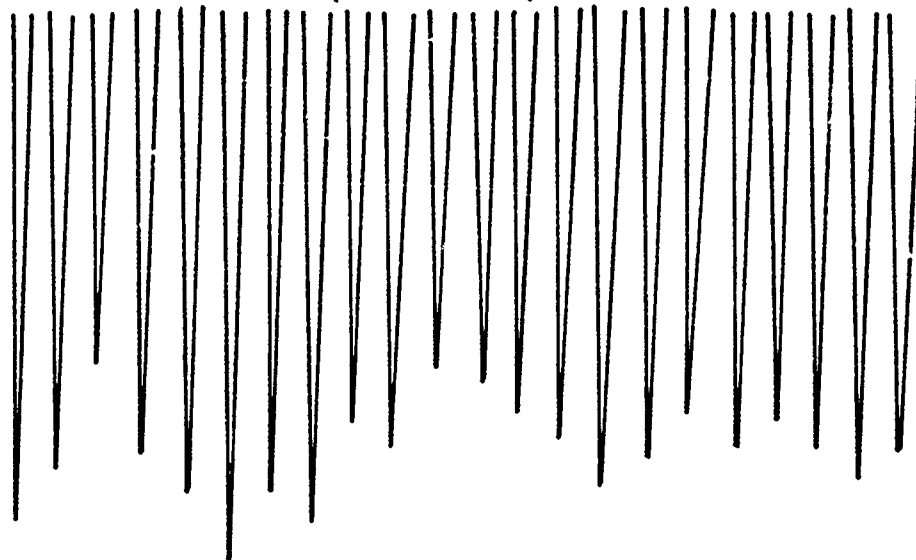
TORSION
.082R
34,700 in-lb/in

NOSEUP ↑

1/REV MARKER

FIGURE 50   TYPICAL STALL FLUTTER INSTABILITY TIME
HISTORY

103

of the modal frequency plots, lines are drawn to indicate the observed frequency versus rotor speed, and the symbol for a flap-lag or a stall flutter boundary designate actual boundary conditions at that point.

5.2 Sensitivity of Stability Boundaries to Configuration Parameters

The sensitivity of the stability boundaries of the flap-lag instabilities and the stall flutter instabilities to the configuration parameters will be presented for each parameter in the order given in Table 6. In the sections which follow, the test data used for the stability boundary plots was selected as the most representative of a given parameter. This was accomplished primarily through the observation of the repeatability of a given parameter effect in several test runs.

It was found that the effects of each parameter depend, to some extent, on the values of the others. The effects of some parameters are individually nonlinear; i.e., stability boundaries did not always move in direct proportion to the amount of parameter change. Consequently, this leads to the necessity of relying on extensive configuration trials to establish the aeroelastic effect of the parameters.

5.2.1 Clevis Angle

Effects of clevis angle on the flap-lag instability are shown in Figure 51. Increasing the clevis angle from 9° to 26° in the selected configuration raised the "C" mode flap-lag boundary and either lowered or left unchanged the stall flutter boundary, to the extent that stall flutter occurred before the flap-lag boundary was reached. The figure does not permit quantitative conclusions about the effect of clevis angle, but represents the only direct comparison obtained to show the influence of this parameter. Increased clevis angles beyond 26° were not investigated.

The observed modal frequencies at the stability boundaries for the two modes of instability, the "C" mode and the stall flutter mode, are shown in Figure 52. In this case, there is no direct comparison of the modal frequencies for the flap-lag or stall flutter mode between the two configurations.

The effect of clevis angle on the stall flutter boundary is shown in Figure 53. As shown in this figure, the 9° clevis configuration is quite stable, reaching the operating limits at all rotor speeds between 1200 and 1600 rpm. At the two highest rotor speeds, a stall flutter condition is encountered near a C_p/σ of 0.028. The 26° clevis configuration displays a stall flutter boundary at all of the rotor speeds tested. At 1400, for example, the boundary conditions appear at a

104

BVWT 124 - RUNS 2-10

4.4" Straps
VR-7.2 Airfoils
Elastomeric Hub Inserts
K_ζ = 350,000 In-Lb/Rad
δ_3 = -45°
Λ = 0°
No Cruciform
No Tip Weights
Radial Pitch Links

O   "C" MODE FLAP-LAG LIMIT CYCLE

☐   STALL FLUTTER

△   MODEL TESTING LIMIT
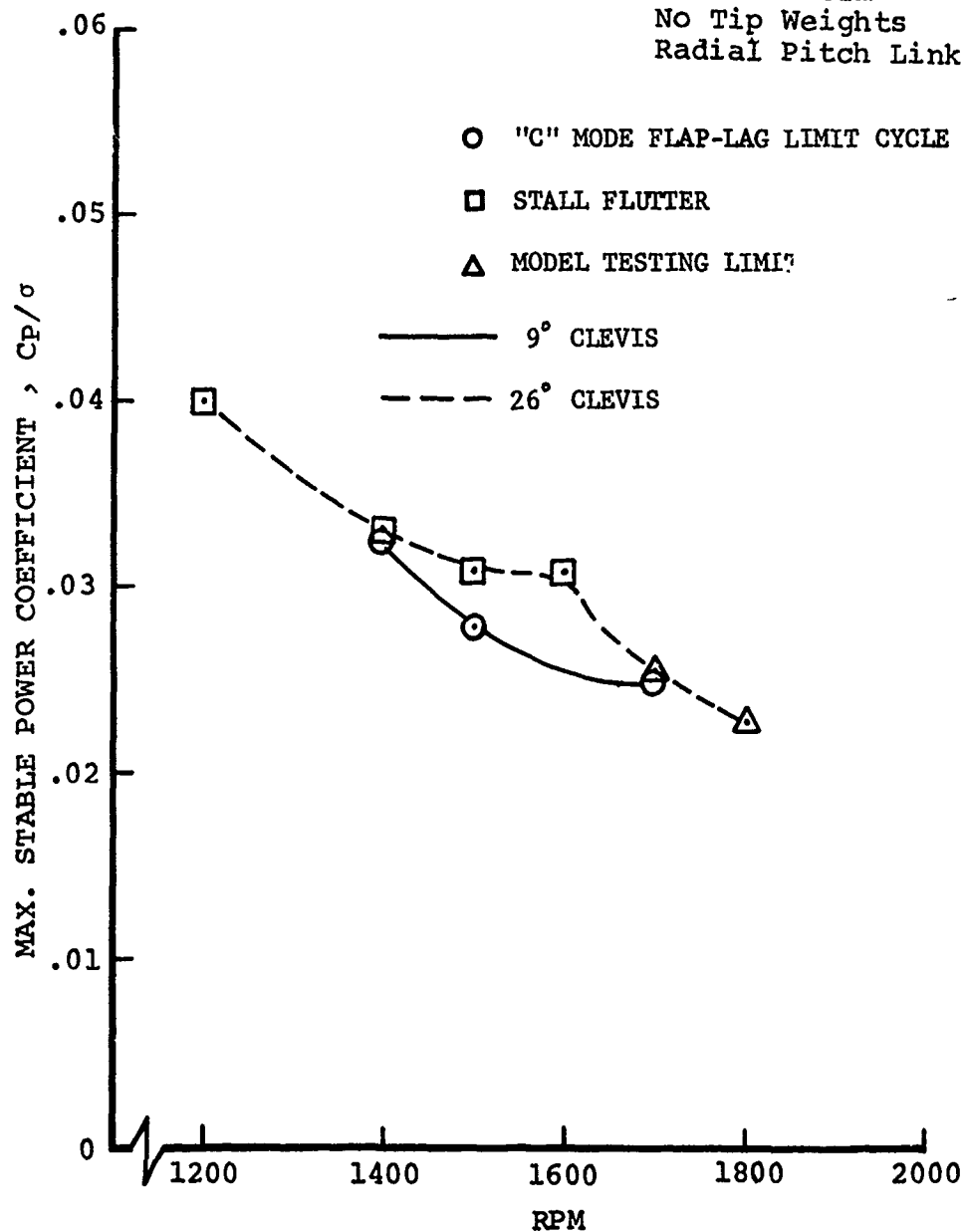
———————   9° CLEVIS

— — — —   26° CLEVIS

FIGURE 51   EFFECT OF CLEVIS ANGLE ON FLAP-LAG
STABILITY BOUNDARY

105
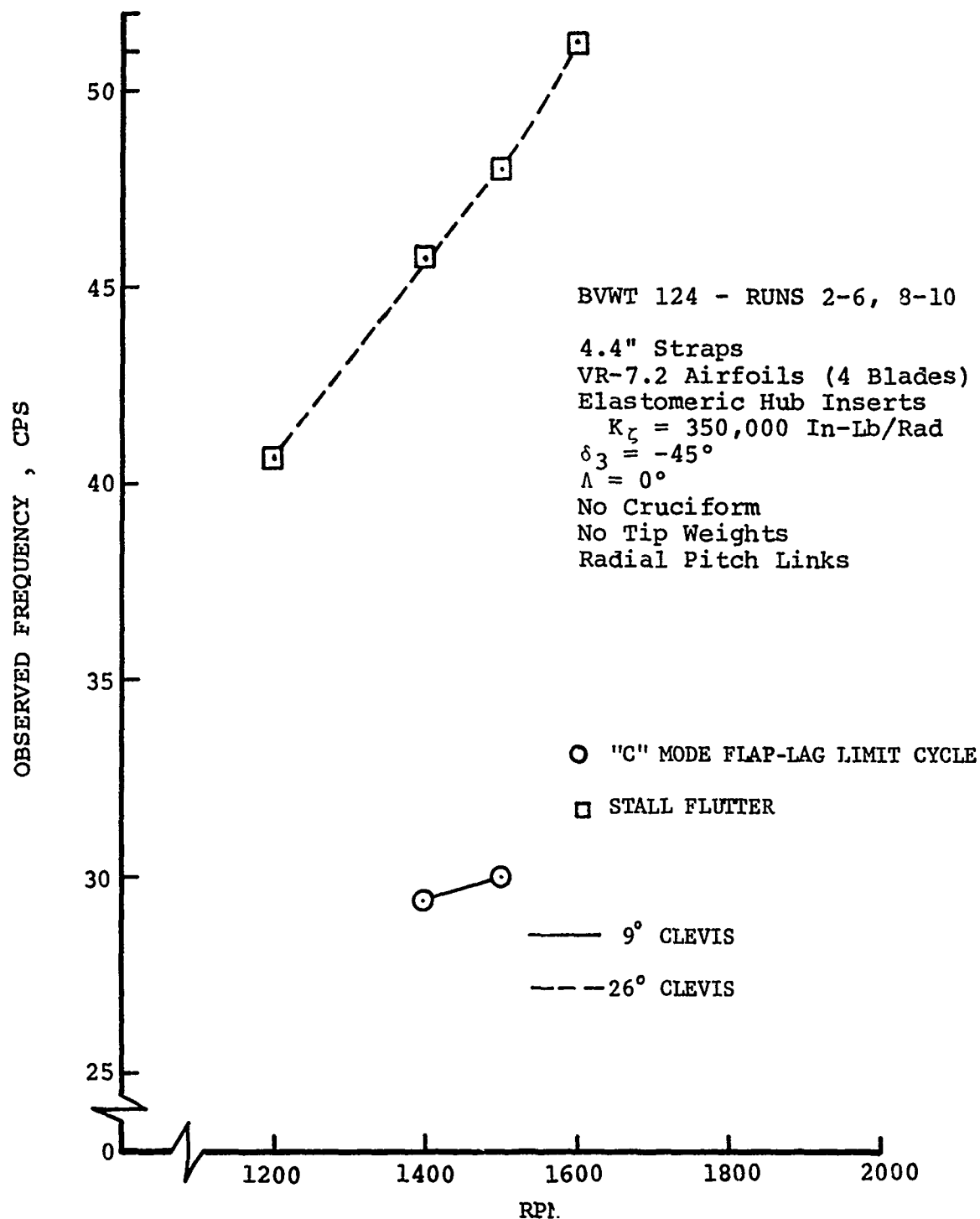
FIGURE 52   EFFECT OF CLEVIS ANGLE ON FIRST
INPLANE FREQUENCIES

BVWT 124 - RUNS 39, 52

4.4" Straps
2-VR-7.2 Repaired Airfoils
Elastomeric Hub Inserts
  K_ζ = 350,000 In-Lb/Rad
δ_3 = -65°
Λ = 4°
No Cruciform
No Tip Weights
Radial Pitch Links
No Pitch Arm Weight

□   STALL FLUTTER

△   MODEL TESTING LIMIT
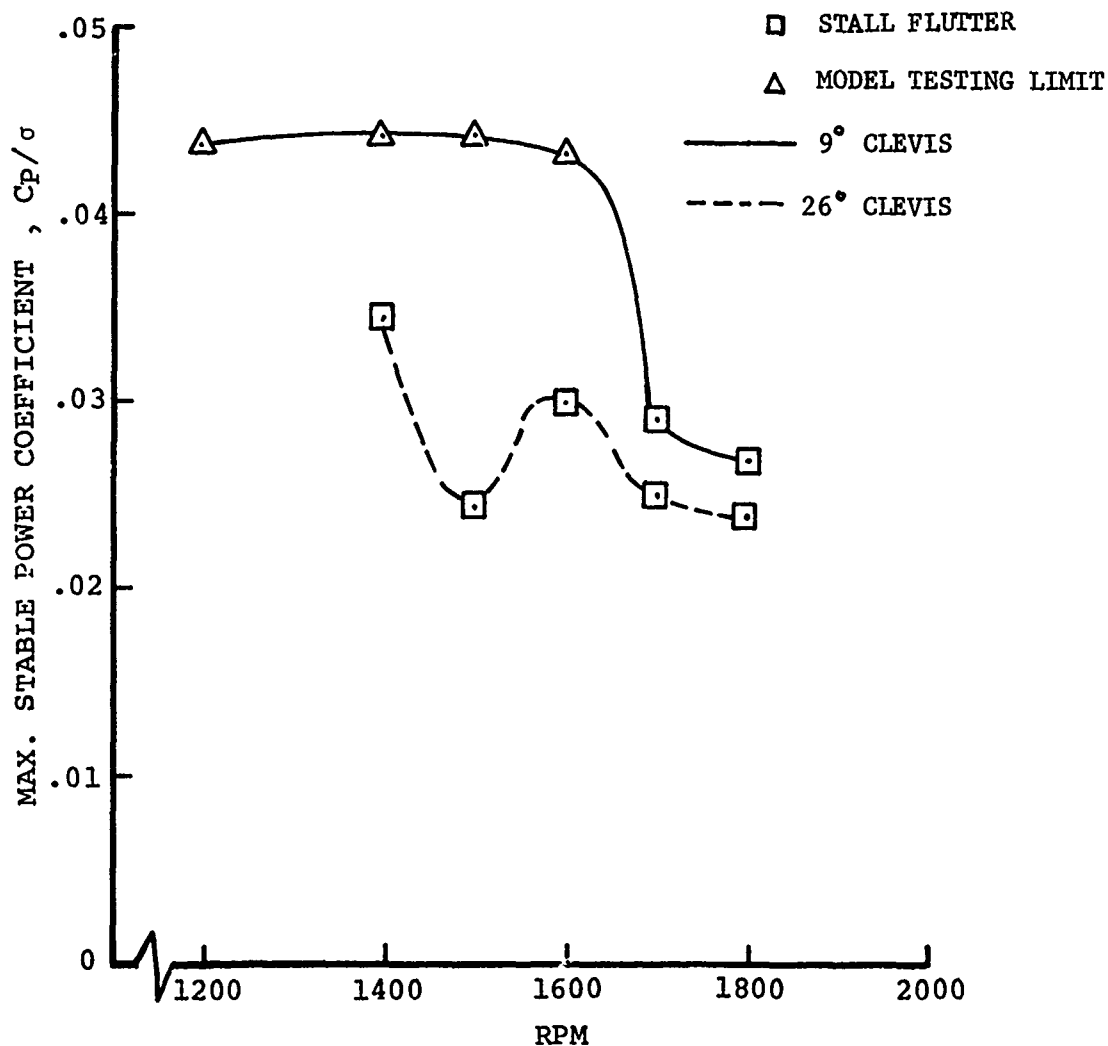
———   9° CLEVIS

- - - -   26° CLEVIS

FIGURE 53   EFFECT OF CLEVIS ANGLE ON STALL
FLUTTER BOUNDARY

107
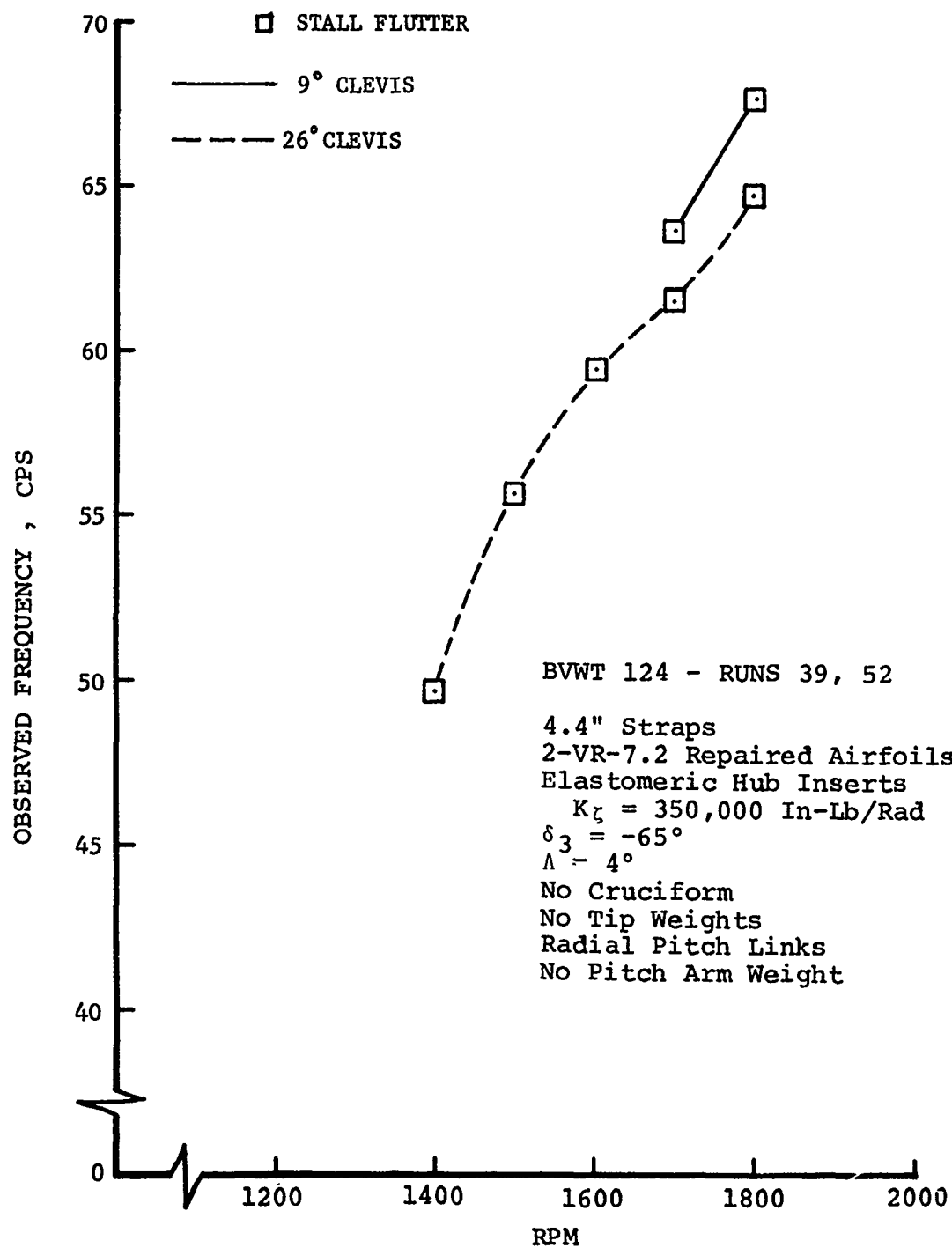
FIGURE 54   EFFECT OF CLEVIS ANGLE ON HIGHER
              MODE FREQUENCIES

108

$C_p/\sigma = 0.0345$. This indicates that the boundary for the 26°
clevis configuration is at least of a C_p/σ value of 0.01 lower
than the boundary of the 9° clevis at the same rotor speed.
At the higher rotor speeds, 1700 and 1800 rpm, the stability
boundaries for the configurations occur within a C_p/σ of
0.0025 of each other.

The observed frequencies of these stall flutter boundaries are
presented in Figure 54. The frequencies of this stall flutter
mode for both configurations are near 2.3 times the rotor speed.
The 26° clevis configuration, however, displays a modal fre-
quency about 2.5 cps lower than the 9° configuration near opera-
ting rotor speed, 1670 rpm.

5.2.2 Pitch Link Tilt

The effect of pitch link tilt is shown in Figure 55. Although
this parameter was studied during several test phases, it was
not conclusively determined whether pitch link tilt signifi-
cantly influences the stability characteristics of the model.
As shown in the figure, the boundary points in the flap-lag "S"
mode for both configurations lay in close proximity to each
other.

Figure 56 shows the observed frequencies for these configura-
tions. In the flap-lag "S" mode, there is no measurable
difference between the tilt and the no-tilt configurations,
both having a modal frequency of 38.5 cps at 1670 rpm. The
"C" mode frequencies also show little difference.

5.2.3 Delta-3 Coupling

Effects of delta-3 coupling on the flap-lag instability are
shown in Figures 57 and 58. Reducing δ_3 is beneficial to flap-
lag stability, principally because it lowers the first flap
frequency, shifting the boundary valleys to higher rpm's.
Specifically, first flap frequency is 1.18/rev for $\delta_3 = -45°$
compared to approximately 1.3/rev for $\delta_3 = -65°$. Figure 58
indicates that a secondary benefit is gained by a small in-
crease in the scissors mode frequency. Figure 57 shows the net
effect for one configuration: a shift in the "C" mode boundary
sufficient to place it above the stall flutter boundary. Delta-
3 reduction was not investigated extensively because of the
adverse effects of this change on strap loads in forward flight
as discussed on page 65 of Reference 2.

5.2.4 Blade Sweep

Figures 59 and 60 illustrate the effects of blade sweep, which
was found to be strongly beneficial in all model configurations.
In the configuration selected for the figures, 11° sweep
approximately doubled the maximum stable C_p/σ at each rpm. The

BVTC 009 - RUNS 125, 158

4.4" Straps
2 VR-7.2 Airfoils
No Hub Inserts
9° Clevis
$\delta_3 = -65°$
$\Lambda = 6°$
Outboard Cruciform, Low EI
No Tip Weights

PITCH LINK TILT

— — NO PITCH LINK TILT

O "S" MODE
● "C" MODE
△ MODEL TESTING LIMIT
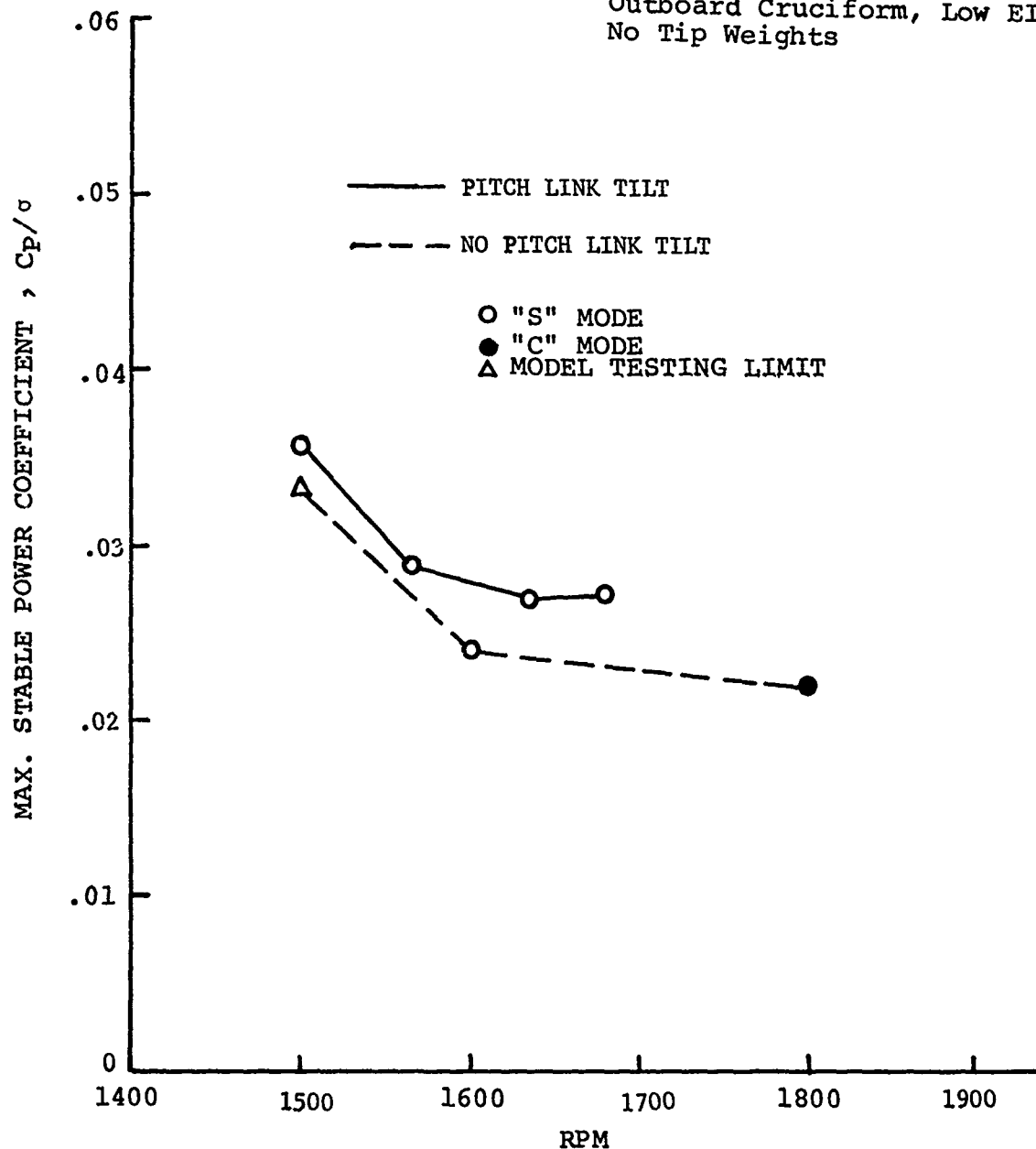
FIGURE 55   EFFECT OF PITCH LINK TILT ON
FLAP-LAG STABILITY BOUNDARY

110

FIGURE 56   EFFECT OF PITCH LINK TILT ON FIRST
            INPLANE FREQUENCIES

111

O "S" MODE ⎫
           ⎬ FLAP-LAG LIMIT CYCLE
● "C" MODE ⎭

▢ STALL FLUTTER

△ MODEL TESTING LIMIT

——— $\delta_3 = -45°$

- - - $\delta_3 = -65°$

BVWT 129 - RUNS 42, 61

4.4" Straps
VR-7.2, VR-7.4 Airfoils
Elastomeric Hub Inserts
  $K_\zeta = 350,000$ In-Lb/Rad
9° Clevis
$\Lambda = 0°$
Outboard Cruciform, Low EI
No Tip Weights
Radial Pitch Links
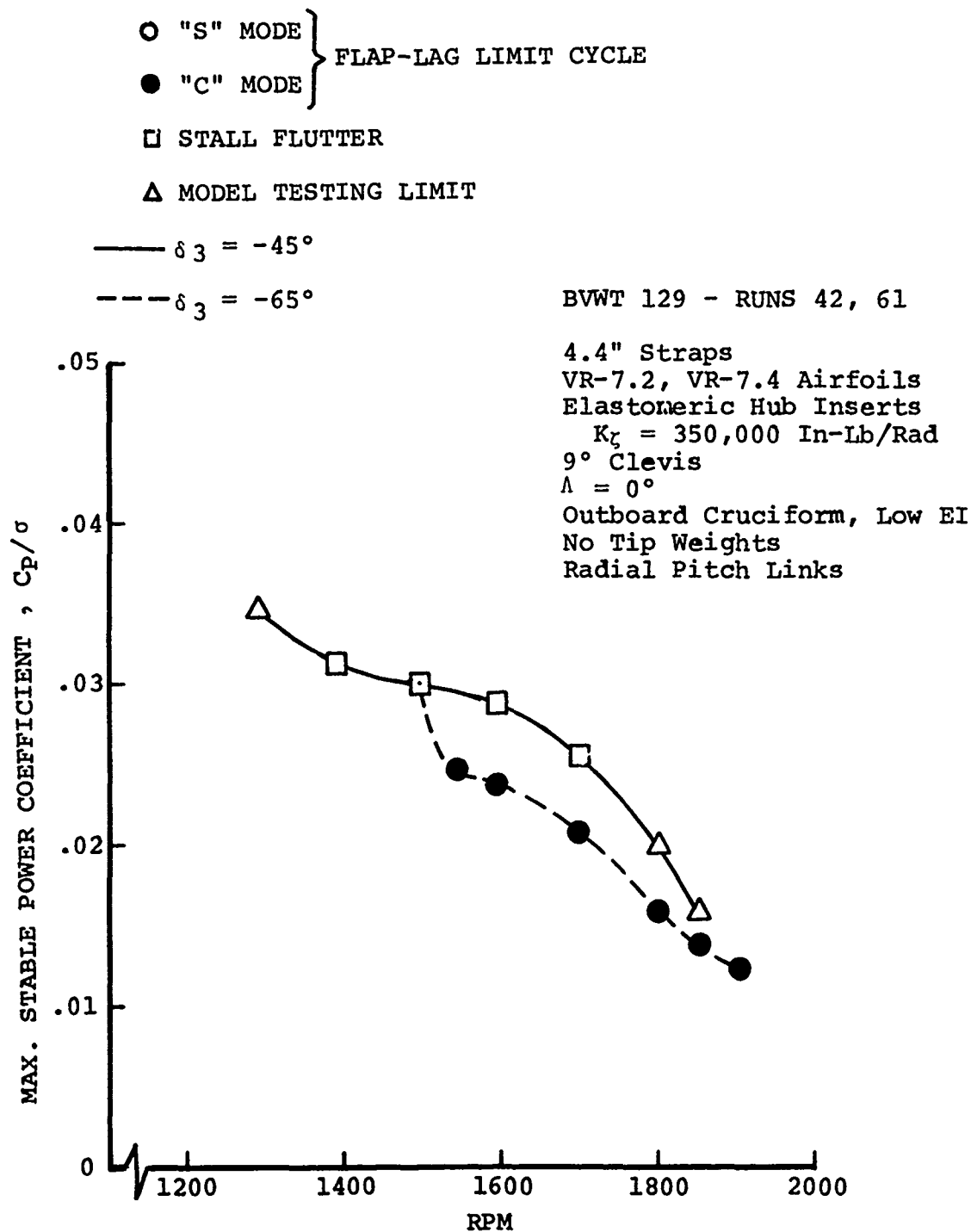
FIGURE 57   EFFECT OF DELTA-3 COUPLING ON
                       FLAP-LAG STABILITY BOUNDARY
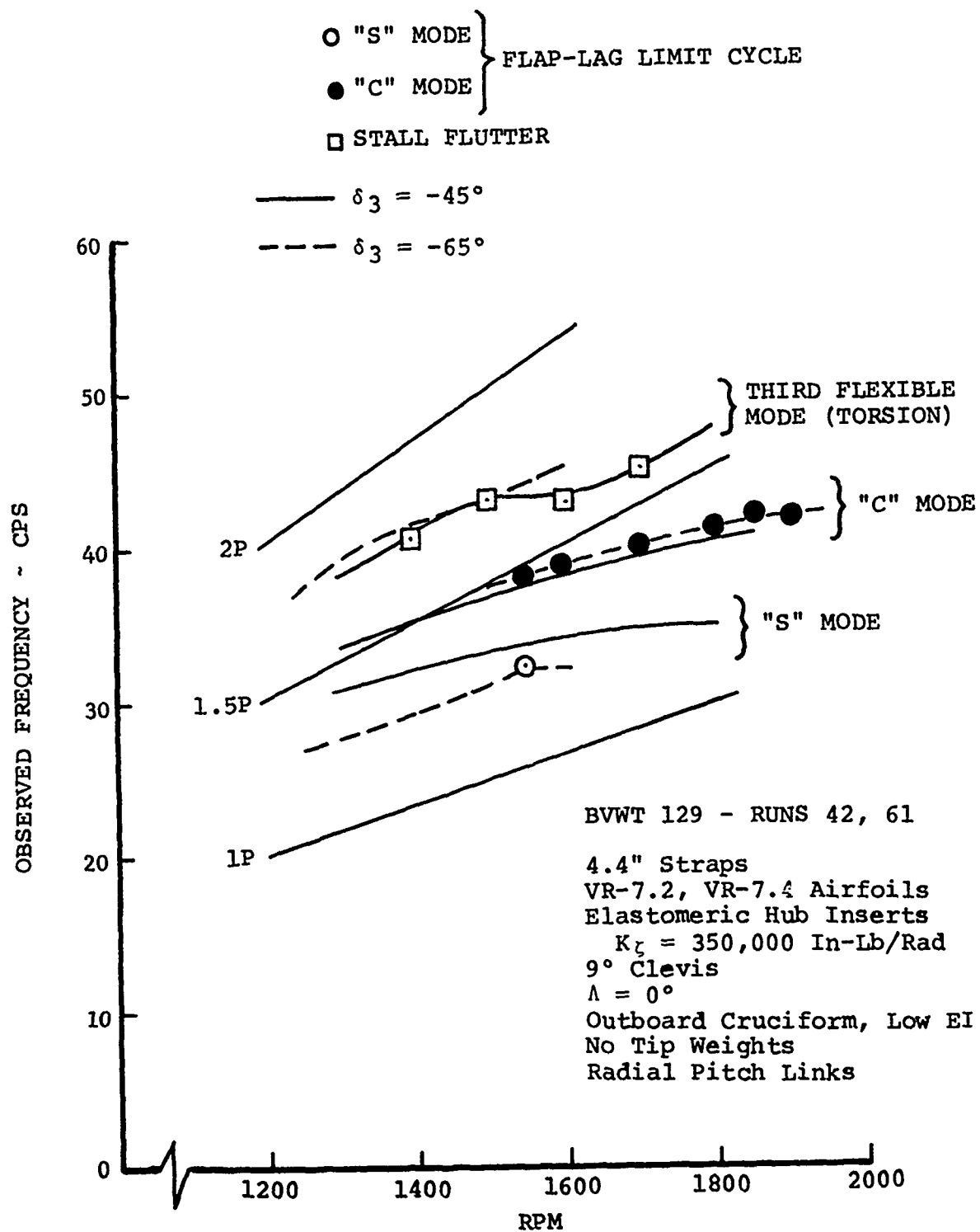
FIGURE 58   EFFECT OF DELTA-3 ON FIRST INPLANE
FREQUENCIES

effect on inplane frequencies was small--a slight chordwise
stiffening, which is shown in Figure 60 and reflected in
Figure 59 as a slight increase in the rpm of the scissors mode
boundary valley. (Frequencies shown in the Figure 60 plot are,
as in all plots of this type, frequencies observed at maximum
attainable collective. Higher collectives were reached in the
swept configurations, so the observations for these configura-
tions were therefore made at higher collectives, where chord
frequencies are somewhat reduced by strap twist. It can be
seen that these configurations would have slightly higher fre-
quencies than the unswept configuration if both were observed
at the same collective.)

Figure 59 shows that sweep raises the stability boundary by
much smaller absolute amounts at high rpm's than at low rpm's.
This suggests that centrifugal force may reduce the effects of
sweep at high rpm by reducing the sweep itself. The data does
not indicate the mechanism by which sweep produces such strong
stabilizing effects. However, some insight into this matter
was gained through the Y-69 analysis which appears in Section
7.3.

The effects of blade sweep on stall flutter are shown in
Figures 61 and 62. Figure 61 illustrates the strongly benefi-
cial effect of small amounts of sweep on the stall flutter
boundary. The modal frequencies associated with this stall
flutter indicate that the instability in this configuration
occurred in both the third and fourth flexible modes, depending
on rpm and sweep, as shown in Figure 62. Sweep raised the fre-
quencies of both of these modes.

The data does not indicate the mechanism of the stabilizing
effects of sweep on flap-lag and stall flutter stability. It
is believed, however, that the effect is probably due to a
combination of factors, one of which is an increase in the
a.c.-c.g. offset measured in the direction of the strap chord,
which was not swept. The other is apparently related to a
change in the reaction of the C.F. in the strap area. A dis-
cussion of the latter is presented in Section 7.0.

5.2.5 Radius of Sweep Point

The effect of the blade sweep point is shown in Figures 63 and
64. For this parameter sensitivity, a fixed sweep angle of 6°
was selected. The two spanwise sweep points are 19.5 inches
when sweep at the blade to clevis junction and 16.15 inches
when sweep at the strap to clevis junction, as detailed in
Section 3.5. As shown in Figure 63, this parameter had little
effect on the placement of the flap-lag boundaries, in parti-
cular the "C" mode boundary. The "S" mode boundary is shown
to have a significant difference between the two configurations
at only one rotor speed, 1450 rpm. It is not clear why this
difference exists.

OPEN SYMBOLS – "S" MODE } FLAP-LAG LIMIT CYCLE
SOLID SYMBOLS – "C" MODE

BVWT 011 – RUNS 1,3,4,15

3.6" Straps (334, 337)
VR-7.2, VR-7.4 Airfoils
No Hub Inserts
9° Clevis
$\delta_3 = -65°$
Full Cruciform, Low EI
No Tip Weights
Radial Pitch Links

MAX. STABLE POWER COEFFICIENT , C_P/σ

RPM

□———— $\Lambda = 0°$
○— — — $\Lambda = 6°$
△—·—·— $\Lambda = 11°$
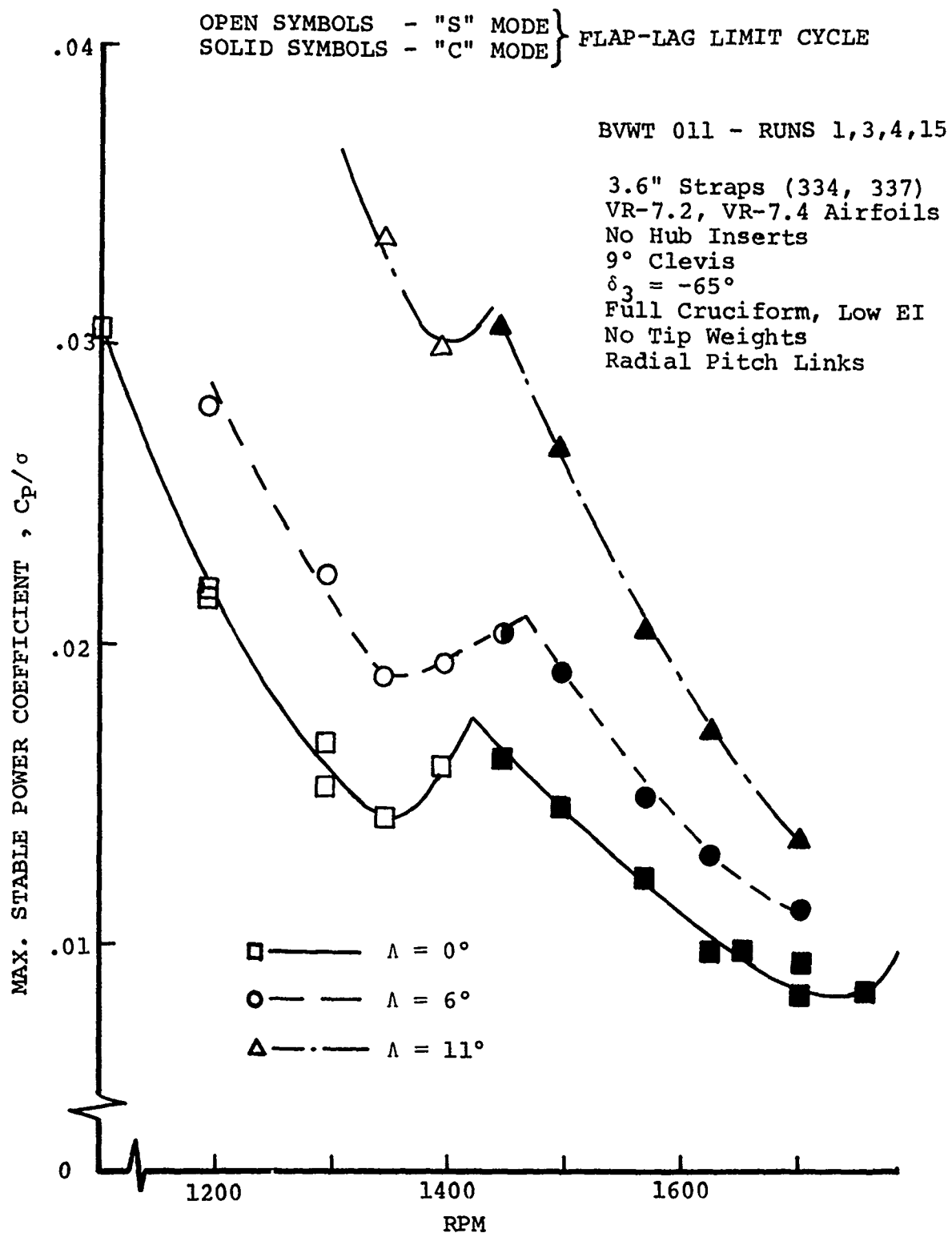
FIGURE 59   EFFECT OF BLADE SWEEP ON FLAP-LAG
              STABILITY BOUNDARY
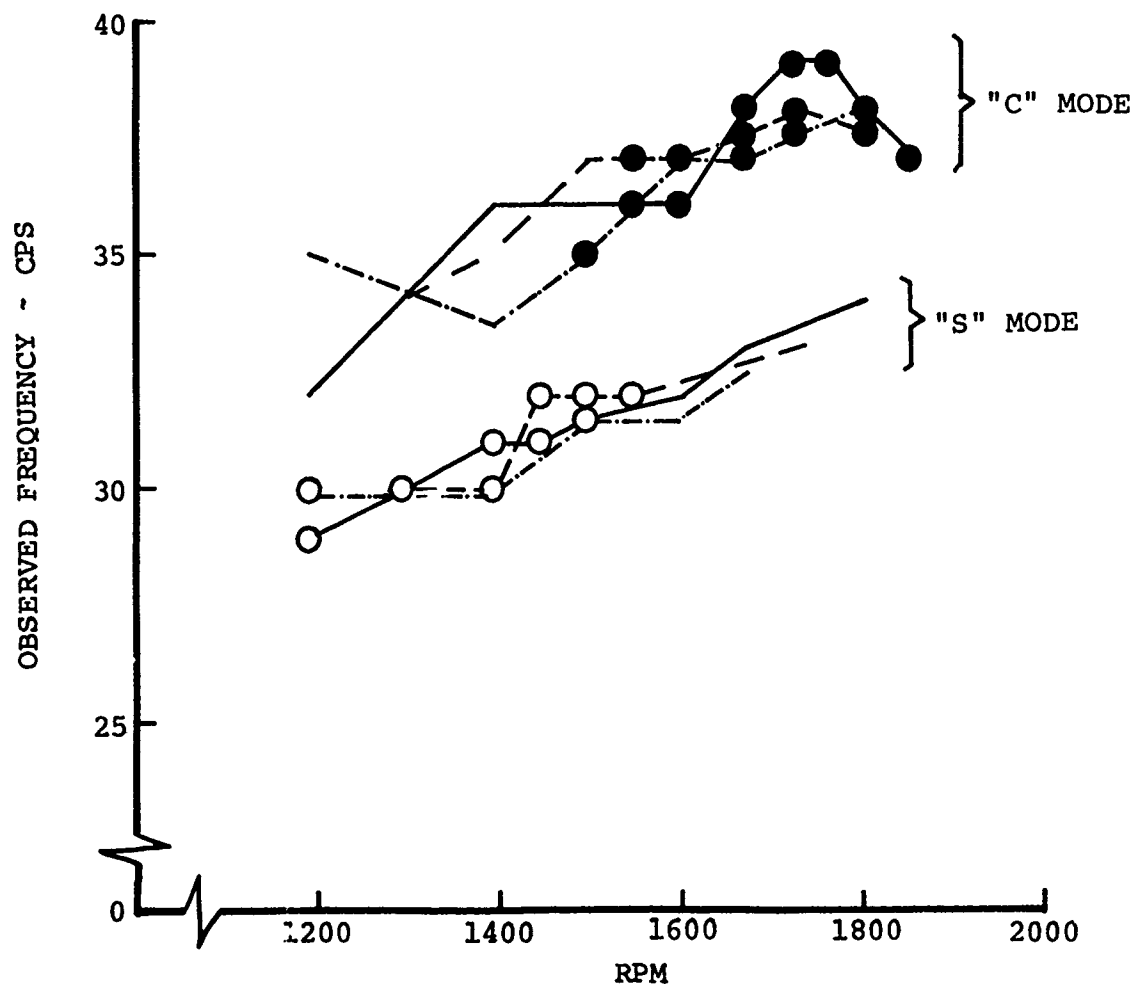
FIGURE 60   EFFECT OF BLADE SWEEP ON FIRST
              INPLANE FREQUENCIES

116

FIGURE 61   EFFECT OF BLADE SWEEP ON STALL
              FLUTTER BOUNDARY

117

BVTC 009 - RUNS 19-22, 27, 29

4.4" Straps (335, 336)
Elastomeric Hub Inserts
  K_ζ = 350,000 In-Lb/Rad
9° Clevis
δ_3 = -65°
Inboard Cruciform
Tip Weight 88 Fwd/0 Aft
Radial Pitch Links

□ STALL FLUTTER

——— Λ = 0°

—·—·— Λ = 2°

—··—··— Λ = 4°

— — — Λ = 6°

FOURTH FLEXIBLE
MODE (2ND FLAP)

THIRD
FLEXIBLE
MODE
(TORSION)
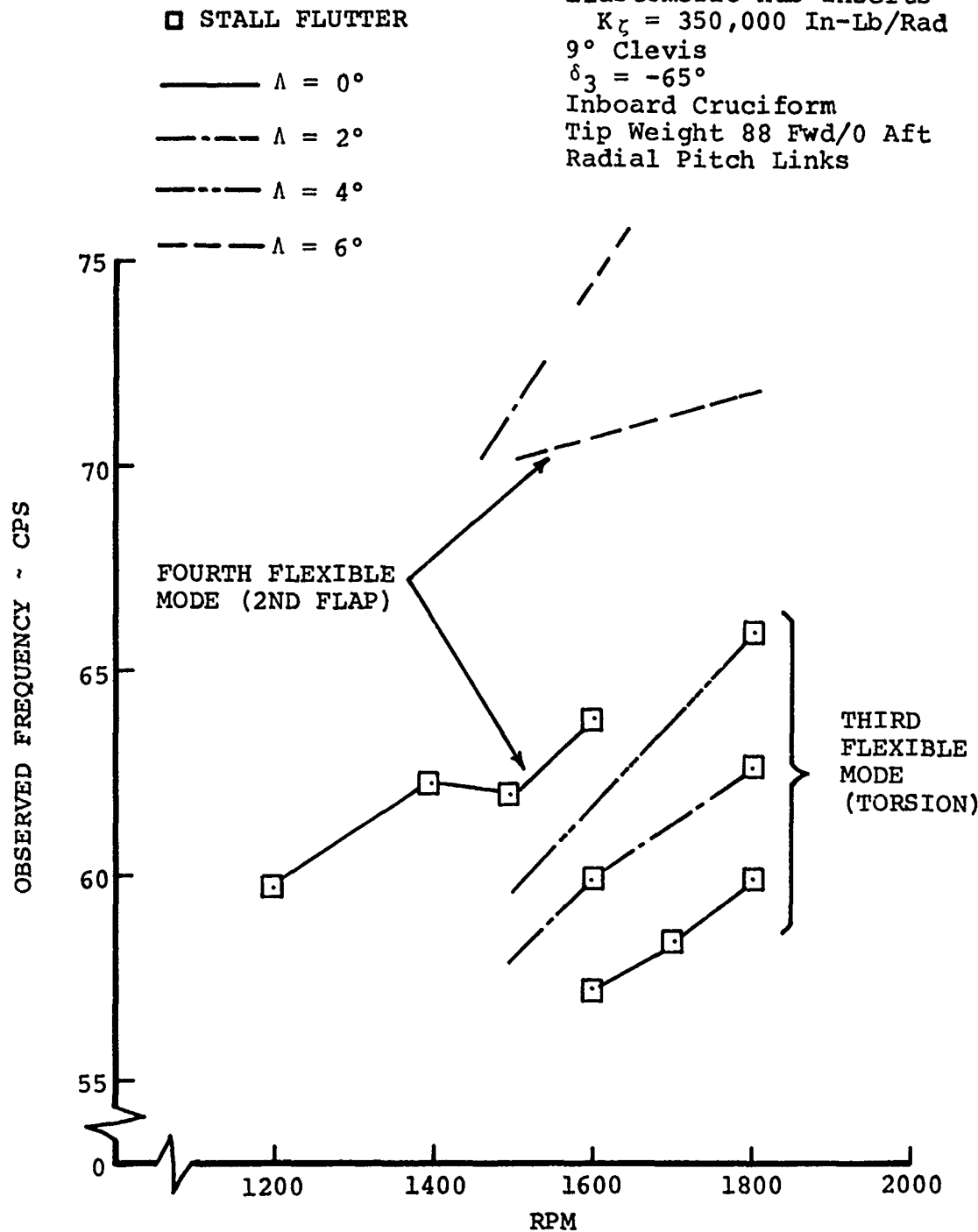
FIGURE 62   EFFECT OF BLADE SWEEP ON HIGHER
MODE FREQUENCIES

118

FIGURE 63   EFFECT OF RADIUS OF SWEEP POINT ON
FLAP-LAG STABILITY BOUNDARY

119

BVTC 011 - RUNS 4,6

3.6" Straps
VR-7.2, VR-7.4 Airfoils
No Hub Inserts
9° Clevis
$\delta_3 = -65°$
$\Lambda = 6°$
Full Cruciform, Low Ef
No Tip Weights
Radial Pitch Links
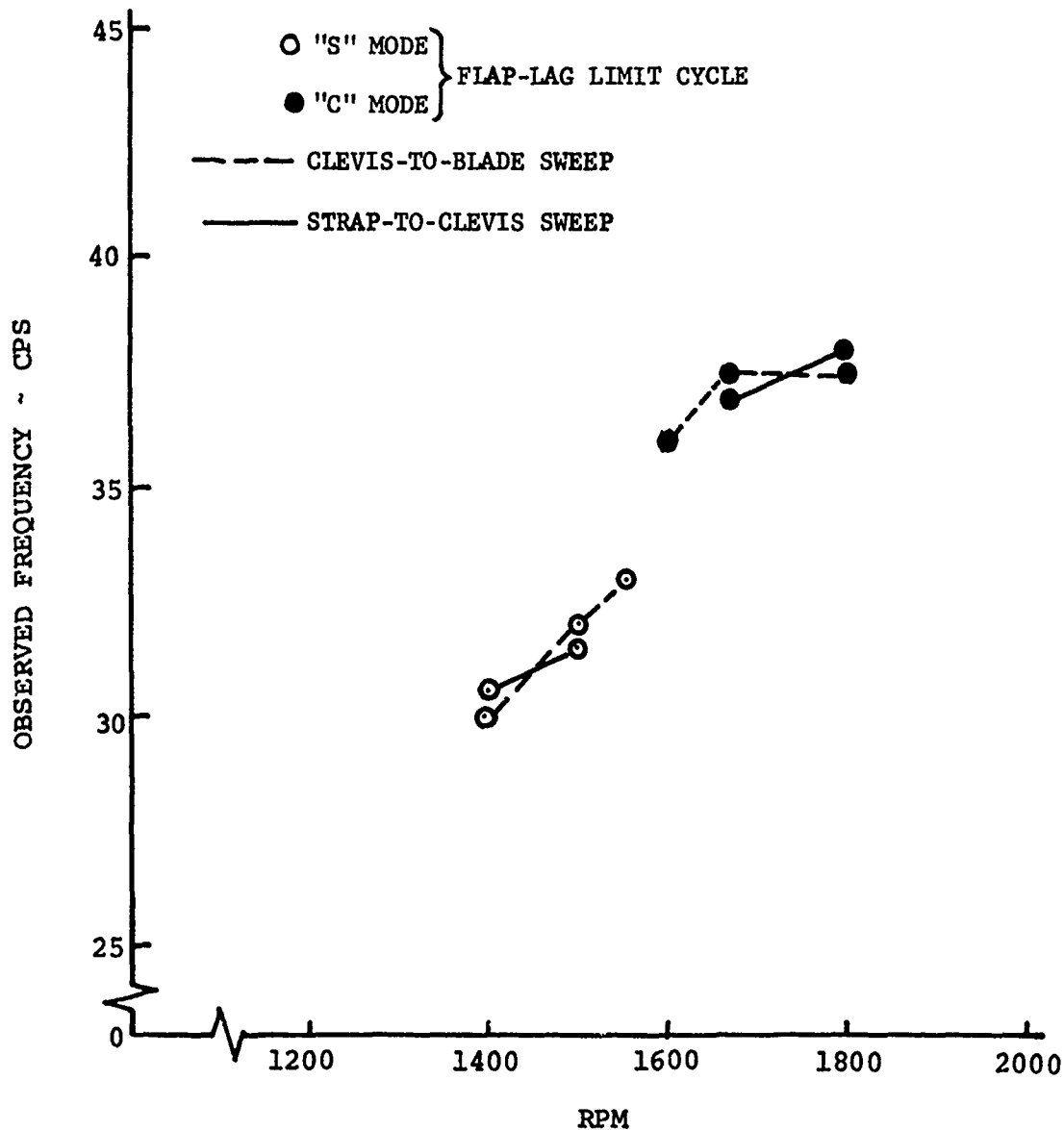
FIGURE 64   EFFECT OF RADIUS OF SWEEP POINT ON
FIRST INPLANE FREQUENCIES

120

The modal frequencies plotted in Figure 63 were indistinguishable between the two configurations. The "C" and "S" mode frequencies were clearly recorded and appeared to be separated by 2 cps if extrapolated to the nominal rotor speed of 1670 rpm.

5.2.6 Blade Chordwise Position Relative to Strap

The effect of varying the chordwise position of the blade relative to the strap is presented in Figures 65 through 68. This parameter variation was performed for two different blade sweep angles, $\Lambda = 0$ and $\Lambda = 6°$.

Figures 65 and 66 show the comparison of the blade quarter chord aligned with the centerline of the strap and the blade quarter chord moved 0.61 inch aft of the centerline of the strap in the zero sweep configuration. The boundary plotted in Figure 65 indicates that the "C" mode stability between 1550 and 1850 rpm was the same for both configurations. The frequency of the "C" mode shown in Figure 66 also shows little difference.

The "S" mode boundary appears to be slightly more stable with the blade quarter chord aligned with the strap at the rotor speeds from 1200 rpm to 1550 rpm. Minimum stability for both blade positions occurs at 1450 rpm. The frequency of the "S" mode for both configurations was observed to be about 1.33 per rev at 1400 rpm. At rotor speeds below 1425 rpm, the "S" mode frequency of the blade aft configuration was below the aligned configuration by up to 1.0 cps.

Figures 67 and 68 illustrate the effect of the blade chordwise position with a sweep of 6°. The overall "S" and "C" mode boundaries in Figure 67 are considerably higher than the unswept configurations discussed above due to the blade sweep. For the three blade chordwise positions, blade quarter chord, 0.25 inch forward, blade aligned with strap and blade 0.25 inch aft, shown in this parameter variation, there was little change in the location of the "C" mode boundary or frequency. The "S" mode boundary, on the other hand, appeared to be sensitive to the chordwise blade position. This can be traced to the change in the frequency of the "S" mode due to the chordwise position change. As shown in Figure 68, there is a difference of 1.5 cps between the three "S" mode frequencies, the blade forward having the highest frequency, and the blade aft having the lowest. This has the effect of moving the point of coalescence of the first flap mode and the "S" type chordwise modes. Thus, the rotor speed at which the minimum stability occurs (meaning the rotor speed of the point of minimum C_p/σ on a particular boundary as explained in Section 5.1), differed for the three configurations. Considering the minimum boundary points and the modal frequencies, a flap of 1.24 per rev at 1500 rpm is suggested for the nominal and the blade aft positions. The first flap frequency of the blade 0.25 inch forward configuration is 1.28 per rev.

121

BVTC 011 - RUNS 1, 12

3.6" Straps
VR-7.2, VR-7.4 Airfoils
No Hub Inserts
9° Clevis
$\delta_3 = -65°$
$\Lambda = 0°$
Full Cruciform, Low EI
No Tip Weights
Radial Pitch Links

O   "S" MODE INSTABILITY

●   "C" MODE INSTABILITY

— — — .25C ALIGNED WITH C/L OF STRAP
————— .25C MOVED .61"AFT

FIGURE 65   EFFECT OF BLADE CHORDWISE POSITION ON
              FLAP-LAG STABILITY BOUNDARY, $\Lambda = 0°$

122

BVTC 011 - RUNS 1, 12

3.6" Straps
VR-7.2, VR-7.4 Airfoils
No Hub Inserts
9° Clevis
$\delta_3 = -65°$
$\Lambda = 0°$
Full Cruciform, Low EI
No Tip Weights
Radial Pitch Links

O "S" MODE ⎫
⎬ FLAP- LAG LIMIT CYCLE
● "C" MODE ⎭

— — — .25C ALIGNED WITH C/L OF STRAP

———— .25C MOVED .61" AFT

FIGURE 66   EFFECT OF BLADE CHORDWISE POSITION ON FIRST
INPLANE FREQUENCIES, $\Lambda = 0°$

FIGURE 67   EFFECT OF BLADE CHORDWISE POSITION ON
FLAP-LAG STABILITY, $\Lambda = 6°$

124

BVTC 011 - RUNS 6, 11, 13

3.6" Straps
VR-7.2, VR-7.4 Airfoils
No Hub Inserts
9° Clevis
$\delta_3 = -65°$
$\Lambda = 6°$
Full Cruciform, Low EI
No Tip Weights
Radial Pitch Links
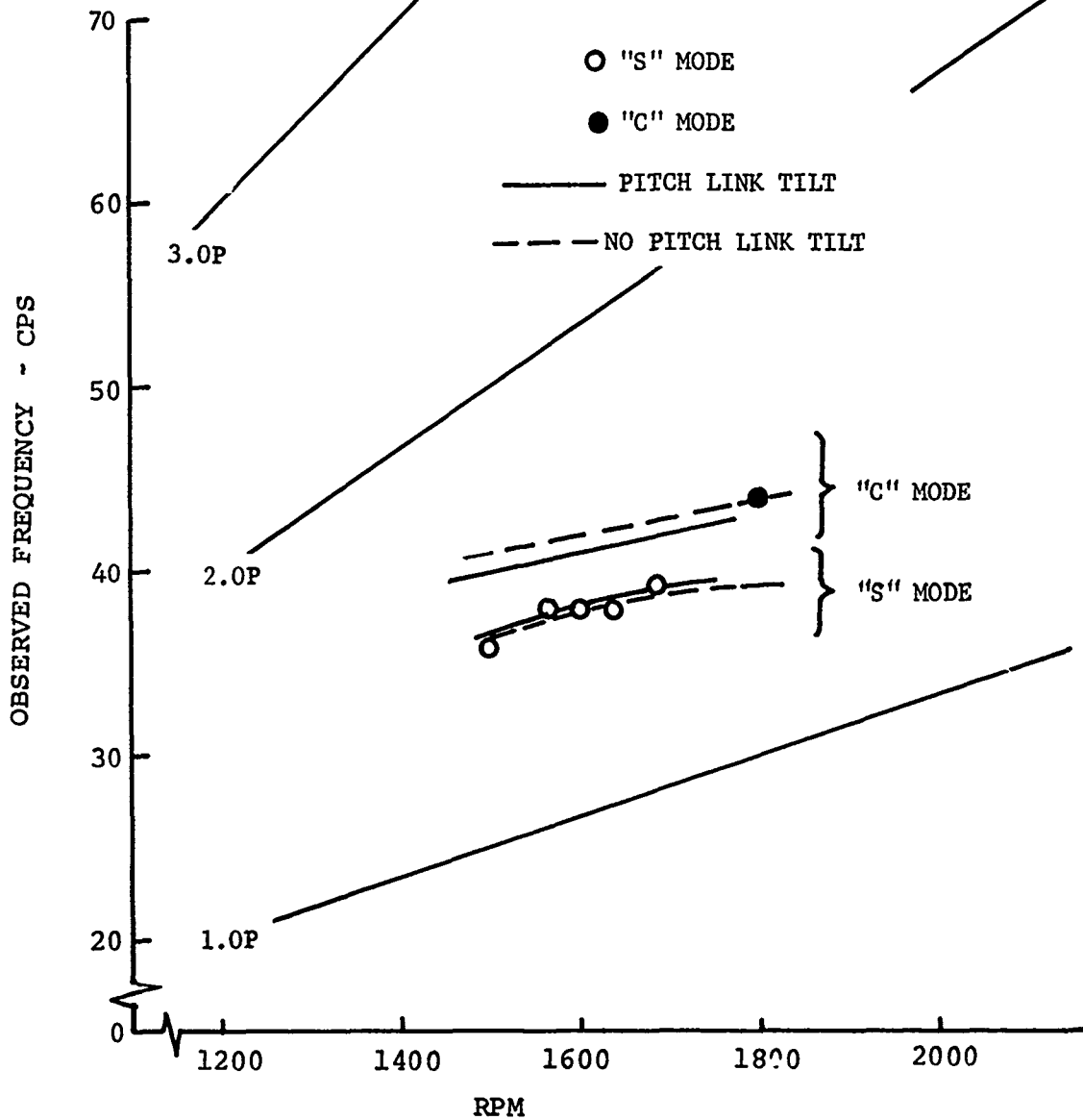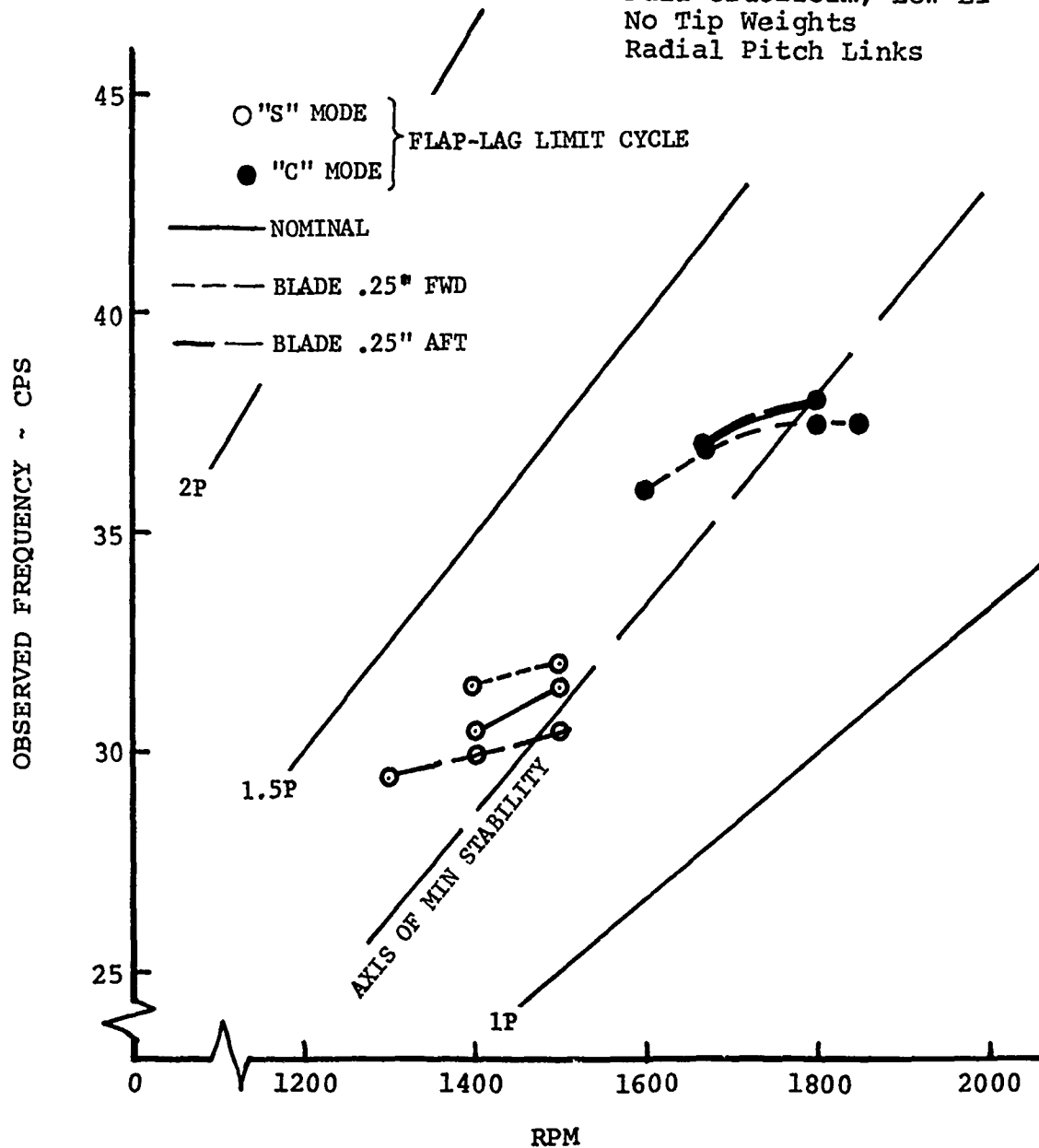
FIGURE 68   EFFECT OF BLADE CHORDWISE POSITION ON FIRST
INPLANE FREQUENCIES, $\Lambda = 6°$

125

5.2.7 Tip Weight

Figures 69 through 73 illustrate the effects of tip weight on the flap-lag instability. The first two figures focus on "C" mode effects; the second two, with a wider strap and higher inplane frequencies, show "S" mode effects; the last of these figures shows the effects on both modes for a strap of intermediate width. The figures show that tip weight influences the flap-lag stability boundary in two ways simultaneously. First, it lowers inplane frequencies, thereby lowering the rotor speed where the valley of minimum stability occurs along the stability boundary. In this respect, the scissors and "C" modes are affected approximately the same amount (see Figure 72). Second, tip weight increases stability for any given proximity of flap and inplane frequencies, thereby raising the boundary valleys. The scissors mode stability is improved much more than the "C" mode stability.

For the "C" mode, the combined result of the two tip weight effects is that valley of minimum stability moves to lower rotor speeds and higher C_T/σ values as the tip weights are increased. The relationship between these two changes is such that for rotor speeds below the minimum stability there is virtually no change in the position of the stability boundary. This is shown in Figure 69 and in particular Figure 73.

The scissors mode boundary, however, reflects a net improvement in stability due to tip weights that enables the model to reach a significantly higher C_p/σ value before encountering a stability boundary or model testing limit. This is shown in Figures 71 and 73.

As in the case of sweep, the mechanism by which tip weight improves flap-lag stability in the scissors mode is not proven by the data. It is possible that the improvement results from a change in the first flapwise mode shape which significantly reduces flap-lag dynamic coupling. Figure 73 indicates that the stabilizing mechanism is nonlinear, in that the scissors mode valley was not raised in direct proportion to tip weight.

Effects of tip weight on stall flutter are shown in Figures 74 and 75. The figures include the effect of chordwise position of the tip weight, demonstrating that in the configuration shown any chordwise position is beneficial but the forward position is superior. Figure 75 indicates that the stall flutter encountered in this configuration involved the third flexible mode (torsion), and that this mode was significantly stiffened by the addition of tip weight. Forward tip weight had a stronger stiffening effect than weight on the quarter chord and aft weight, whose effects were nearly the same. The weights had little effect on the fourth flexible mode. The stall flutter stabilization is evidently related to changes in flap-torsion coupling.

126

BVWT 129 - RUNS 13, 14, 15

3.3" Straps (335, 336)
VR-7.2, VR-7.4 Airfoils
No Hub Inserts
9° Clevis
$\delta_3 = -65°$
$\Lambda^3 = 6°$
Outboard Cruciform, Low EI
Radial Pitch Links

O "S" MODE } FLAP-LAG LIMIT CYCLE
● "C" MODE

△ MODEL TESTING LIMIT

——— 0   GRAMS
– – – 88 GRAMS
–·–·– 113 GRAMS

MAX. STABLE POWER COEFFICIENT , C_P/σ

RPM

FIGURE 69   EFFECT OF TIP WEIGHT ON FLAP-LAG STABILITY
              BOUNDARY ("C" MODE)

127
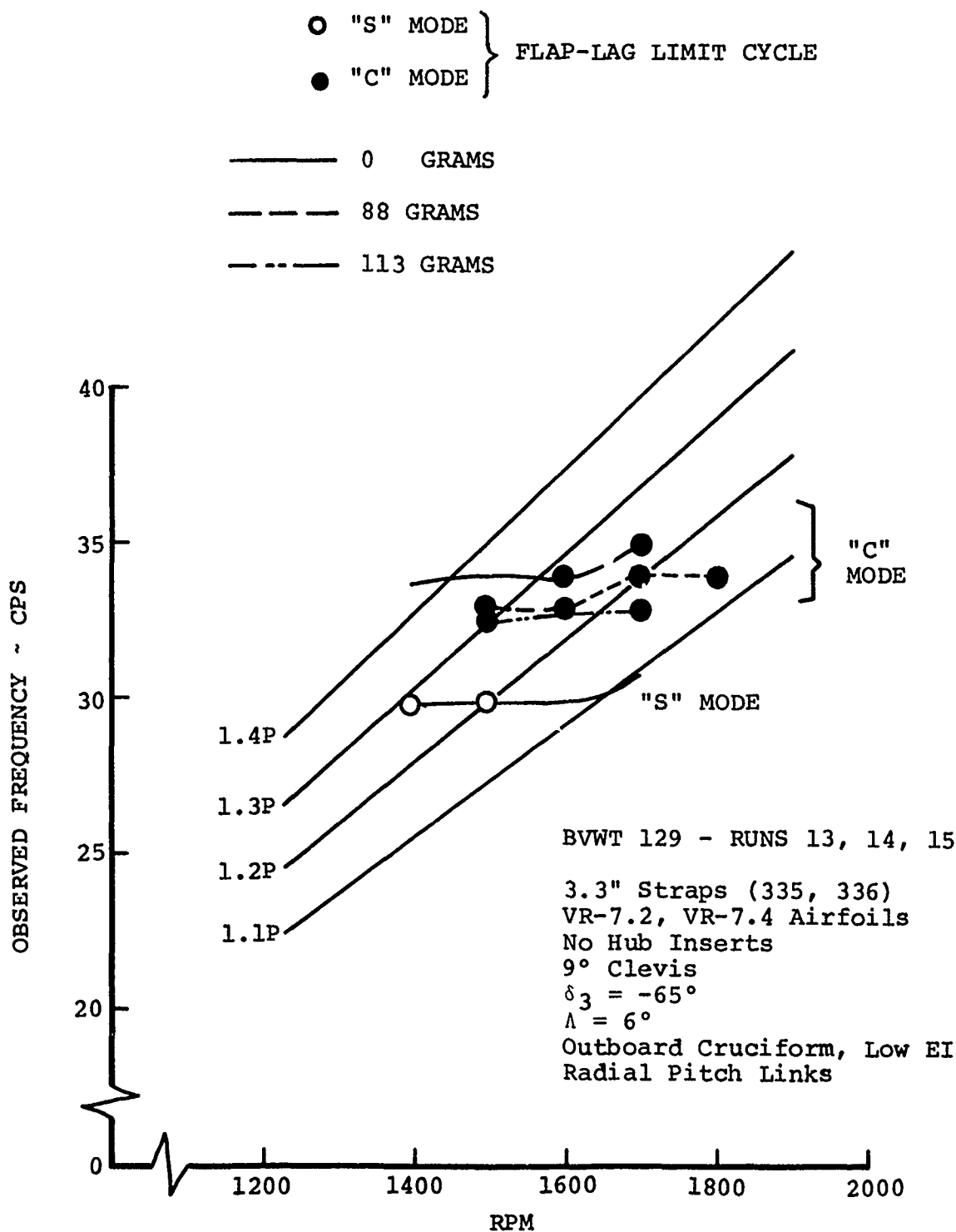
FIGURE 70   EFFECT OF TIP WEIGHT ON FIRST INPLANE
             FREQUENCIES

128

BVWT 129 - RUNS 31, 32, 35

4.4" Straps (337, 338)
VR-7.2, VR-7.4 Airfoils
No Hub Inserts
9° Clevis
$\delta_3 = -65°$
$\Lambda = 11°$
Full Cruciform, Low EI
Radial Pitch Links

O "S" MODE FLAP-LAG LIMIT CYCLE

△ MODEL TESTING LIMIT

—————— NO TIP WEIGHT
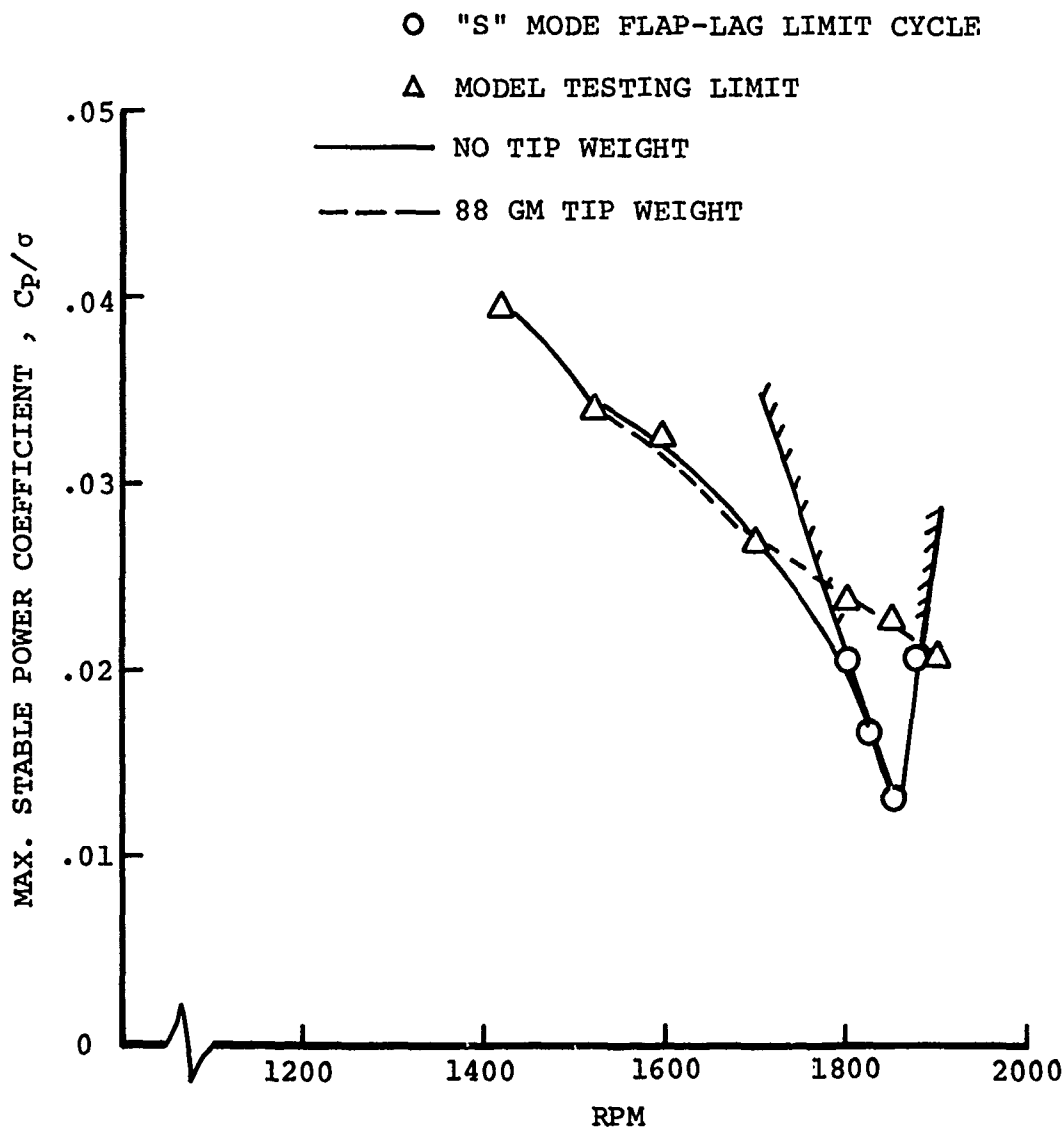
— — — — 88 GM TIP WEIGHT

FIGURE 71   EFFECT OF TIP WEIGHTS ON FLAP-LAG STABILITY
BOUNDARY (SCISSORS MODE)
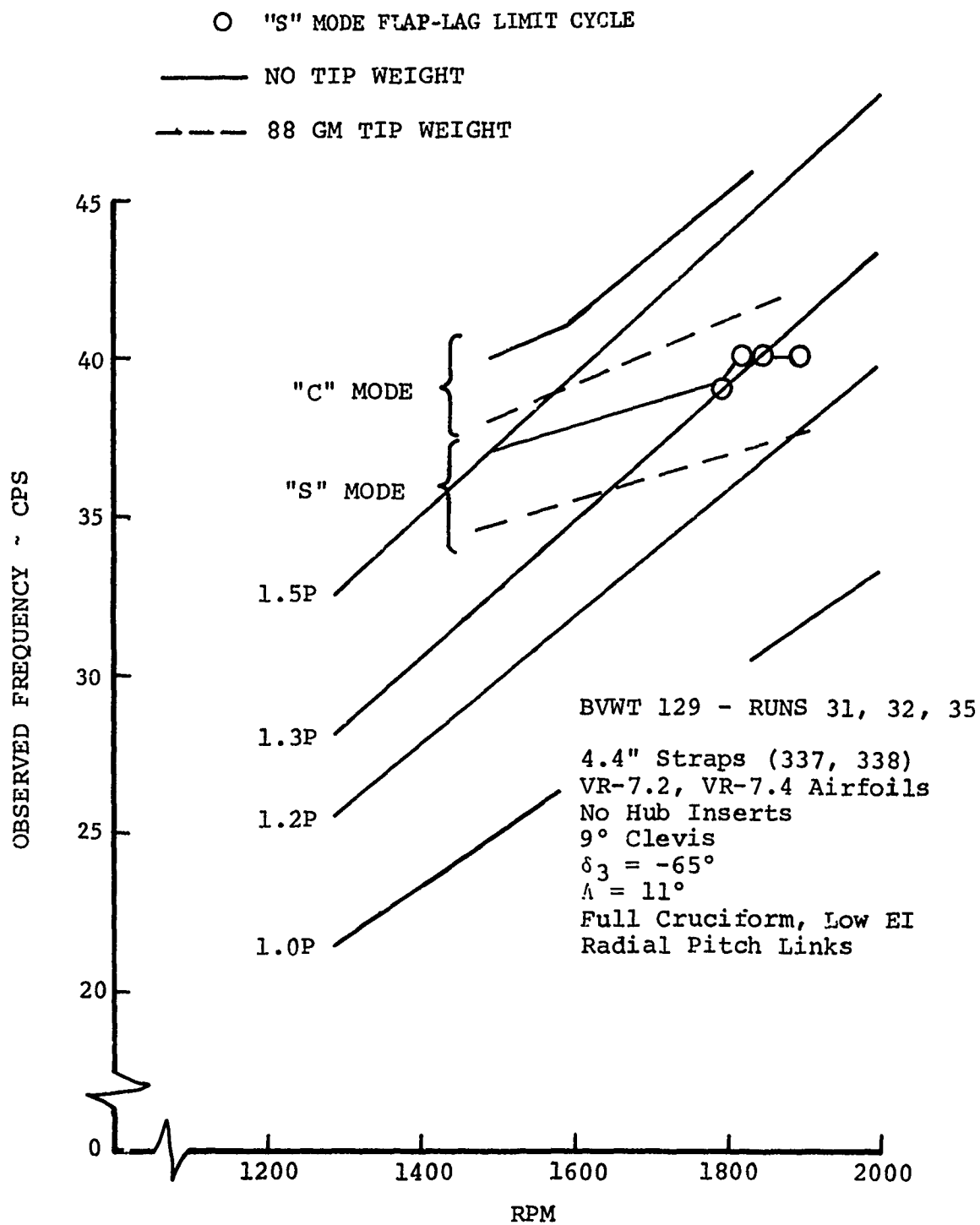
FIGURE 72   EFFECT OF TIP WEIGHTS ON FIRST INPLANE
            FREQUENCIES

130

OPEN SYMBOLS - "S" MODE } FLAP-LAG LIMIT CYCLE
SOLID SYMBOLS - "C" MODE }

BVTC 011 - RUNS 6-9

3.6" Straps (334, 337)
VR-7.2, VR-7.4 Airfoils
No Hub Insers
9° Clevis
$\delta_3 = -65°$
$\Lambda = 6°$
Full Cruciform, Low EI
Radial Pitch Links

O   0 TIP WEIGHT
△   30 GRAM TIP WT
□   60 GRAM TIP WT
◇   88 GRAM TIP WT
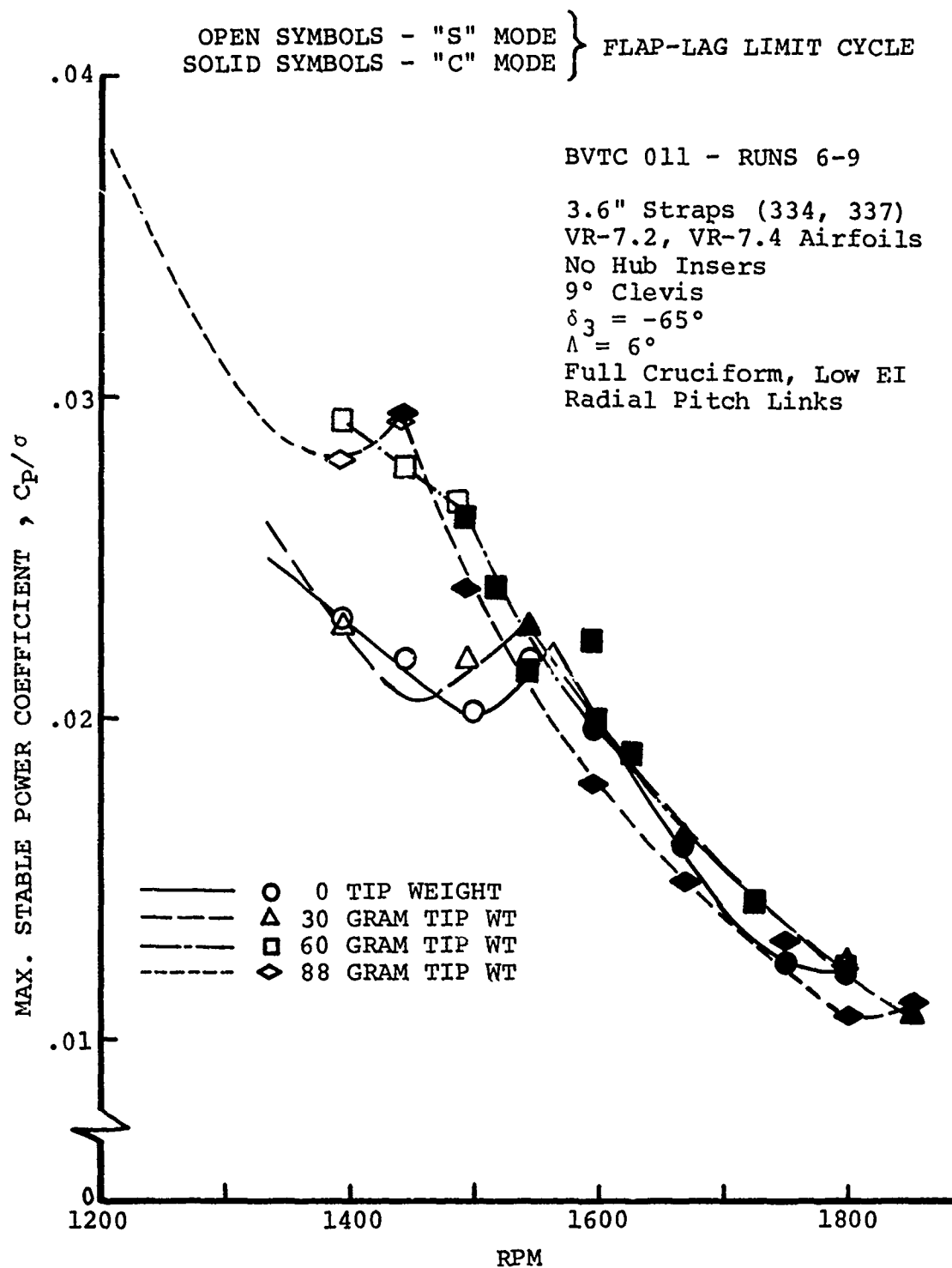
FIGURE 73   EFFECT OF TIP WEIGHTS ON FLAP-LAG
             STABILITY BOUNDARY (BOTH MODES)

FIGURE 74   EFFECT OF TIP WEIGHTS ON STALL
FLUTTER BOUNDARY

132

TIP WEIGHT		BLADE C.G.
FWD	AFT	% CHORD
0	0	——————— 25
0	88	——·—— 26
44	44	——— — —— 25
88	0	——·—·—— 24

□ STALL FLUTTER

2.5P

FOURTH FLEXIFLE
MODE (SECOND FLAP)

3P

THIRD
FLEXIBLE
MODE
(TORSION)

OBSERVED FREQUENCY ~ CPS

80

75

70

65

60

0

BVWT 009
RUNS 29, 32, 36, 38

4.4" Straps (334, 337)
2 BLADES
VR-6.9 Airfoil
Elastomeric Hub Inserts
$K_\zeta = 350,000$ In-Lb/Rad
9° Clevis
$\delta_3 = -65°$
$\Lambda = 6°$
Inboard Cruciform
Radial Pitch Links

2P

1200   1400   1600   1800   2000

RPM
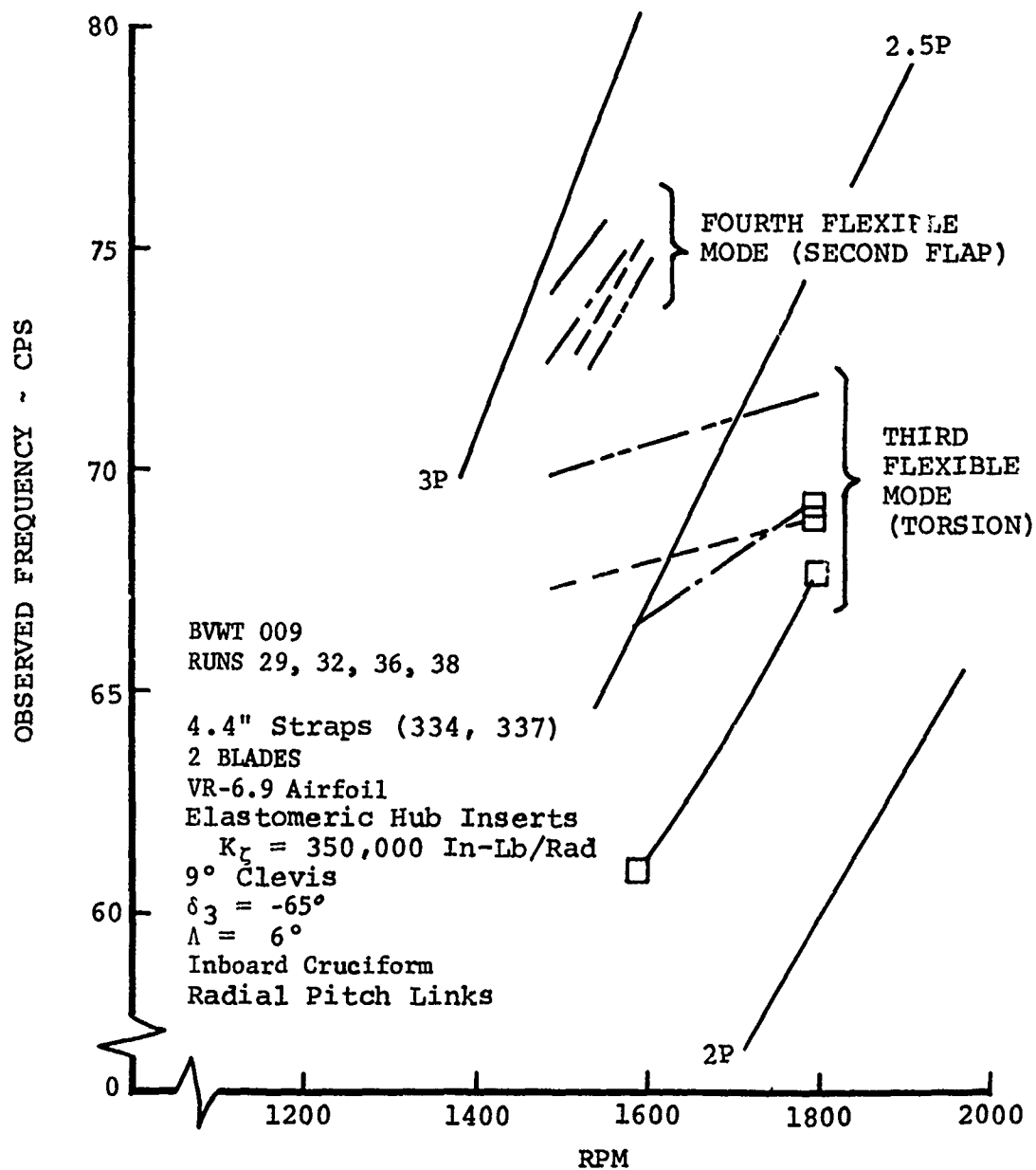
FIGURE 75   EFFECT OF TIP WEIGHTS ON HIGHER INPLANE
FREQUENCIES

133

BVTC 009 - Runs 158,164

4.4" Straps
VR-7.2, VR-7.4 Airfoils
No Hub Inserts
9° Clevis
$\delta_3 = -65°$
$\Lambda = 6°$
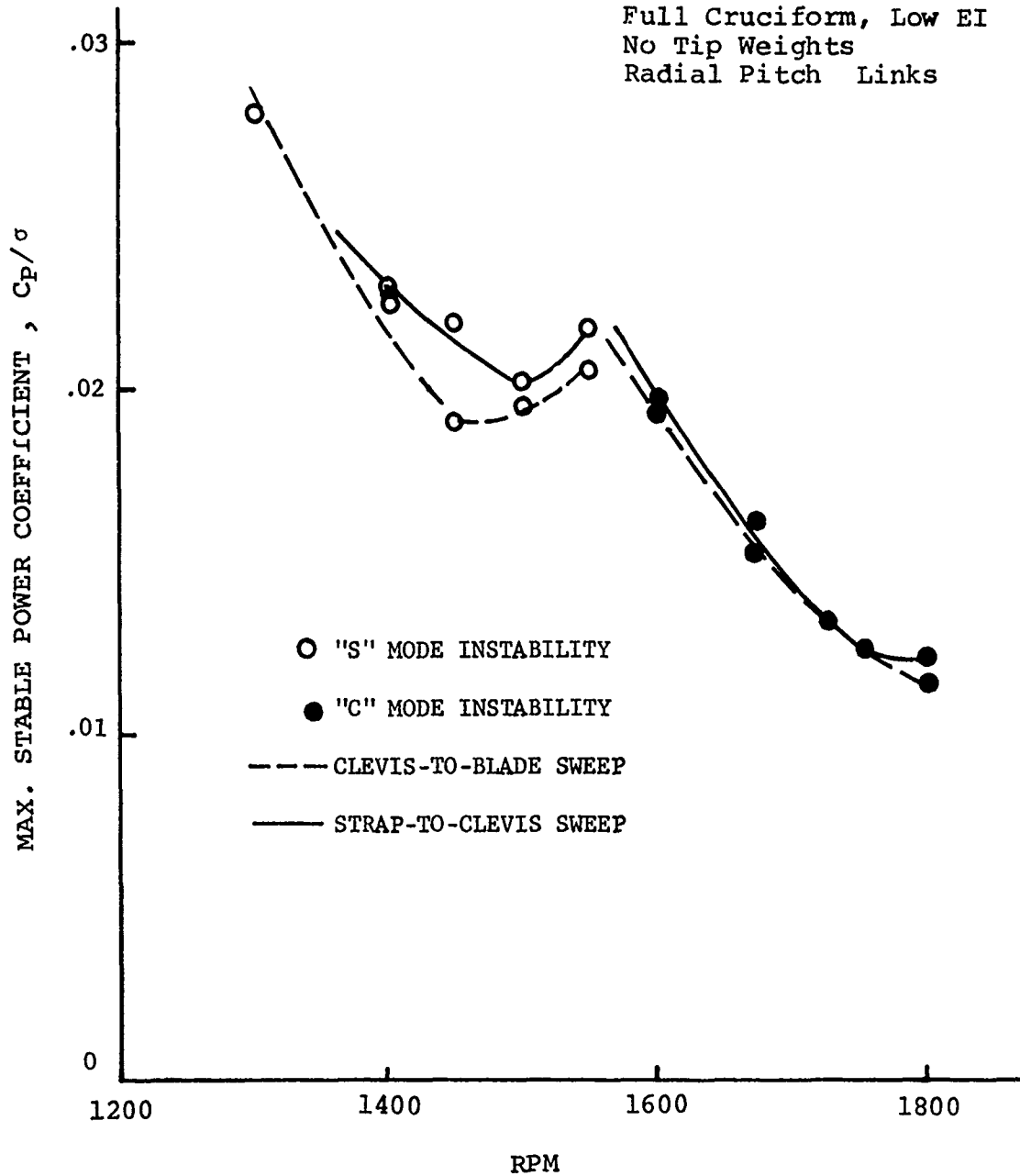Outboard Cruciform, Low EI
No Tip Weight
Tilted Pitch Links

⊙ "S" MODE, FLAP-LAG LIMIT CYCLE

△ MODEL TESTING LIMIT

LINE SYMBOL	CONFIGURATION	
	STRAP 334 VR-7.4	STRAP 337 VR-7.2
———————	NOTHING	WEIGHTS
- - - - - - -	NOTHING	NOTHING
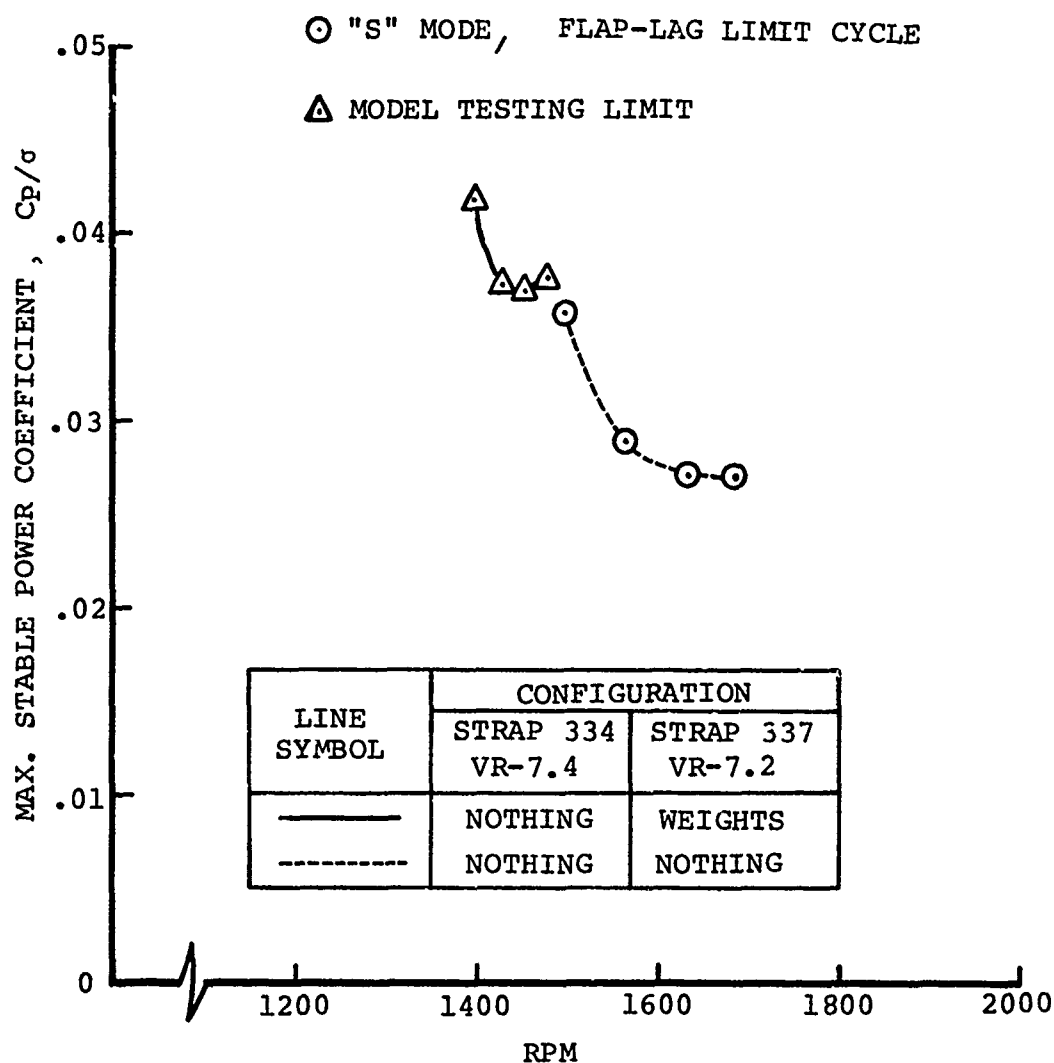
FIGURE 76   EFFECT OF INBOARD WEIGHTS ON
FLAP-LAG STABILITY BOUNDARY

134

BVTC 009 - Runs 158, 164

4.4" Straps
VR-7.2, VR-7.4 Airfoils
No Hub Inserts
9° Clevis
$\delta_3 = -65°$
$\Lambda = 6°$
Outboard Cruciform, Low EI
No Tip Weight
Tilted Pitch Links

⊙ "S" MODE

LINE SYMBOL	CONFIGURATION	
	STRAP 334 VR-7.4	STRAP 337 VR-7.2
————	NOTHING	WEIGHTS
----------	NOTHING	NOTHING

1.5P

OBSERVED FREQUENCY ~ CPS

RPM
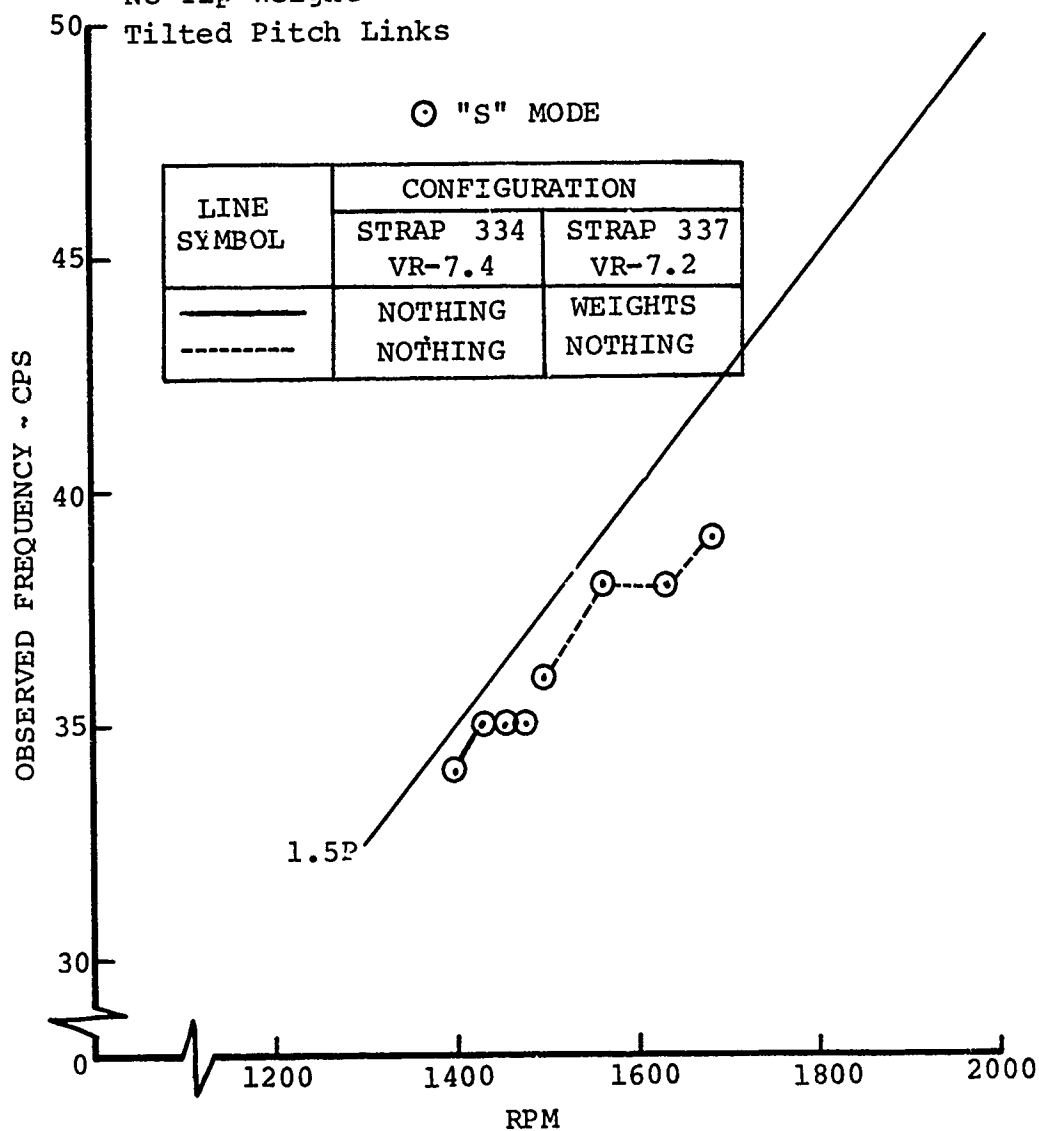
FIGURE 77   EFFECT OF INBOARD WEIGHTS ON
FIRST INPLANE FREQUENCIES

135

BVTC 009 - RUNS 167, 174, 176

4.4" Straps (334,337)
VR-7.2, VR-7.4 Airfoils
No Hub Inserts
9° Clevis
δ_3 = -65°
Λ = 6°
Strap 337 - Outboard Cruciform, Low EI
Strap 334 - No Cruciform
No Tip Weights
Tilted Pitch Links

FIGURE 78   EFFECT OF DAMPERS AND INBOARD WEIGHTS ON
FLAP-LAG STABILITY BOUNDARY

136

BVTC 009 - RUNS 167, 174, 176

4.4" Straps (334,337)
VR-7.2, VR-7.4 Airfoils
No Hub Inserts
9° Clevis
$\delta_3 = -65°$
$\Lambda = 6°$
Strap 337 - Outboard Cruciform, Low EI
Strap 334 - No Cruciform
No Tip Weights
Tilted Pitch Links

LINE SYMBOL	CONFIGURATION	
	STRAP 334 VR-7.4	STRAP 337 VR-7.2
—————	DAMPERS	WEIGHTS
——— ———	DAMPERS	NOTHING
————————	NOTHING	NOTHING

⊙ "S" MODE ⎫ FLAP-LAG
● "C" MODE ⎭ LIMIT CYCLE

"C" MODE

"S" MODE

1.5P

OBSERVED FREQUENCY - CPS

RPM
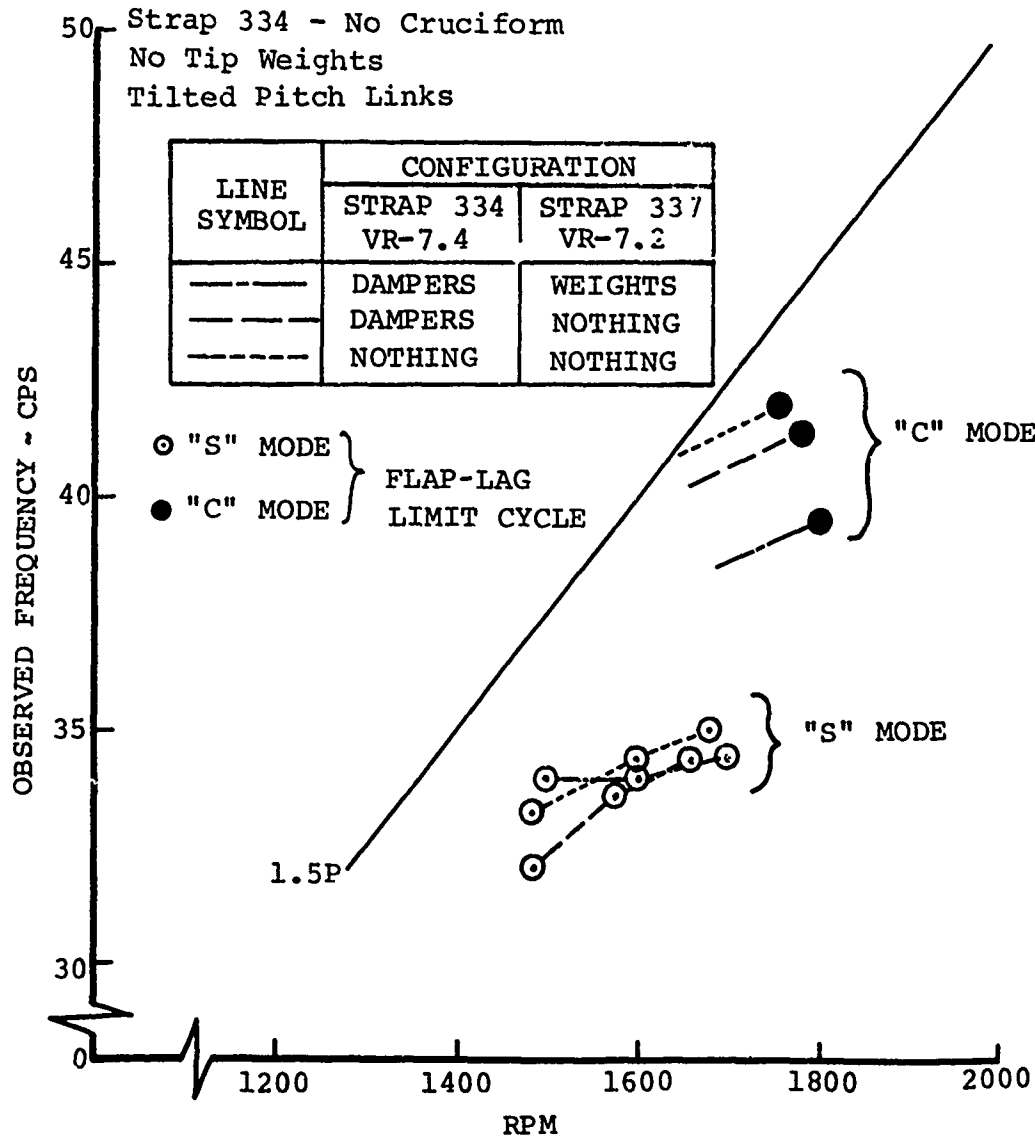
FIGURE 79   EFFECT OF DAMPERS AND INBOARD WEIGHTS ON
FIRST INPLANE FREQUENCIES

137

5.2.8 Inboard Weight and Lag Damping

During the model test BVTC 009, the effects of blade lag damp-
ing and inboard blade weights were observed. The details of
these configurations are presented in Section 3.8.

It was realized that the addition of blade dampers to the model
blades would produce two physical effects. First, as intended,
the dampers would add additional damping to the rotor blades at
the blade span station $x/R = 0.34$. Second, the damper unit it-
self would act as a form of inboard weight that could possibly
influence the rotor natural frequencies and intermodal coup-
ling. This latter effect was evaluated by use of the inboard
weight.

Figures 76 and 77 show the stability test results and measured
frequencies with the inboard weights. As shown in the figures,
the configuration with the weights (only strap 337 was modified
to accept weights--strap 334 was unchanged) reached a model
testing limit from 1400 to 1475 rpm. This testing limit was
due to high 2P loads. However, at this test limit, the flap-
lag "S" mode was only marginally stable and it seemed as though
this flap-lag boundary should be nearby. Comparing this data
to the same configuration with no weights, it indeed indicates
that these test limit points do closely correspond to the "S"
mode boundary of the configuration without inboard weights. A
plot of the observed modal frequency in Figure 77 shows little
difference between the "S" mode frequency in the two configura-
tions. Both the stability boundaries and the modal frequencies
suggest that the inboard weights have little effect on the "S"
mode flap-lag stability.

The results of the tests with the dampers installed are shown
in Figures 78 and 79. As shown in the first figure, the ob-
served "S" mode flap-lag stability boundary varied little for
the three configurations shown. The blade dampers, as they
were mounted on the model, did not have a significant effect
on the stability boundary. The modal frequencies presented in
the second figure also show that the lag damper configura-
tions had little effect on "S" type modal frequencies. With
respect to the C" mode frequencies, there is a significant
reduction in frequency with the dampers on.   Unfortunately,
however, there is no sufficient data for the "C" mode stability
to show the damper's influence on that mode.

5.2.9 Strap Width

Effects of strap width on the flap-lag instability are illus-
trated by Figures 80 and 81. The figures show that increasing
strap width had a strongly beneficial effect on the stability
boundary, principally as a result of inplane stiffening in both
the scissors and "C" modes. The amount of stiffening achieved

138

BVTC 009 - RUNS 125, 146, 152

Straps 335, 336
VR-7.2, VR-7.4 Airfoils
No Hub Inserts
9° Clevis
$\delta_3 = -65°$
$\Lambda = 6°$
Outboard Cruciform, Low ET
No Tip Weight
Radial Pitch Links

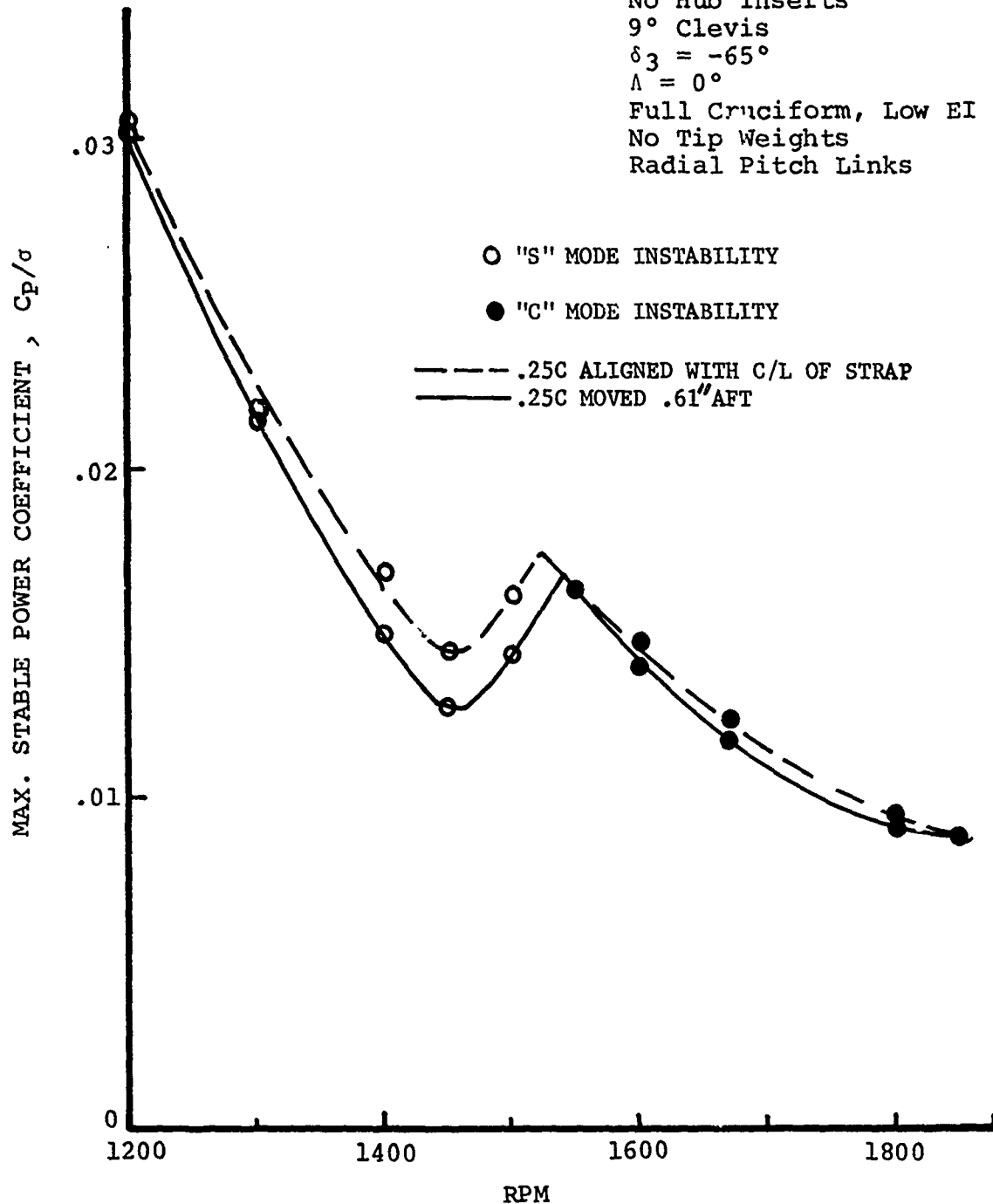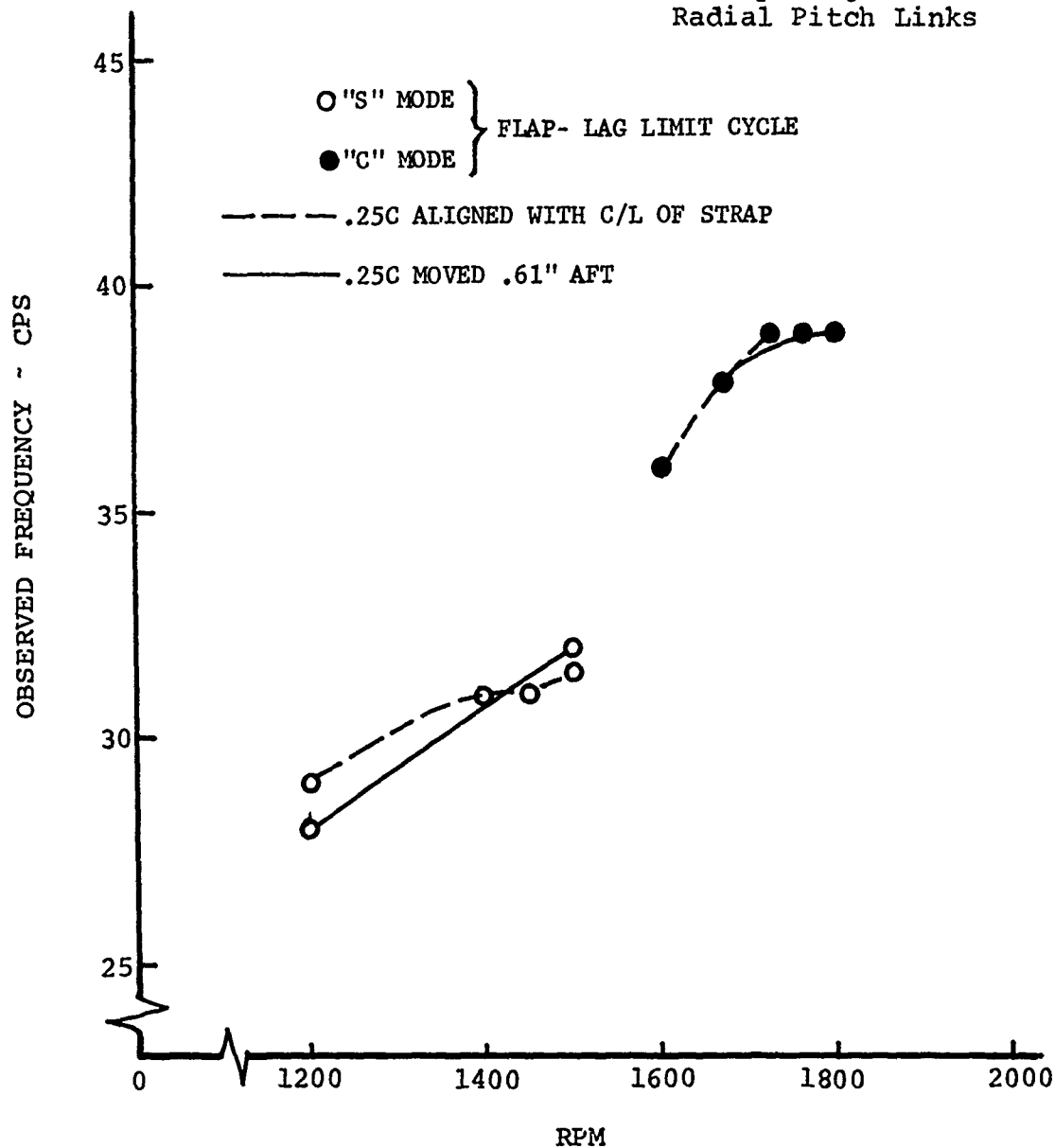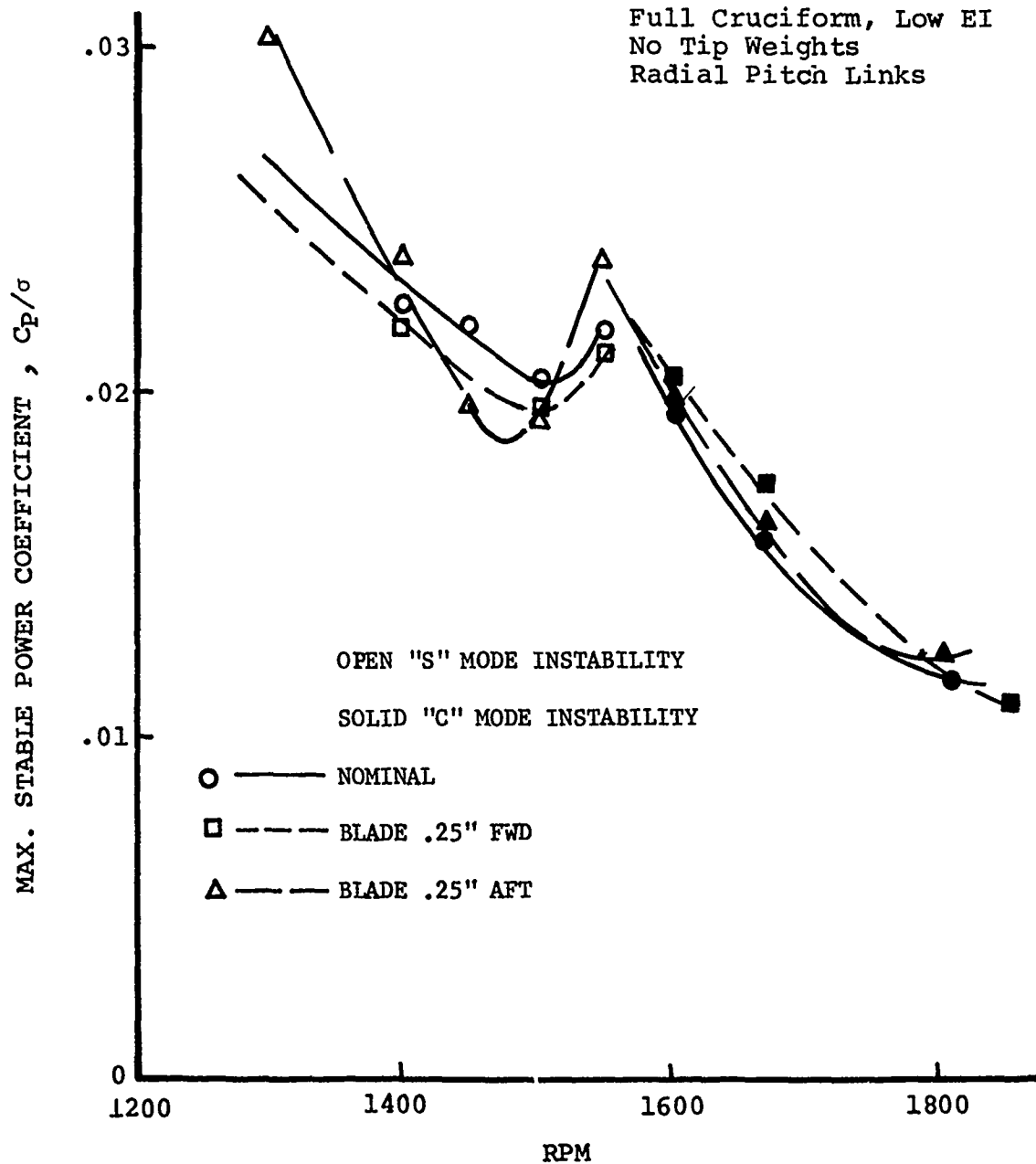———— 4.4" STRAP
— — — 3.8" STRAP
—·—·— 3.3" STRAP

O "S" MODE ⎫
● "C" MODE ⎬ FLAP-LAG LIMIT CYCLE
△ MODEL TESTING LIMIT
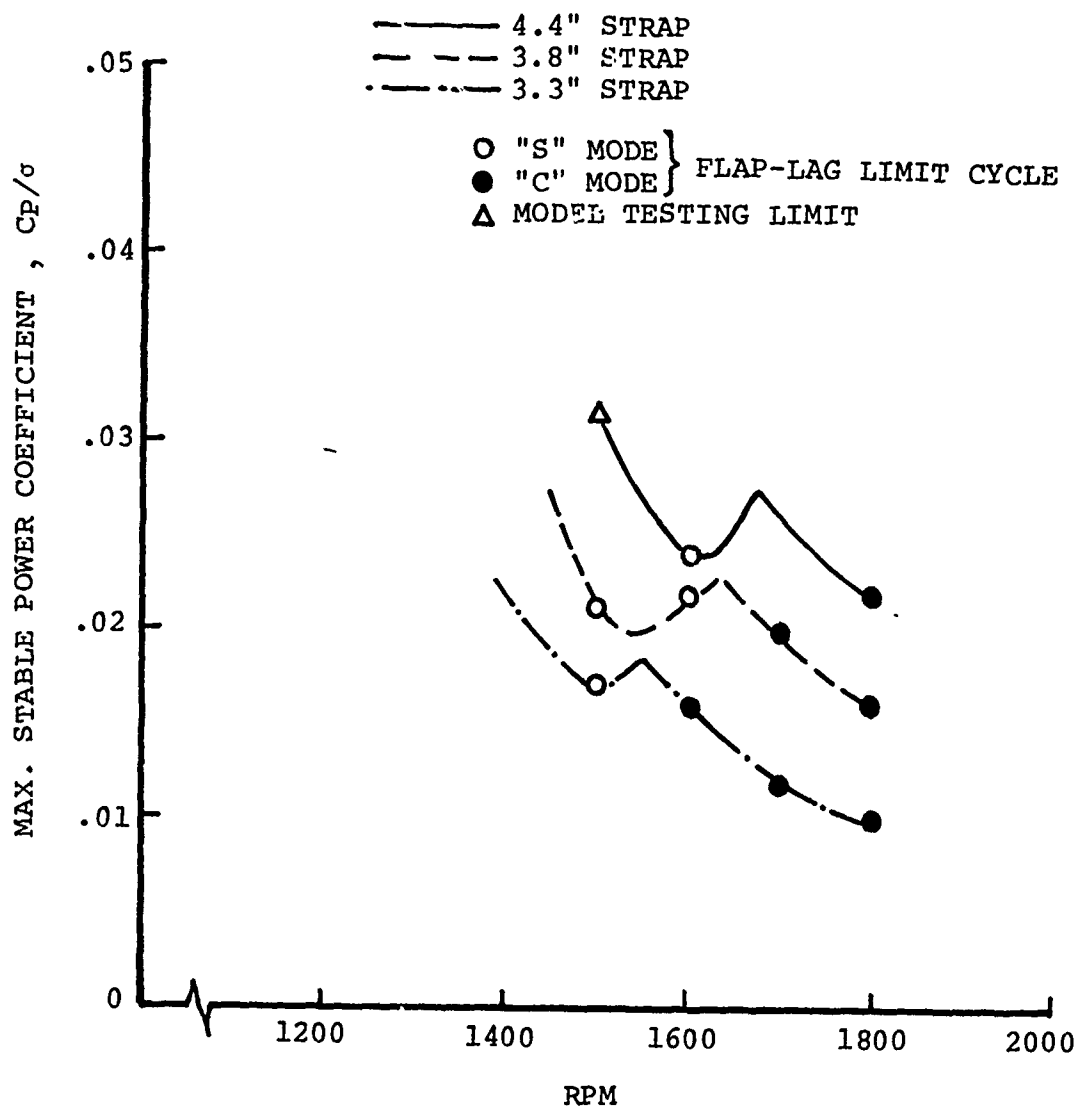
FIGURE 80   EFFECT OF STRAP WIDTH ON FLAP-LAG
STABILITY BOUNDARY

BVTC 009 - RUNS 125, 146, 152

Straps 335, 336
VR-7.2, VR-7.4 Airfoils
No Hub Inserts
9° Clevis
$\delta_3 = -65°$
$\Lambda = 6°$
Outboard Cruciform, Low EI
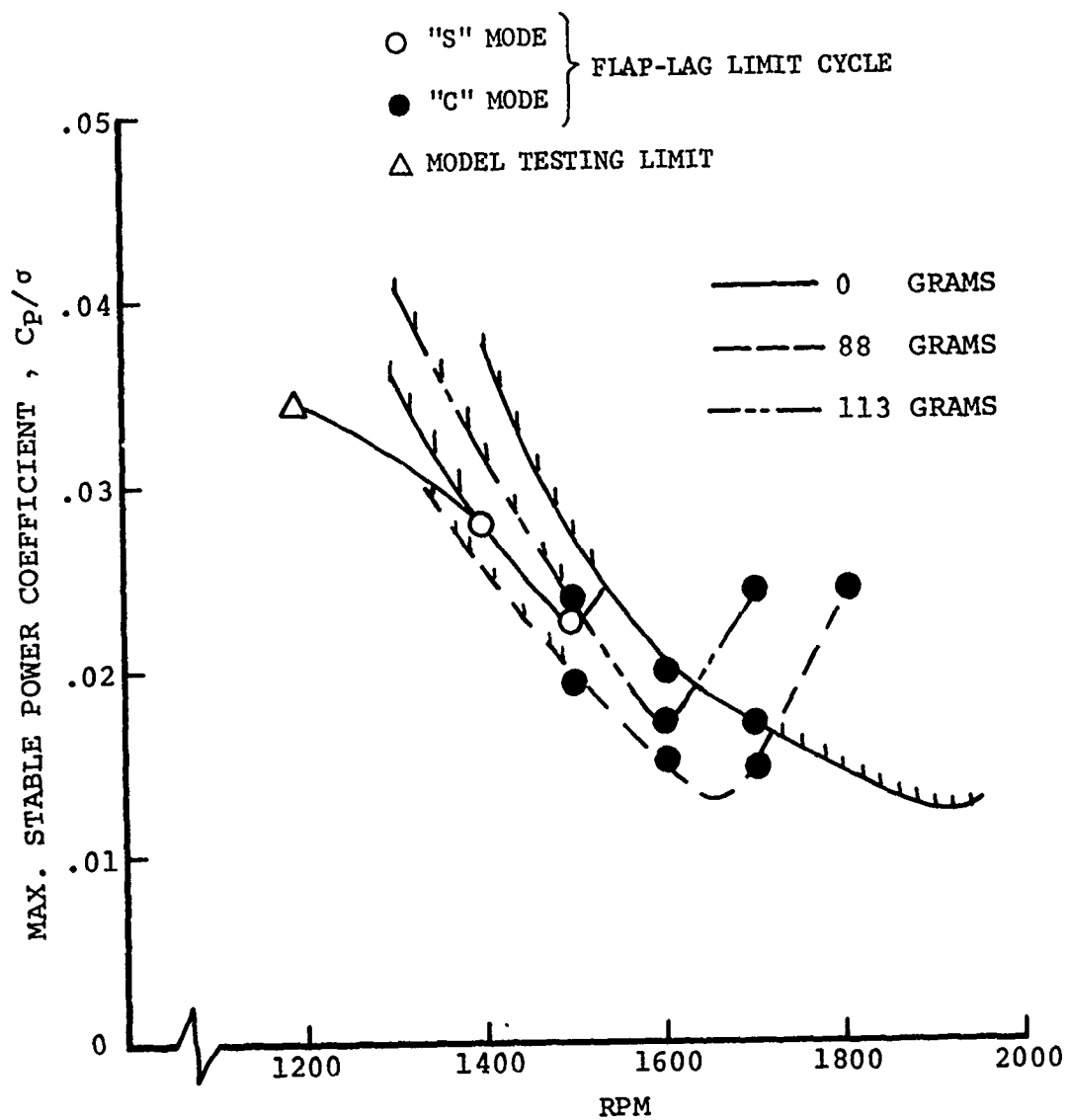No Tip Weight
Radial Pitch Links
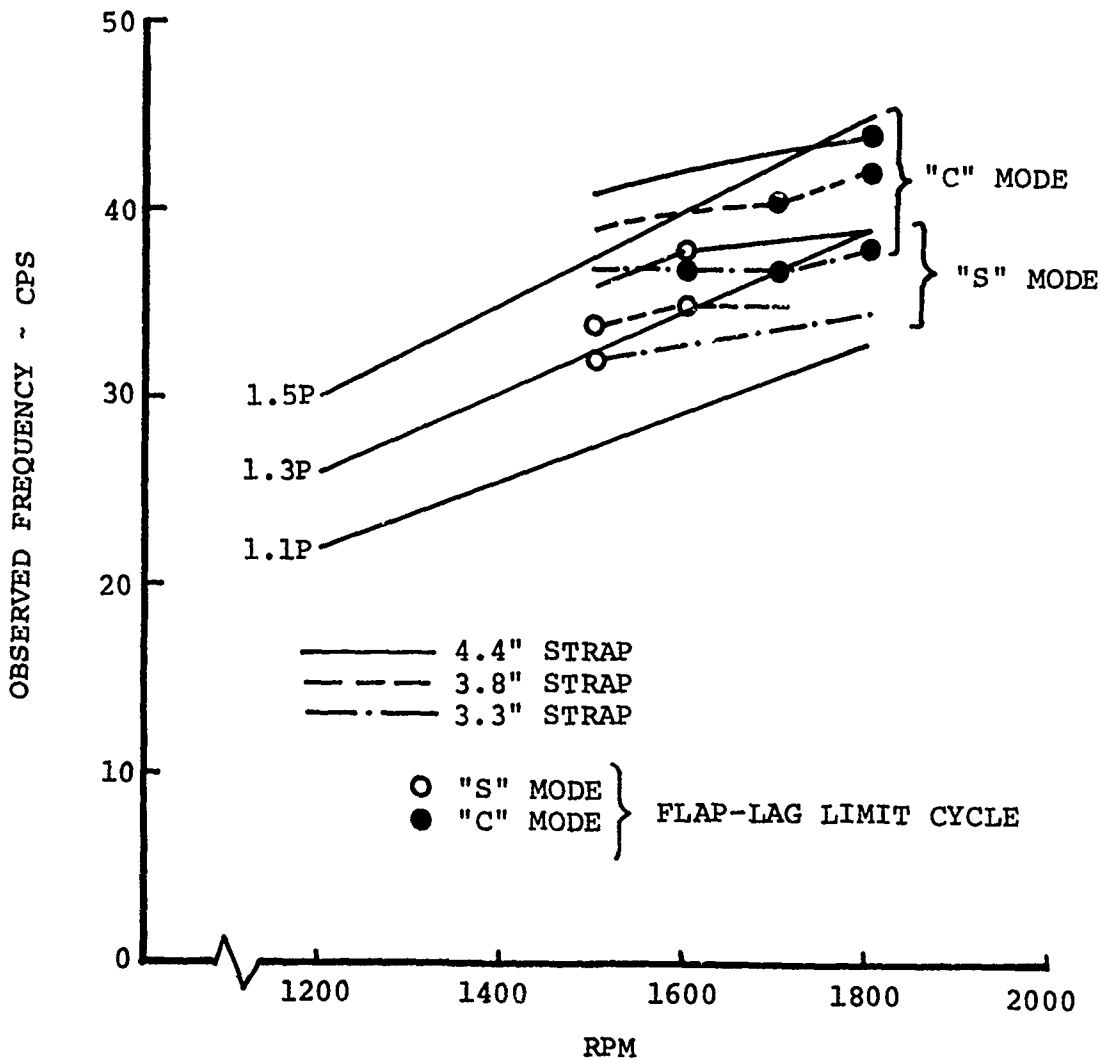
FIGURE 81   EFFECT OF STRAP WIDTH ON FIRST INPLANE
             FREQUENCIES

140

by a width increase was approximately the same in both modes.
(See Figure 81.) Inplane stiffening increased the rpm's at
which the scissors and "C" mode frequencies crossed the first
flap frequency, thereby raising the rpm's of the valleys in
the stability boundary (see Figure 80, note that the "C" mode
valley was above the testing range and is not shown in the
figure). Figure 80 shows, moreover, that increased strap width
raised the scissors mode boundary valley, i.e., increased the
stability of the scissors mode for a given proximity of flap
and inplane frequencies. Although the "C" mode valley is not
shown, the shape of the boundary implies that this valley was
raised even more than the scissors mode valley, and thus the
"C" mode was stabilized even more than the scissors mode. This
stabilization evidently results from a change in the elastic
coupling of flap and inplane motion.

5.2.10   Elastomeric Hub Inserts

Effects of elastomeric hub inserts on the flap-lag instability
are illustrated by Figures 82 and 83. The figures show that
the inserts affect only the scissors mode significantly and
that their effect is independent of their stiffness over a wide
range of stiffness. Inserts whose stiffnesses differed by a
factor of two lowered the scissors mode frequency by the same
amount: approximately 4 cps (see Figure 83). Based on this
fact, the inserts lowered the crossing of the scissors mode
frequency and the first flap frequency (and the corresponding
boundary valley) by about 400 rpm. More significantly, how-
ever, the inserts stabilized the scissors mode in two ways.
First, the boundary valley was raised. Second, a flap-lag
limit cycle which occurred on and above the boundary caused
only moderate strap loads, independent of collective (chord
bending loads at 40% of the fatigue allowable, for example).
The "incipient" scissors mode boundary illustrated for the
softer hub inserts in Figure 82 was therefore less restrictive
than the other boundaries shown in the figure.

The hub inserts probably achieved their partially stabilizing
effects in two ways. First, they contributed damping to the
scissors mode. This would account for the raised boundary
valley observed in Figure 82 but would not explain the unusual
phenomenon of a limit cycle with amplitude independent of
collective. The explanation for this behavior may be that the
collective inserts also reduced chord bending loads for a given
limit cycle amplitude. The "incipient" limit cycles shown in
the figure may have been very similar to the limit cycles ob-
served in other configurations, having blade motions of similar
amplitude (determined by aerodynamic nonlinearities indepen-
dent of configuration) but appearing smaller because the chord
bending loads were reduced by the hub inserts. This explana-
tion depends on the unproven hypothesis that the limit cycles
observed in configurations without hub inserts would have

141

BVWT 129 - RUNS 41, 42, 62

4.4" Straps
VR-7.2/7.4 Airfoil
9° Clevis
$\delta_3 = -65°$
$\Lambda = 0°$
Outboard Cruciform, Low EI
No Tip Weights
Radial Pitch Links

——— NO INSERTS
— — — INSERTS, K_ζ = 350,000 IN-LB/RADIAN
—·—·— INSERTS, K_ζ = 175,000 IN-LB/RADIAN

○ "S" MODE } FLAP-LAG LIMIT CYCLE
● "C" MODE }
⌐ STALL FLUTTER

Flag on Symbol Indicates
Incipient Instability –
Chord Bending Loads at
40% Fatigue Allowable
in Mode Shown
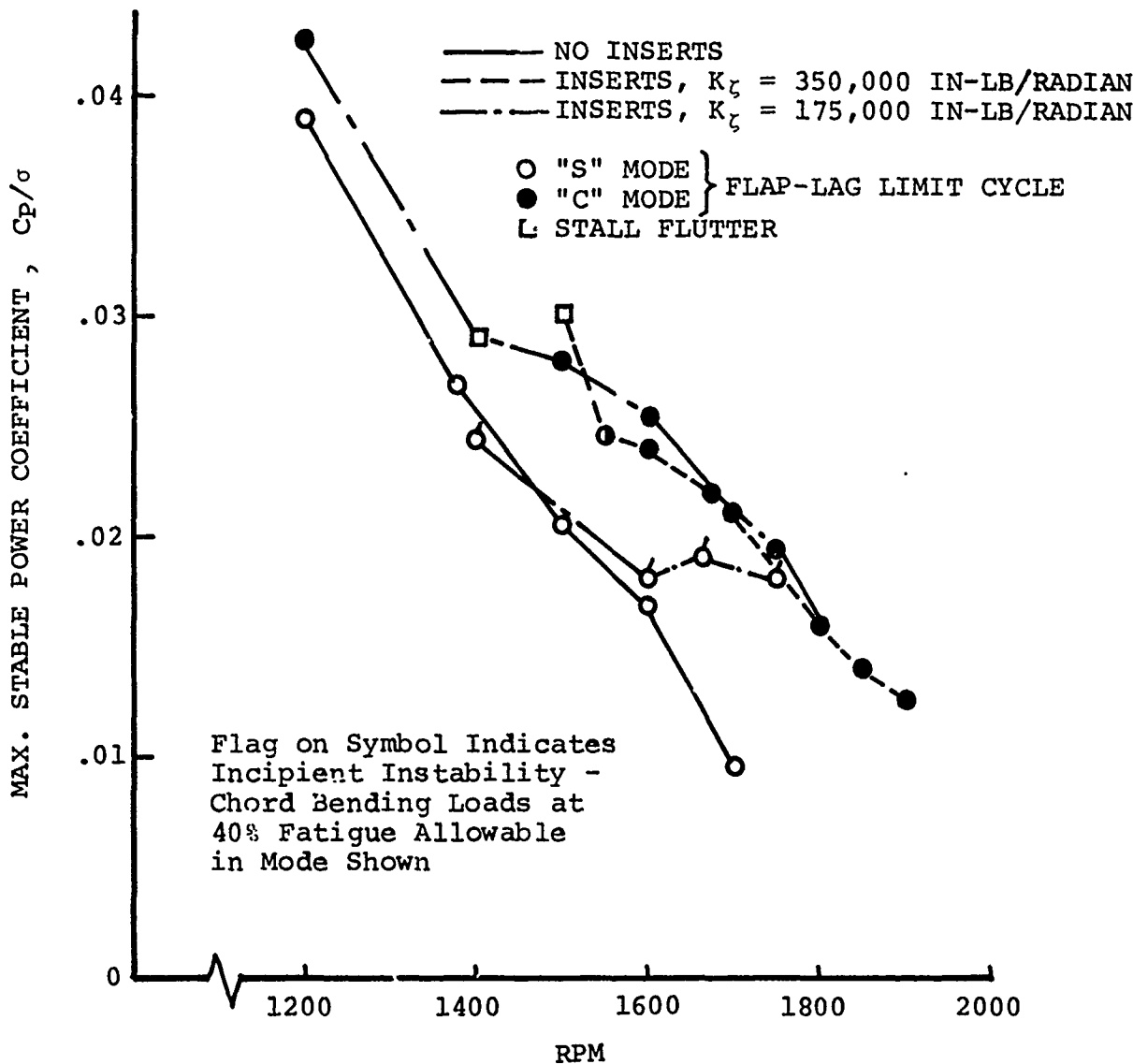
FIGURE 82   EFFECT OF ELASTOMERIC HUB INSERTS ON
FLAP-LAG STABILITY BOUNDARY

142
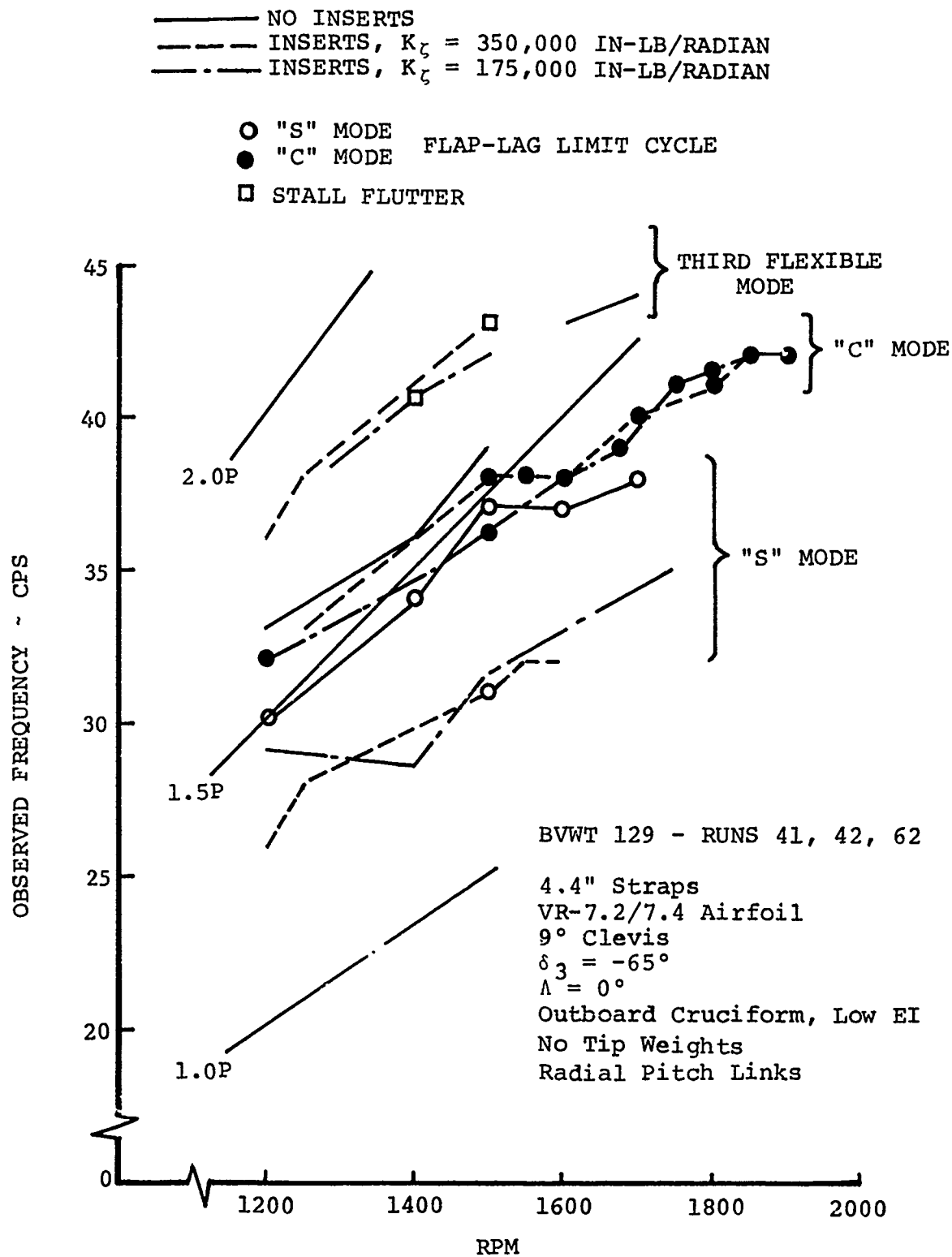
FIGURE 83   EFFECT OF ELASTOMERIC HUB INSERTS ON
             FIRST INPLANE FREQUENCIES

143

reached steady amplitudes independent of collective just beyond the instability boundaries shown in the figures. This hypothesis could not be checked without exceeding the fatigue allowable levels for strap loads.

5.2.11 Cruciform Strap Attachments

The effects of cruciform strap attachments on the flap-lag instability are shown in Figures 84 and 85. The first figure shows significant benefits obtained by inboard attachments and additional benefits obtained by full, low EI attachments. These benefits are explained by the chordwise stiffening shown in the second figure. (Chordwise frequencies are shown for only two of the Figure 84 configurations because the full, low EI attachment configuration was so well damped in the chord modes throughout the testing range that no frequencies were observed on the spectral analyzer.) The chordwise stiffening was produced by the bolt-on flanges of the attachments, as detailed in Section 3.11.

The effects of cruciform strap attachments on stall flutter are illustrated by Figures 86 and 87. These attachments were specifically designed to stabilize stall flutter by reducing second flap-type strap displacements included in the fourth, and to a lesser extent, the third flexible mode. It was observed that the pitch arms designed for negative δ_3 (flap up/nosedown coupling in the first flap mode) would produce outboard flap up/noseup coupling in the second flap-type blade motion. Early testing and analysis had indicated that positive δ_3 destabilized the first flap mode near stall. Therefore, it appeared likely that outboard flap up/noseup coupling was destabilizing the third and fourth flexible modes near stall through the second flap components of these modes (major in the fourth mode, secondary in the third mode). The cruciform attachments were designed to reduce second flap displacements in the area of the pitch arm and thereby lessen the destabilizing coupling.

Figure 86 shows the stall flutter boundaries of a four-bladed configuration with outboard, low EI cruciform attachments and with full-length, low EI attachments. This shows that the full-length, low EI attachments had a significant stabilizing effect on the selected configuration. The test stand power limits were such that the new stall flutter boundary could not be located, however. Furthermore, the full cruciform configuration was so stable that no modal frequencies could be located on the spectral analyzer for comparison with those of the baseline configuration.

Figure 87 shows the stall flutter boundaries of a two-bladed configuration with outboard low EI attachments, full-length, low EI attachments, and full-length, full EI attachments.

144

FIGURE 84   EFFECT OF CRUCIFORM STRAP ATTACHMENTS
ON FLAP-LAG STABILITY BOUNDARY

145
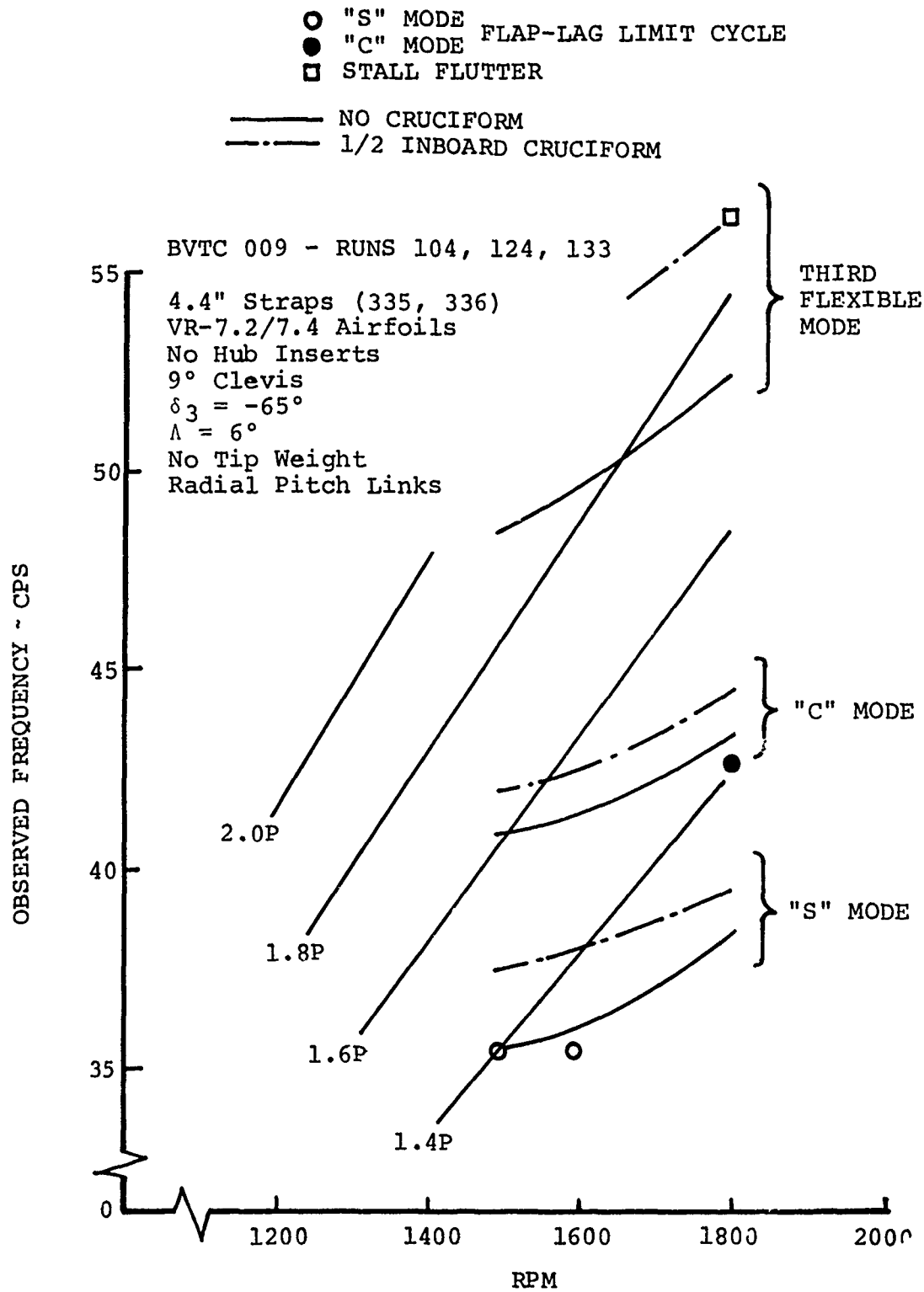
FIGURE 85   EFFECT OF CRUCIFORM STRAP ATTACHME
ON FIRST INPLANE FREQUENCIES

146

BVWT 129 - RUNS 60, 61

4.4" Straps (334, 337)
VR-7.2/7.4 Airfoils
Elastomeric Hub Inserts
K_ζ = 350,000 In-Lb/Rad
9^δ Clevis
δ_3 = -45°
Λ = 0°
No Tip Weight
Radial Pitch Links

□ STALL FLUTTER
△ MODEL TESTING LIMIT

— — — OUTBOARD CRUCIFORM, LOW EI
———— FULL CRUCIFORM, LOW EI
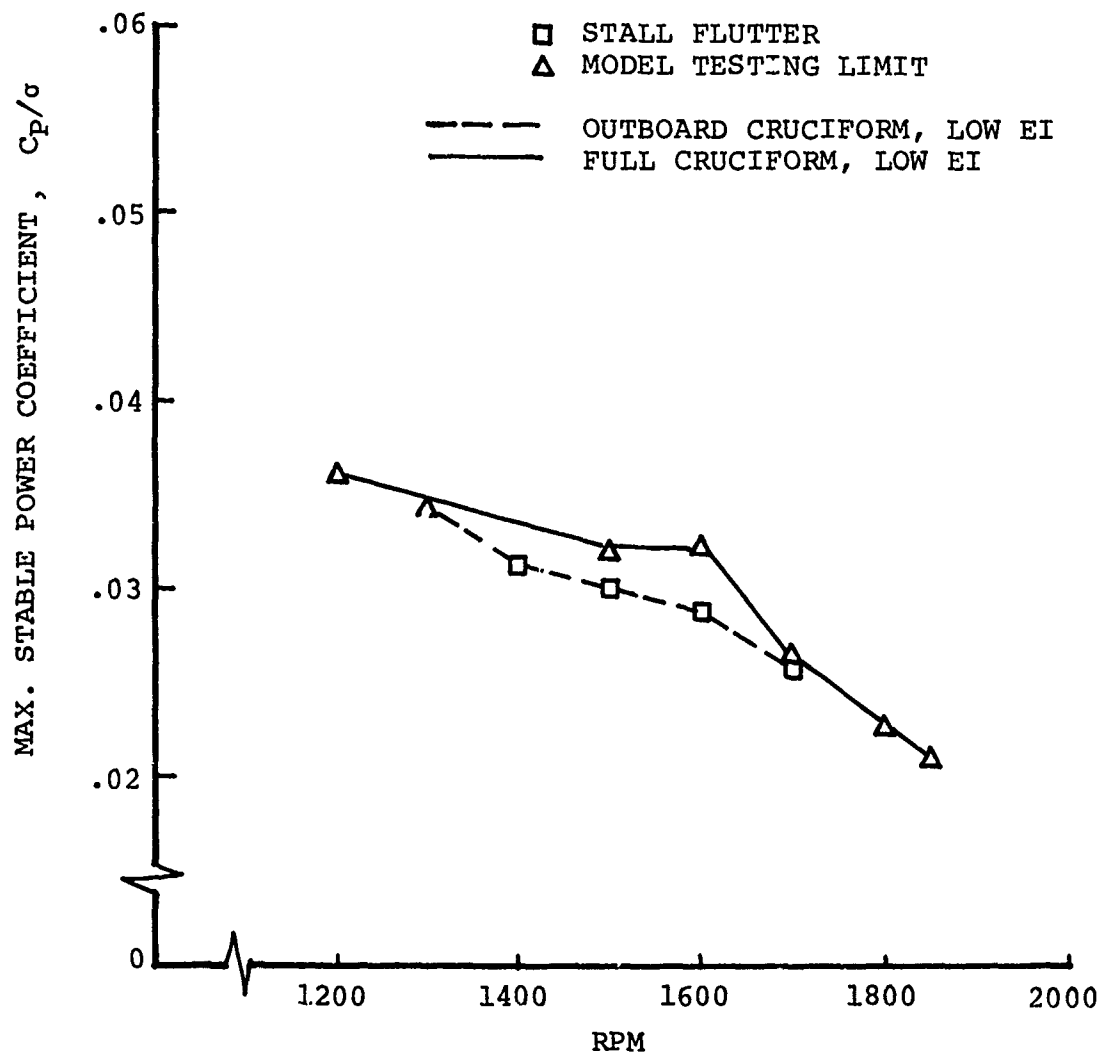
FIGURE 86   EFFECT OF CRUCIFORM STRAP ATTACHMENTS
ON STALL FLUTTER BOUNDARY

147

4.4" Straps (335, 336)
2 Blades
VR-7.2 Airfoil
No Hub Inserts
9° Clevis
$\delta_3 = -65°$
$\Lambda = 6°$
No Tip Weight
Radial Pitch Links
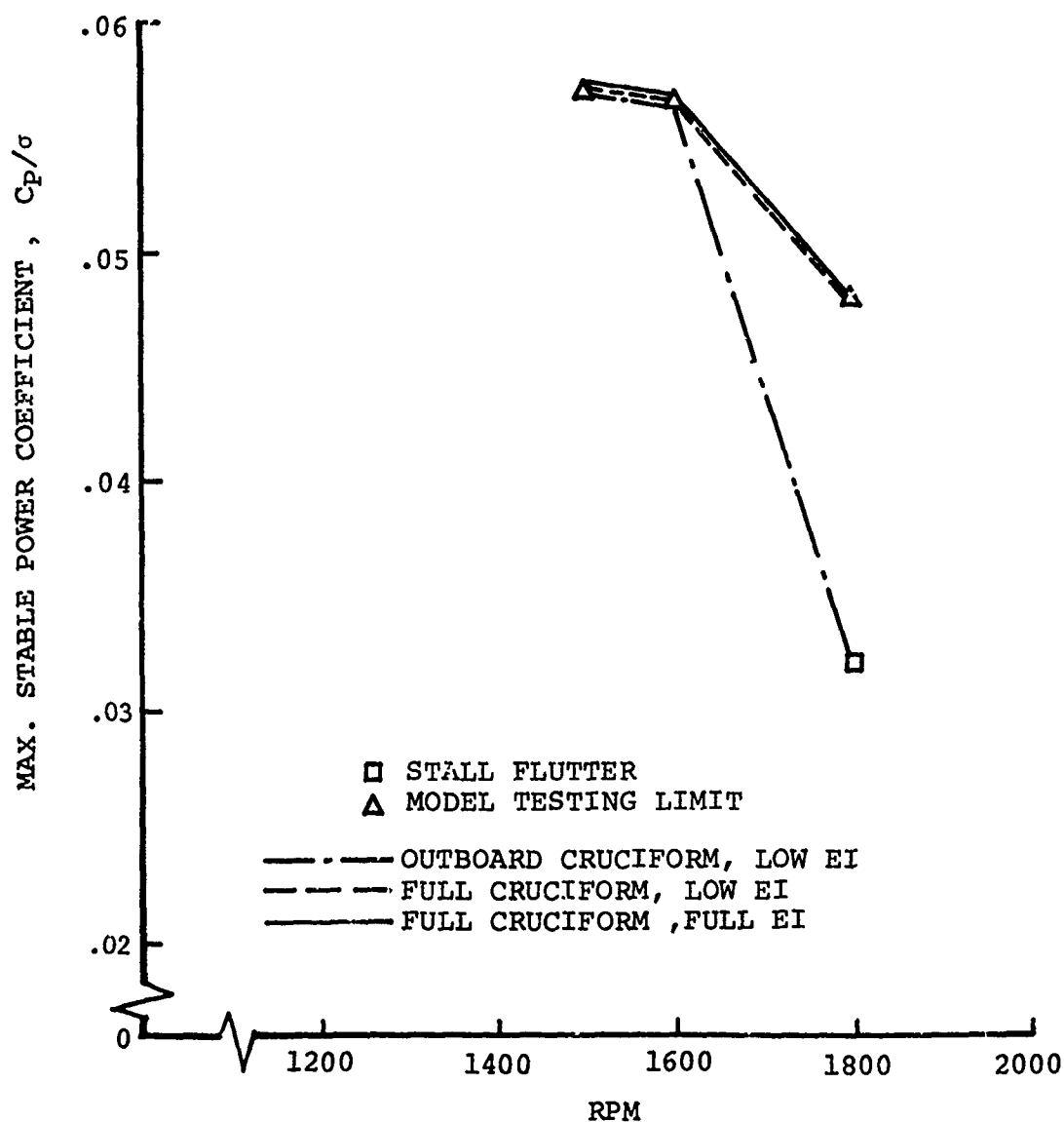
FIGURE 87   EFFECT OF CRUCIFORM STRAP ATTACHMENTS ON
STALL FLUTTER BOUNDARY

148

Two-bladed testing was used in this case to explore operation at collectives beyond those attainable with four blades. The boundaries show the strongly stabilizing effects of the full length attachments and demonstrate that low EI is adequate to obtain the benefits of these attachments.

5.2.12 Airfoil Nose Blunting

The effects of a slight blunting of the airfoil nose are shown in Figure 88. The figure compares the stall flutter boundaries of a selected configuration with three different airfoils: VR-6.9, VR-7.2, and VR-7.4 (listed in order of increasing nose bluntness). (See Section 3.12.) The results show that a small amount of blunting yielded a large boundary improvement but that further blunting had no significant effect. The explanation lies in the mechanism of stabilization. Blunting the airfoil is known to suppress leading-edge stall when it exists, thereby greatly reducing lift hysteresis and the associated negative damping during periodic pitching motions. The effect is nonlinear, in that leading-edge stall can be largely eliminated by a small amount of blunting but can be affected very little by additional blunting.

As a result of this finding, the VR-7.2 and VR-7.4 airfoils were considered interchangeable during the last two test phases. In many configurations, these airfoils were mixed: the VR-7.2 on one strap and the VR-7.4 on the other.

5.2.13 Flap-Lag Stability in Forward Flight

Finally, data was obtained to show the effects of forward speed on the boundary of the flap-lag instability. Rpm was set at 1600, and the maximum stable C_p/σ was found as a function of advance ratio. The results, shown in Figure 89, indicate some degradation of stability in the transition region, which appears to lessen at higher advance ratios. Data could not be obtained at advance ratios above .25 without exceeding balance load allowables.

5.3 Modal Damping Test

During the test phase BVTC 011, tests were made to determine the modal damping in the flap-lag "C" mode of the 8-foot-diameter tail rotor model. The configuration which was examined in the modal damping test had:

        3.6-inch strap width
        9° clevis angle
        VR-7.2 and VR-7.4 blades
        no elastomeric hub inserts
        full cruciform, reduced EI
        5° blade sweep
        $\delta_3 = -65°$

149

BVTC 009 - RUNS 14, 21, 26

4.4" Straps (335, 336)
2 Blades
Elastomeric Hub Inserts
K_ζ = 350,000 In-Lb/Rad
9° Clevis
δ_3 = -65°
Λ = 0°
Inboard Cruciform
Tip Weight, 88 Fwd/0 Aft
Radial Pitch Links
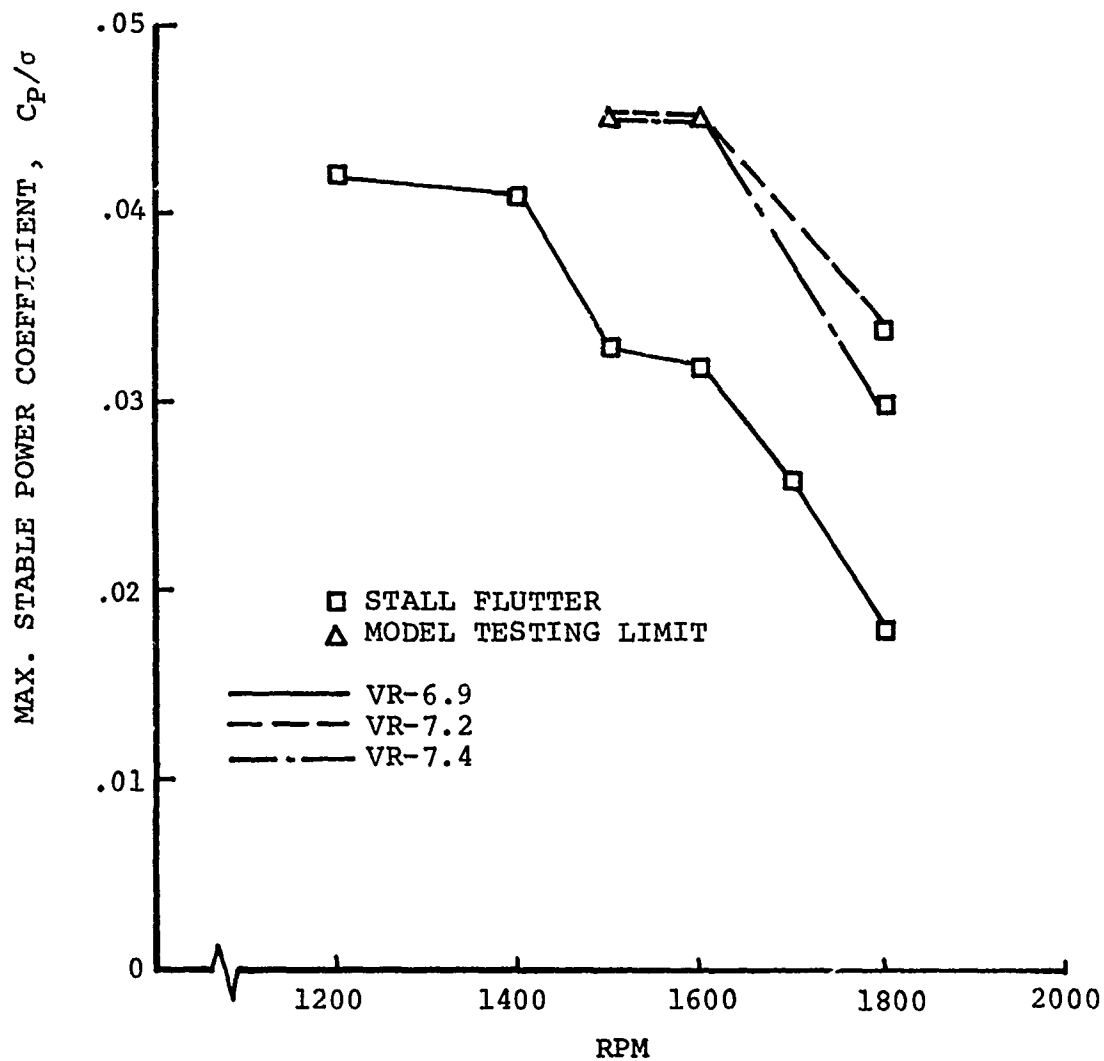
FIGURE 88   EFFECT OF AIRFOIL NOSE BLUNTING ON
             STALL FLUTTER BOUNDARY

150

BVWT 129 - RUN 63

4.4" Straps (334, 337)
VR-7.2, VR-7.4 Airfoils
Elastomeric Hub Inserts
K_ζ = 175,000 In-Lb/Rad
9^δ Clevis
δ_3 = -65°
Λ^3 = 0°
Outboard Cruciform, Low EI
No Tip Weights
Radial Pitch Links

α_{stand} = 0

1600 RPM

● "C" MODE FLAP-LAG LIMIT CYCLE
△ MODEL TESTING LIMIT
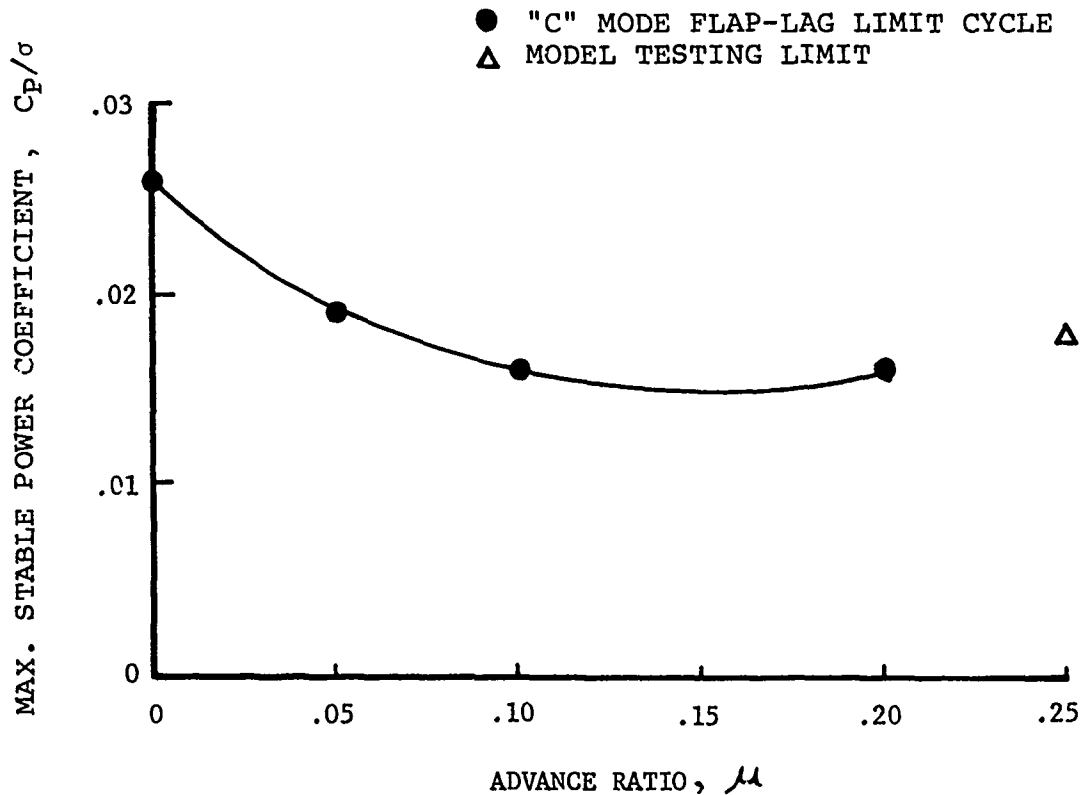
FIGURE 89   EFFECT OF FORWARD SPEED ON FLAP-LAG
             STABILITY BOUNDARY

151

This configuration is the same as that shown in Figure 63.

The modal damping was determined from the model by observing the rate of decay of the flap-lag "C" mode from an excited state. (Only stable test conditions were explored.) Excitation for the test was provided by an oscillator connected through the cyclic pitch control. The excitation amplitude and frequency could be varied with this device. The input frequency to the swashplate cyclic pitch control was nominally rotor speed minus the lag natural frequency. This produced an excitation to the blades at the rotating lag frequency.

In a typical test sequence, the desired model operating condition (rotor speed and C_p/σ) was selected. Then using a narrow band pass filter, the frequency of maximum inplane response was determined by observing the magnitude of the chord bending moment at the "C" mode inplane frequency. Oscillograph recorders, monitoring rotor speed, inplane moment and cyclic pitch input, were then started. The excitation was restarted and the blade inplane response was permitted to grow to a steady amplitude. The excitation was then terminated and the decay recorded on the oscillograph.

The decay from the oscillograph records was measured, and the percentage of critical modal damping was calculated. Plots of these measured modal damping values are shown in Figures 90 and 91. The first plot shows the same data plotted as a function of C_p/σ for constant rotor speeds. The second plot displays the data as a function of rotor speed at constant C_p/σ values. Data from these two figures were cross-plotted to produce the modal damping contours for the "C" mode, Figure 92.

As shown by the damping contours there are two areas of relatively high damping: 1.8% critical at approximately 1400 rpm and $C_p/\sigma = 0.013$ and 2.0% critical between 1200 and 1400 rpm at $C_p/\sigma \doteq 0.025$. The lowest damping recorded was at the stability boundary, which is indicated as 0% modal damping.

Note that the contours as plotted are not influenced by the presents of the marginally damped "S" mode near 1500 rpm and a C_p/σ of 0.02 (see Figure 63). This seems to imply that very little coupling exists between the two modes.
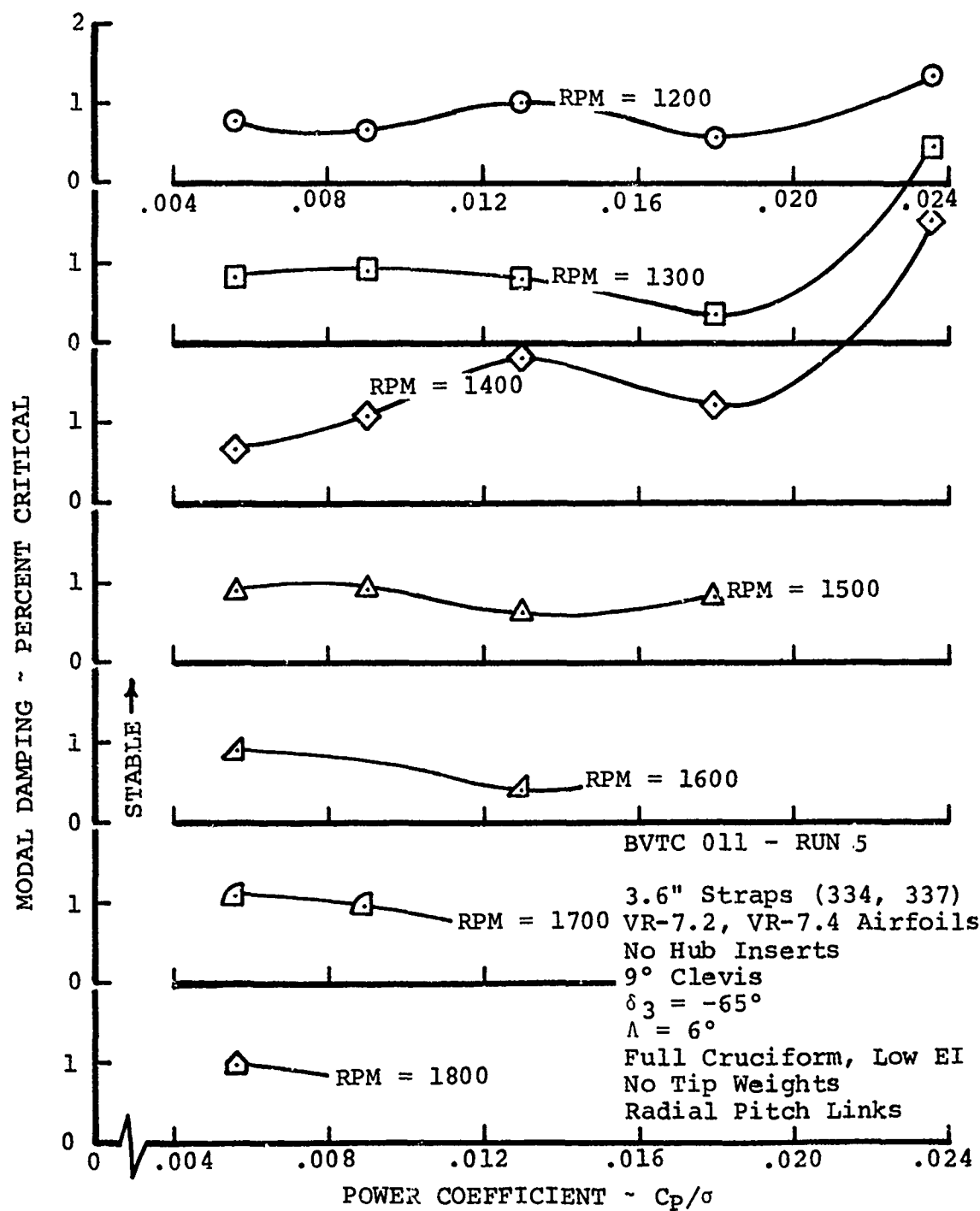
FIGURE 90   MODAL DAMPING RATIO AS A FUNCTION OF C_P/σ AT
CONSTANT RPM

153

BVTC 011 - RUN 5

3.6" Straps (334, 337)
VR-7.2, VR-7.4 Airfoils
No Hub Inserts
9° Clevis
$\delta_3 = -65°$
$\Lambda = 6°$
Full Cruciform, Low EI
No Tip Weights
Radial Pitch Links

$C_P/\sigma = .0056$

$C_P/\sigma = .009$

$C_P/\sigma = .013$

$C_P/\sigma = .018$

$C_P/\sigma = .0236$

STABLE

MODAL DAMPING ~ PERCENT CRITICAL

RPM
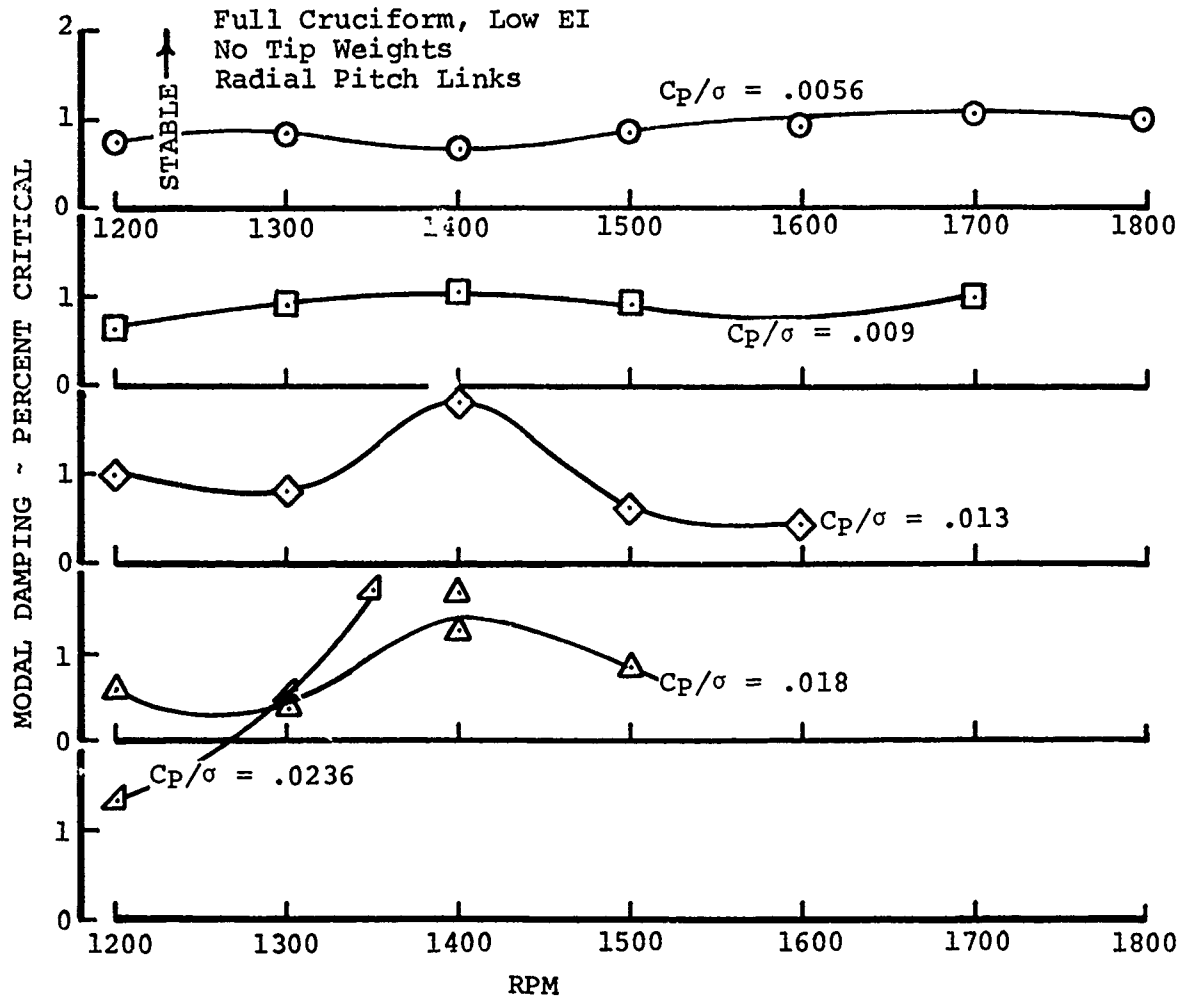
FIGURE 91   MODAL DAMPING RATIO AS A FUNCTION OF RPM AT
             CONSTANT C_P/σ

154

3.6" Straps
No Hub Inserts
9° Clevis
VR-7.2, VR-7.4 Airfoils
Λ = 5°
Full Cruciform
No Tip Weights
Radial Pitch Links
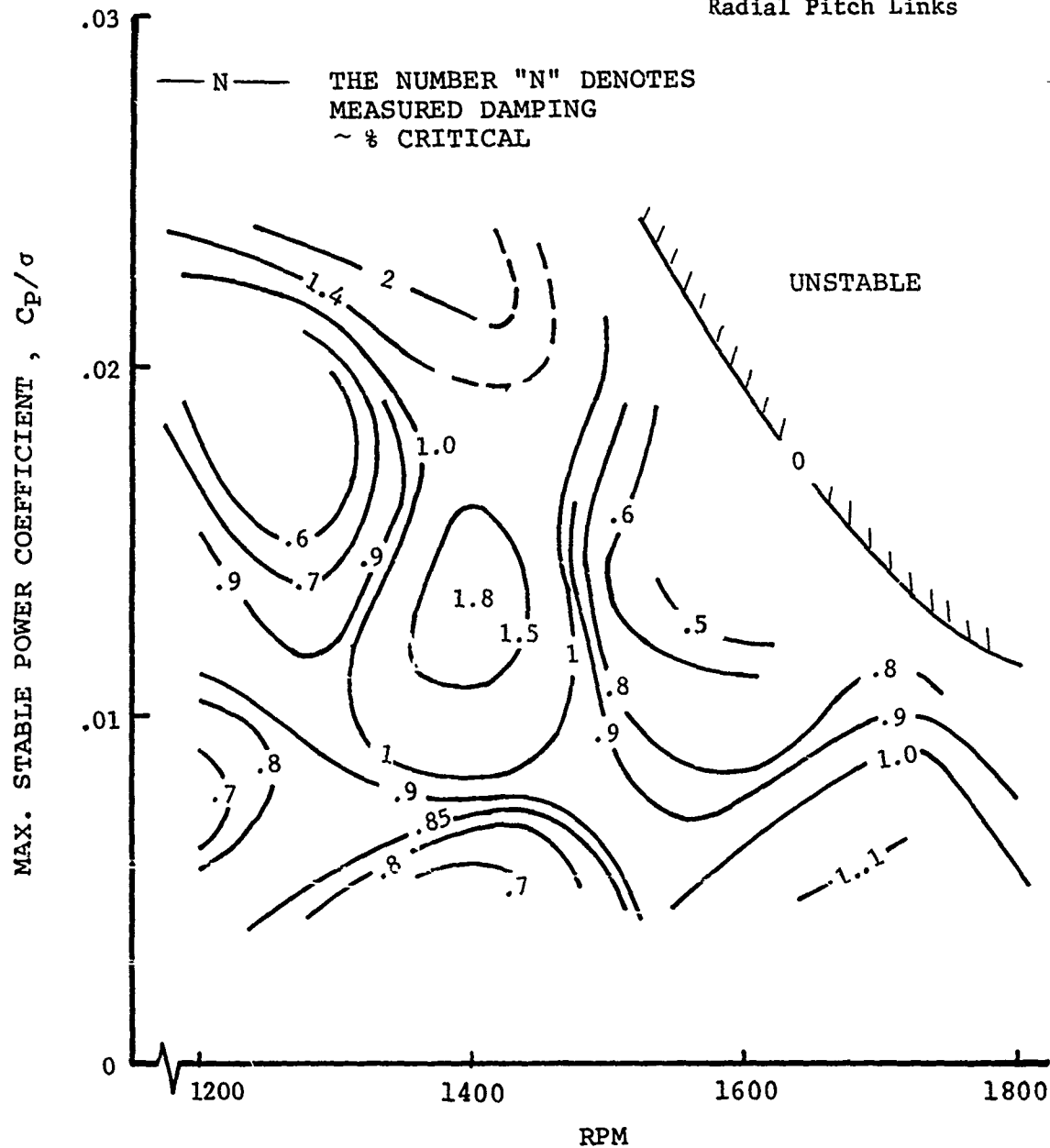
FIGURE 92   MODAL DAMPING CONTOUR – PERCENT CRITICAL

6.0   TEST RESULTS - LOADS AND PERFORMANCE

The rotor performance data is provided in this section to aid
in the interpretation of the strap loads data which follow in
Section 6.2.1.   It is important to remember, however, that the
8-foot-diameter tail rotor model was built primarily to examine
the rotor aeroelastic stability characteristics.   Therefore,
the performance of this model is not indicative of the potent-
ial of rotor systems of this type.

6.1   Performance Data

The power coefficient (C_P/σ) and the indicated blade angle of
attack (θ) are the only two performance indicators used
throughout all four test phases.   During the BVWT 129 test, a
thrust balance was incorporated in the DRTS, and thrust data,
C_T/σ, is available from that test.   Figure 93 shows the varia-
tion of C_T/σ against C_P/σ in hover for a four-bladed configur-
ation.

The thrust coefficient may be converted to rotor thrust by the
expression,

$$\frac{C_T}{\sigma} = \frac{T}{\rho bc\Omega^2 R^3}$$

where the number of blades, b, is 4; the blade chord, c, is
7.08 inches; the rotor radius is 48 inches, and the density,
ρ, is 0.1147×10^{-6} lb-sec^2/in^4.   Similarly, the power coeffi-
cient can be converted to rotor torque by the expression,

$$\frac{C_P}{\sigma} = \frac{Q}{\rho bc\Omega^2 R^4}$$

Figure 94 shows C_P/σ versus the indicated collective pitch,
$\theta_{.75}$(IND), for the same test run as that in Figure 93.   The
value $\theta_{.75}$(IND) in this figure is the collective pitch value
recorded directly from the model swashplate position based on
nonrotating calibration of blade collective pitch.   This
$\theta_{.75}$(IND) value was not the true blade collective pitch, be-
cause of the so-called "strap heave" effect, a flapwise de-
flection which tends to reduce collective pitch.   A more de-
tailed discussion can be found in Reference 2.   The relation
between $\theta_{.75}$(IND) and the true angle of attack, as determined
from the blade steady torsion loads, is shown in Figure 95.
As shown in the figure, $\theta_{.75}$ is considerably less than the
$\theta_{.75}$(IND).   For an example, when $\theta_{.75}$(IND) = 24°, the $\theta_{.75}$
(from strap torsion loads) = 14°.

156

SYMBOL	RPM
⊙	1200
⬙	1400
⊡	1500
◇	1600
◺	1800
⬠	1900

4.4" Straps (337, 338)
VR-7.2, VR-7.4 Airfoils
Elastomeric Hub Inserts
K_ζ = 350,000 In-Lb/Rad
9° Clevis
δ_3 = -65°
Λ = 11°
Outboard Cruciform, Low EI
No Tip Weights
Radial Pitch Links

FIGURE 93   THRUST VS. POWER, FOUR BLADES

BVWT 129 - RUN 45

4.4" Straps (337, 338)
VR-7.2, VR-7.4 Airfoils
Elastomeric Hub Inserts
K_ζ = 350,000 In-Lb/Rad
9° Clevis
δ_3 = -65°
Λ = 11°
Outboard Curciform, Low EI
No Tip Weights
Radial Pitch Links

SYMBOL	RPM
⊙	1200
◁	1400
⊡	1500
◇	1600
△	1800
⬠	1900
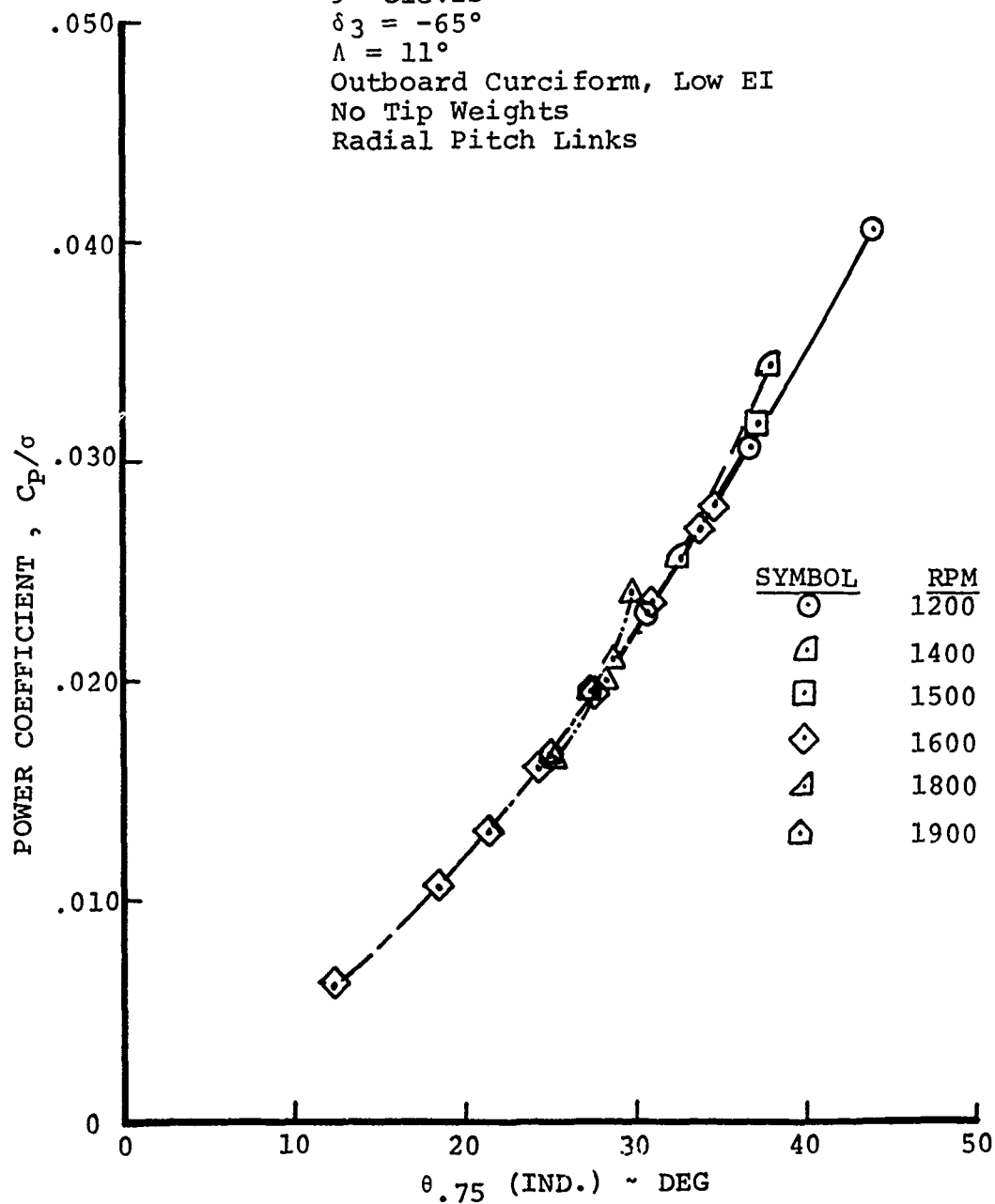
FIGURE 94   POWER VS. COLLECTIVE, FOUR BLADES

158

BVWT 129 - RUN 47, 53

4.4" Straps (334, 337)
VR-7.2, VR-7.4 Airfoils
Elastomeric Hub Inserts
  $K_\zeta = 350,000$ In-Lb/Rad
9° Clevis
$\delta_3 = -65°$
$\Lambda = 11°$
Full Cruciform, Low EI
No Tip Weights
Radial Pitch Links
1670 RPM
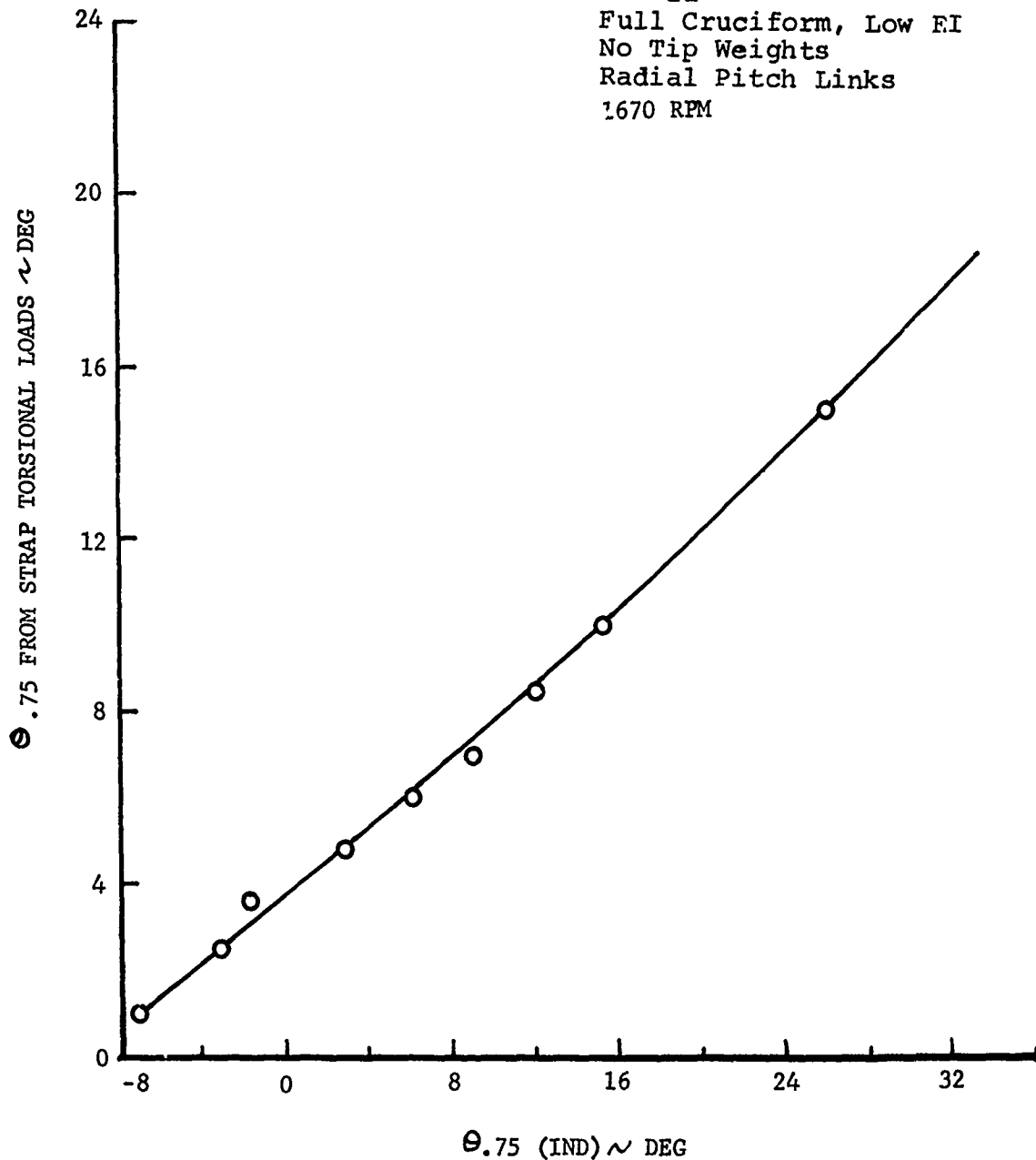
FIGURE 95   COMPARISON OF INDICATED AND TRUE
            COLLECTIVE PITCH

159

The performance of the model in a two-bladed configuration is shown in Figures 96 and 97. Comparison of the two-bladed data in Figure 96 and the four-bladed data in Figure 93 indicates that the thrust coefficient for the two-bladed model is higher by 0.016 for the same C_p/σ in the low thrust range and somewhat more at high thrust range. Figure 97 shows C_p/σ versus $\theta_{.75}$(IND) for the two-bladed configuration.

Performance data was collected for a four-bladed configuration in forward flight. This data is shown in Figure 98. The measured C_p/σ value for advance ratio, μ, of 0.1 to 0.45 and thrusts, T, from 400 to 1200 lb are plotted.

6.2 Strap Bending Loads

The flex-strap portion of the model was instrumented for the measurement of bending loads. The details of this instrumentation are presented in Section 4.1.1. However, only during the test BVWT 129 were these loads recorded and analyzed through the analog-digital processor described in Section 4.2.

The data presented in this section was taken directly from this test and represents the best data available to describe the strap loads of the model. Where possible the loads are shown from all three strap gage systems: flap bending (FB), chord bending (CB), and torsion bending (TB). The alternating loads are presented against four operating parameters for a wide range of conditions. These operating parameters are:

- Advance ratio - the ratio of the velocity of flow past the model to the model tip speed (ΩR)

- Shaft angle - indicated in Figure 27

- Cyclic pitch angle - longitudinal pitch

- Rotor thrust

Finally, the harmonic content of the alternating loads for the three gages is shown from 1/rev through 4/rev for two rotor configurations.

6.2.1 Presentation of Data

To assist the reader in the use of the loads data in this section, two tables have been selected to summarize the data. Table 10 summarizes the configurations by test run number used in the loads testing. As shown, five configurations are tested with various combinations of five configuration parameters.
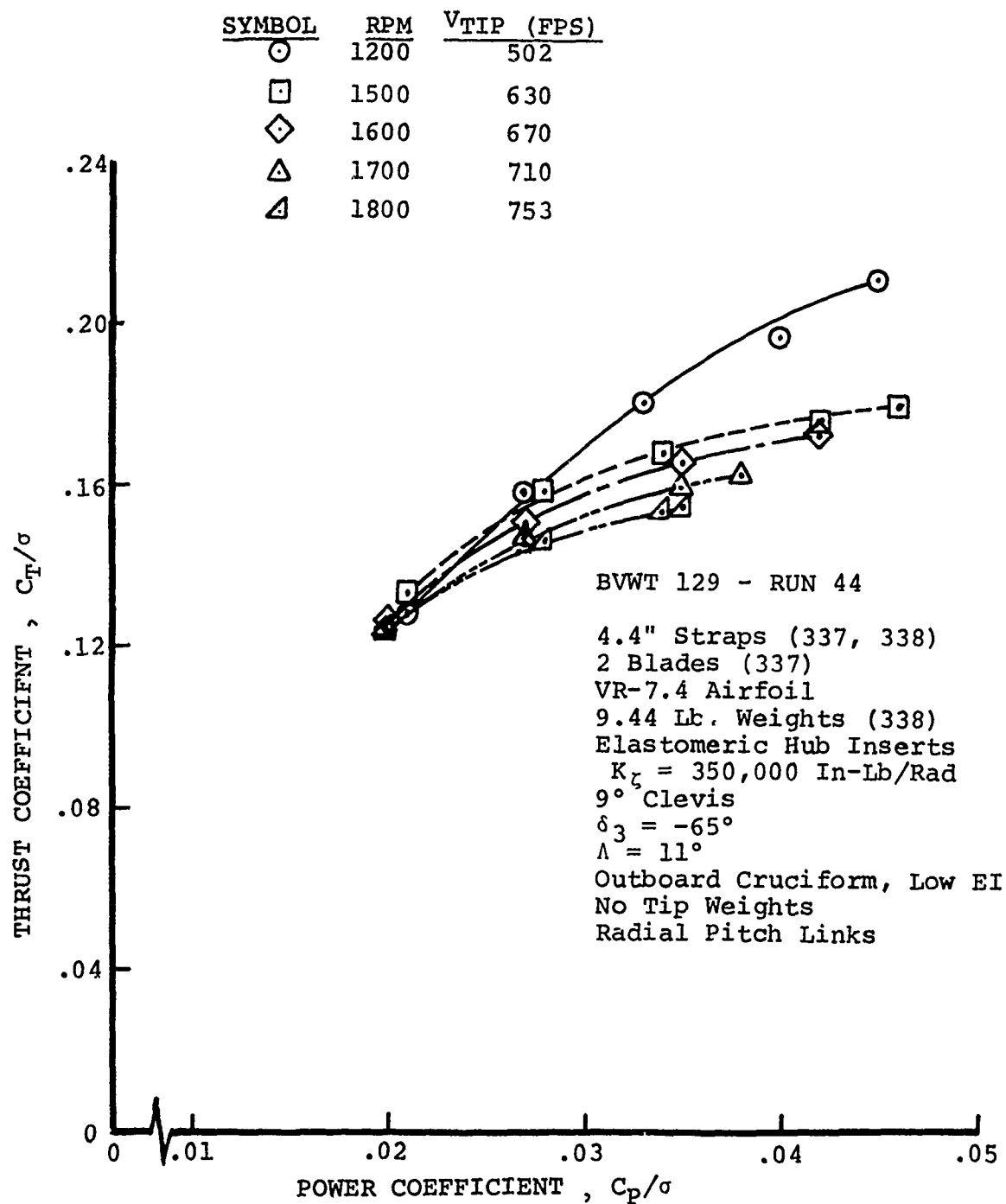
FIGURE 96   THRUST VS. POWER, TWO BLADES

The figure shows Thrust Coefficient, C_T/σ versus Power Coefficient, C_P/σ.

SYMBOL	RPM	V_{TIP} (FPS)
⊙	1200	502
□	1500	630
◇	1600	670
△	1700	710
◭	1800	753

BVWT 129 - RUN 44

4.4" Straps (337, 338)
2 Blades (337)
VR-7.4 Airfoil
9.44 Lb. Weights (338)
Elastomeric Hub Inserts
 K_ζ = 350,000 In-Lb/Rad
9° Clevis
$\delta_3 = -65°$
$\Lambda = 11°$
Outboard Cruciform, Low EI
No Tip Weights
Radial Pitch Links

BVWT 129 - RUN 44

4.4" Straps (337, 338)
2 Blades (337)
VR-7.4 Airfoil
9.44 Lb. Weights (338)
Elastomeric Hub Inserts
$K_\zeta = 350,000$ In-Lb/Rad
9° Clevis
$\delta_3 = -65°$
$\Lambda = 11°$
Outboard Cruciform, Low EI
No Tip Weights
Radial Pitch Links

SYMBOL	RPM	V_{TIP} (FPS)
⊙	1200	502
⊡	1500	630
◇	1600	670
△	1700	710
◿	1800	753

POWER COEFFICIENT , C_P/σ

$\theta_{.75}$ (IND.) ~ DEG
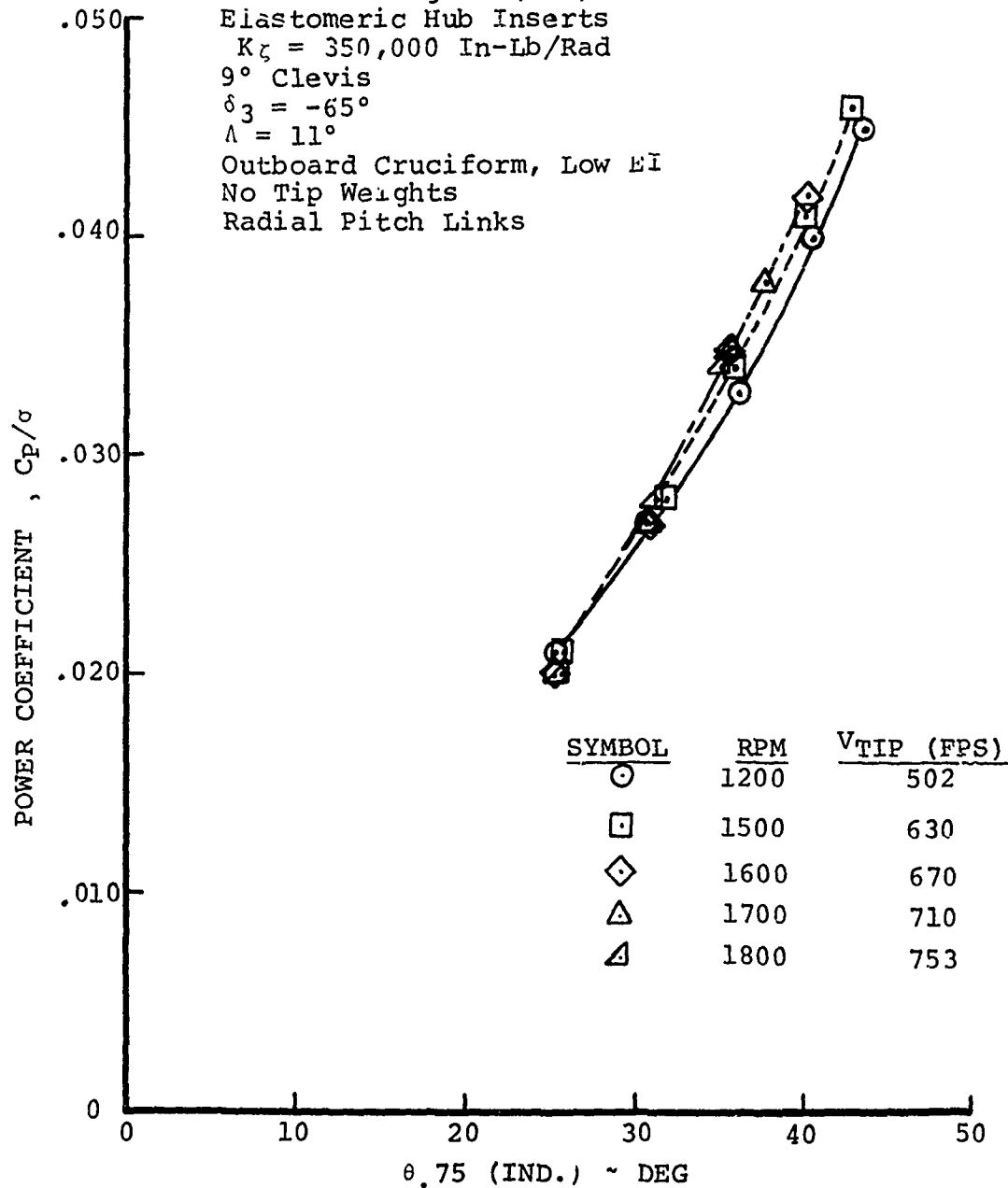
FIGURE 97   POWER VS. COLLECTIVE, TWO BLADES

162
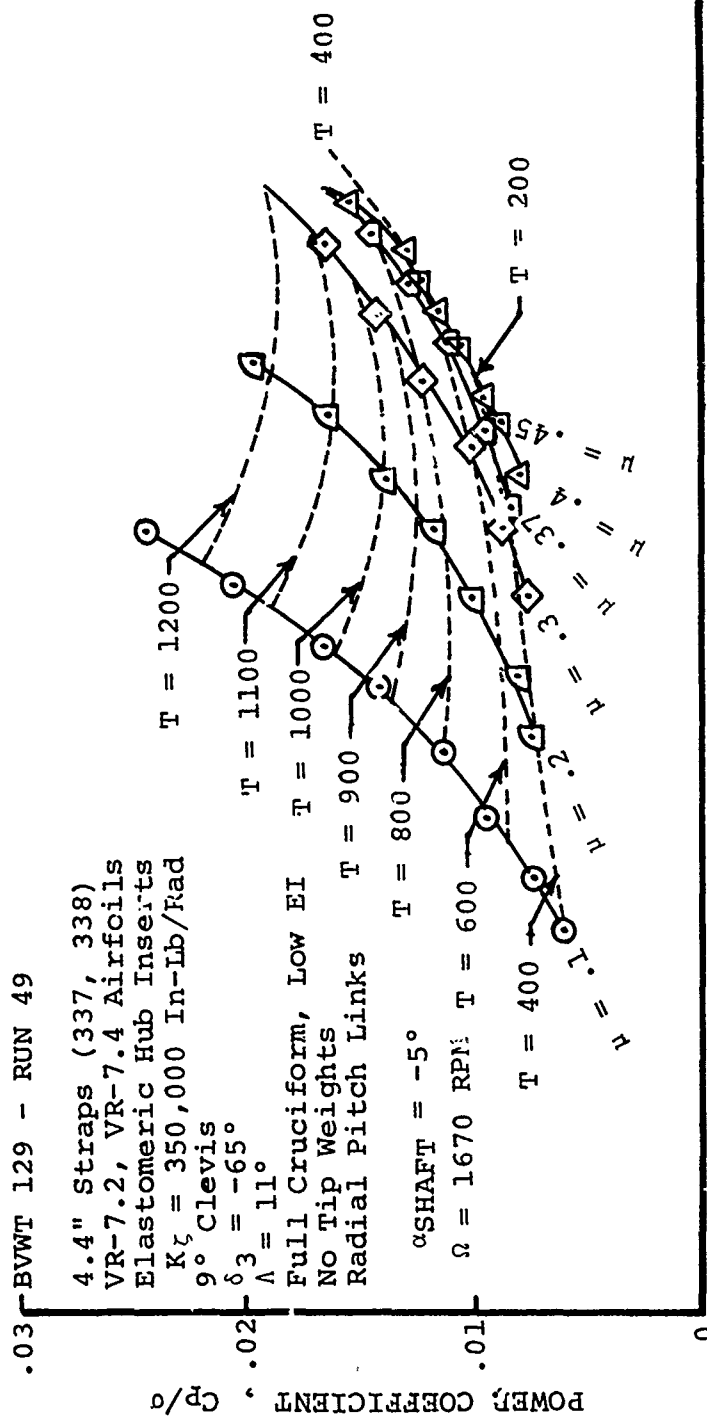
FIGURE 98   TAIL ROTOR PERFORMANCE IN FORWARD FLIGHT,
             FOUR BLADES

TABLE 10   SUMMARY OF CONFIGURATIONS USED FOR LOADS TESTING

CONFIGURATION	RUN NO.	DESCRIPTIONS					
		STRAP WIDTH (IN)	HUB INSERTS	DELTA-3 (DEG)	SWEEP ANGLE (DEG)	PITCH LINK	
A	5→7	3.3	No	-65	6	Tilted	
B	18→19	3.3	No	-65	0	Tilted	
C	21→22	3.3	No	-65	11	Tilted	
D	47→54	4.4	Yes	-65	11	Radial	
E	55→59	4.4	Yes	-45	11	Radial	

NOTE: All configurations tested had VR-7.2 and VR-7.4 airfoils, 9° clevis angle, full cruciform with reduced EI, and no tip weight.

Table 11 summarizes the test conditions that were explored during each test run and indicates in which figure or figures that the data from that run appears. This table is useful to make any additional loads data comparisons between rotor parameters or operating conditions which do not directly appear in this report.

Advance Ratio - Figures 99 through 101 show the effect of advance ratio on strap loads. The plots reflect alternating flap bending, chord bending, and torsion bending loads, respectively, for the configuration designated "D" in Table 10.

Shaft Angle - Figures 102 through 105 show the effect of shaft angle on the alternating chord bending and torsion bending loads. No flap bending data was available during Run 52 in which the shaft sweeps were made. The sweeps were made at a constant advance ratio of 0.1, using configuration "D".

Cyclic Pitch - The effect of cyclic pitch on alternating strap loads is shown in Figures 106 through 122. These test runs provide data for all five of the test configurations.

Configuration "A" data appears in Figures 106 through 108, for a hovering rotor, $\mu = 0$.

Figures 109 through 111 present cyclic pitch data for the configuration "B". This test was also performed in hover.

The cyclic pitch sweep was also performed for the configuration "C" in hover. Results of this test are plotted in Figures 112 through 114.

Figures 115 through 117 present the measured alternating loads for configuration "D". In these plots the loads are taken at a constant collective pitch setting, $\theta = 12.5°$, in hover. Three different rotor speeds were explored: 1400, 1670, and 1900 rpm. All of the data in these plots were taken from Run 47. Figures 118 through 120 show additional data from this run plotted for a constant rotor speed of 1670 rpm and three indicated collective pitch settings, 12.5°, 26°, and 32.8°.

The data plotted in Figures 121 and 122 were gathered from Run 56, configuration "E". During this data run, the flap bending gages were not operating and no usable flap bending exists. Figure 121 summarizes the alternating chord bending loads and Figure 122 summarizes the alternating torsion bending loads. A rotor speed of 1670 rpm and indicated collective settings of 10° and 26° were used in this data run.

Rotor Thrust - Data indicating the effect of rotor thrust on alternating flap bending, chord bending, and torsion bending loads are plotted in Figures 123 through 138. For these plots,

165

TABLE 11 SUMMARY OF TEST CONDITIONS AND CORRESPONDING FIGURE NUMBERS FOR STRAP BENDING LOADS

RUN NO.	ROTOR SPEED	COLLECTIVE PITCH	SHAFT ANGLE	ADVANCE RATIO	CYCLIC PITCH	FIGURE NUMBERS FLAP @ X/R=0.059	CHORD @ X/R=0.0822	TORSION @ X/R=0.0822
5	1600	9	78	0	VARY	106	107	108
6	1600	26	78	0	VARY	106	107	111
7	1600	30	78	0	VARY	106	107	111
18	1600	10	0	0	VARY	109	110	111
19	1600	26	0	0	VARY	109	110	114
21	1600	10	0	0	VARY	112	113	114
22	1600	26	0	0	VARY	112	113	117
47	1400	12.5	0	0	VARY	115	116	117
	1670	12.5	0	0	VARY	115, 118	116, 119	117, 120
	1670	26.0	0	0	VARY	118	119	120
	1670	32.8	0	0	VARY	118	119	120
	1900	12.5	0	0	VARY	115	116	117
48	1670	15	0	0	0	99	100	101
49	1670	VARY	+ 5	VARY .1,.2,.3,.37,.4,.45	0	123	124	125
50	1670	VARY	0,-10,-15	.4	0	159H→162H	163H→166H	167H→170H
51	1670	VARY	+5,+10	.4	0	126	127	128
52	1500	15	-15,-10,-5, 0,5,10,15	.1	0		129	130
	1670	9, 15	-15,-10,-5, 0,5,10,15	.1	0		103	105
54	1900	9	-15,-10,-5, 0,5,10,15	.1	0		102, 103	104, 105
55	1670	VARY	-5,0,5,10,15	.4	0		102	104
	1670	VARY	- 5	0, .1	0	133	131	132
56	1670	10	0	0	VARY		151H→154H	155H→158H
	1670	26	0	0	VARY		134	135
58	1670	VARY	- 5	.3, .4, .45	0	133	143H→146H	147H→150H
						139H→142H	121	122
59	1670	VARY	0,+10,-16	.4	0	136	121	122
							134	135
							143H→146H	147H→150H
							137	138

*H is for figures that contain harmonic loads of first through fourth harmonics while the other plots display alternating loads.

166

a wide range of advance ratios and shaft angles were examined. In all of the tests summarized in this section, the rotor cyclic pitch angles were zero.

Figures 123 through 125 show the alternating loads for configuration "D" as a function of rotor thrust for advance ratios of 0.1 to 0.45. These loads are all for a rotor speed of 1670 rpm and a shaft angle of 5°. The flap bending loads appear in Figure 123; the alternating chord bending loads appear in Figure 124; and the alternating torsion bending loads appear in Figure 125.

Figures 126 through 128 present the effect of rotor thrust on the alternating strap loads for the "D" configuration rotor. In these plots the advance ratio is 0.4 and the rotor speed is 1670 rpm. The measured alternating loads are shown for three values of shaft angle: -15°, -10°, and 0° (the sense of α_S appears in Figure 27).

Additional shaft angles, 5° and 10°, for the same configuration and test conditions are shown in Figures 129 and 130. During the data run for these two plots, the blade flap bending gage was not functioning, so only the alternating chord and torsion bending data are presented. This data should be directly comparable to the data shown in Figures 127 and 128.

The thrust sweep for this configuration was repeated during Run 54 for the shaft angles: -5°, 0°, 5°, 10°, and 15°. The advance ratio was held consta⋅ ⁻ᵗ 0.4 and the rotor speed at 1670 rpm. This data is plot⋅ Figure 131 for chord bending and in Figure 132 for strap rsion bending.

Figures 133 through 135 show the effect of thrust on alternating flap bending, chord bending, and torsion bending loads, respectively, for a range of advance ratios. The data for these plots were taken from the test runs 55 and 58 of the configuration "E". The rotor speed for these test runs was 1670 rpm and the shaft angle was -5°.

The alternating loads for an advance ratio of 0.4 in the configuration "E" are shown in Figures 136, 137, and 138. The configuration was tested at three shaft angles (0°, +10°, -16°) and a rotor speed of 1670 rpm.

Alternating Loads Harmonic Content - The alternating loads presented above are the peak-to-peak amplitudes. These amplitudes are harmonically analyzed during several of the BVWT 129 test runs by using the analog-digital data processing system.

The amplitudes of the first through fourth harmonic loads are shown in Figures 139 through 170. These figures present data for the configurations "D" and "E" and indicate the effect of
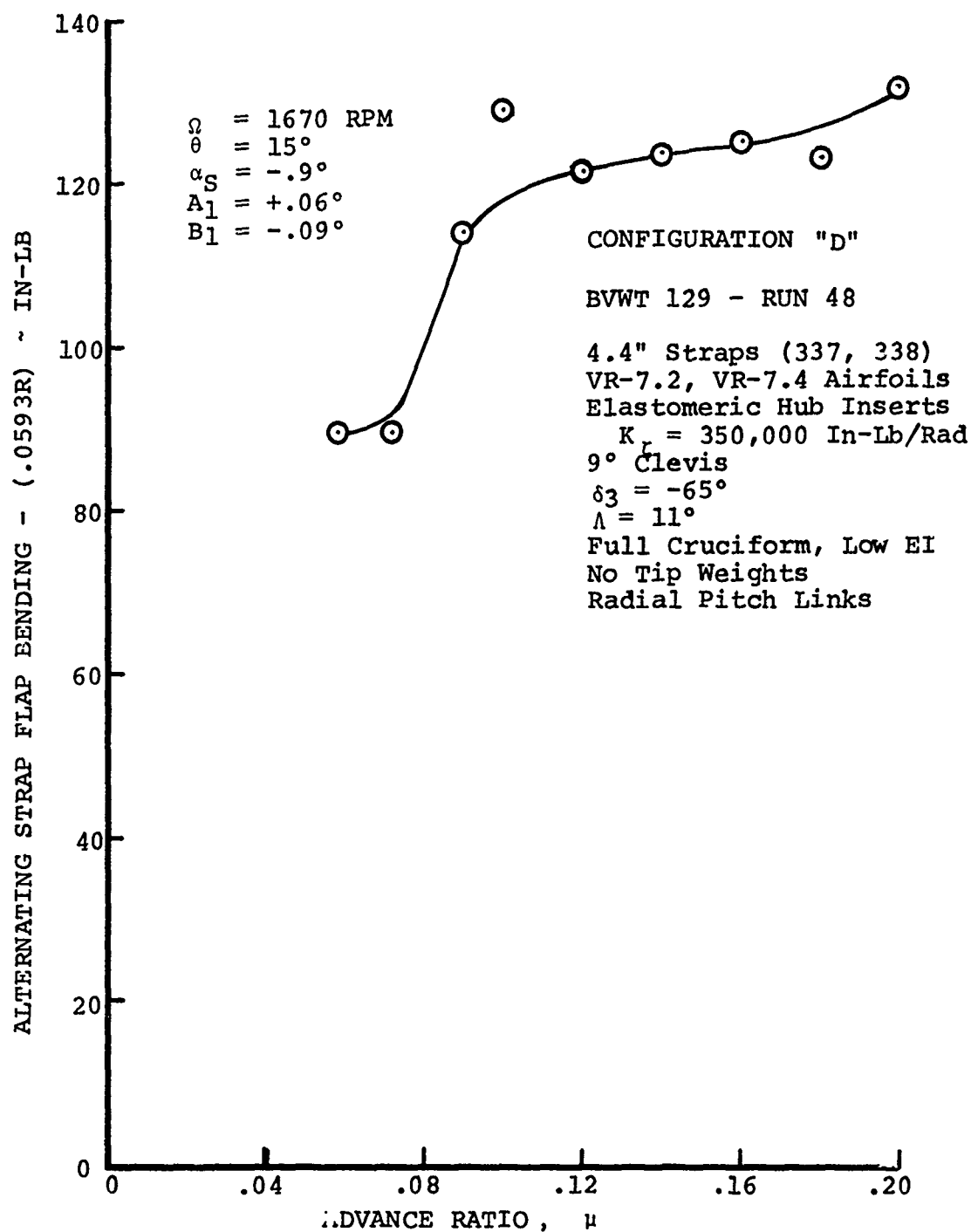
FIGURE 99   ALTERNATING FLAP BENDING LOADS IN FORWARD
             FLIGHT AT $\alpha_{SHAFT} = -.9°$

CONFIGURATION "D"

BVWT 129 - RUN 48

Ω = 1670 RPM
θ = 15°
α_S = -.9°
A_1 = +.06°
B_1 = -.09°

4.4" Straps (337, 338)
VR-7.2, VR-7.4 Airfoils
Elastomeric Hub Inserts
K_ζ = 350,000 In-Lb/Rad
9° Clevis
δ_3 = -65°
Λ = 11°
Full Cruciform, Low EI
No Tip Weights
Radial Pitch Links

FIGURE 100   ALTERNATING CHORD BENDING LOADS IN FORWARD
FLIGHT AT α_{SHAFT} = -.9°

169

Graph axes:
- Y-axis: ALTERNATING STRAP TORSION BENDING - (.0822R) IN-LB
- X-axis: ADVANCE RATIO, μ

Annotations on plot:

$\Omega = 1670$ RPM
$\theta = 15°$
$\alpha_S = -.9°$
$A_1 = +.06°$
$B_1 = -.09°$

CONFIGURATION "D"

BVWT 129 - RUN 48

4.4" Straps (337, 338)
VR-7.2, VR-7.4 Airfoils
Elastomeric Hub Inserts
$\quad K_\zeta = 350,000$ In-Lb/Rad
9° Clevis
$\delta_3 = -65°$
$\Lambda = 11°$
Full Cruciform, Low EI
No Tip Weights
Radial Pitch Links
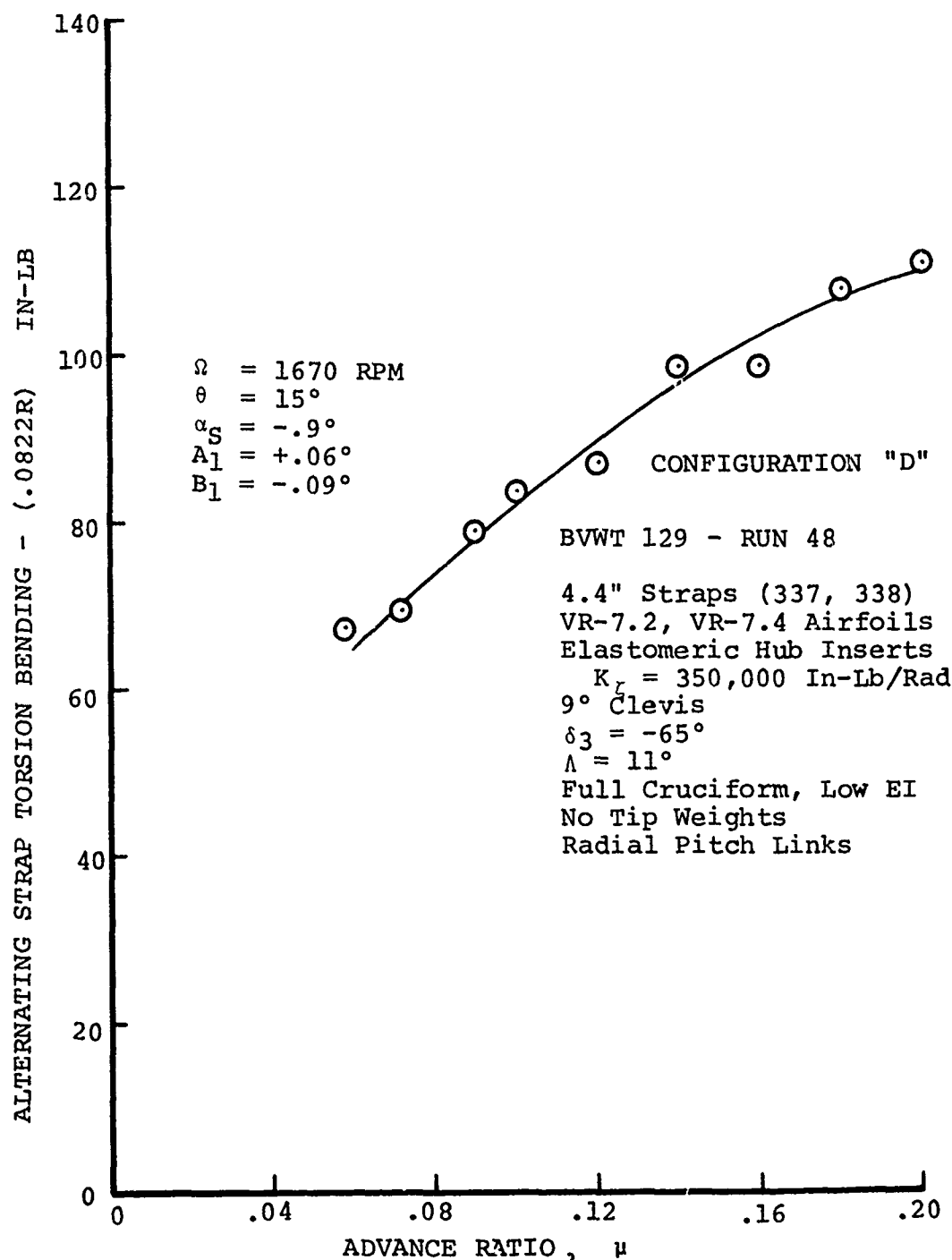
FIGURE 101   ALTERNATING TORSION BENDING LOADS IN FORWARD
FLIGHT AT $\alpha_{SHAFT} = -.9°$

170
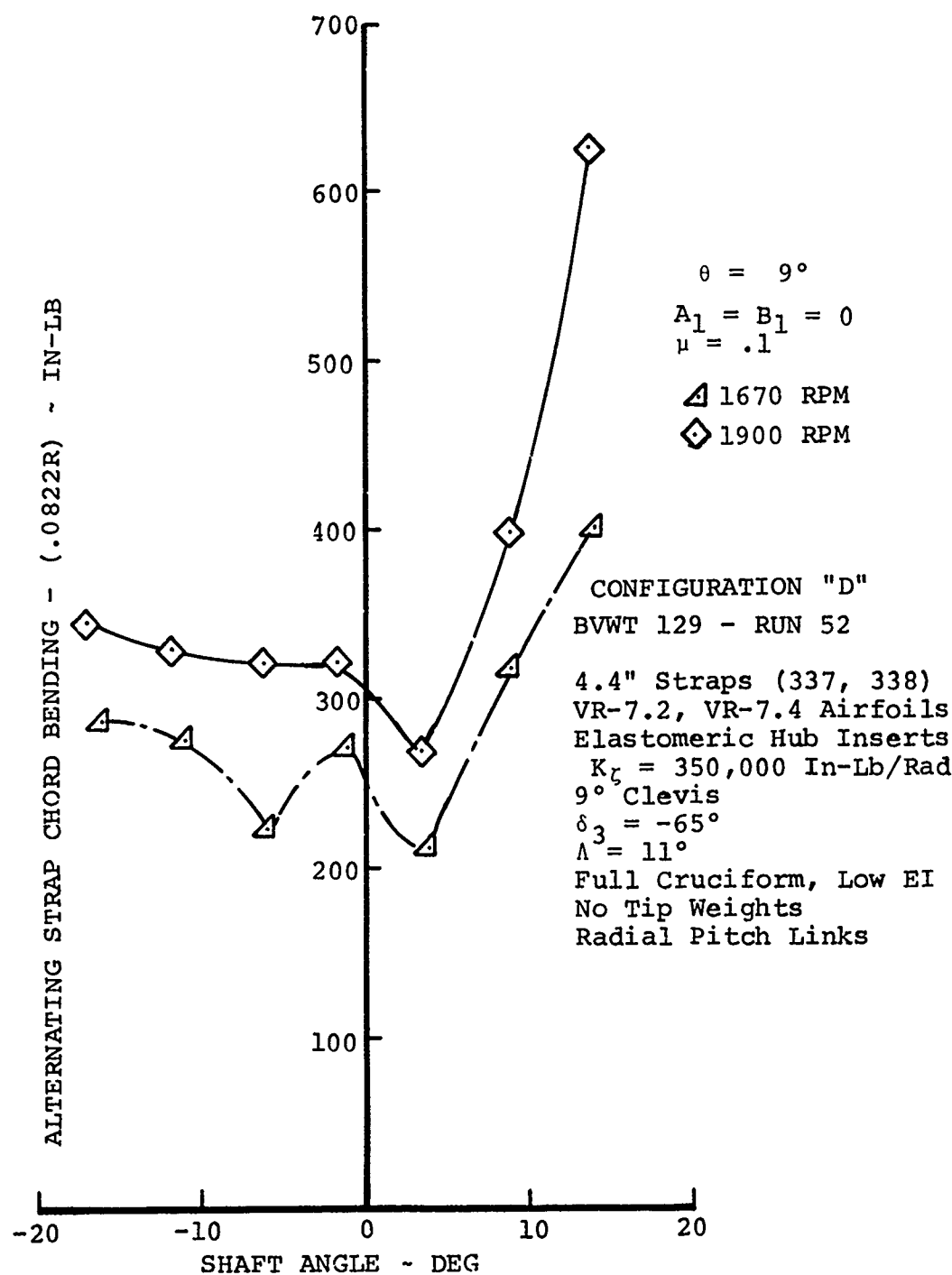
FIGURE 102   EFFECT OF RPM ON CHORD BENDING LOADS IN FORWARD
              FLIGHT FOR A SHAFT ANGLE SWEEP

171

FIGURE 103   EFFECT OF RPM ON CHORD BENDING LOADS IN FORWARD
FLIGHT FOR A SHAFT ANGLE SWEEP

CONFIGURATION "D"

BVWT 129 - RUN 52

4.4" Straps (337, 338)
VR-7.2, VR-7.4 Airfoils
Elastomeric Hub Inserts
  K_ζ = 350,000 In-Lb/Rad
9° Clevis
δ_3 = -65°
Λ = 11°
Full Cruciform, Low EI
No Tip Weights
Radial Pitch Links

θ = 9°

$A_1 = B_1 = 0$
μ = .1

△ 1670 RPM

◇ 1900 RPM
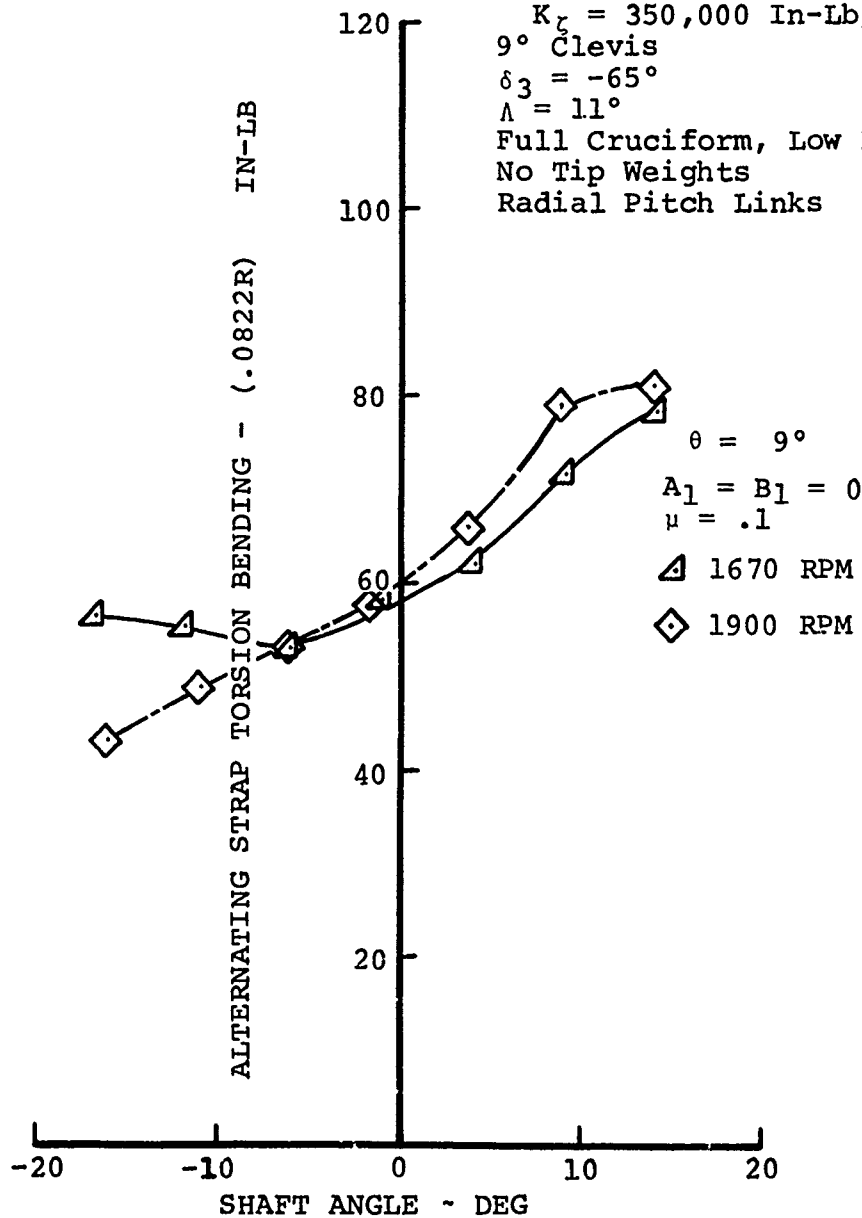
FIGURE 104   EFFECT OF RPM ON TORSION BENDING LOADS IN
FORWARD FLIGHT FOR A SHAFT ANGLE SWEEP
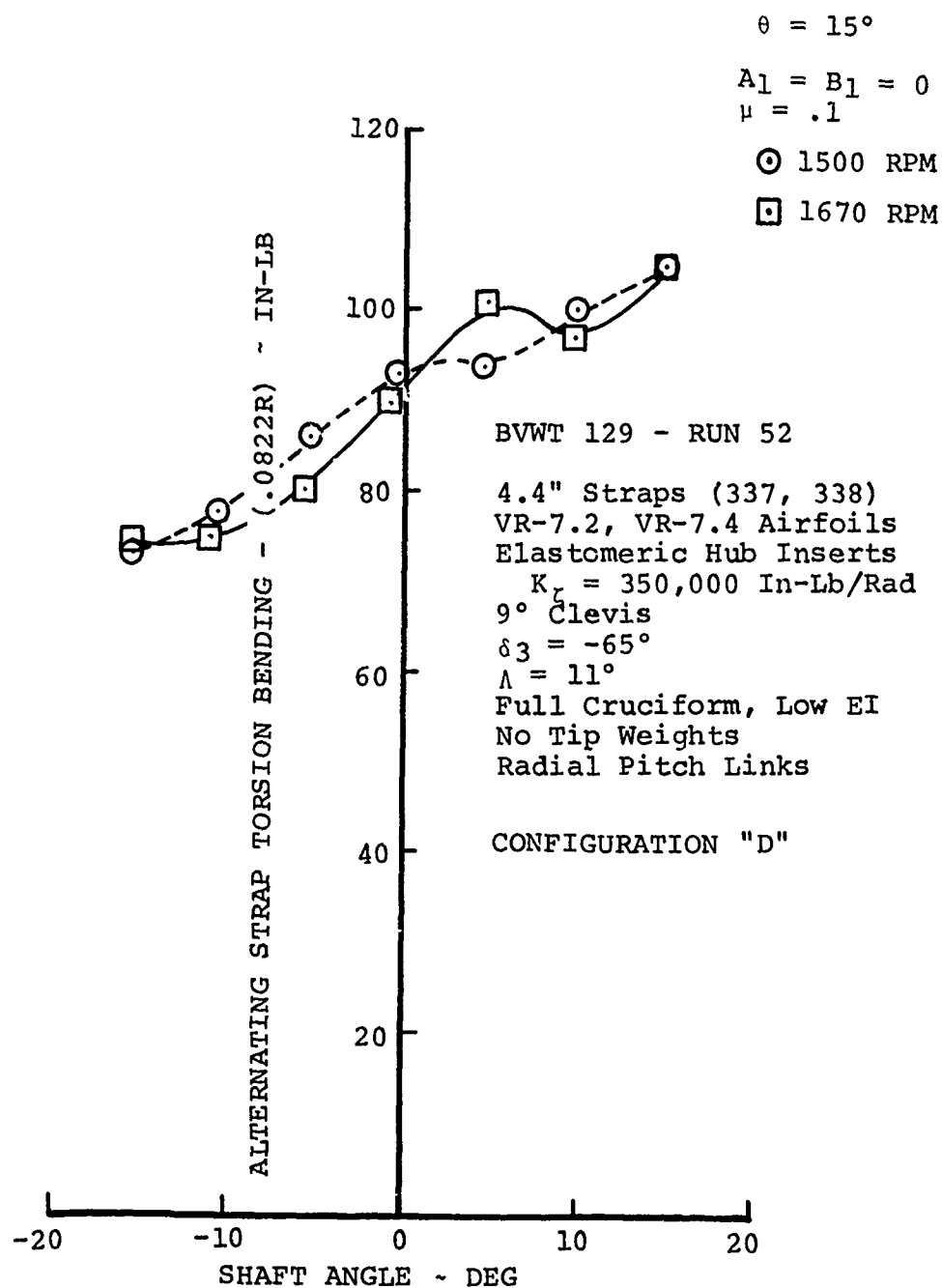
FIGURE 105   EFFECT OF RPM ON TORSION BENDING LOADS IN
              FORWARD FLIGHT FOR A SHAFT ANGLE SWEEP

CONFIGURATION "A"

BVWT 129 - RUNS 5, 6, 7

3.3" Straps (336, 335)
VR-7.2, VR-7.4 Airfoils
No Hub Inserts
9° Clevis
$\delta_3 = -65°$
$\Lambda = 6°$
Full Cruciform, Low EI
No Tip Weights
Canted Pitch Links

$\Omega = 1600$ RPM

⊙ $\theta = 9°$
△ $\theta = 26°$
⊡ $\theta = 30°$

ALTERNATING STRAP FLAP BENDING ~ (.0593R) ~ IN-LB

LONGITUDINAL CYCLIC , B1 ~ DEG
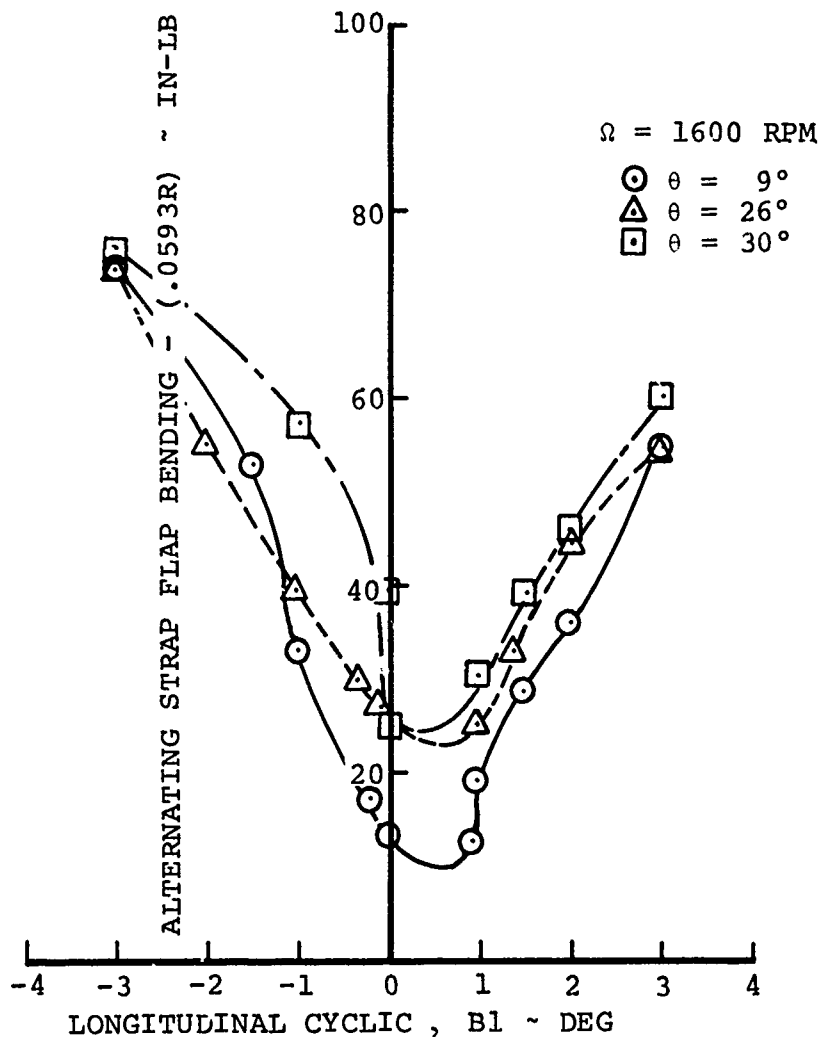
FIGURE 106   EFFECT OF COLLECTIVE ON FLAP BENDING LOADS
FOR A CYCLIC SWEEP IN HOVER

175

CONFIGURATION "A"

BVWT 129 - RUNS 5, 6, 7

3.3" Straps (336, 335)
VR-7.2, VR-7.4 Airfoils
No Hub Inserts
9° Clevis
$\delta_3 = -65°$
$\Lambda = 6°$
Full Cruciform, Low EI
No Tip Weights
Canted Pitch Links

$\Omega = 1600$ RPM

$\odot$ $\theta = 9°$
$\triangle$ $\theta = 26°$
$\boxdot$ $\theta = 30°$

ALTERNATING STRAP CHORD BENDING - $(.0322R) \sim$ IN-LB

LONGITUDINAL CYCLIC , B1 $\sim$ DEG

FIGURE 107   EFFECT OF COLLECTIVE ON CHORD BENDING LOADS
              FOR A CYCLIC SWEEP IN HOVER

176

CONFIGURATION "A"

BVWT 129 - RUN 5

3.3" Straps (336, 335)
VR-7.2, VR-7.4 Airfoils
No Hub Inserts
9° Clevis
$\delta_3 = -65°$
$\Lambda = 6°$
Full Cruciform, Low EI
No Tip Weights
Canted Pitch Links

$\Omega = 1600$ RPM

$\odot \quad \theta = 9°$
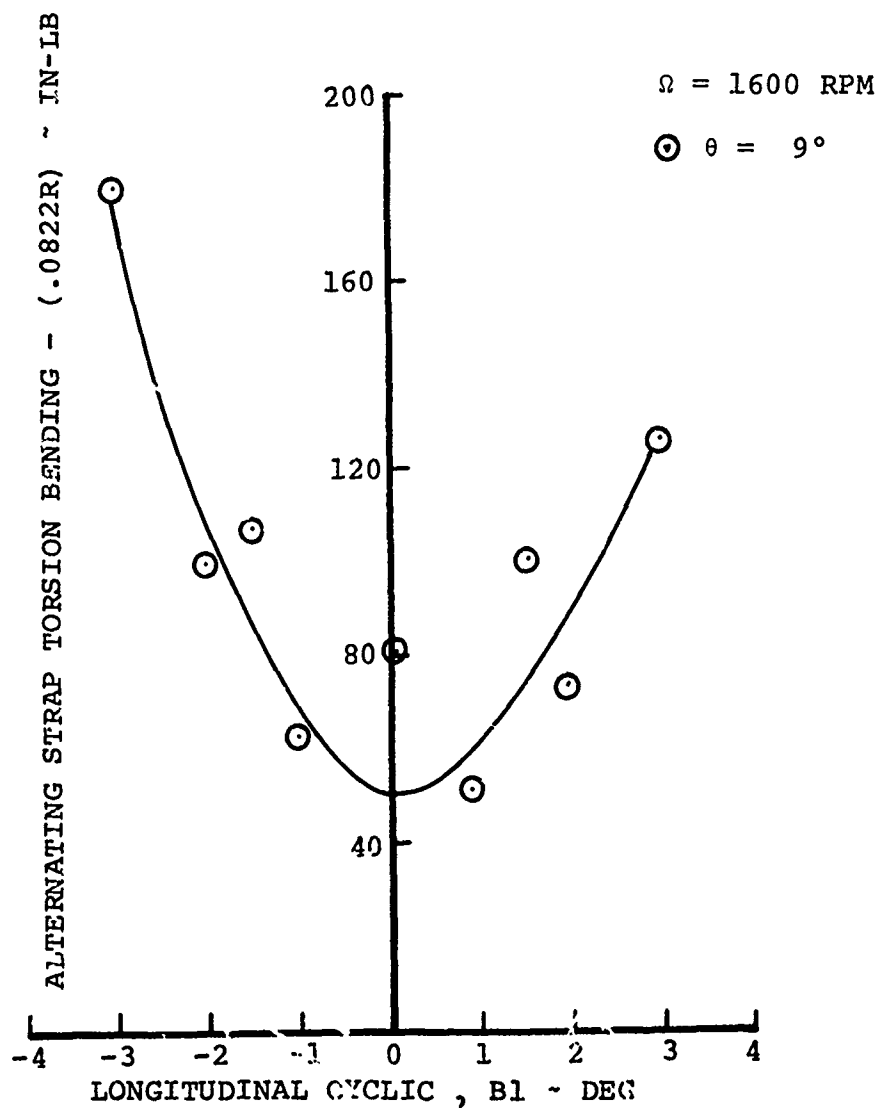
FIGURE 108   EFFECT OF COLLECTIVE ON TORSION BENDING LOADS
FOR A CYCLIC SWEEP IN HOVER

177

CONFIGURATION "B"

BVWT 129 - RUNS 18, 19

3.3" Straps (336, 335)
VR-7.2, VR-7.4 Airfoils
No Hub Inserts
9° Clevis
$\delta_3 = -65°$
$\Lambda = 0°$
Full Cruciform, Low EI
No Tip Weights
Canted Pitch Links

$\Omega = 1600$ RPM

$\odot$ $\theta = 10°$
$\triangle$ $\theta = 26°$

ALTERNATING STRAP FLAP BENDING − (.0593R) ~ IN-LB

LONGITUDINAL CYCLIC , B_1 ~ DEG
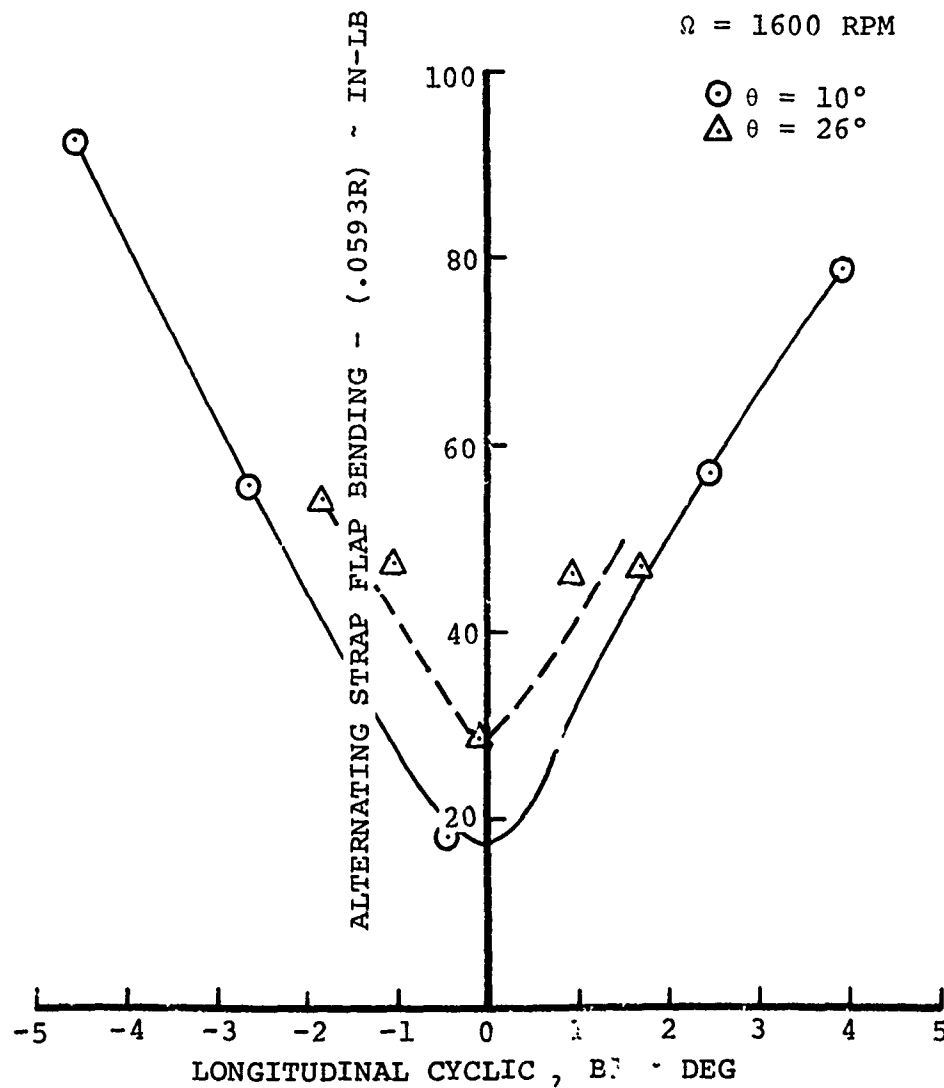
FIGURE 109   EFFECT OF COLLECTIVE ON FLAP BENDING LOADS
FOR A CYCLIC SWEEP IN HOVER
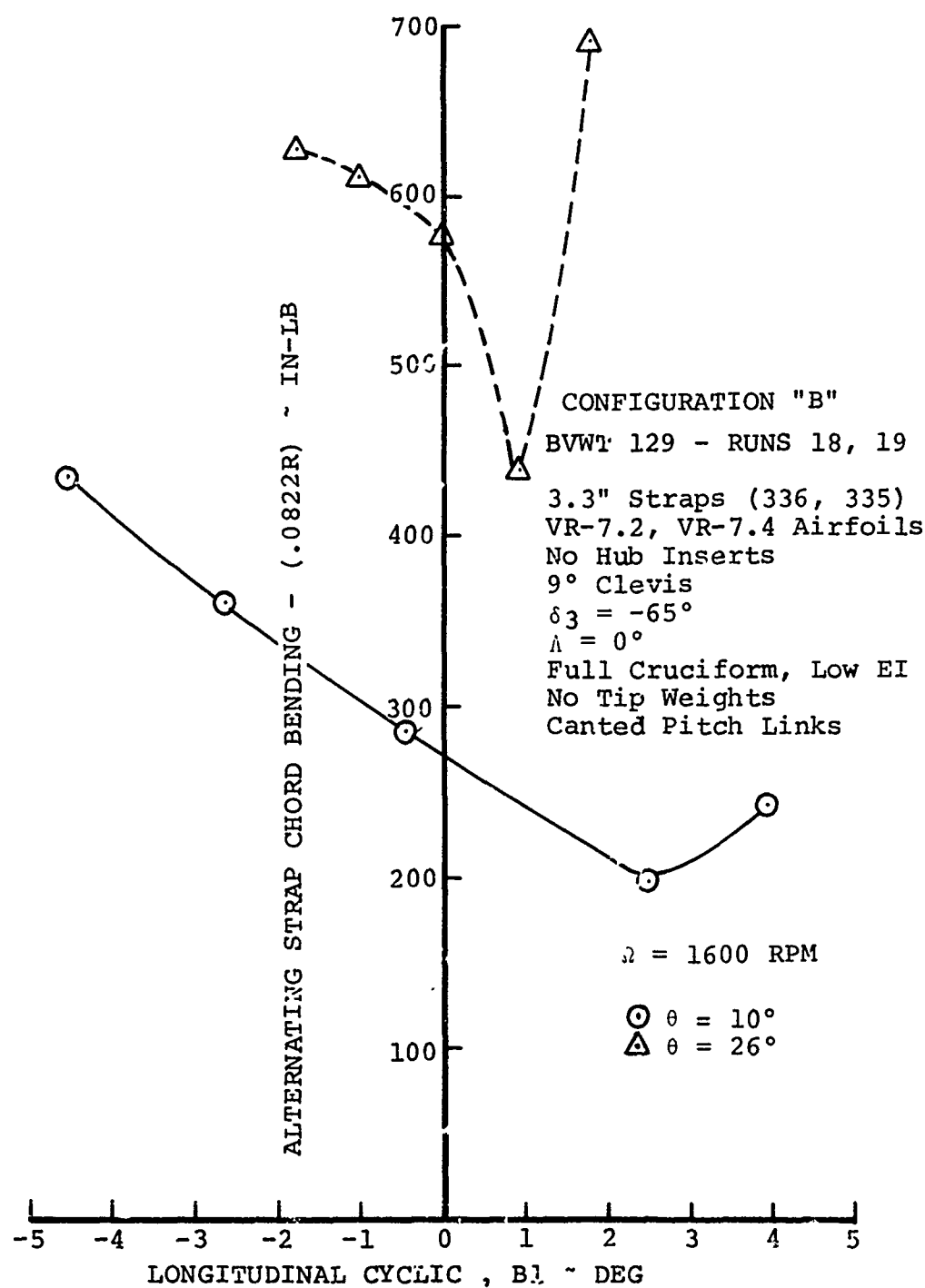
FIGURE 110   EFFECT OF COLLECTIVE ON CHORD BENDING LOADS
FOR A CYCLIC SWEEP IN HOVER

179
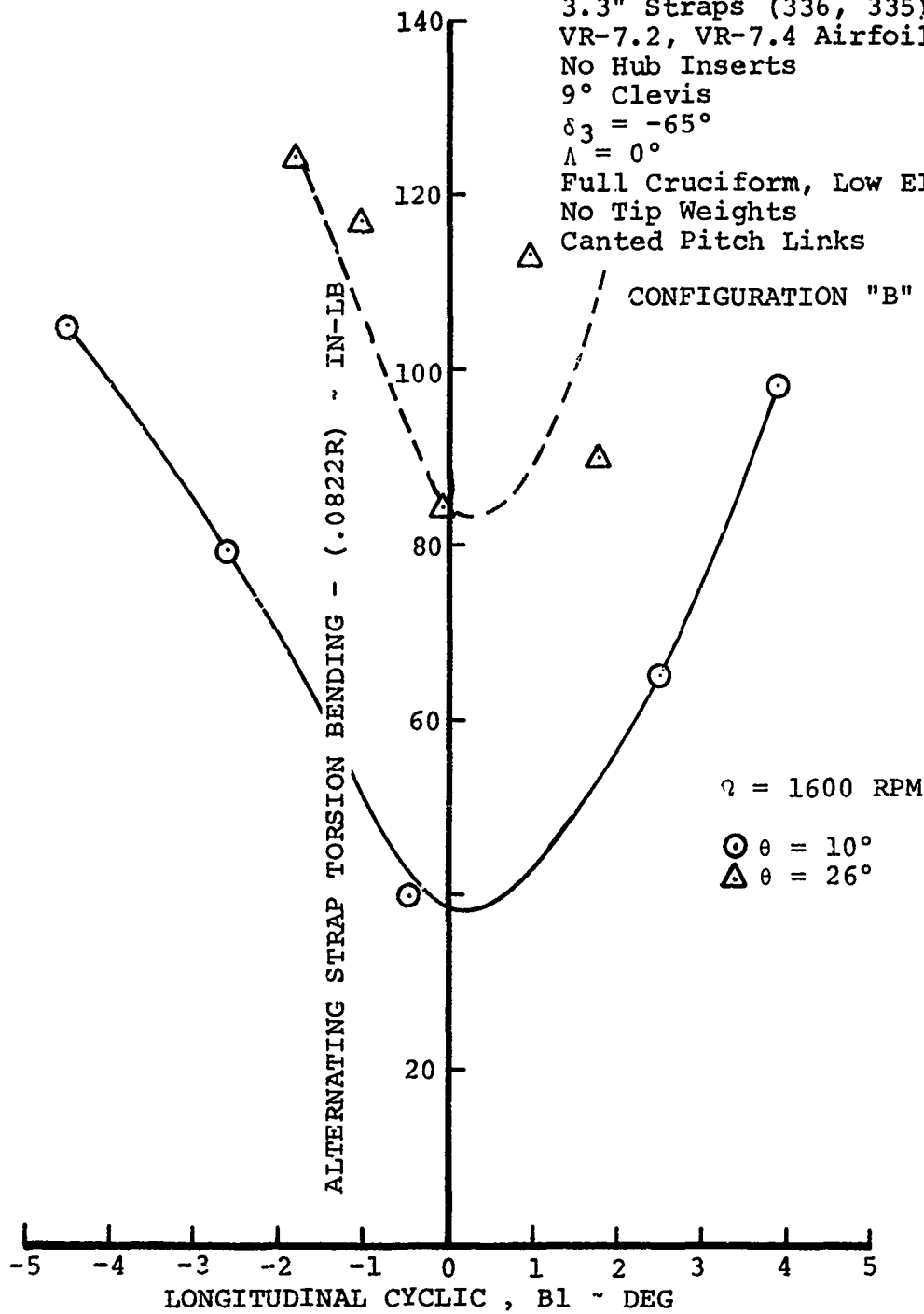
FIGURE 111   EFFECT OF COLLECTIVE ON TORSION BENDING LOADS
FOR A CYCLIC SWEEP IN HOVER
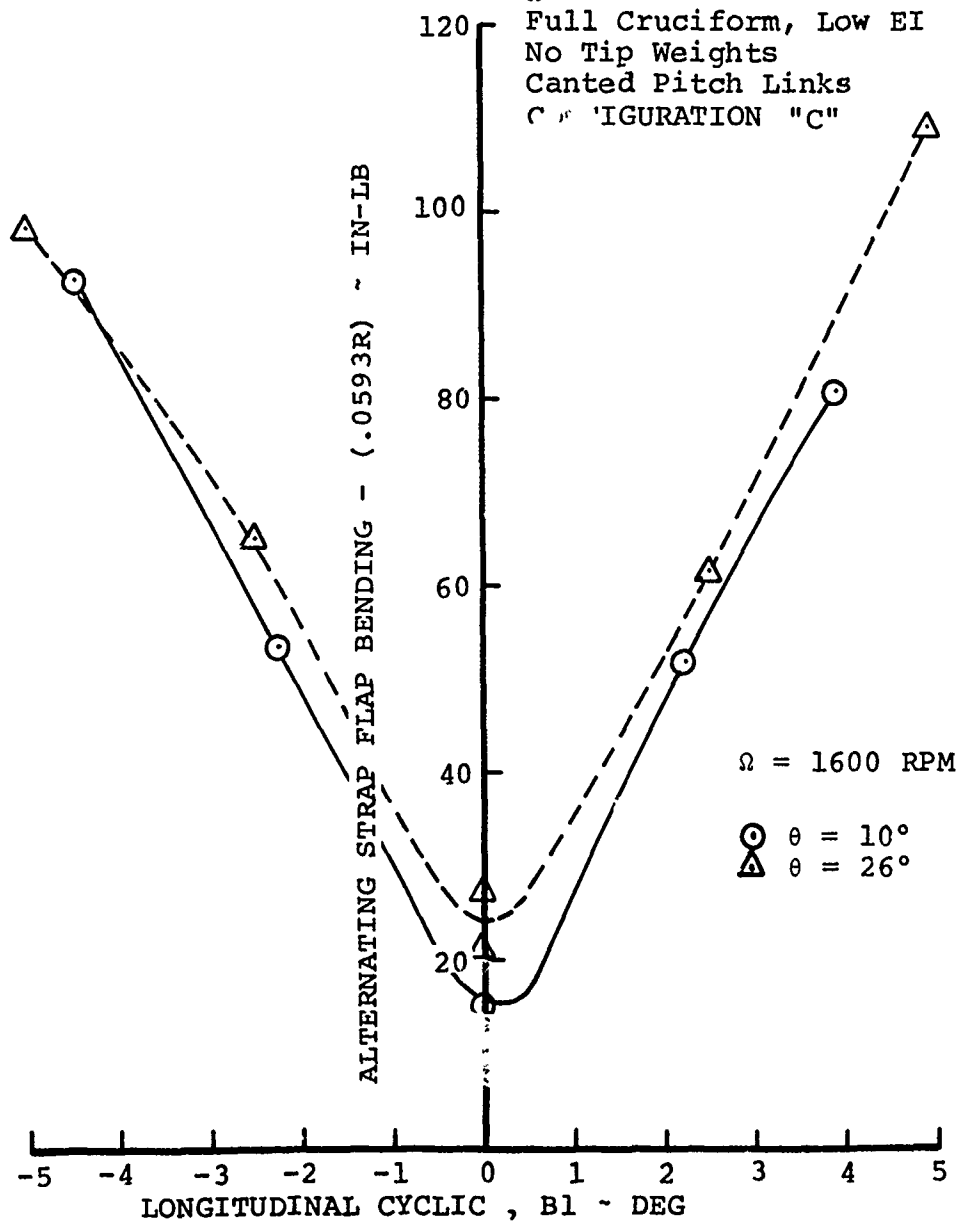
FIGURE 112 EFFECT OF COLLECTIVE ON FLAP BENDING LOADS
FOR A CYCLIC SWEEP IN HOVER

181

CONFIGURATION "C"

BVWT 129 - RUNS 21, 22

3.3" Straps (336, 335)
VR-7.2, VR-7.4 Airfoils
No Hub Inserts
9° Clevis
$\delta_3 = -65°$
$\Lambda = 11°$
Full Cruciform, Low EI
No Tip Weights
Canted Pitch Links

$\Omega = 1600$ RPM

$\odot$ $\theta = 10°$
$\triangle$ $\theta = 26°$

ALTERNATING STRAP CHORD BENDING - (.0822R) ~ IN-LB

LONGITUDINAL CYCLIC , B1 ~ DEG

FIGURE 113   EFFECT OF COLLECTIVE ON CHORD BENDING LOADS
FOR A CYCLIC SWEEP IN HOVER

CONFIGURATION "C"

BVWT 129 - RUNS 21, 22

3.3" Straps (336, 335)
VR-7.2, VR-7.4 Airfoils
No Hub Inserts
9° Clevis
$\delta 3 = -65°$
$\Lambda = 11°$
Full Cruciform, Low EI
No Tip Weights
Canted Pitch Links

$\Omega = 1600$ RPM

$\odot$ $\theta = 10°$
$\triangle$ $\theta = 26°$

ALTERNATING STRAP TORSION BENDING - (.0822R) ~ IN-LB

LONGITUDINAL CYCLIC , B1 ~ DEG
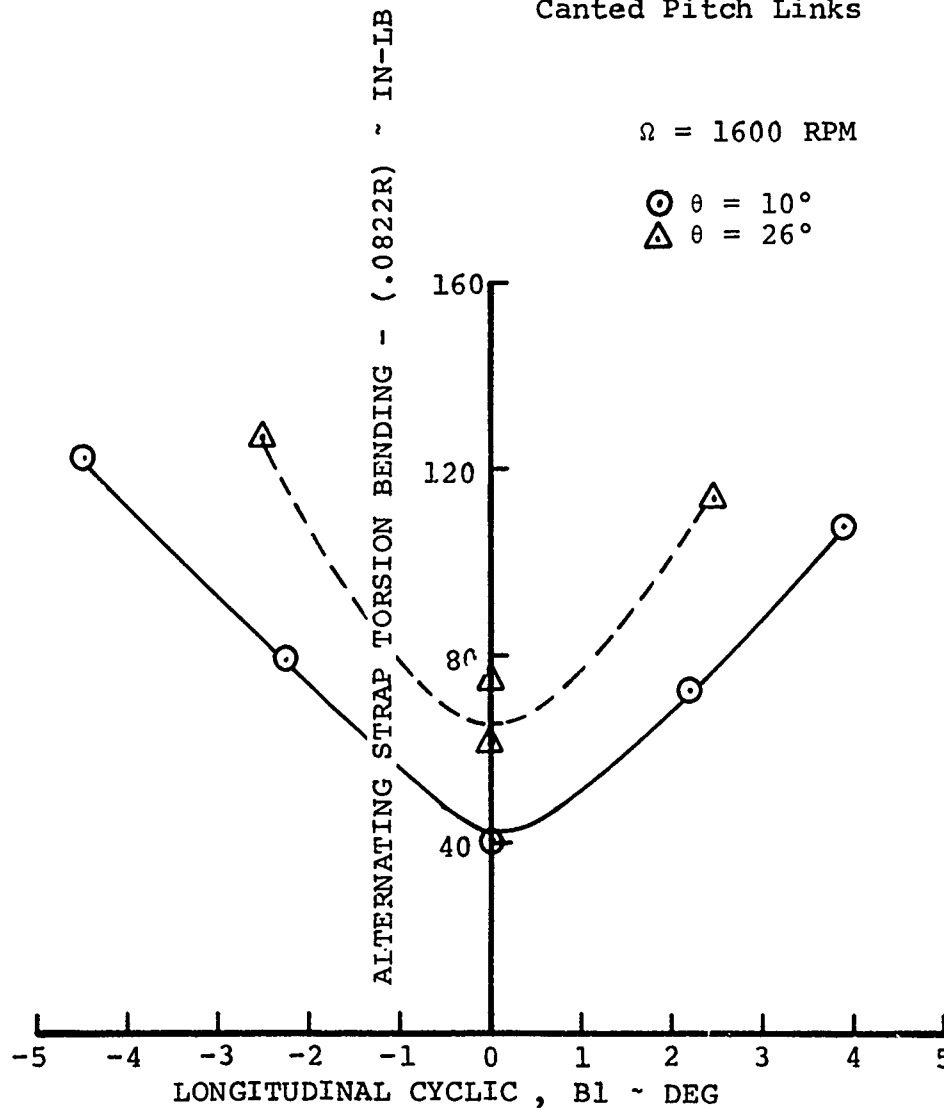
FIGURE 114   EFFECT OF COLLECTIVE ON TORSION BENDING LOADS
FOR A CYCLIC SWEEP IN HOVER

183

BVWT 129 – RUN 47

4.4" Straps (337, 338)
VR-7.2, VR-7.4 Airfoils
Elastomeric Hub Inserts
 K_ζ = 350,000 In-Lb/Rad
9° Clevis
δ_3 = -65°
Λ = 11°
Full Cruciform, Low EI
No Tip Weights
Radial Pitch Links

CONFIGURATION "D"

θ = 12.5°

◇ 1400 RPM
◁ 1670 RPM
◁ 1900 RPM
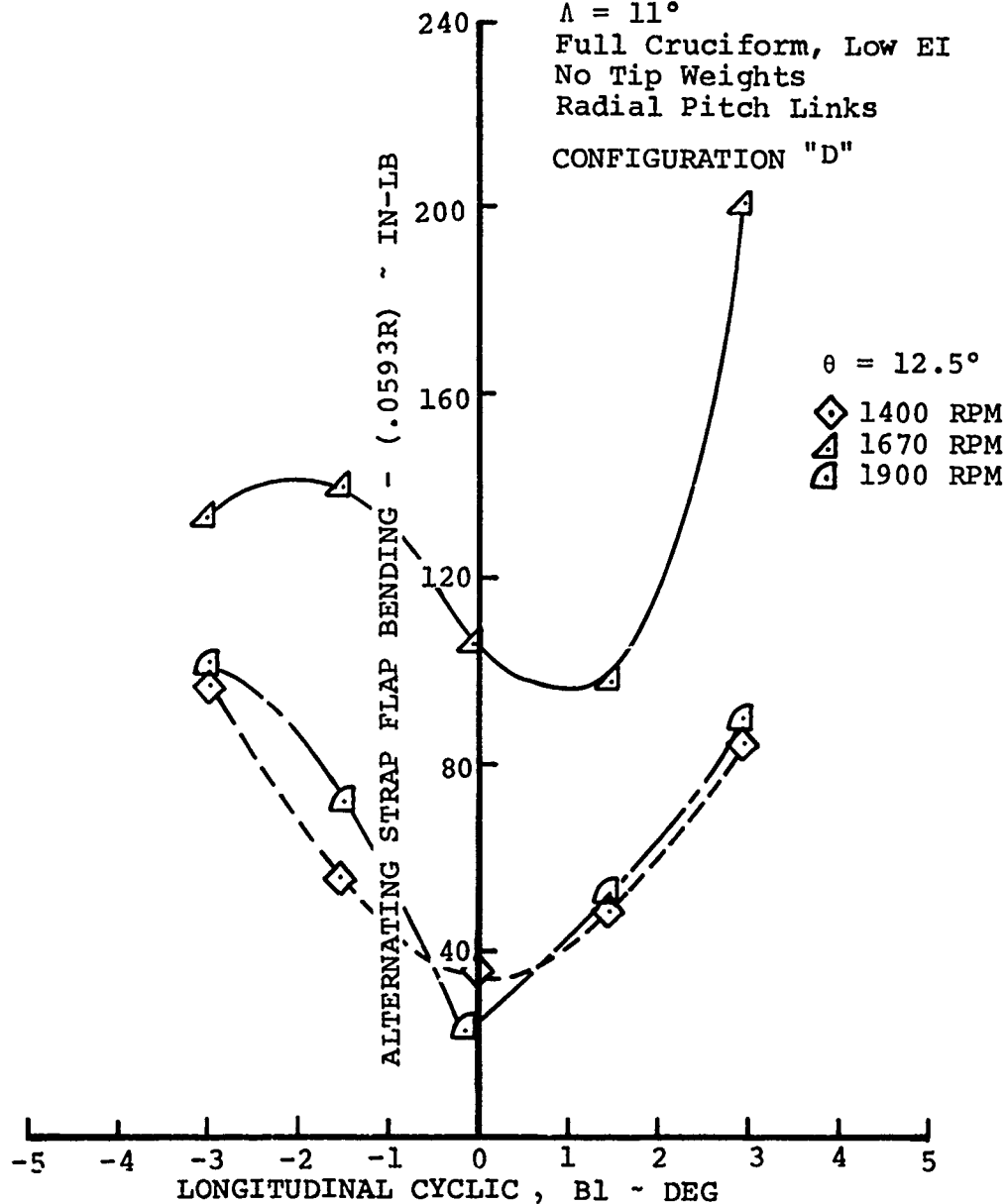
FIGURE 115   EFFECT OF R.M AT 12.5° COLLECTIVE ON FLAP
BENDING LOADS FOR A CYCLIC SWEEP IN HOVER

184

CONFIGURATION "D"

BVWT 129 - RUN 47

4.4" Straps (337, 338)
VR-7.2, VR-7.4 Airfoils
Elastomeric Hub Inserts
  K_ζ = 350,000 In-Lb/Rad
9° Clevis
δ_3 = -65°
Λ = 11°
Full Cruciform, Low EI
No Tip Weights
Radial Pitch Links

θ = 12.5°

◇ 1400 RPM
◁ 1670 RPM
◁ 1900 RPM

FIGURE 116   EFFECT OF RPM AT 12.5° COLLECTIVE ON CHORD
BENDING LOADS FOR A CYCLIC SWEEP IN HOVER

185

CONFIGURATION "D"

BVWT 129 - RUN 47

4.4" Straps (337, 338)
VR-7.2, VR-7.4 Airfoils
Elastomeric Hub Inserts
  K_ζ = 350,000 In-Lb/Rad
9° Clevis
δ_3 = -65°
Λ = 11°
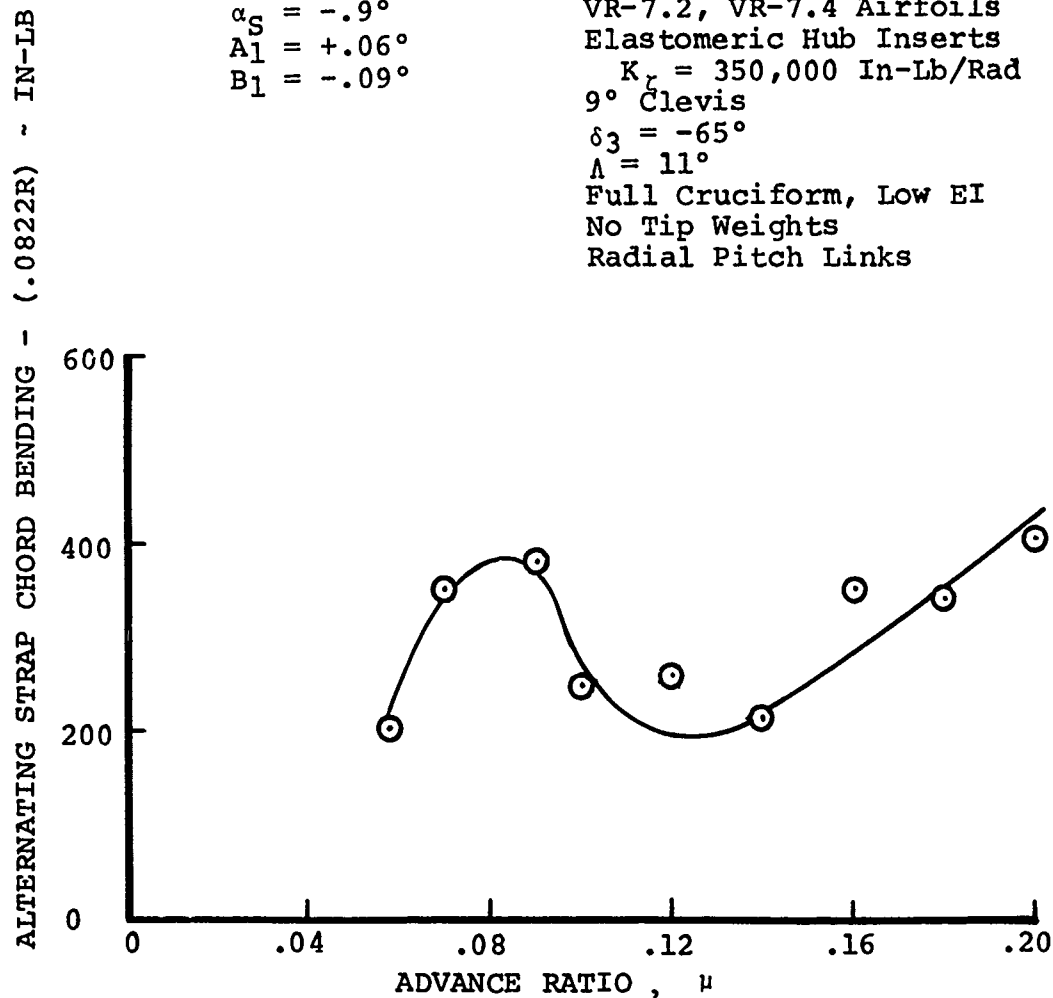Full Cruciform, Low EI
No Tip Weights
Radial Pitch Links

θ = 12.5°
◇ 1400 RPM
△ 1670 RPM
◁ 1900 RPM

FIGURE 117   EFFECT OF RPM AT 12.5° COLLECTIVE ON TORSION
BENDING LOADS FOR A CYCLIC SWEEP IN HOVER

186
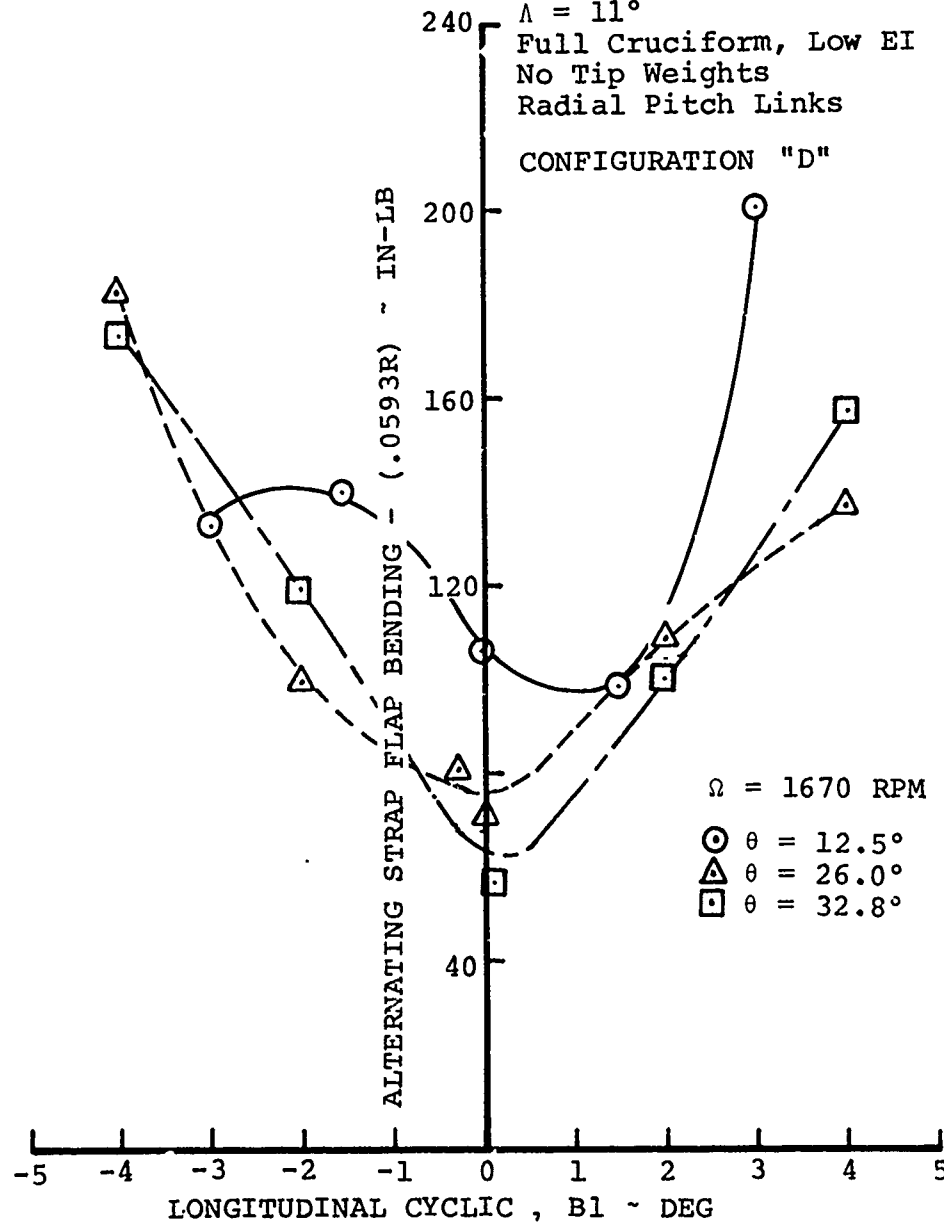
FIGURE 118   EFFECT OF COLLECTIVE ON FLAP BENDING LOADS
FOR A CYCLIC SWEEP IN HOVER

127

BVWT 129 - RUN 47

4.4" Straps (337, 338)
VR-7.2, VR-7.4 Airfoils
Elastomeric Hub Inserts
 K_ζ = 350,000 In-Lb/Rad
9° Clevis
δ_3 = -65°
Λ = 11°
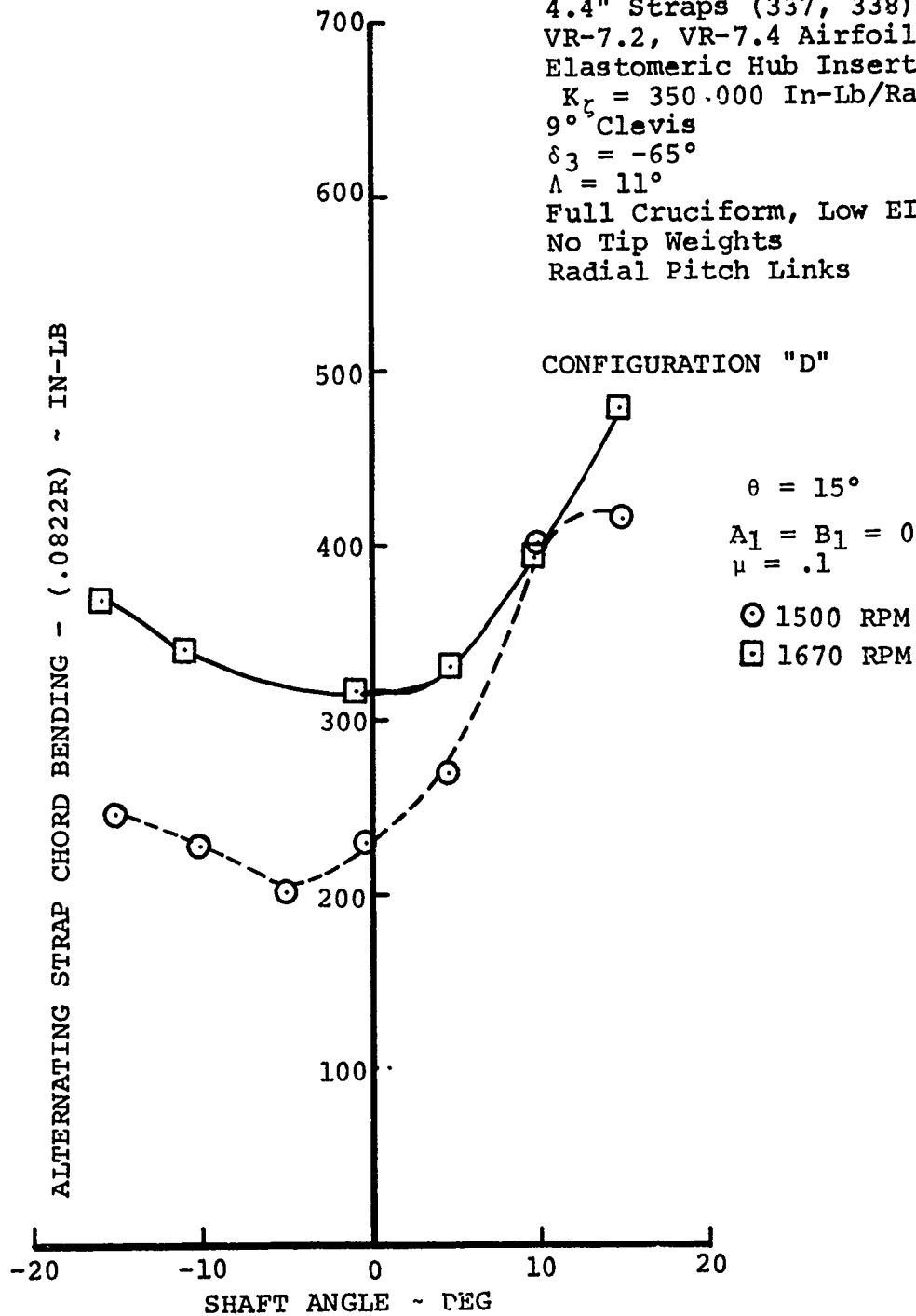Full Cruciform, Low EI
No Tip Weights
Radial Pitch Links

CONFIGURATION "D"

Ω = 1670 RPM

⊙ θ = 12.5°
△ θ = 26.0°
⊡ θ = 32.8°
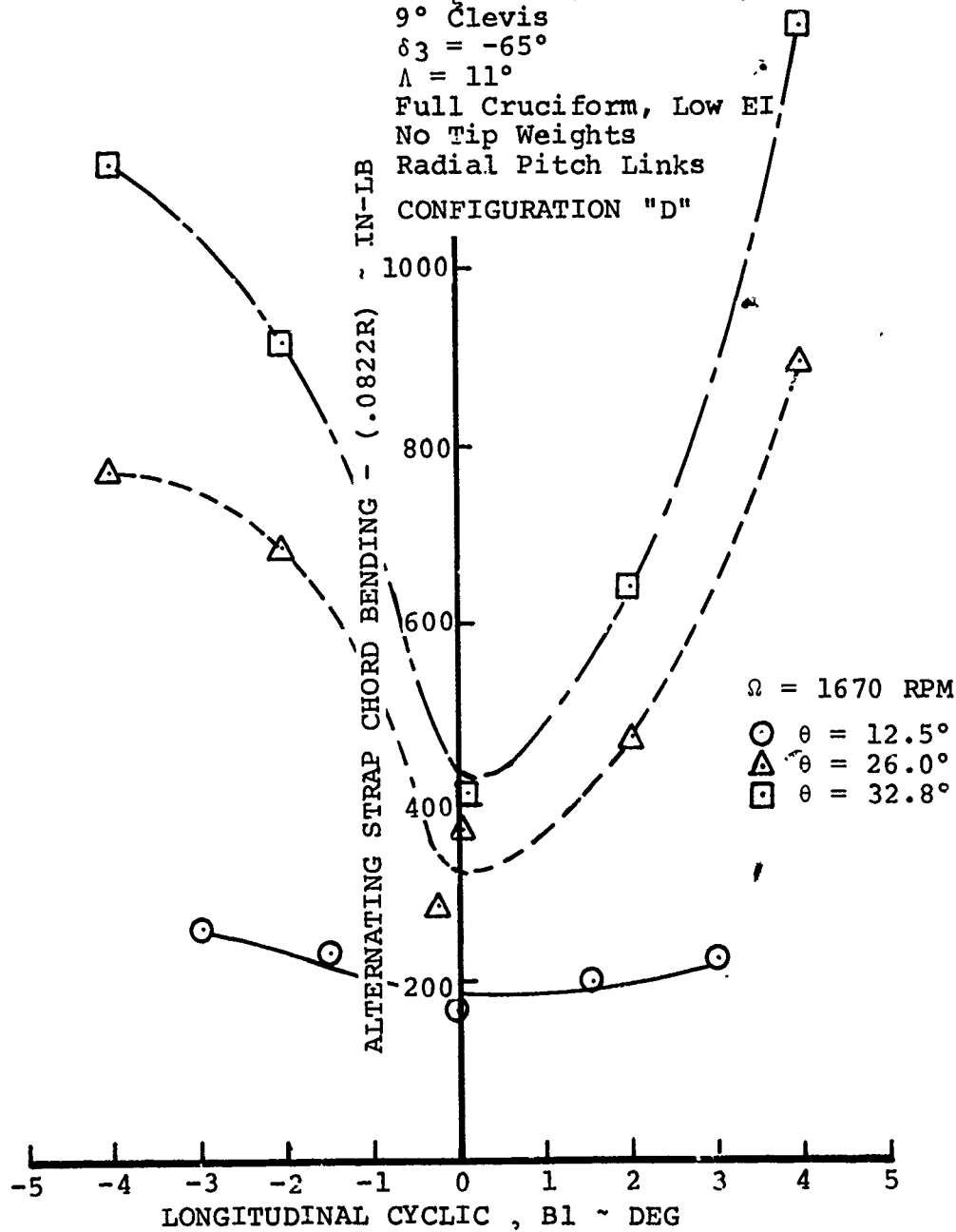
FIGURE 119   EFFECT OF COLLECTIVE ON CHORD BENDING LOADS
FOR A CYCLIC SWEEP IN HOVER

188

FIGURE 120   EFFECT OF COLLECTIVE ON TORSION BENDING LOADS
FOR A CYCLIC SWEEP IN HOVER

189

FIGURE 121   EFFECT OF COLLECTIVE ON CHORD BENDING LOADS
FOR A CYCLIC SWEEP IN HOVER

FIGURE 122   EFFECT OF COLLECTIVE ON TORSION BENDING LOADS
FOR A CYCLIC SWEEP IN HOVER

191

BVWT 129 - RUN 49

4.4" Straps (337, 338)
VR-7.2, VR-7.4 Airfoils
Elastomeric Hub Inserts
K_ζ = 350,000 In-Lb/Rad
9° Clevis
δ_3 = -65°
Λ = 11°
Full Cruciform, Low EI
No Tip Weights
Radial Pitch Links
CONFIGURATION "D"

Ω = 1670 RPM

α_{SHAFT} = +5°

☐ μ = .1
◁ μ = .2
◇ μ = .3
◈ μ = .37
△ μ = .4
◮ μ = .45

FIGURE 123 EFFECT OF ADVANCE RATIO ON FLAP BENDING LOADS
FOR δ_3 = -65°

192

CONFIGURATION "D"
BVWT 129 - RUN 49

4.4" Straps (337, 338)
VR-7.2, VR-7.4 Airfoils
Elastomeric Hub Inserts
 K_ζ = 350,000 In-Lb/Rad
9° Clevis
δ_3 =,-65°
Λ = 11°
Full Cruciform, Low EI
No Tip Weights
Radial Pitch Links

Ω = 1670 RPM
αSHAFT = +5°

$\square$ μ = .1
$\triangleleft$ μ = .2
$\Diamond$ μ = .3
$\pentagon$ μ = .37
$\triangle$ μ = .4
$\triangleleft$ μ = .45

FIGURE 124 EFFECT OF ADVANCE RATIO ON CHORD BENDING LOADS
FOR δ_3 = -65°
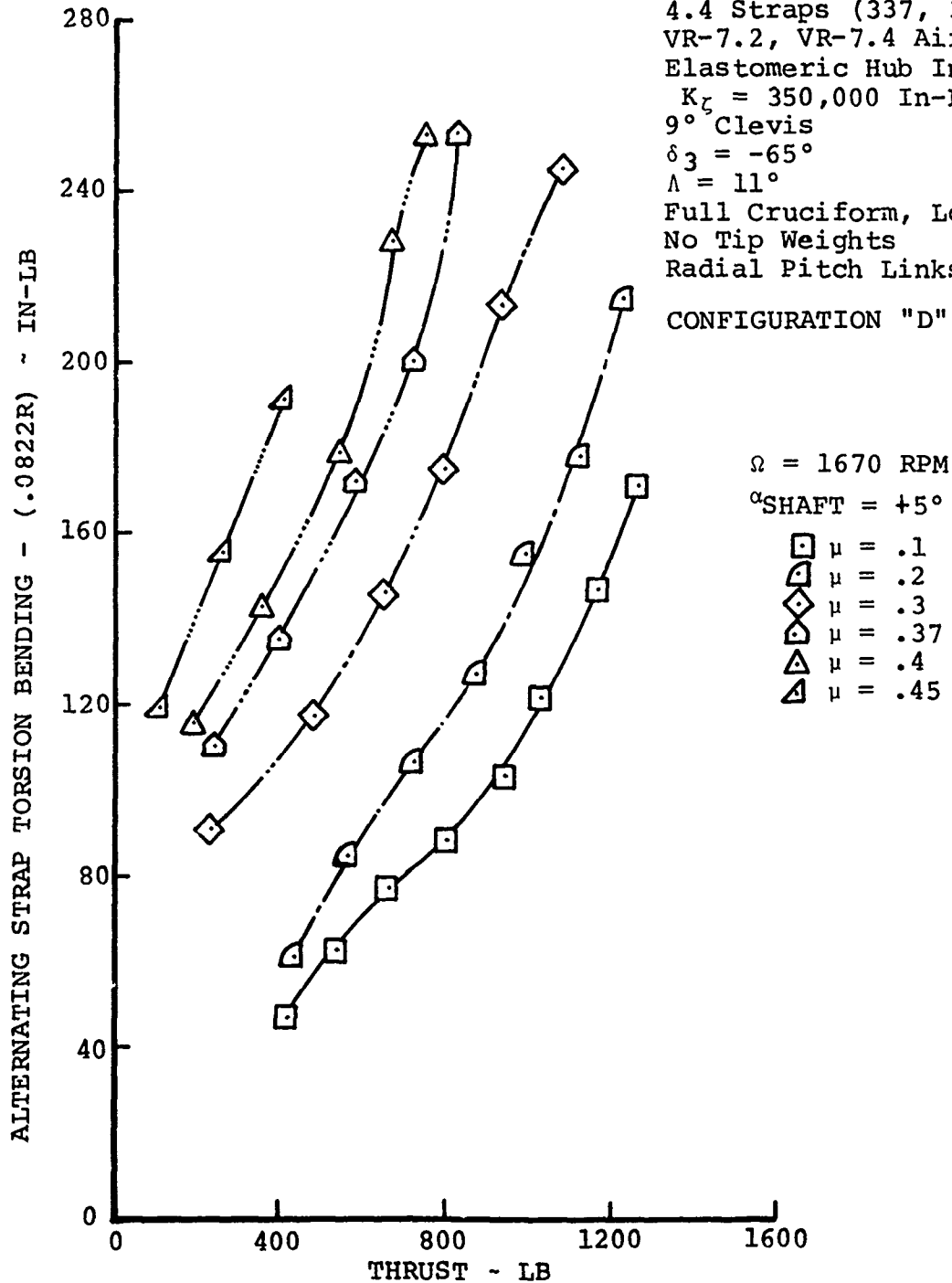
FIGURE 125 EFFECT OF ADVANCE RATIO ON TORSION BENDING LOADS FOR $\delta_3 = -65°$

194

BVWT 129 - RUN 50

4.4" Straps (337, 338)
VR-7.2, VR-7.4 Airfoils
Elastomeric Hub Inserts
  K_ζ = 350,000 In-Lb/Rad
9° Clevis
δ_3 = -65°
Λ = 11°
Full Cruciform, Low EI
No Tip Weights
Radial Pitch Links
CONFIGURATION "D"

μ = .4

Ω = 1670 RPM

$\Diamond$ α SHAFT =   0°
$\Diamond$ α SHAFT = -10°
$\Diamond$ α SHAFT = -15°

ALTERNATING STRAP FLAP BENDING - (.0593R) ~ IN-LB

THRUST ~ LB

FIGURE 126   EFFECT OF SHAFT ANGLE ON FLAP BENDING LOADS
IN FORWARD FLIGHT

195

BVWT 129 - RUN 50

4.4" Straps (337, 338)
VR-7.2, VR-7.4 Airfoils
Elastomeric Hub Inserts
K_ζ = 350,000 In-Lb/Rad
9° Clevis
δ_3 = -65°
Λ = 11°
Full Cruciform, Low EI
No Tip Weights
Radial Pitch Links
CONFIGURATION "D"

μ = .4

Ω = 1670 RPM

◇ α SHAFT = 0°
◁ α SHAFT = -10°
⬠ α SHAFT = -15°
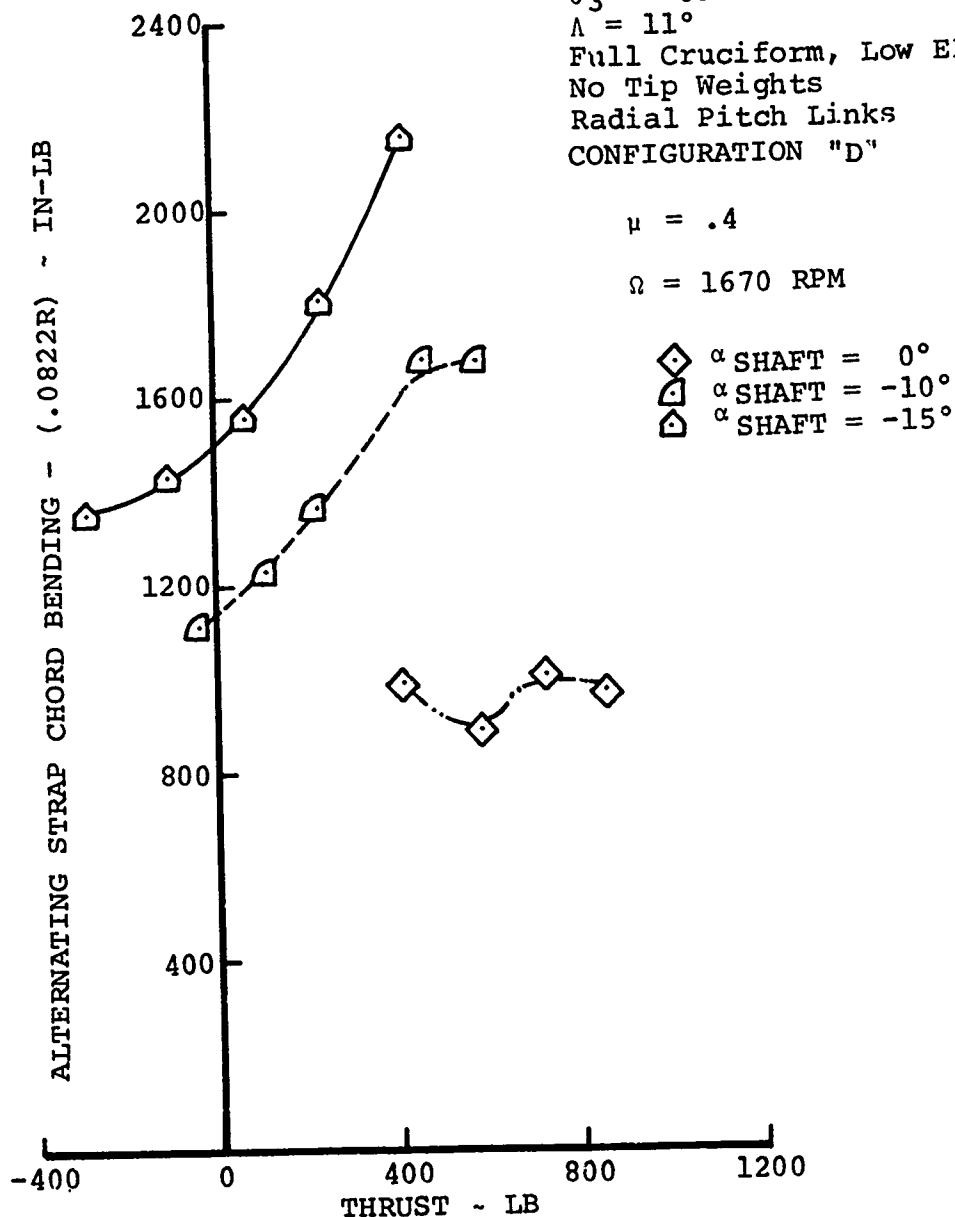
**FIGURE 127   EFFECT OF SHAFT ANGLE ON CHORD BENDING LOADS
IN FORWARD FLIGHT**
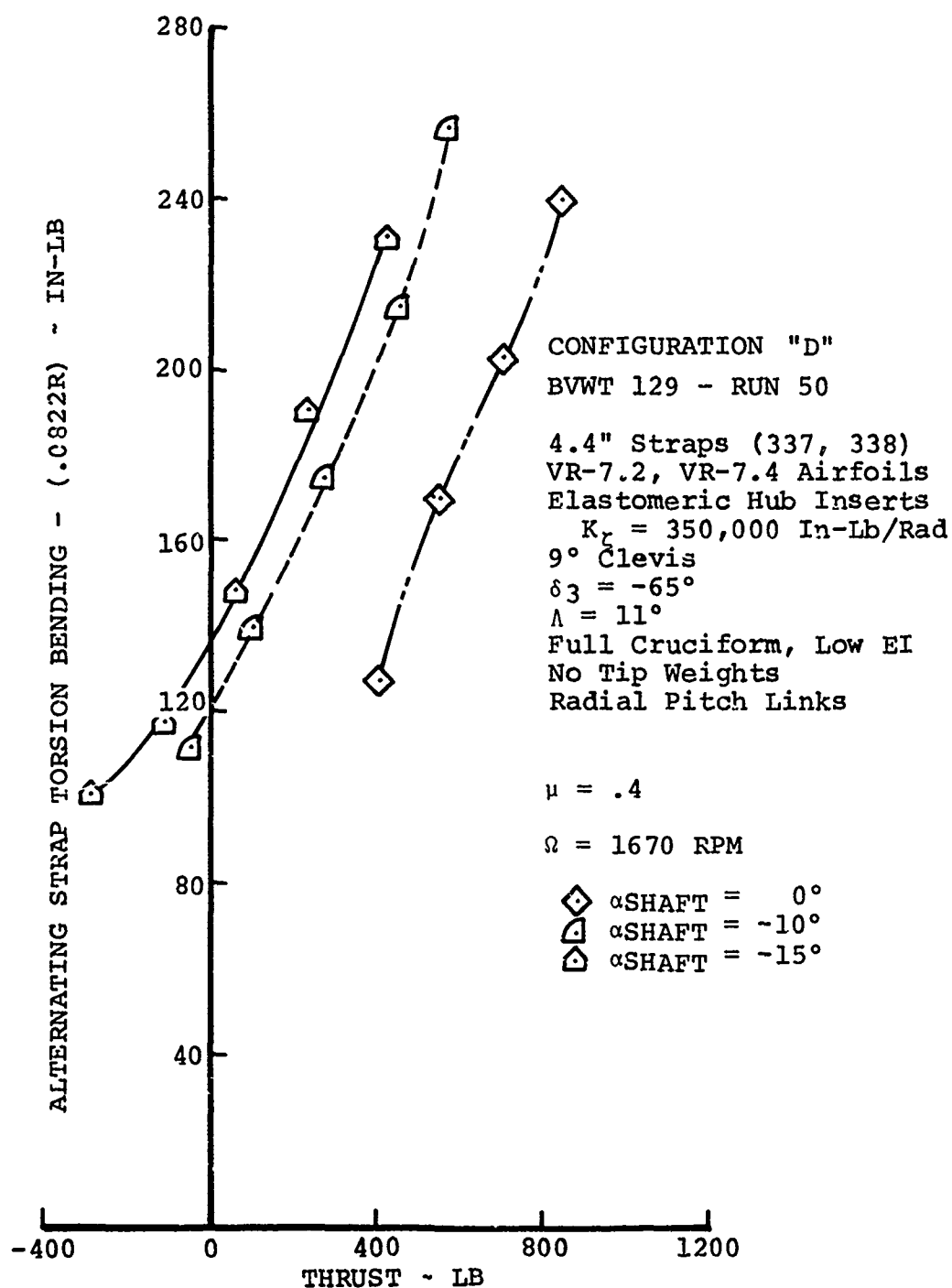
FIGURE 128   **EFFECT OF SHAFT ANGLE ON TORSION BENDING LOADS IN FORWARD FLIGHT**

CONFIGURATION "D"

BVWT 129 - RUN 51

4.4" Straps (337, 338)
VR-7.2, VR-7.4 Airfoils
Elastomeric Hub Inserts
K_ζ = 350,000 In-Lb/Rad
9° Clevis
δ_3 = -65°
Λ = 11°
Full Cruciform, Low EI
No Tip Weights
Radial Pitch Links

Ω = 1670 RPM

μ = .4

☐ α_{SHAFT} = +5°
⊙ α_{SHAFT} = +10°

ALTERNATING STRAP CHORD BENDING - (.0822R) ~ IN-LB

THRUST ~ LB

FIGURE 129   EFFECT OF SHAFT ANGLE ON CHORD BENDING LOADS
IN FORWARD FLIGHT

198
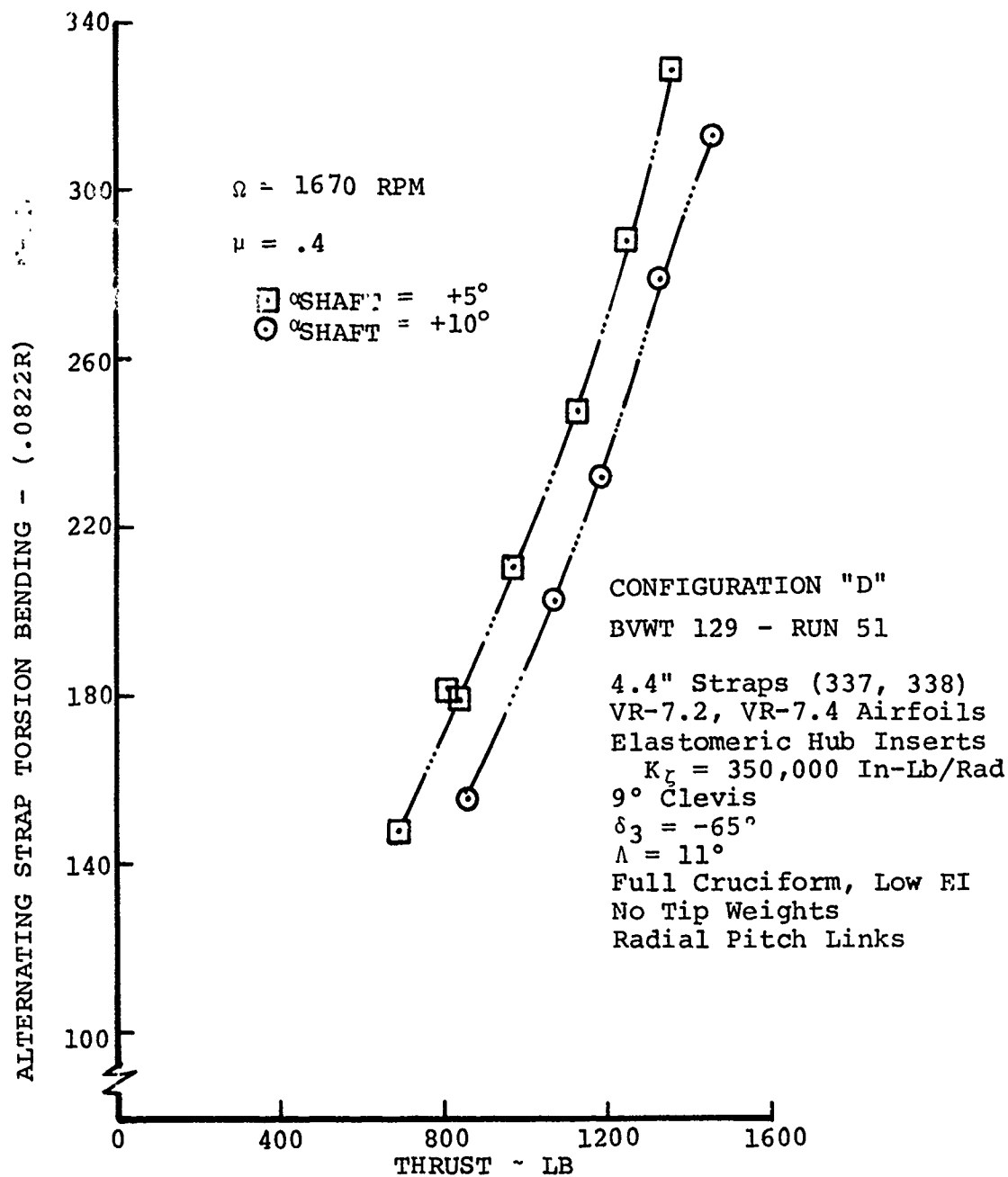
FIGURE 130 EFFECT OF SHAFT ANGLE ON TORSION BENDING LOADS
IN FORWARD FLIGHT

199

μ = .4

Ω = 1670 RPM

αSHAFT = -5°
αSHAFT = 0°
αSHAFT = +5°
αSHAFT = +10°
αSHAFT = +15°

CONFIGURATION "D"

BVWT 129 - RUN 54

4.4" Straps (337, 338)
VR-7.2, VR-7.4 Airfoils
Elastomeric Hub Inserts
K_ζ = 350,000 In-Lb/Rad
9° Clevis
δ_3 = -65°
Λ = 11°
Full Cruciform, Low EI
No Tip Weights
Radial Pitch Links

ALTERNATING STRAP CHORD BENDING - (.0822R) - IN-LB

THRUST - LB
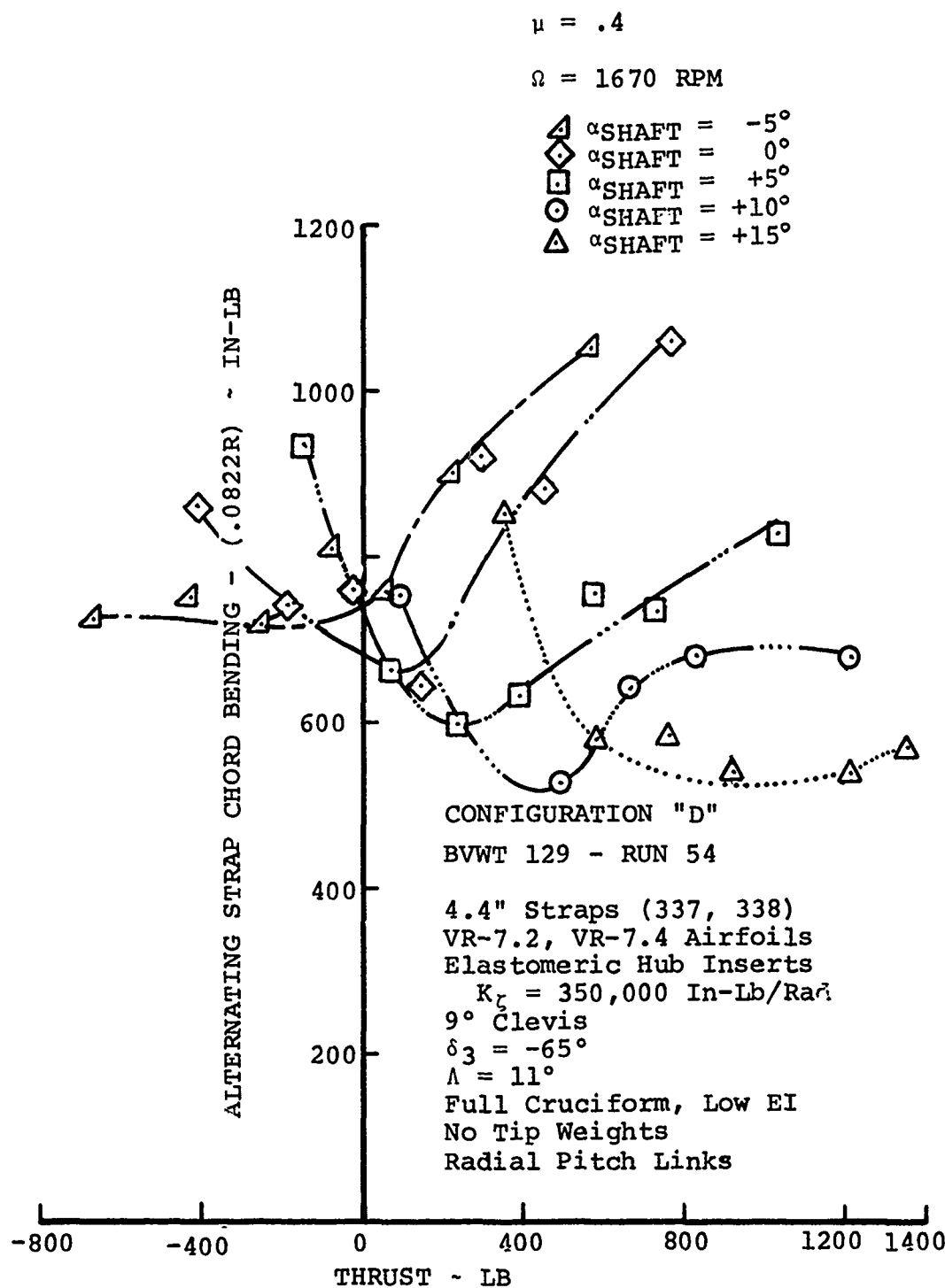
FIGURE 131 EFFECT OF SHAFT ANGLE ON CHORD BENDING LOADS
IN FORWARD FLIGHT

200

FIGURE 132   EFFECT OF SHAFT ANGLE ON TORSION BENDING LOADS
IN FORWARD FLIGHT

CONFIGURATION "E"

BVWT 129 - RUNS 55, 58

$\alpha_{SHAFT} = -5°$
$\Omega = 1670$ RPM

⊙ $\mu = 0$
⊡ $\mu = .1$
◇ $\mu = .3$
△ $\mu = .4$
◁ $\mu = .45$

4.4" Straps (334, 337)
VR-7.2, VR-7.4 Airfoils
Elastomeric Hub Inserts
  $K_\zeta = 350,000$ In-Lb/Rad
9° Clevis
$\delta_3 = -45°$
$\Lambda = 11°$
Full Cruciform, Low EI
No Tip Weights
Radial Pitch Links

FIGURE 133   EFFECT OF ADVANCE RATIO ON FLAP BENDING LOADS
         FOR $\delta_3 = -45°$

202

CONFIGURATION "E"
BVWT 129 - RUNS 55, 58

αSHAFT = -5°
Ω = 1670 RPM

○ μ = 0
□ μ = .1
◇ μ = .3
△ μ = .4
◁ μ = .45

4.4" Straps (334, 337)
VR-7.2, VR-7.4 Airfoils
Elastomeric Hub Inserts
  K_ζ = 350,000 In-Lb/Rad
9° Clevis
δ_3 = -45°
Λ = 11°
Full Cruciform, Low EI
No Tip Weights
Radial Pitch Links
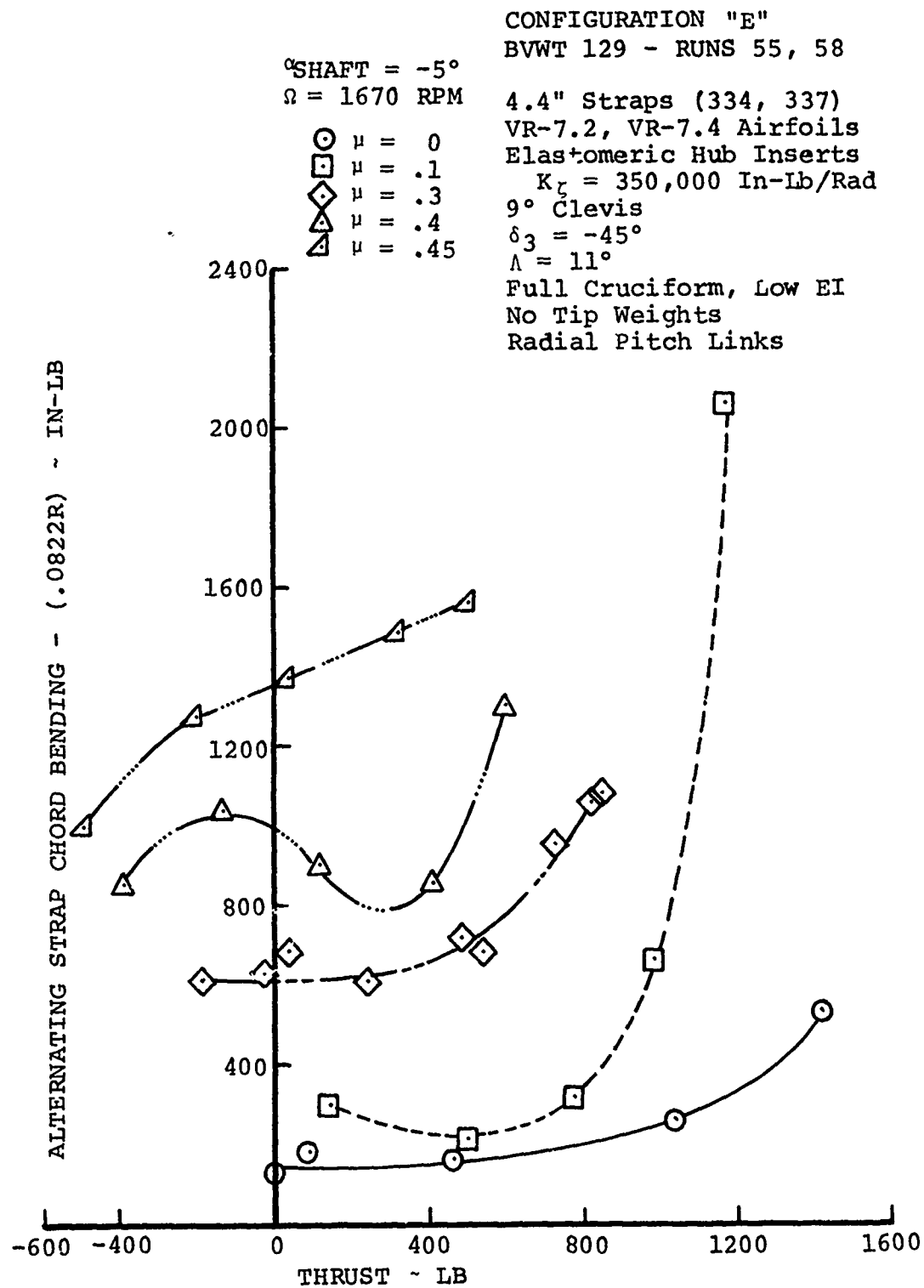
FIGURE 134   EFFECT OF ADVANCE RATIO ON CHORD BENDING LOADS
FOR δ_3 = -45°

203
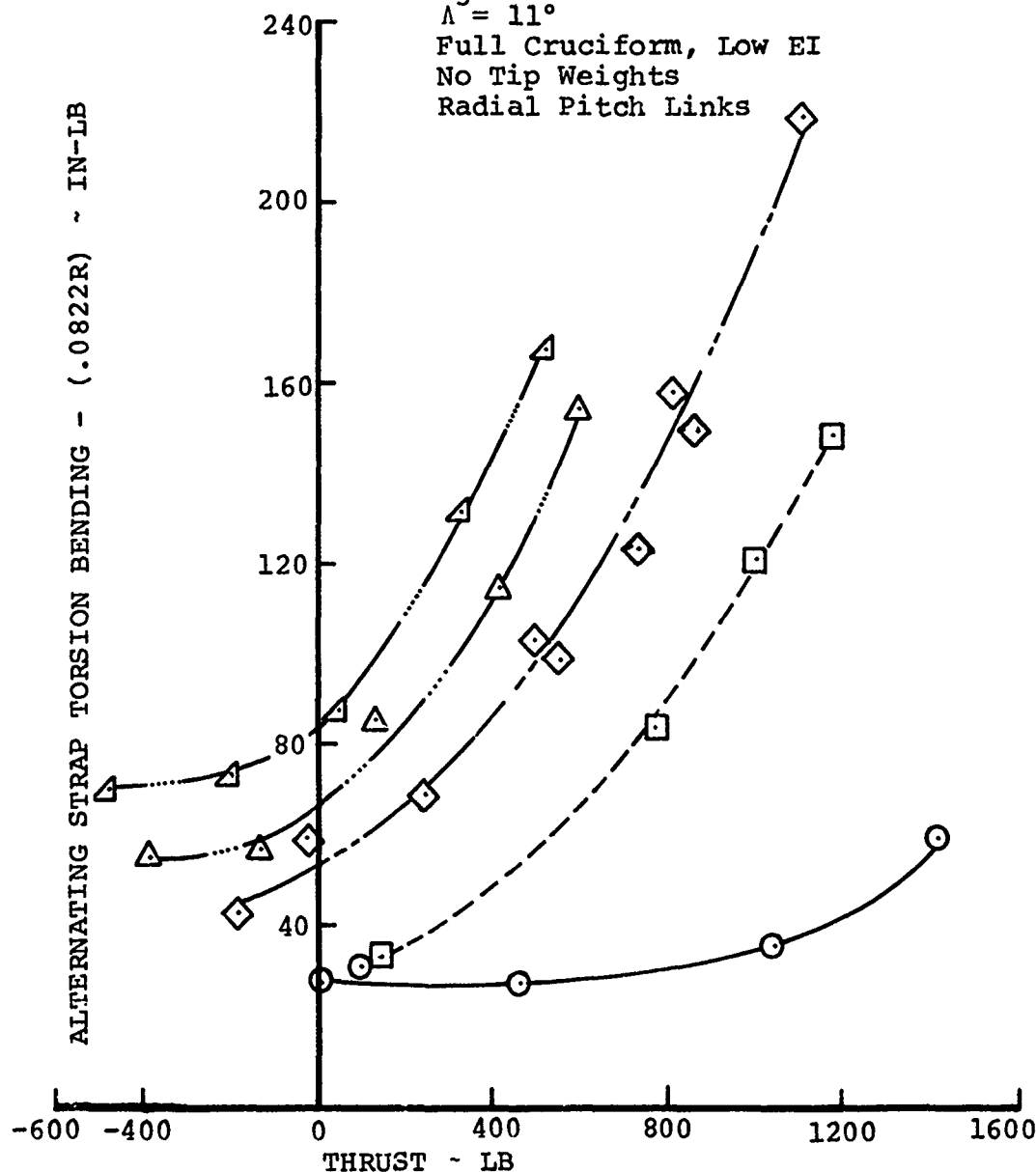
FIGURE 135   EFFECT OF ADVANCE RATIO ON TORSION BENDING
                  LOADS FOR $\delta_3 = -45°$

BVWT 129 - RUN 59

4.4" Straps (334, 337)
VR-7.2, VR-7.4 Airfoils
Elastomeric Hub Inserts
 K = 350,000 In-Lb/Rad
9° Clevis
$\delta_3 = -45°$
$\Lambda^3 = 11°$
Full Cruciform, Low EI
No Tip Weights
Radial Pitch Links

CONFIGURATION "E"

$\mu = .4$

$\Omega = 1670$ RPM

$\alpha_{SHAFT} = - 0.5°$
$\alpha_{SHAFT} = + 9.9°$
$\alpha_{SHAFT} = -16.0°$

ALTERNATING STRAP FLAP BENDING - (.0593R) ~ IN-LB

THRUST ~ LB

FIGURE 136   EFFECT OF SHAFT ANGLE ON FLAP BENDING LOADS
              IN FORWARD FLIGHT

205

BVWT 129 - RUN 59

4.4" Straps (334, 337)
VR-7.2, VR-7.4 Airfoils
Elastomeric Hub Inserts
$K = 350,000$ In-Lb/Rad
9° Clevis
$\delta_3 = -45°$
$\Lambda = 11°$
Full Cruciform, Low EI
No Tip Weights
Radial Pitch Links
CONFIGURATION "E"

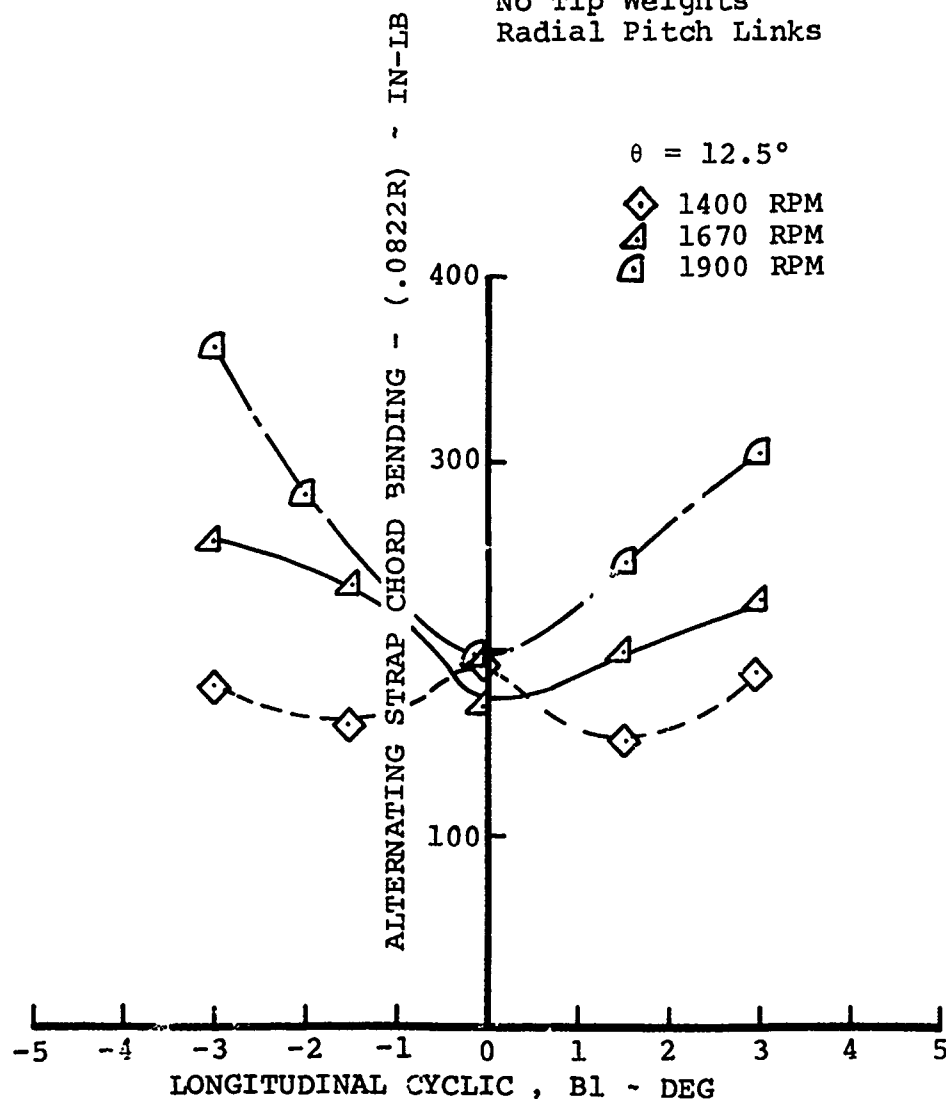$\mu = .4$

$\Omega = 1670$ RPM

⬦ $\alpha_{SHAFT} = -0.5°$
⊙ $\alpha_{SHAFT} = +9.9°$
⬠ $\alpha_{SHAFT} = -16.0°$
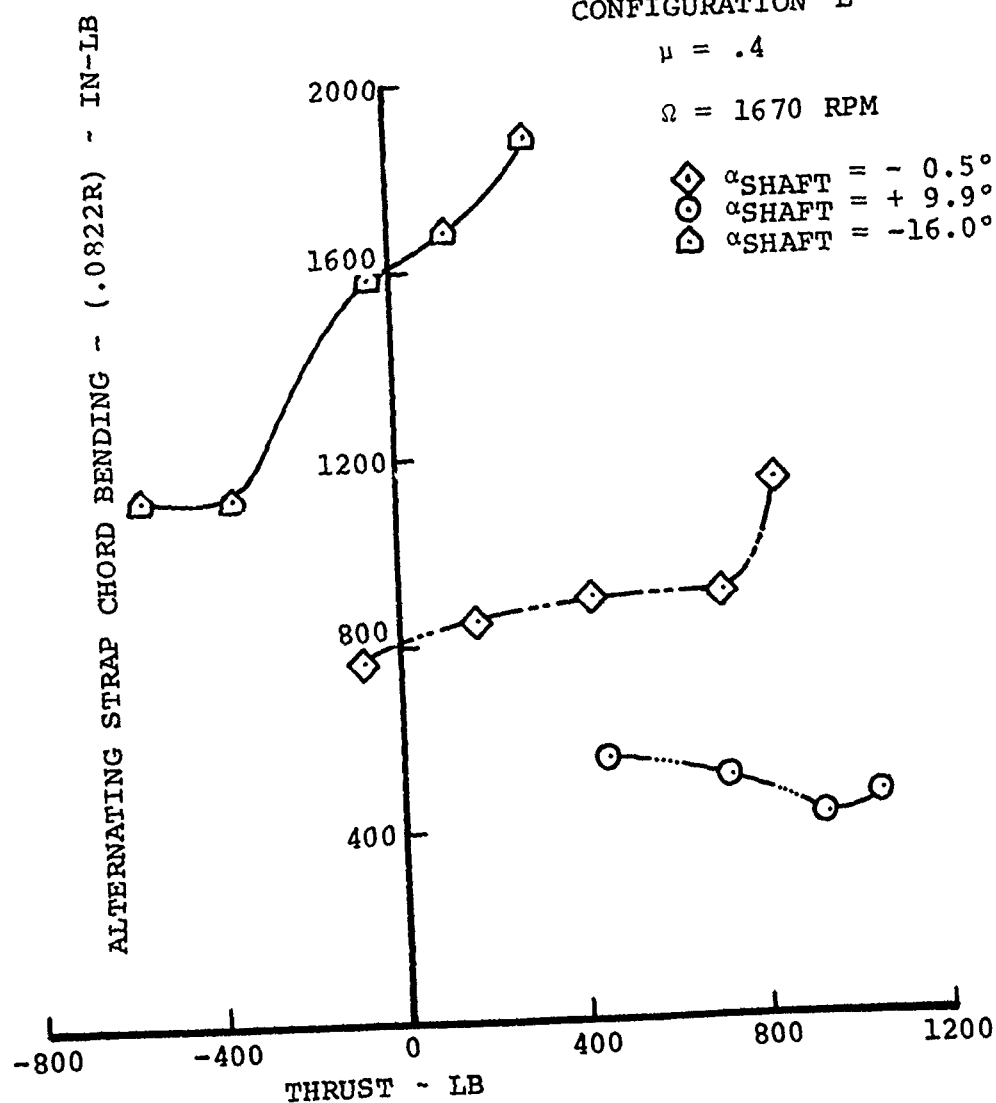
FIGURE 137   EFFECT OF SHAFT ANGLE ON CHORD BENDING LOADS
IN FORWARD FLIGHT

206

BVWT 129 - RUN 59

4.4" Straps (334, 337)
VR-7.2, VR-7.4 Airfoils
Elastomeric Hub Inserts
 K = 350,000 In-Lb/Rad
9° Clevis
δ_3 = -45°
Λ = 11°
Full Cruciform, Low EI
No Tip Weights
Radial Pitch Links

CONFIGURATION ' "

μ =.4

Ω = 1670 RPM

$\diamondsuit$ α_{SHAFT} = - 0.5°
$\odot$ α_{SHAFT} = + 9.9°
$\varhexagon$ α_{SHAFT} = ~16.0°

ALTERNATING STRAP TORSION BENDING - (.0822R) ~ IN-LB
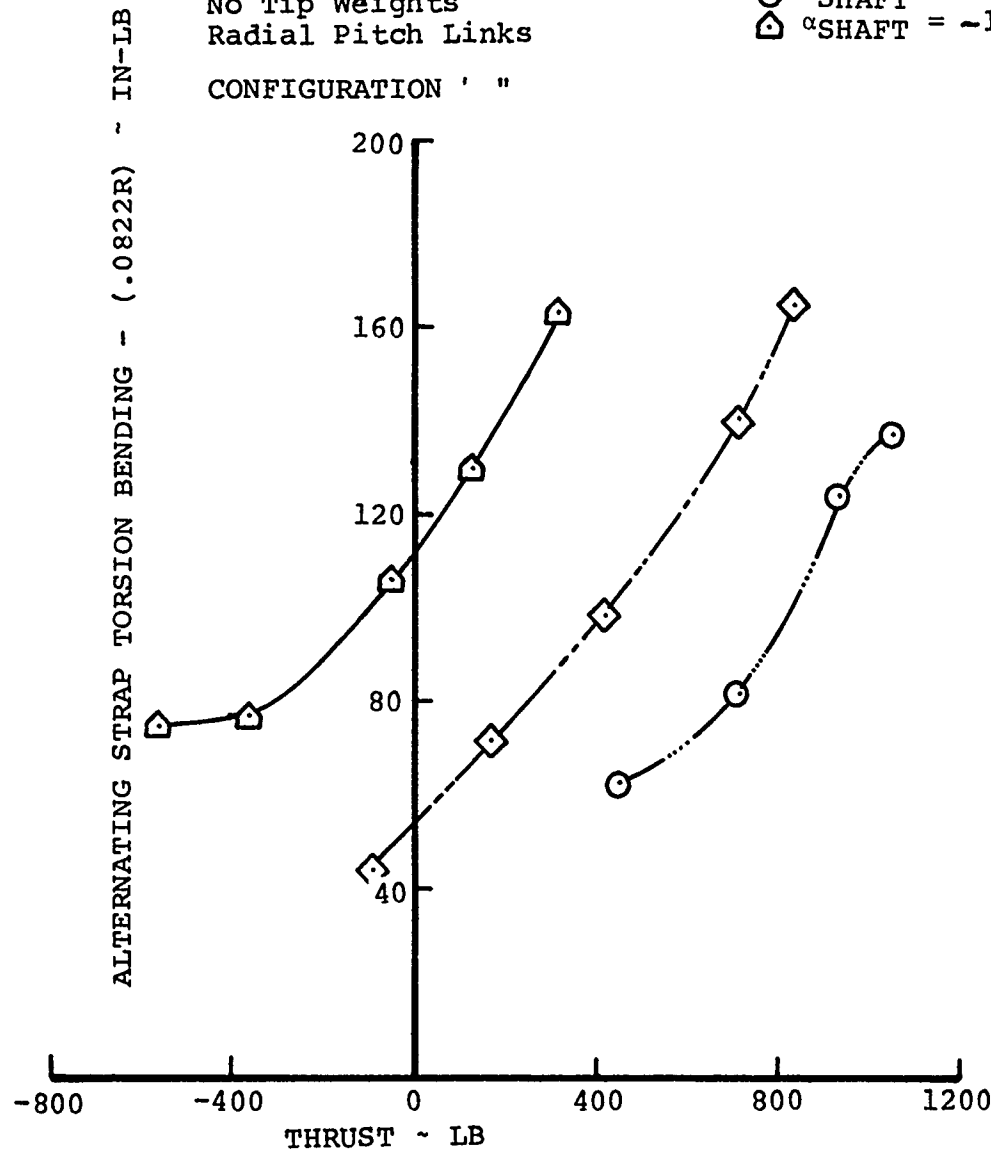
THRUST ~ LB

FIGURE 138   EFFECT OF SHAFT ANGLE ON TORSION BENDING LOADS
IN FORWARD FLIGHT

advance ratio and shaft sweep on the harmonic loads. All of
the loads are plotted versus rotor thrust. Four plots are pre-
sented for each strap bending gage, one for each harmonic load.
For each set of strap bending data, it is presented in the
sequence of flap bending, chord bending, and torsion bending.

The following test runs represent all of the harmonic data
available at this time:

- Data runs 55, 58 (configuration "E") - loads
  for various advance ratios, Figures 139 to 150

- Data run 54 (configuration "D") - loads for
  various shaft angles, Figures 151 to 158

- Data run 49 (configuration "D") - loads for
  various advance ratios, Figures 159 to 170

6.2.2 Discussion

The data that appears in Section 6.2.1 is organized in such a
manner that many loads comparisons between test parameters may
be readily accomplished. In particular, it is interesting to
compare blade sweep and delta-three which have a significant
effect on rotor stability.

In Section 5.2.4, it was shown from test data that an increase
in aft blade sweep increased rotor stability, thus raising the
collective pitch (or C_p/σ) at which the neutral stability bound-
ary was reached. A direct measurable result of this increased
stability is a reduction in rotor blade natural response and
therefore alternating bending loads in the inplane direction.
This is demonstrated in Figures 110 through 113 considering the
$\theta = 26°$ curves. In the first figure, which shows the variation
of longitudinal cyclic pitch for constant values of C_p/σ for a
blade sweep $\Lambda = 0$ configuration, the magnitude of the loads is
near 550 in-lb. In the second figure, for a configuration with
$\Lambda = 11°$, the alternating chord loads are near 400 in-lb for the
same conditions and over the range of cyclic pitch.

The effect of delta-three coupling on strap loads in forward
flight was measured. Delta three is used specifically to re-
duce forward flight loads by reducing cyclic flapping. Since
this coupling has adverse effects on flap-lag stability, as
shown in Section 5.2.3, a bearingless tail rotor should use no
more delta three than necessary.

Figures 171 and 172 show loads measured in collective sweeps at
several high advance ratios with $\delta_3 = -45°$ and $\delta_3 = -65°$. This
data was obtained at the nominal rotor speed, 1670 rpm. The
data shows that the higher δ_3 reduces flap bending loads on the
order of 50 percent. (The 1/rev flap loads shown in the first

208

figure are almost identical to total alternating flap loads.)
Only flap loads were crucial from the fatigue standpoint. For
the tail rotor model detailed in this report, it was found that
$\delta_3 = -45°$ was inadequate to maintain the loads below the allow-
able limit. Using $\delta_3 = -65°$ brings the loads down into an
acceptable range except of higher thrust levels. The satis-
factory amount of δ_3 coupling incorporated in a particular
bearingless configuration is between a maximum value determined
from stability and a minimum value determined by strap flap
bending loads.

FIGURE 139   EFFECT OF ADVANCE RATIO ON FIRST-HARMONIC
FLAP BENDING LOADS FOR $\delta_3 = -45°$

210

CONFIGURATION "E"

BVWT 129 - RUNS 55, 58

4.4" Straps (334, 337)
VR-7.2, VR-7.4 Airfoils
Elastomeric Hub Inserts
  K_ζ = 350,000 In-Lb/Rad
9° Clevis
δ_3 = -45°
Λ = 11°
Full Cruciform, Low EI
No Tip Weights
Radial Pitch Links

αSHAFT = -5°

Ω = 1670 RPM

⊙ μ = 0
⊡ μ = .1
◇ μ = .3
△ μ = .4
◁ μ = .45

2/REV FLAP BENDING - (.0593R) ~ IN-LB

THRUST ~ LB

FIGURE 140   EFFECT OF ADVANCE RATIO ON SECOND-HARMONIC
FLAP BENDING LOADS FOR δ_3 = -45°

211

CONFIGURATION "E"

BVWT 129 - RUNS 55, 58

4.4" Straps (334, 337)
VR-7.2, VR-7.4 Airfoils
Elastomeric Hub Inserts
  K_ζ = 350,000 In-Lb/Rad
9° Clevis
δ_3 = -45°
Λ = 11°
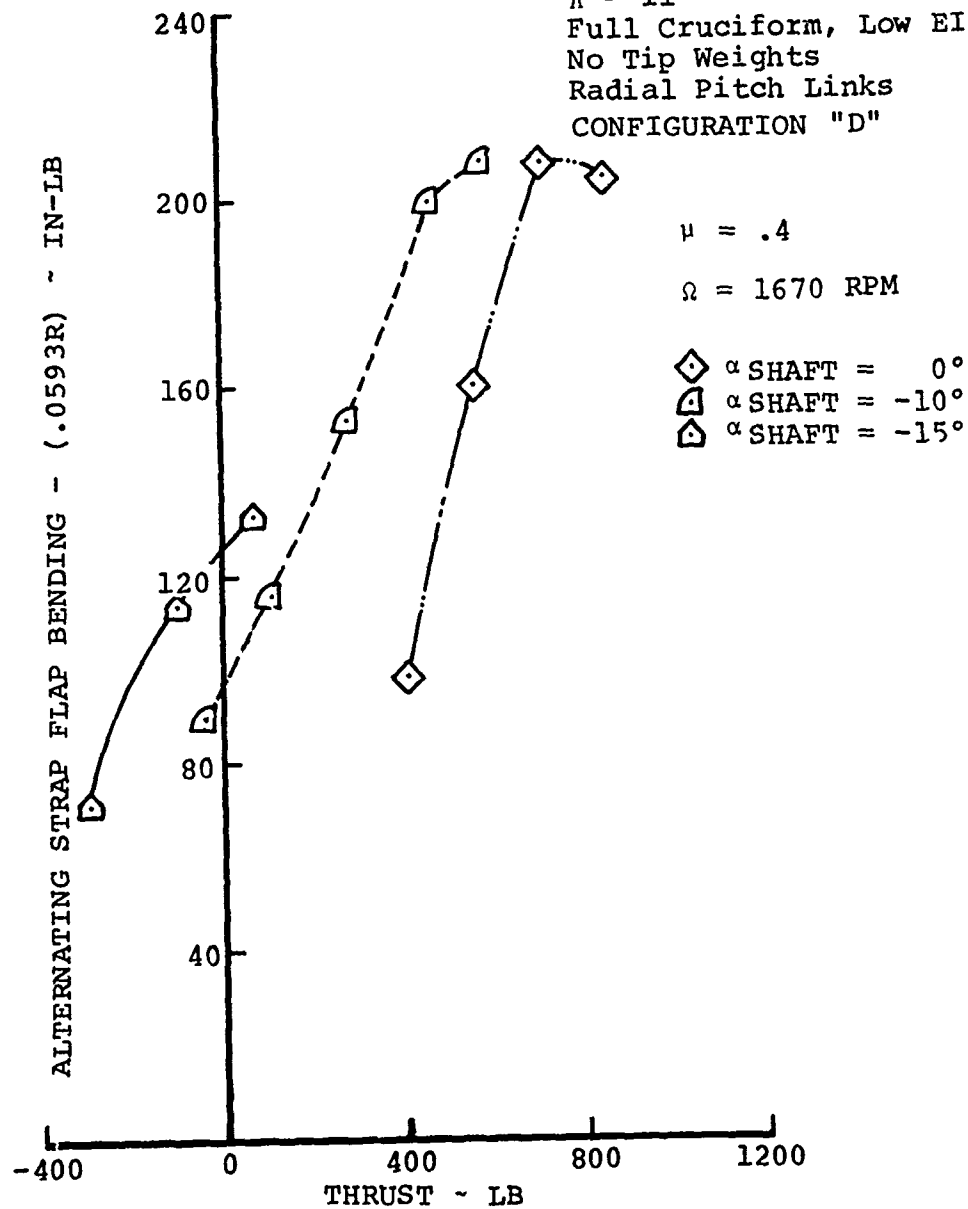Full Cruciform, Low EI
No Tip Weights
Radial Pitch Links

α_{SHAFT} = -5°

Ω = 1670 RPM

⊙ μ = 0
⊡ μ = .1
◇ μ = .3
△ μ = .4
◁ μ = .45

3/REV FLAP BENDING - (.0593R) ~ IN-LB

THRUST ~ LB

FIGURE 141   EFFECT OF ADVANCE RATIO ON THIRD-HARMONIC
FLAP BENDING LOADS FOR δ_3 = -45°

212

CONFIGURATION "E"

BVWT 129 - RUNS 55, 58

4.4" Straps (334, 337)
VR-7.2, VR-7.4 Airfoils
Elastomeric Hub Inserts
$K_\zeta = 350,000$ In-Lb/Rad
9° Clevis
$\delta_3 = -45°$
$\Lambda = 11°$
Full Cruciform, Low EI
No Tip Weights
Radial Pitch Links

$\alpha_{SHAFT} = -5°$

$\Omega = 1670$ RPM

$\mu = 0$
$\mu = .1$
$\mu = .3$
$\mu = .4$
$\mu = .45$

FIGURE 142   EFFECT OF ADVANCE RATIO ON FOURTH-HARMONIC
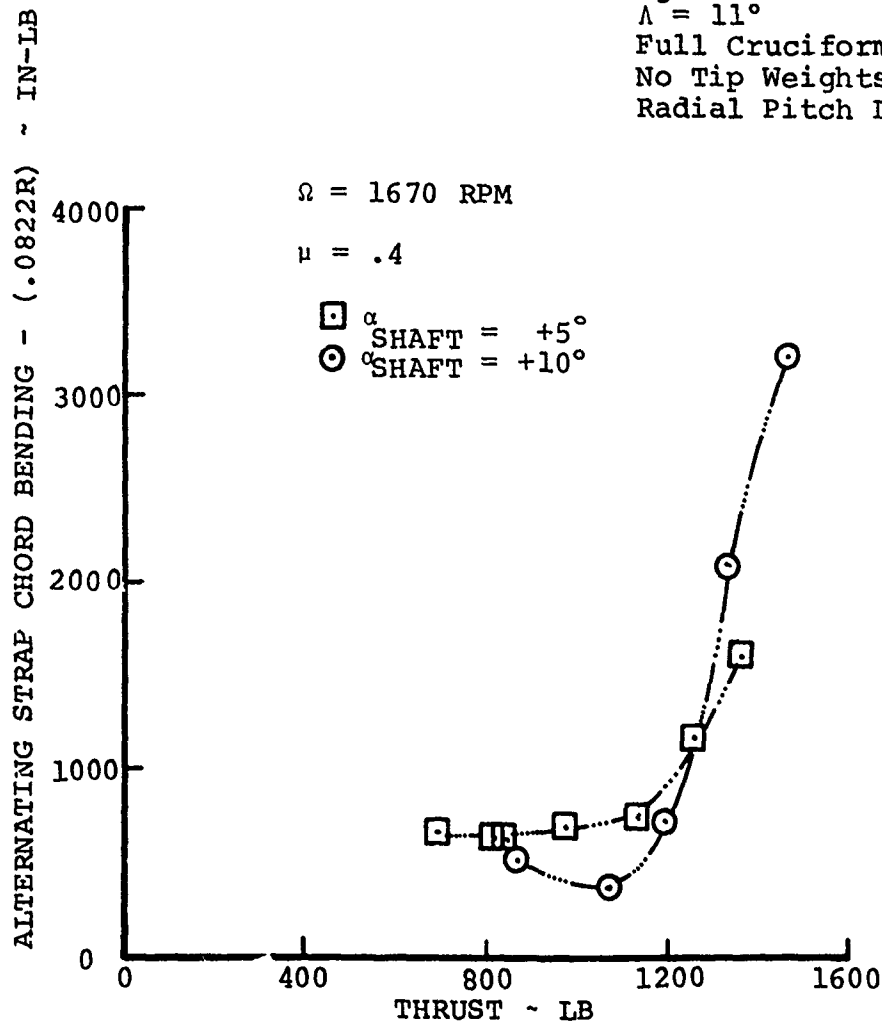FLAP BENDING LOADS FOR $\delta_3 = -45°$

213

BVWT 129 - RUNS 55, 58

Full Cruciform, Low EI
No Tip Weights
Radial Pitch Links

4.4" Straps (334, 337)
VR-7.2, CR-7.4 Airfoils
Elastomeric Hub Inserts
$K_\zeta = 350,000$ In-Lb/Rad
9° Clevis
$\delta_3 = -45°$
$\Lambda = 11°$

CONFIGURATION "E"

$\alpha_{SHAFT} = -5°$

$\Omega = 1670$ RPM

○ $\mu = 0$
▢ $\mu = .1$
◇ $\mu = .3$
△ $\mu = .4$
◁ $\mu = .45$

1/REV CHORD BENDING - (.0822R) ~ IN-LB

THRUST ~ LB

FIGURE 143   EFFECT OF ADVANCE RATIO ON FIRST-HARMONIC
CHORD BENDING LOADS FOR $\delta_3 = -45°$

214

α_{SHAFT} = -5°   CONFIGURATION "E"

Ω = 1670 RPM   BVWT 129 - RUN 55, 58

⊙ μ = 0   4.4" Straps (334, 337)
⊡ μ = .1   VR-7.2, VR-7.4 Airfoils
◇ μ = .3   Elastomeric Hub Inserts
△ μ = .4 K_ζ = 350,000 In-Lb/Rad
◁ μ = .45   9° Clevis
δ_3 = -45°
Λ = 11°
Full Cruciform, Low EI
No Tip Weights
Radial Pitch Links
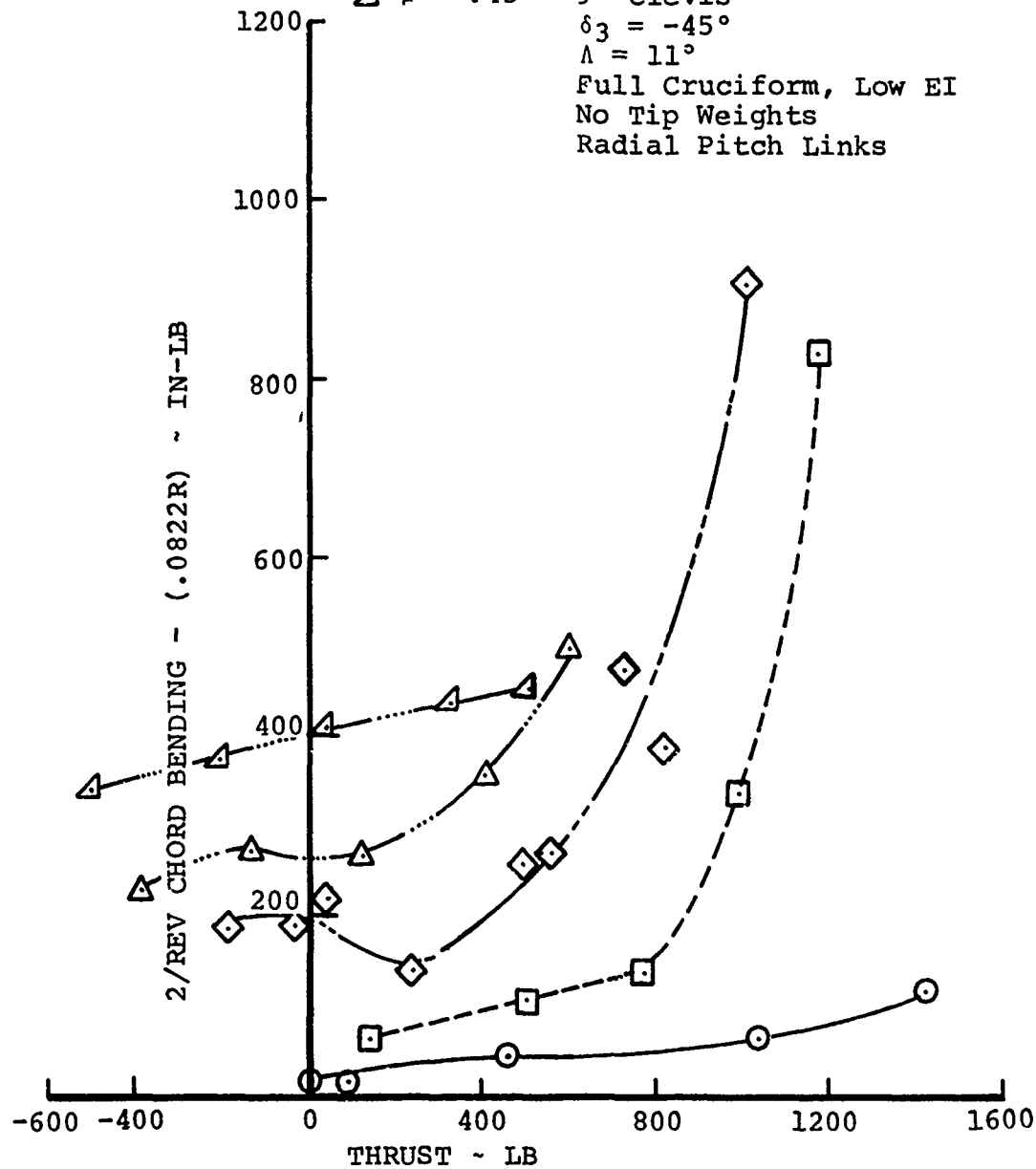
FIGURE 144   EFFECT OF ADVANCE RATIO ON SECOND-HARMONIC
CHORD BENDING LOADS FOR δ_3 = -45°

215

CONFIGURATION "E"

BVWT 129 - RUNS 55, 58

4.4" Straps (334, 337)
VR-7.2, VR-7.4 Airfoils
Elastomeric Hub Inserts
K_ζ = 350,000 In-Lb/Rad
9° Clevis
$\delta_3 = -45°$
$\Lambda = 11°$
Full Cruciform, Low EI
No Tip Weights
Radial Pitch Links

$\alpha_{SHAFT} = -5°$

Ω = 1670 RPM

⊙ μ = 0
⊡ μ = .1
◇ μ = .3
△ μ = .4
◁ μ = .45

FIGURE 145   EFFECT OF ADVANCE RATIO ON THIRD-HARMONIC
CHORD BENDING LOADS FOR $\delta_3 = -45°$

216

CONFIGURATION "E"

BVWT 129 - RUNS 55, 58

4.4" Straps (334, 337)
VR-7.2, VR-7.4 Airfoils
Elastomeric Hub Inserts
K_ζ = 350,000 In-Lb/Rad
9° Clevis
δ_3 = -45°
Λ = 11°
Full Cruciform, Low EI
No Tip Weights
Radial Pitch Links

α_{SHAFT} = -5°
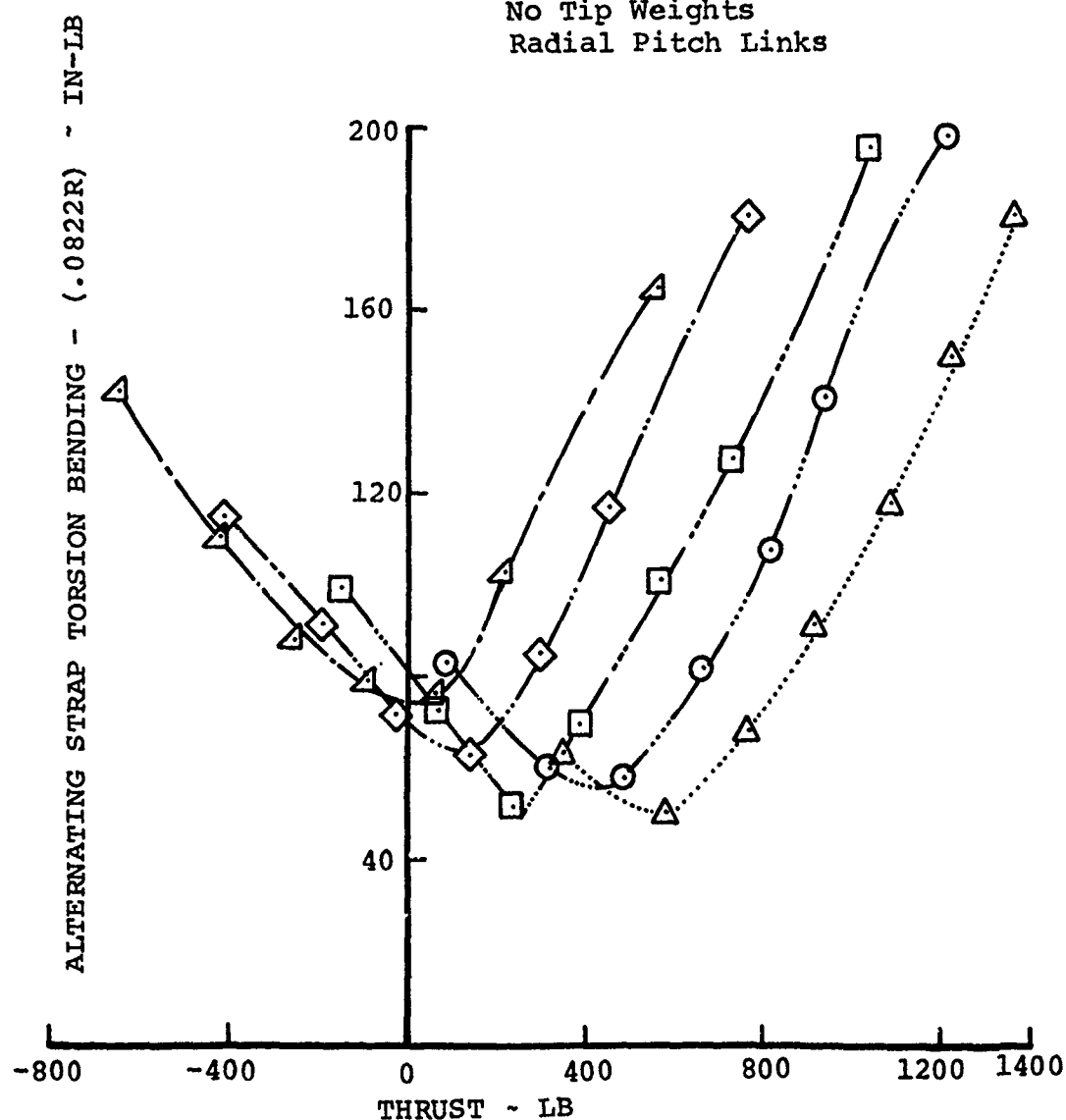
Ω = 1670 RPM

$\odot$ μ = 0
$\boxdot$ μ = .1
$\diamondsuit$ μ = .3
$\triangle$ μ = .4
$\triangleleft$ μ = .45

4/REV CHORD BENDING - (.0822R) ~ IN-LB

THRUST ~ LB

FIGURE 146   EFFECT OF ADVANCE RATIO ON FOURTH-HARMONIC
CHORD BENDING LOADS FOR δ_3 = -45°

217

FIGURE 147   EFFECT OF ADVANCE RATIO ON FIRST-HARMONIC
              TORSION BENDING LOADS FOR $\delta_3 = -45°$

CONFIGURATION "E"

BVWT 129 - RUNS 55, 58

4.4" Straps (334, 337)
VR-7.2, VR-7.4 Airfoils
Elastomeric Hub Inserts
  K_ζ = 350,000 In-Lb/Rad
9° Clevis
δ_3 = -45°
Λ = 11°
Full Cruciform, Low EI
No Tip Weights
Radial Pitch Links

α_{SHAFT} = -5°
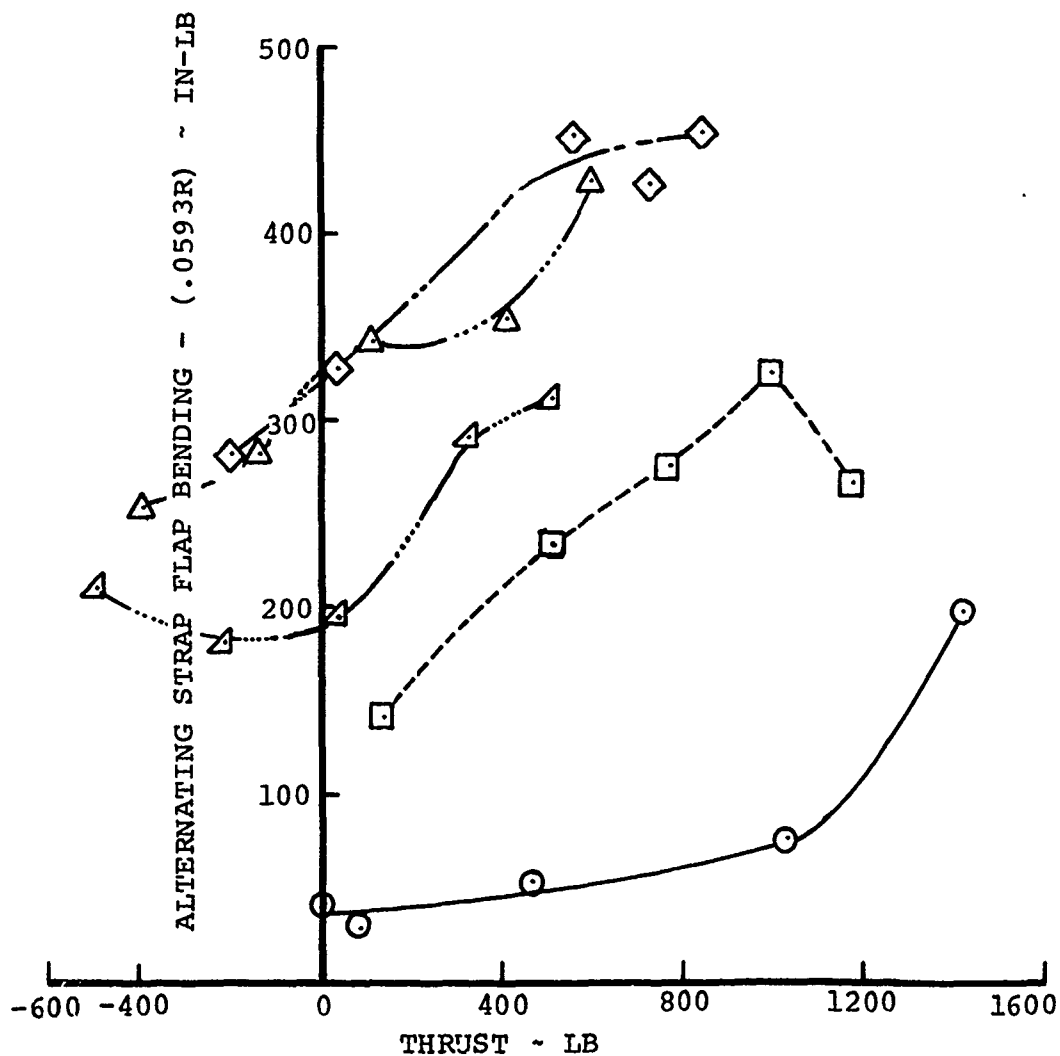
Ω = 1670 RPM

⊙ μ = 0
□ μ = .1
◇ μ = .3
△ μ = .4
◁ μ = .45
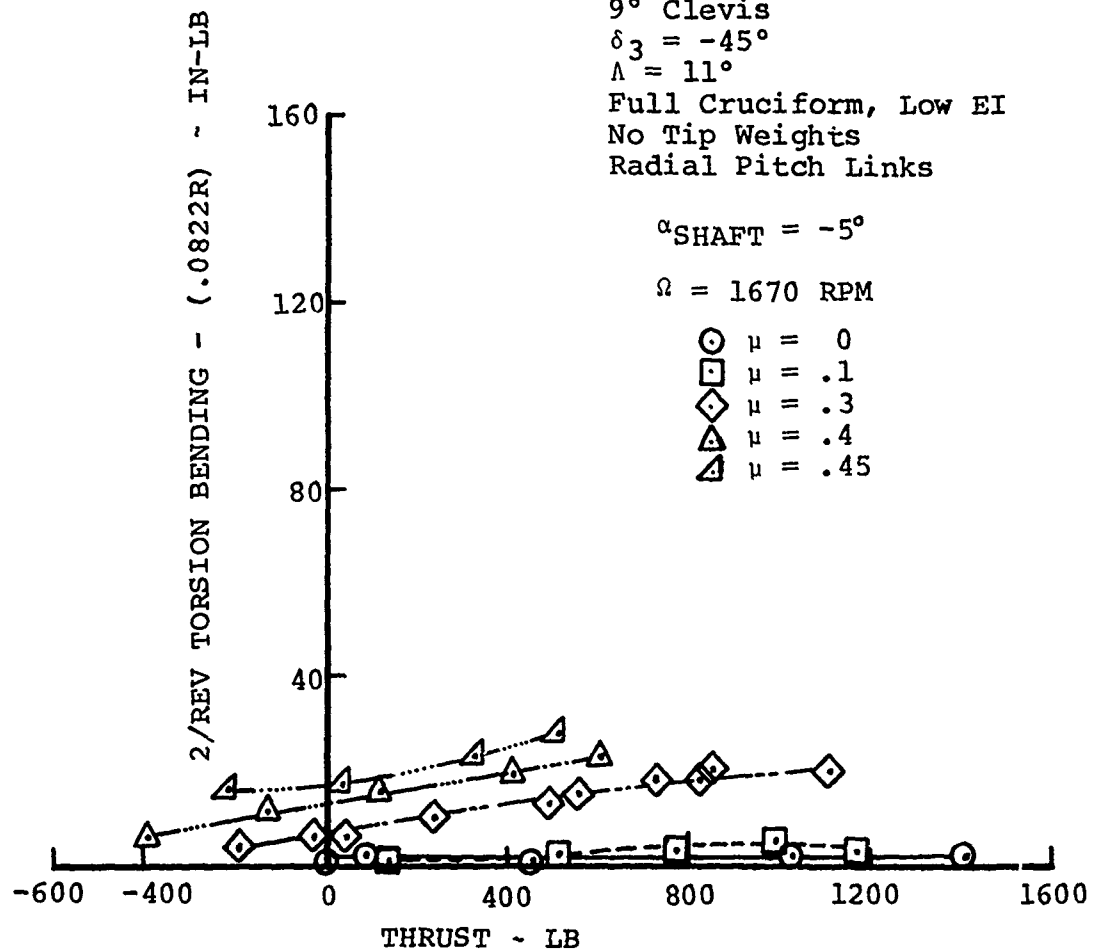
FIGURE 148   EFFECT OF ADVANCE RATIO ON SECOND-HARMONIC
TORSION BENDING LOADS FOR δ_3 = -45°

219

CONFIGURATION "E"

BVWT 129 - RUNS 55, 58

4.4" Straps (334, 337)
VR-7.2, VR-7.4 Airfoils
Elastomeric Hub Inserts
K_ζ = 350,000 In-Lb/Rad
9° Clevis
δ_3 = -45°
Λ = 11°
Full Cruciform, Low EI
No Tip Weights
Radial Pitch Links

α_{SHAFT} = -5°

Ω = 1670 RPM

μ = 0
μ = .1
μ = .3
μ = .4
μ = .45
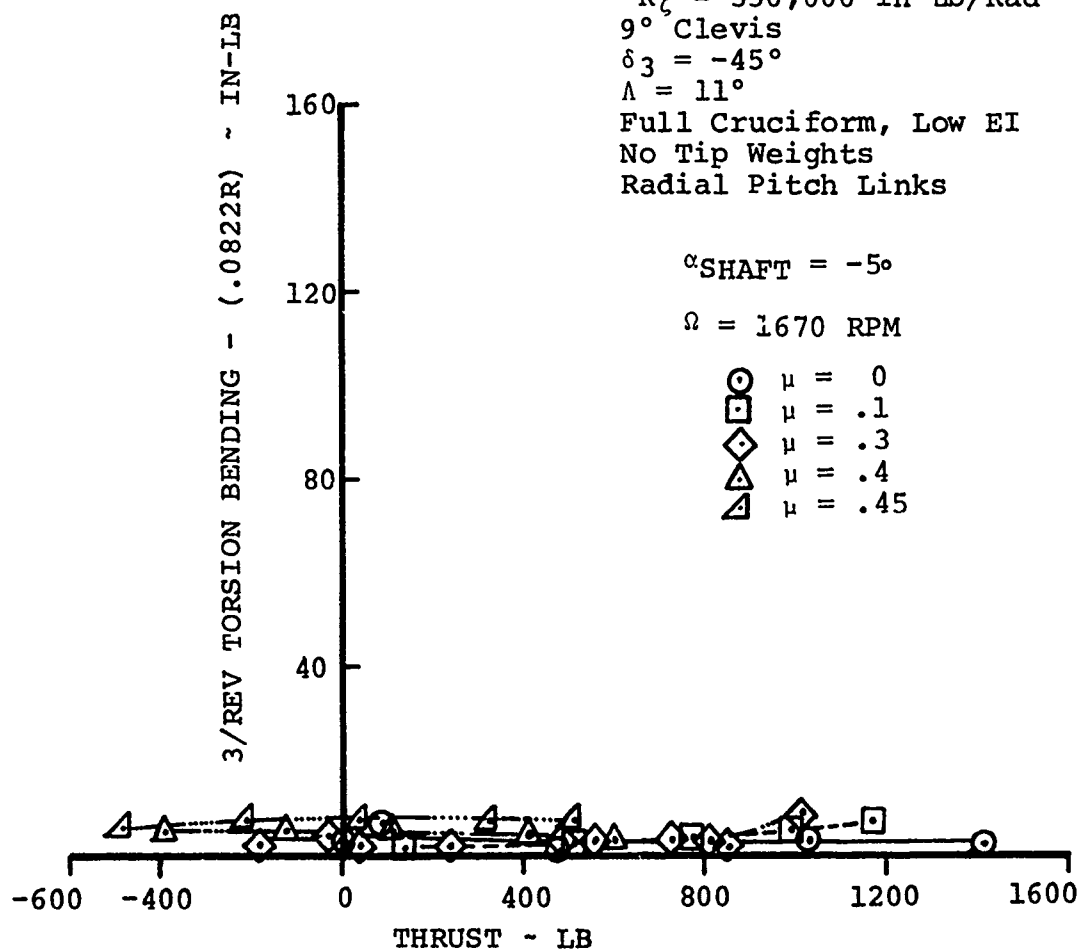
FIGURE 149   EFFECT OF ADVANCE RATIO ON THIRD-HARMONIC
TORSION BENDING LOADS FOR δ_3 = -45°

CONFIGURATION "E"

BVWT 129 - RUNS 55, 58

4.4" Straps (334, 337)
VR-7.2, VR-7.4 Airfoils
Elastomeric Hub Inserts
K_ζ = 350,000 In-Lb/Rad
9° Clevis
δ_3 = -45°
Λ = 11°
Full Cruciform, Low EI
No Tip Weights
Radial Pitch Links

α_{SHAFT} = -5°

Ω = 1670 RPM

$\odot$ μ = 0
$\boxdot$ μ = .1
$\diamondsuit$ μ = .3
$\triangle$ μ = .4
$\triangleleft$ μ = .45

4/REV TORSION BENDING - (.0822R) ~ IN-LB

160

120

80

40

THRUST ~ LB

-600 -400   0   400   800   1200   1600

FIGURE 150   EFFECT OF ADVANCE RATIO ON FOURTH-HARMONIC
TORSION BENDING LOADS FOR δ_3 = -45°

221

μ = .4

Ω = 1670 RPM

◁ α_{SHAFT} = -5°
◇ α_{SHAFT} = 0°
▢ α_{SHAFT} = +5°
◉ α_{SHAFT} = +10°
△ α_{SHAFT} = +15°

BVWT 129 - RUN 54

4.4" Straps (337, 338)
VR-7.2, VR-7.4 Airfoils
Elastomeric Hub Inserts
K_ζ = 350,000 In-Lb/Rad
9° Clevis
δ_3 = -65°
Λ = 11°
Full Cruciform, Low EI
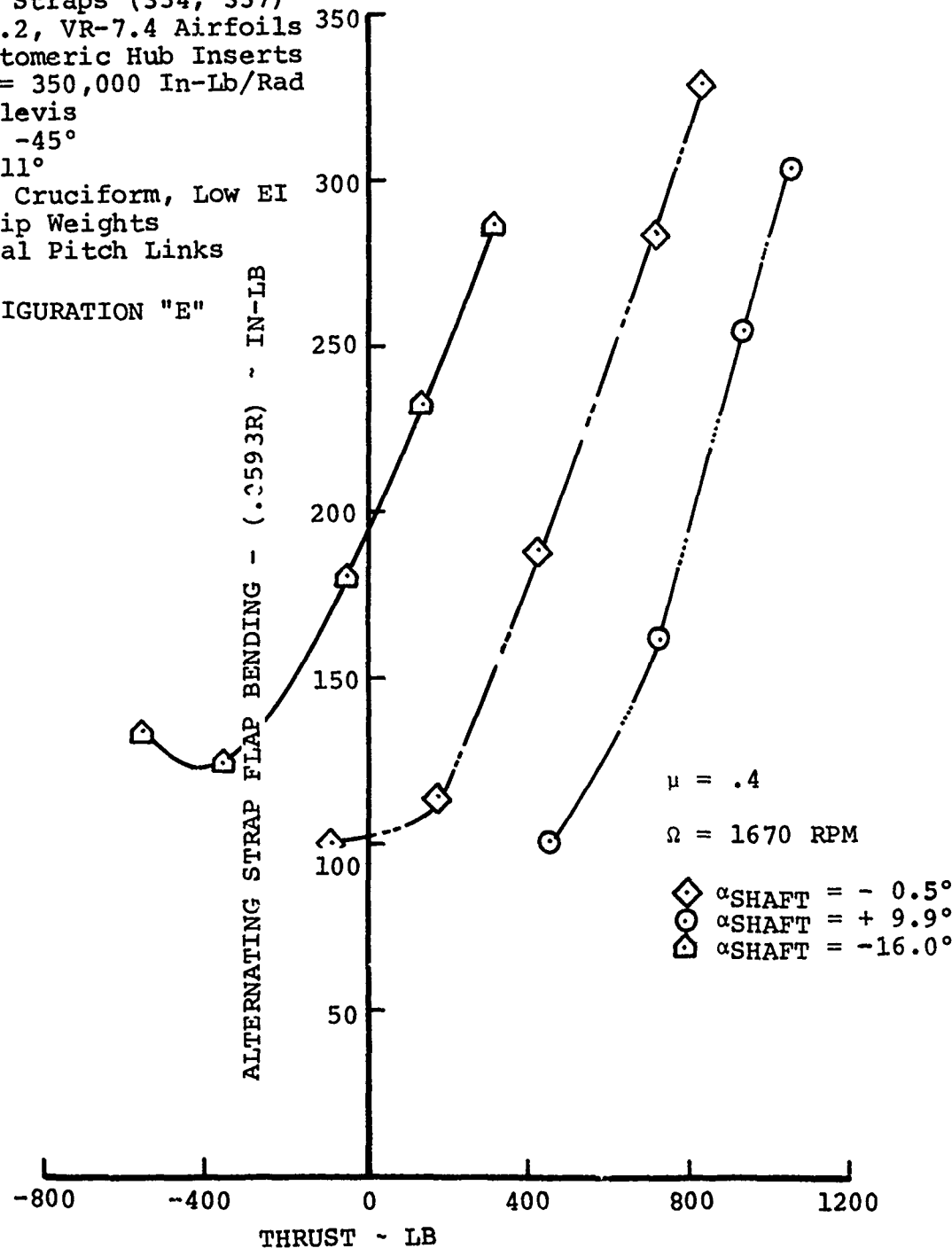No Tip Weights
Radial Pitch Links

CONFIGURATION "D"

FIGURE 151   EFFECT OF SHAFT ANGLE ON FIRST-HARMONIC
              CHORD BENDING LOADS

222

CONFIGURATION "D"

BVWT 129 - RUN 54

$\mu = .4$

$\Omega = 1670$ RPM

$\alpha_{SHAFT} = -5°$
$\alpha_{SHAFT} = 0°$
$\alpha_{SHAFT} = +5°$
$\alpha_{SHAFT} = +10°$
$\alpha_{SHAFT} = +15°$

4.4" Straps (337, 338)
VR-7.2, VR-7.4 Airfoils
Elastomeric Hub Inserts
$K_\zeta = 350,000$ In-Lb/Rad
9° Clevis
$\delta_3 = -65°$
$\Lambda = 11°$
Full Cruciform, Low EI
No Tip Weights
Radial Pitch Links

2/REV CHORD BENDING = $(.0822R) \sim$ IN-LB

THRUST $\sim$ LB
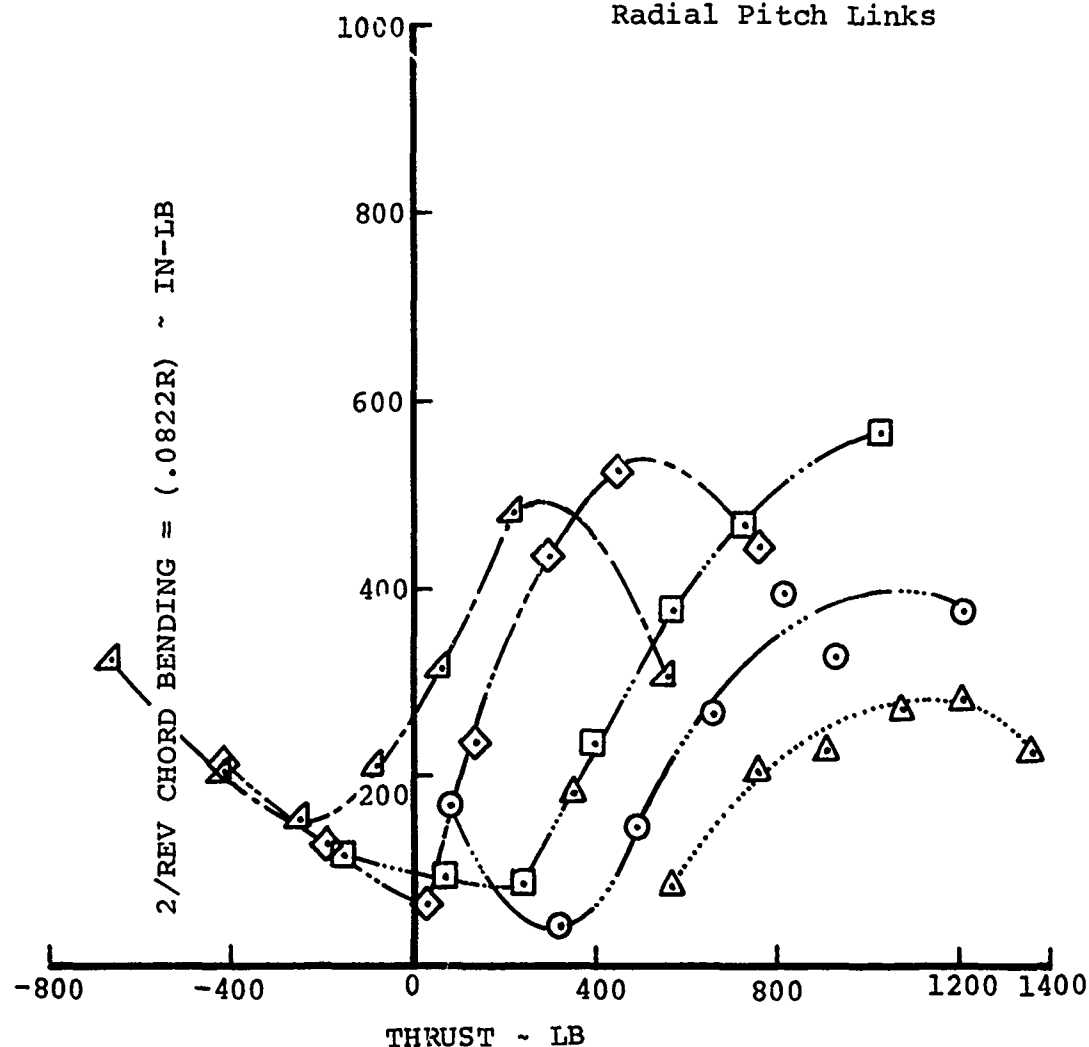
FIGURE 152   EFFECT OF SHAFT ANGLE ON SECOND-HARMONIC
CHORD BENDING LOADS

223

CONFIGURATION "D"
BVWT 129 - RUN 54

4.4" Straps (337, 338)
VR-7.2, VR-7.4 Airfoils
Elastomeric Hub Inserts
$K\zeta = 350,000$ In-Lb/Rad
9° Clevis
$\delta_3 = -65°$
$\Lambda = 11°$
Full Cruciform, Low EI
No Tip Weights
Radial Pitch Links

$\mu = .4$

$\Omega = 1670$ RPM

⊿ $\alpha_{SHAFT} = -5$
◇ $\alpha_{SHAFT} = 0$
□ $\alpha_{SHAFT} = +5$
⊙ $\alpha_{SHAFT} = +10$
△ $\alpha_{SHAFT} = +15$

3/REV CHORD BENDING ~ $(.0822R)$ ~ IN-LB

THRUST ~ LB
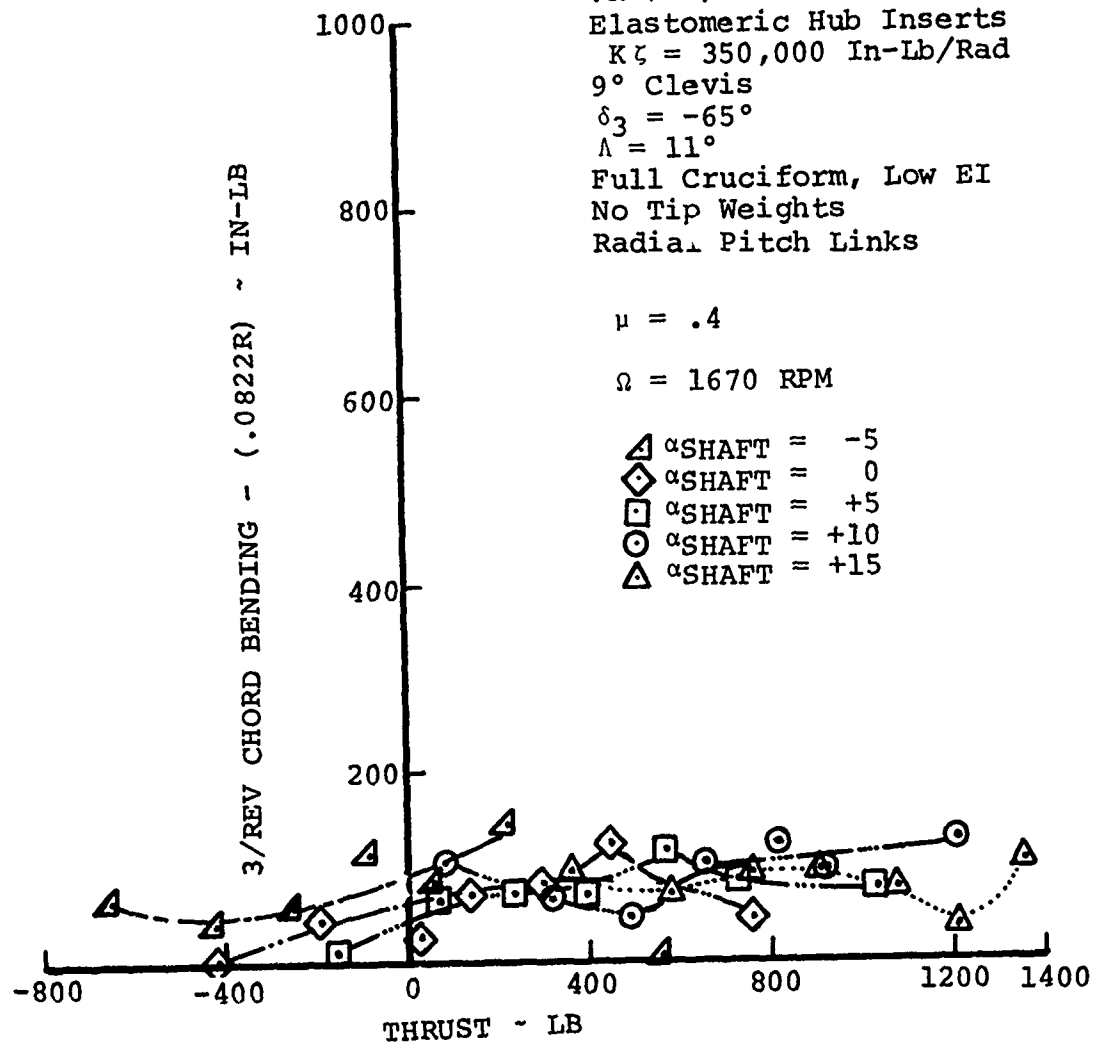
FIGURE 153   EFFECT OF SHAFT ANGLE ON THIRD-HARMONIC
CHORD BENDING LOADS

224

CONFIGURATION "D"

BVWT 129 - RUN 54

4.4" Straps (337, 338)
VR-7.2, VR-7.4 Airfoils
Elastomeric Hub Inserts
K_ζ = 350,000 In-Lb/Rad
9° Clevis
δ_3 = -65°
Λ = 11°
Full Cruciform, Low EI
No Tip Weights
Radial Pitch Links

μ = .4

Ω = 1670 RPM

α_{SHAFT} = -5°
α_{SHAFT} = 0°
α_{SHAFT} = +5°
α_{SHAFT} = +10°
α_{SHAFT} = +15°
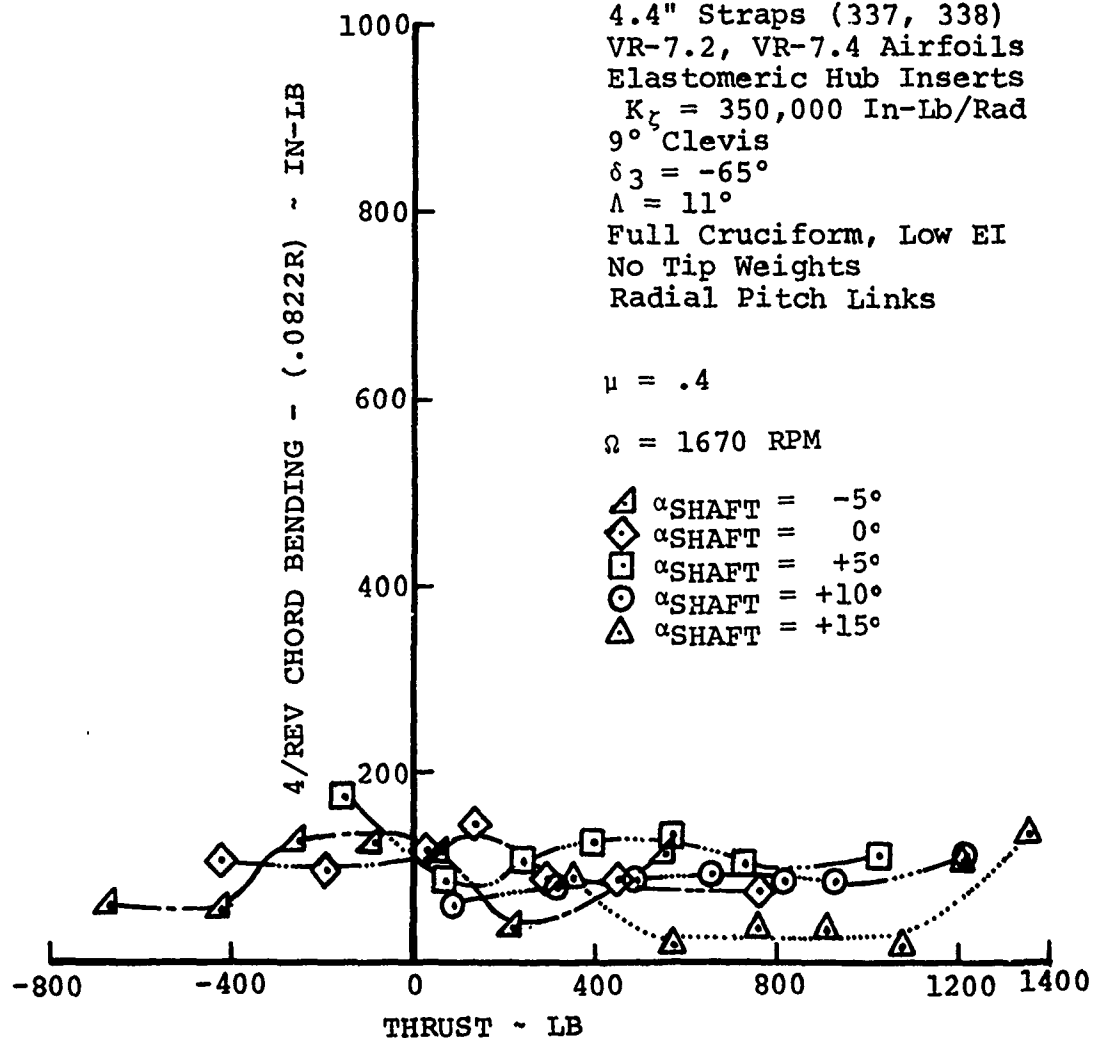
FIGURE 154   EFFECT OF SHAFT ANGLE ON FOURTH-HARMONIC
              CHORD BENDING LOADS

225

CONFIGURATION "D"

BVWT 129 - RUN 54

μ = .4

Ω = 1670 RPM

△ α_{SHAFT} = -5°
◇ α_{SHAFT} = 0°
☐ α_{SHAFT} = +5°
⊙ α_{SHAFT} = +10°
△ α_{SHAFT} = +15°

4.4" Straps (337, 338)
VR-7.2, VR-7.4 Airfoils
Elastomeric Hub Inserts
K_ζ = 350,000 In-Lb/Rad
9° Clevis
δ_3 = -65°
Λ = 11°
Full Cruciform, Low EI
No Tip Weights
Radial Pitch Links
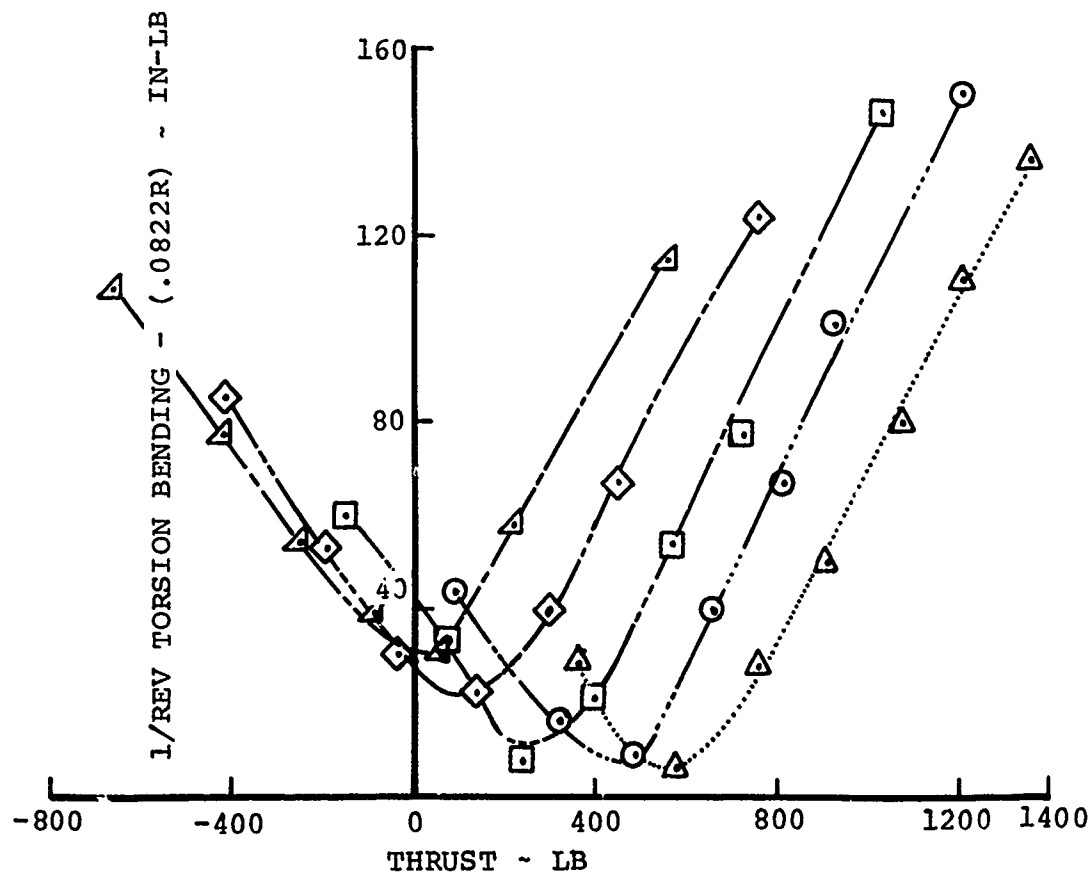
FIGURE 155   EFFECT OF SHAFT ANGLE ON FIRST-HARMONIC
TORSION BENDING LOADS

226

CONFIGURATION "D"

BVWT 129 - RUN 54

4.4" Straps (337, 338)
VR-7.2, VR-7.4 Airfoils
Elastomeric Hub Inserts
K_ζ = 350,000 In-Lb/Rad
9° Clevis
δ_3 = -65°
Λ = 11°
Full Cruciform, Low EI
No Tip Weights
Radial Pitch Links

μ = .4

Ω = 1670 RPM

α_{SHAFT} =   -5°
α_{SHAFT} =   0°
α_{SHAFT} =   +5°
α_{SHAFT} = +10°
α_{SHAFT} = +15°
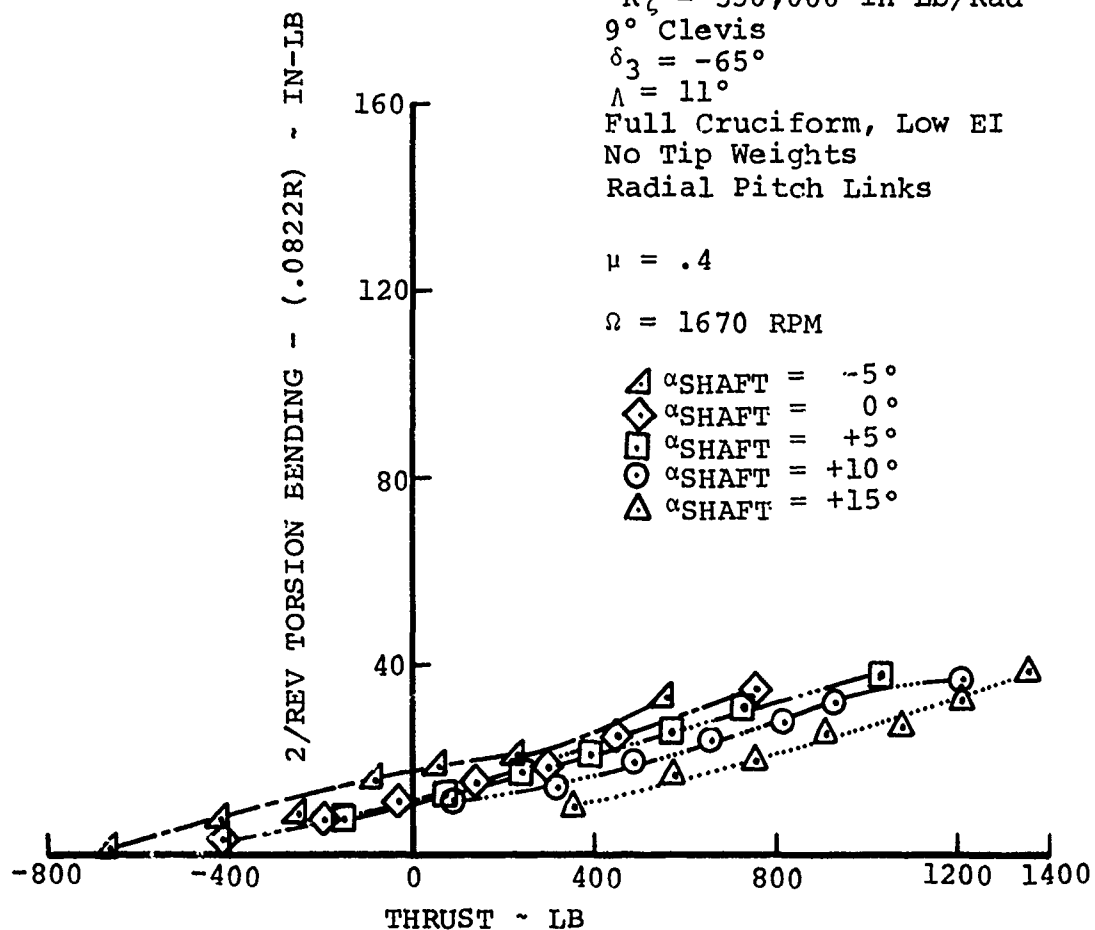
FIGURE 156   EFFECT OF SHAFT ANGLE ON SECOND-HARMONIC
TORSION BENDING LOADS

227

CONFIGURATION "D"

BVWT 129 - RUN 54

4.4" Straps (337, 338)
VR-7.2, VR-7.4 Airfoils
Elastomeric Hub Inserts
$K_\zeta = 350,000$ In-Lb/Rad
9° Clevis
$\delta_3 = -65°$
$\Lambda = 11°$
Full Cruciform, Low EI
No Tip Weights
Radial Pitch Links

$\mu = .4$

$\Omega = 1670$ RPM

⊲ $\alpha_{SHAFT} = -5°$
◇ $\alpha_{SHAFT} = 0°$
⊡ $\alpha_{SHAFT} = +5°$
⊙ $\alpha_{SHAFT} = +10°$
△ $\alpha_{SHAFT} = +15°$

3/REV TORSION BENDING - (.0822R) ~ IN-LB

THRUST ~ LB
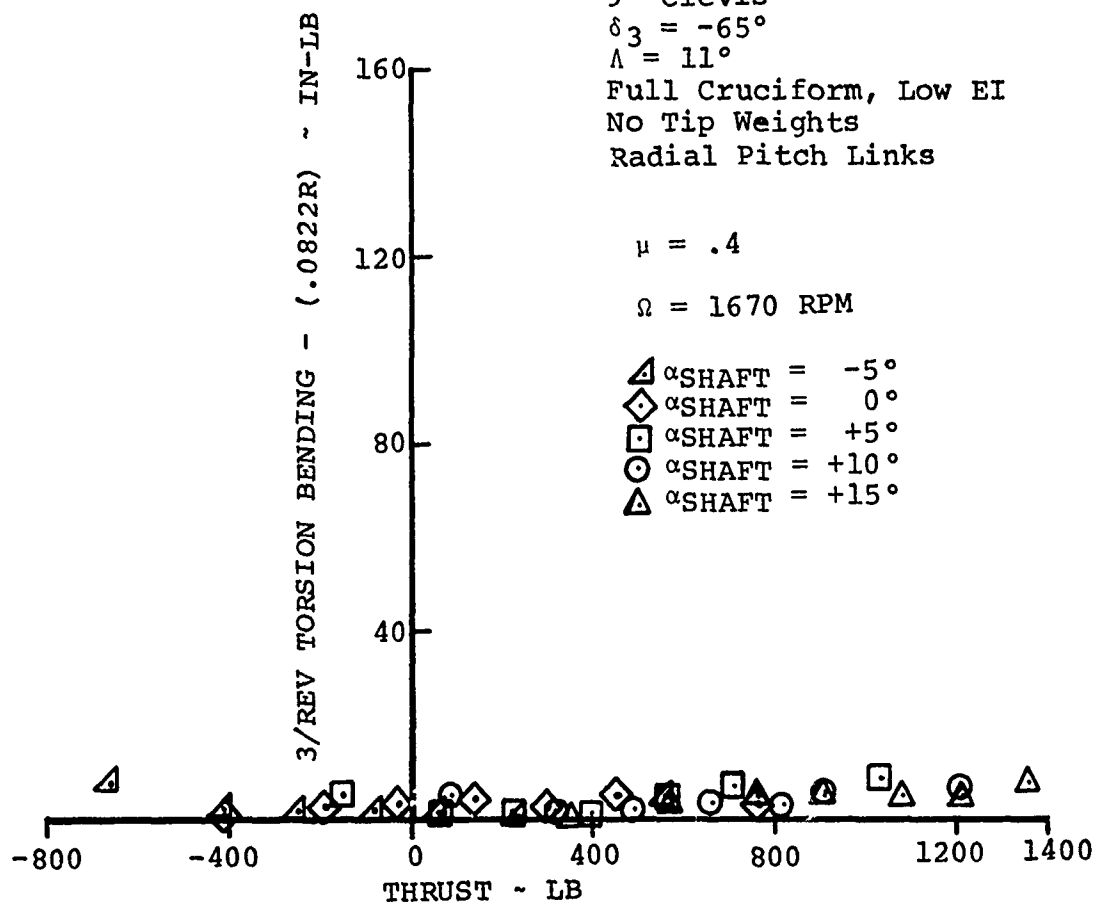
FIGURE 157   EFFECT OF SHAFT ANGLE ON THIRD-HARMONIC
               TORSION BENDING LOADS

228

CONFIGURATION "D"

BVWT 129 - RUN 54

4.4" Straps (337, 338)
VR-7.2, VR-7.4 Airfoils
Elastomeric Hub Inserts
K_ζ = 350,000 In-Lb/Rad
9° Clevis
δ_3 = -65°
Λ = 11°
Full Cruciform, Low EI
No Tip Weights
Radial Pitch Links

μ = .4

Ω = 1670 RPM

α_{SHAFT} = -5 °
α_{SHAFT} =   0 °
α_{SHAFT} = +5 °
α_{SHAFT} = +10 °
α_{SHAFT} = +15 °
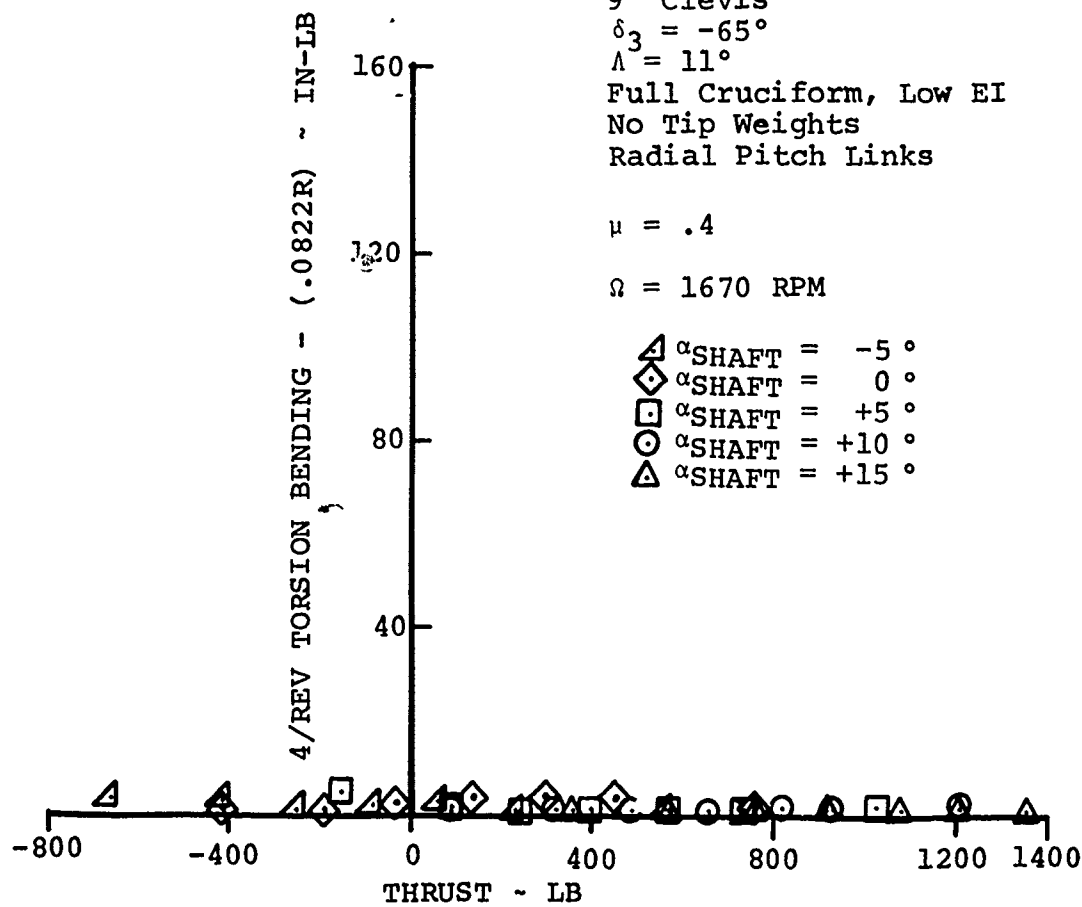
FIGURE 158   EFFECT OF SHAFT ANGLE ON FOURTH-HARMONIC
                TORSION BENDING LOADS

229

CONFIGURATION "D"

BVWT 129 - RUN 49

4.4" Straps (337, 338)
VR-7.2, VR-7.4 Airfoils
Elastomeric Hub Inserts
K_ζ = 350,000 In-Lb/Rad
9° Clevis
δ_3 = -65°
Λ = 11°
Full Cruciform, Low EI
No Tip Weights
Radial Pitch Links

α_{SHAFT} = -5°

Ω = 1670 RPM

□ μ = .1
◁ μ = .2
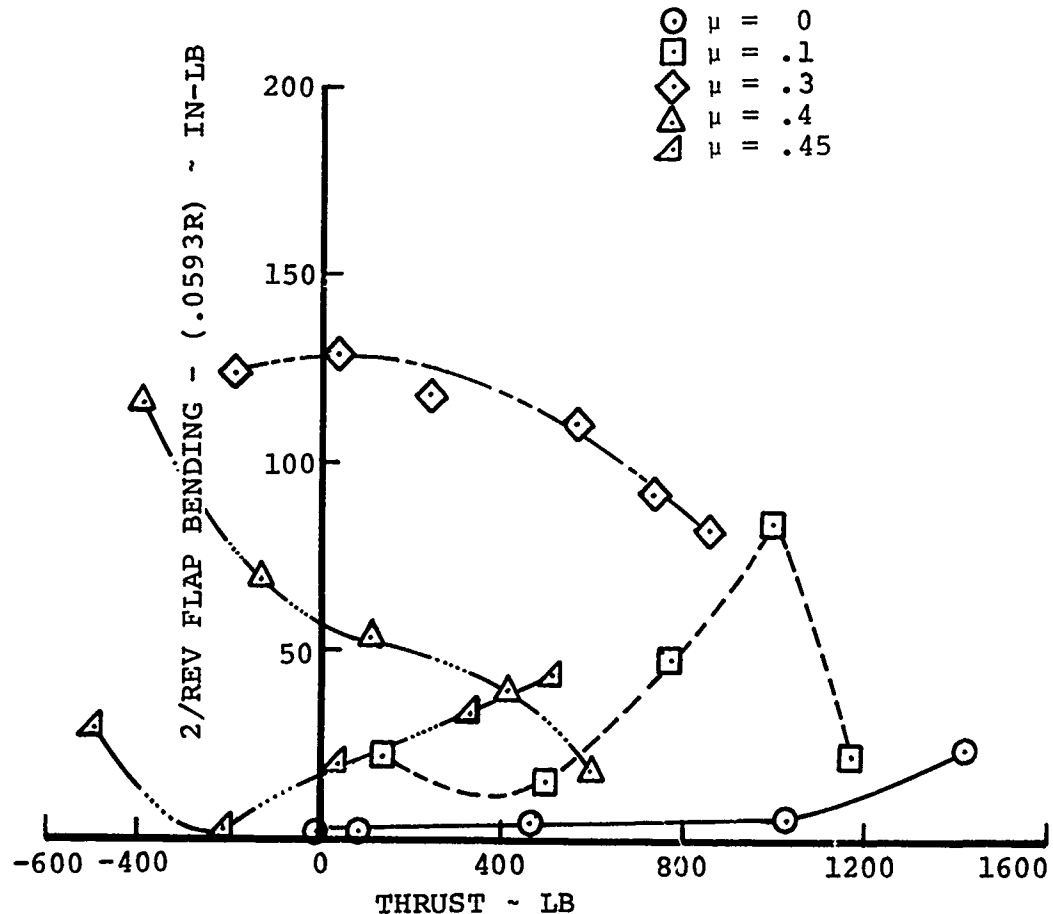◇ μ = .3
⬡ μ = .37
△ μ = .4
◁ μ = .45
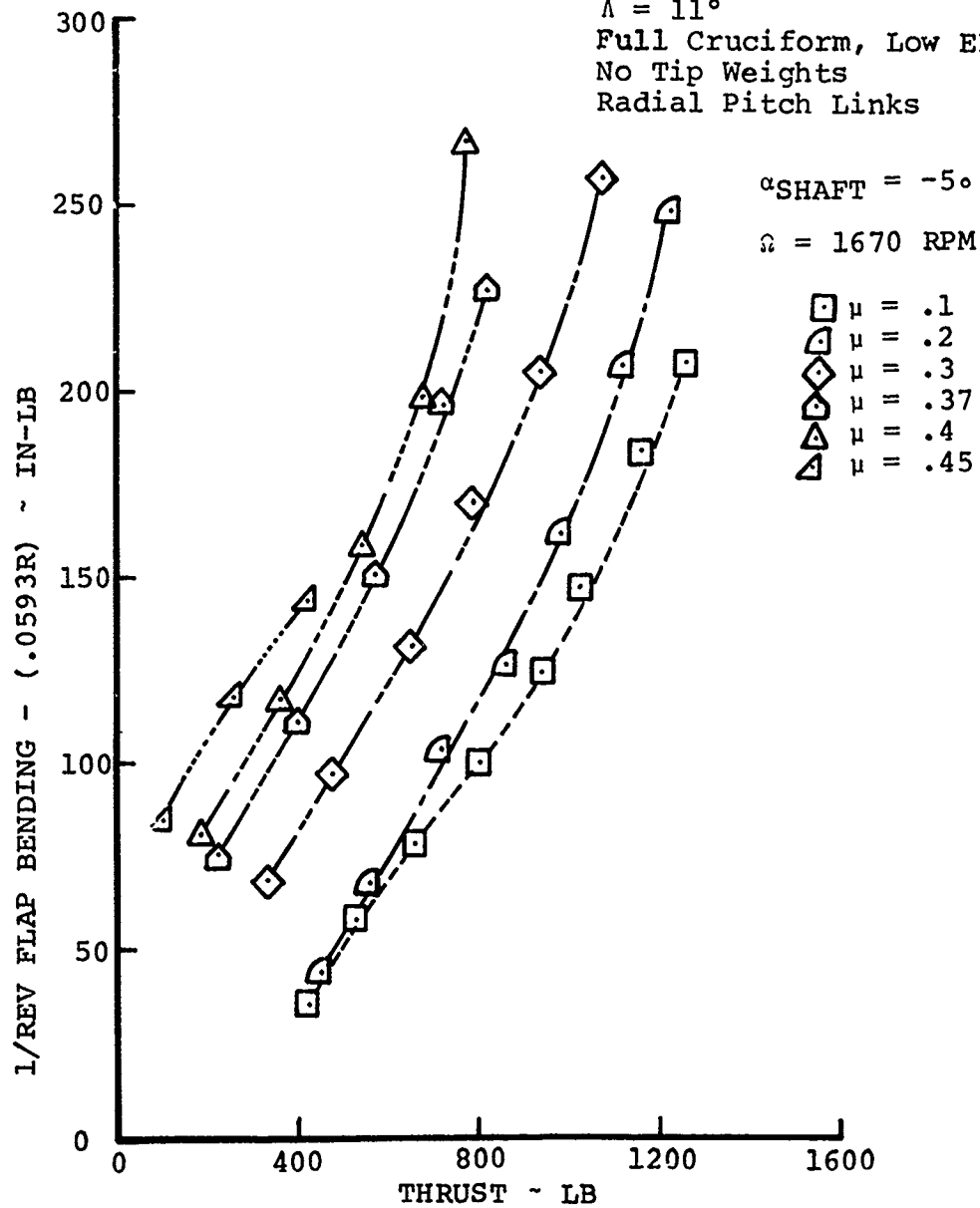
FIGURE 159   EFFECT OF ADVANCE RATIO ON FIRST-HARMONIC
FLAP BENDING LOADS FOR δ_3 = -65°

230

CONFIGURATION "D"

BVWT 129 - RUN 49

4.4" Straps (337, 338)
VR-7.2, VR-7.4 Airfoils
Elastomeric Hub Inserts
K_ζ = 350,000 In-Lb/Rad
9° Clevis
δ_3 = -65°
Λ = 11°
Full Cruciform, Low EI
No Tip Weights
Radial Pitch Links

α_{SHAFT} = -5°

Ω = 1670 RPM

μ = .1
μ = .2
μ = .3
μ = .37
μ = .4
μ = .45
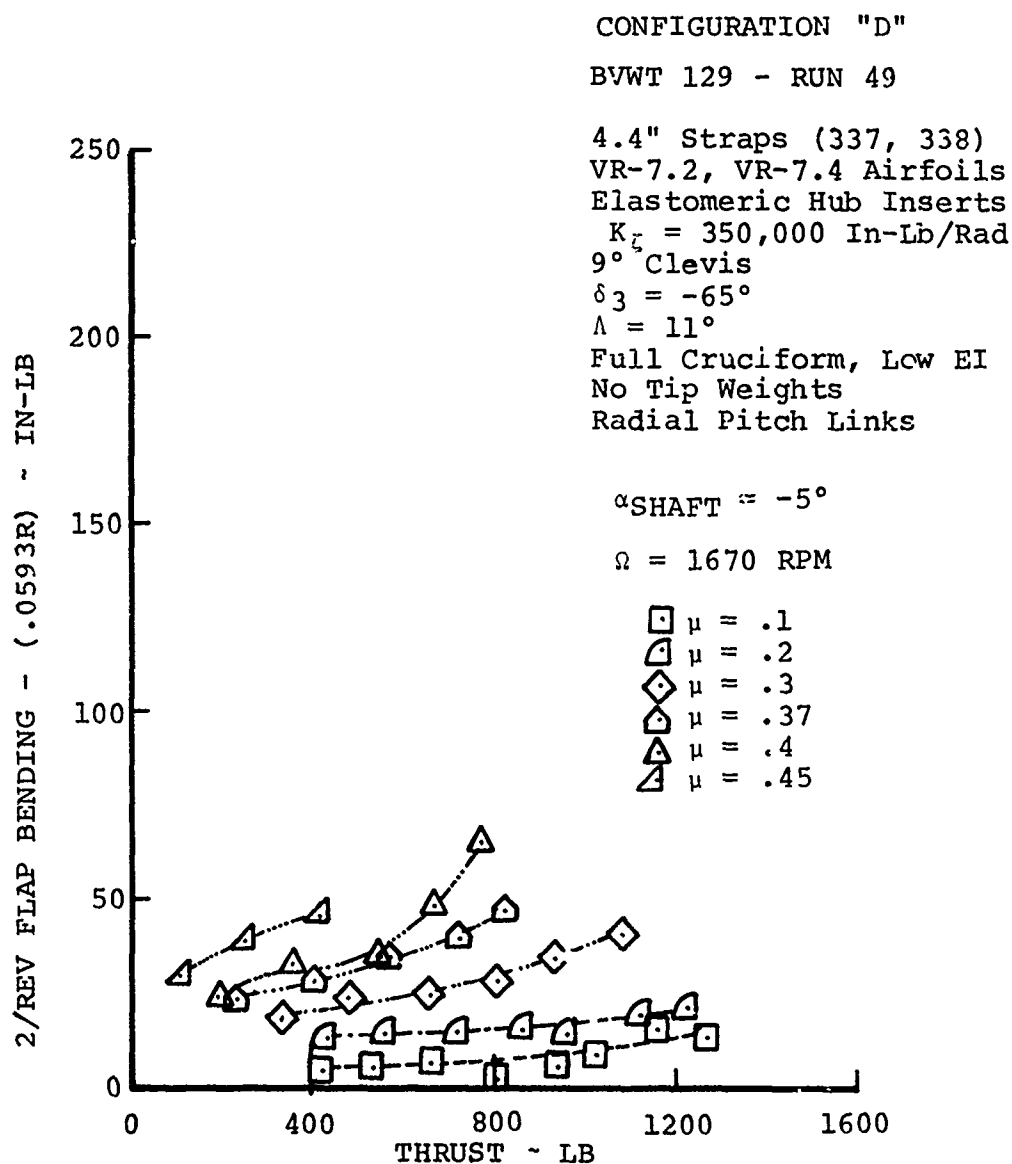
FIGURE 160   EFFECT OF ADVANCE RATIO ON SECOND-HARMONIC
FLAP BENDING LOADS FOR δ_3 = -65°

231
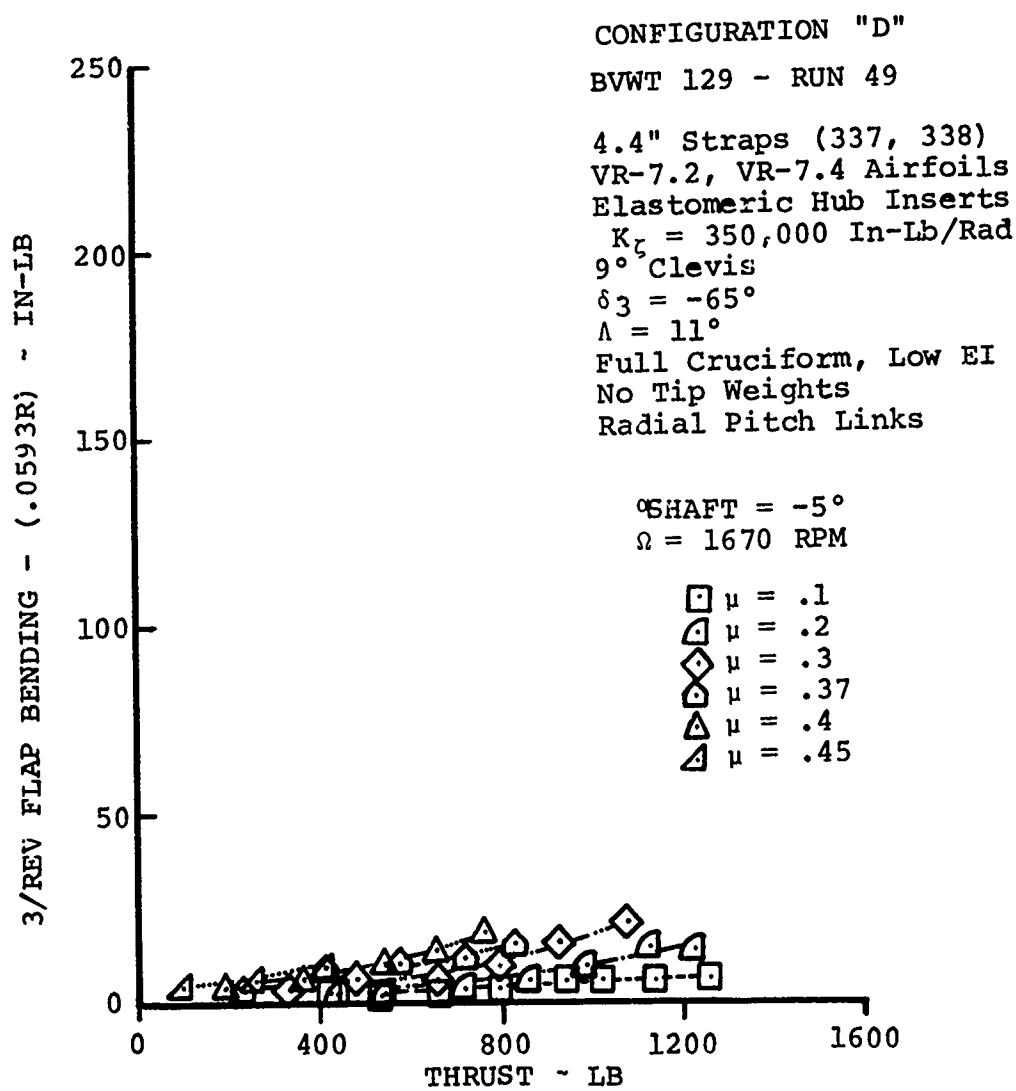
FIGURE 161   EFFECT OF ADVANCE RATIO ON THIRD-HARMONIC
FLAP BENDING LOADS FOR $\delta_3 = -65°$
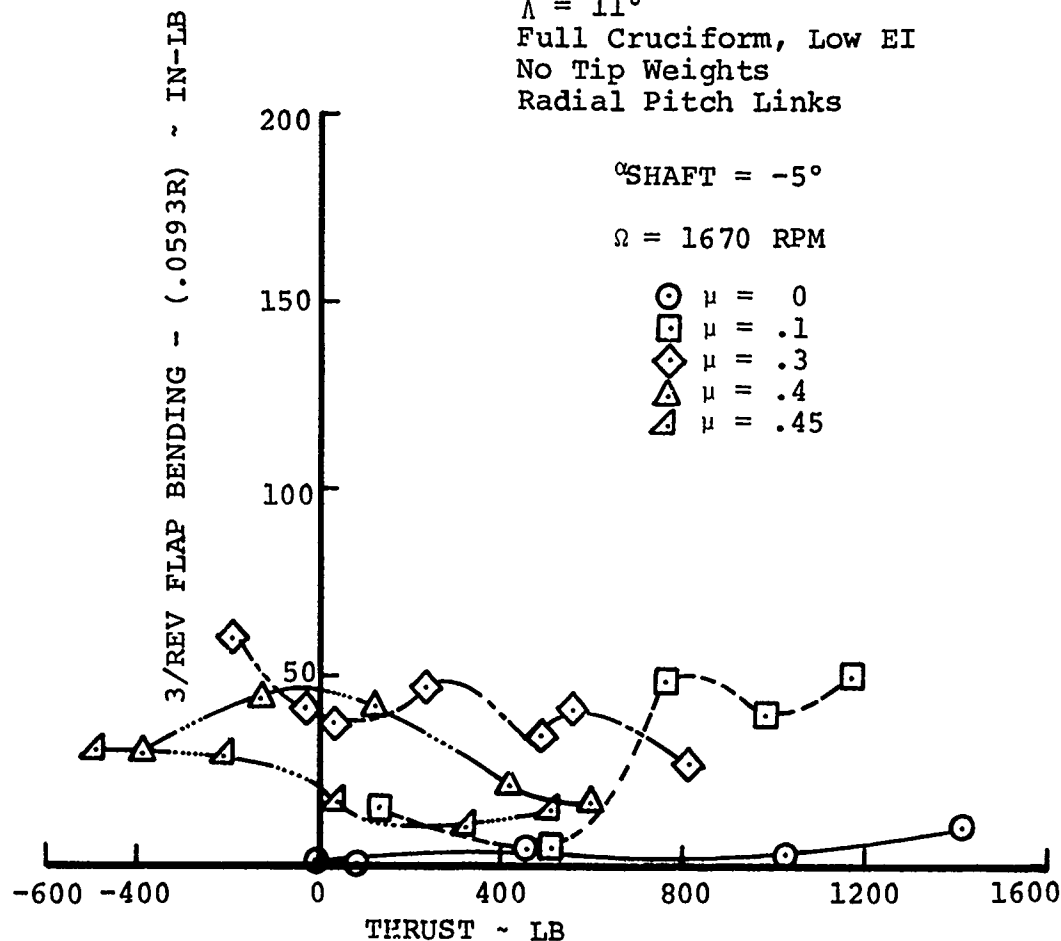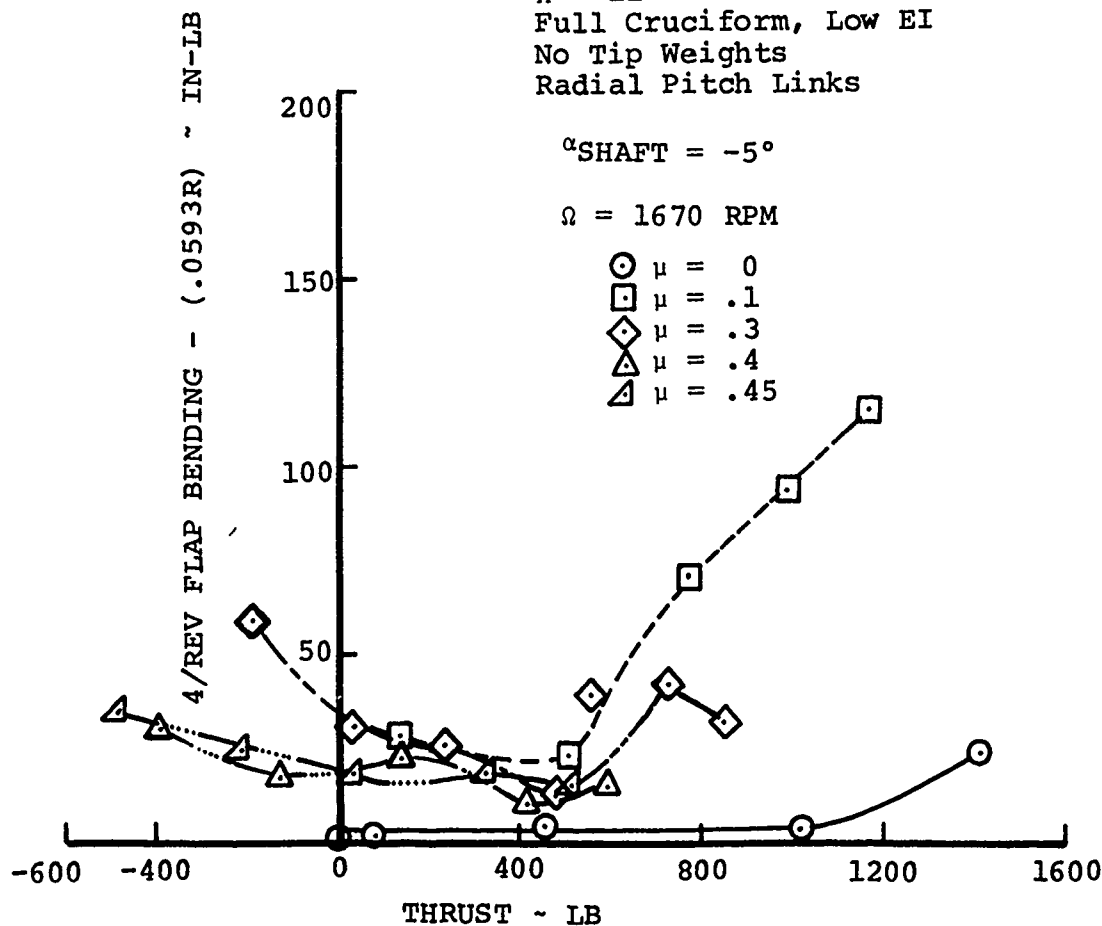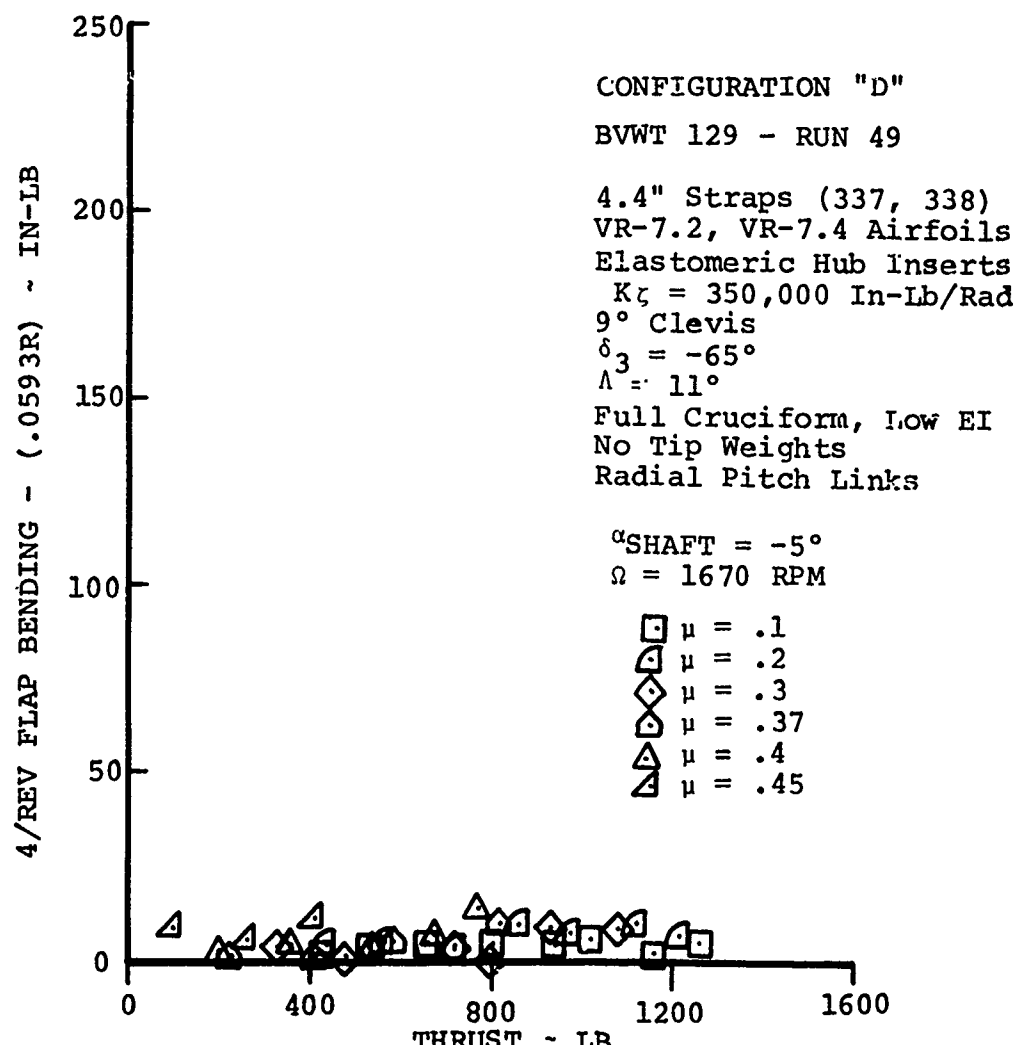
FIGURE 162   EFFECT OF ADVANCE RATIO ON FOURTH-HARMONIC
FLAP BENDING LOADS FOR $\delta_3 = -65°$

CONFIGURATION "D"

BVWT 129 - RUN 49

4.4" Straps (337, 338)
VR-7.2, VR-7.4 Airfoils
Elastomeric Hub Inserts
K_ζ = 350,000 In-Lb/Rad
9° Clevis
δ_3 = -65°
Λ = 11°
Full Cruciform, Low EI
No Tip Weights
Radial Pitch Links

α_{SHAFT} = -5°
Ω = 1670 RPM

μ = .1
μ = .2
μ = .3
μ = .37
μ = .4
μ = .45
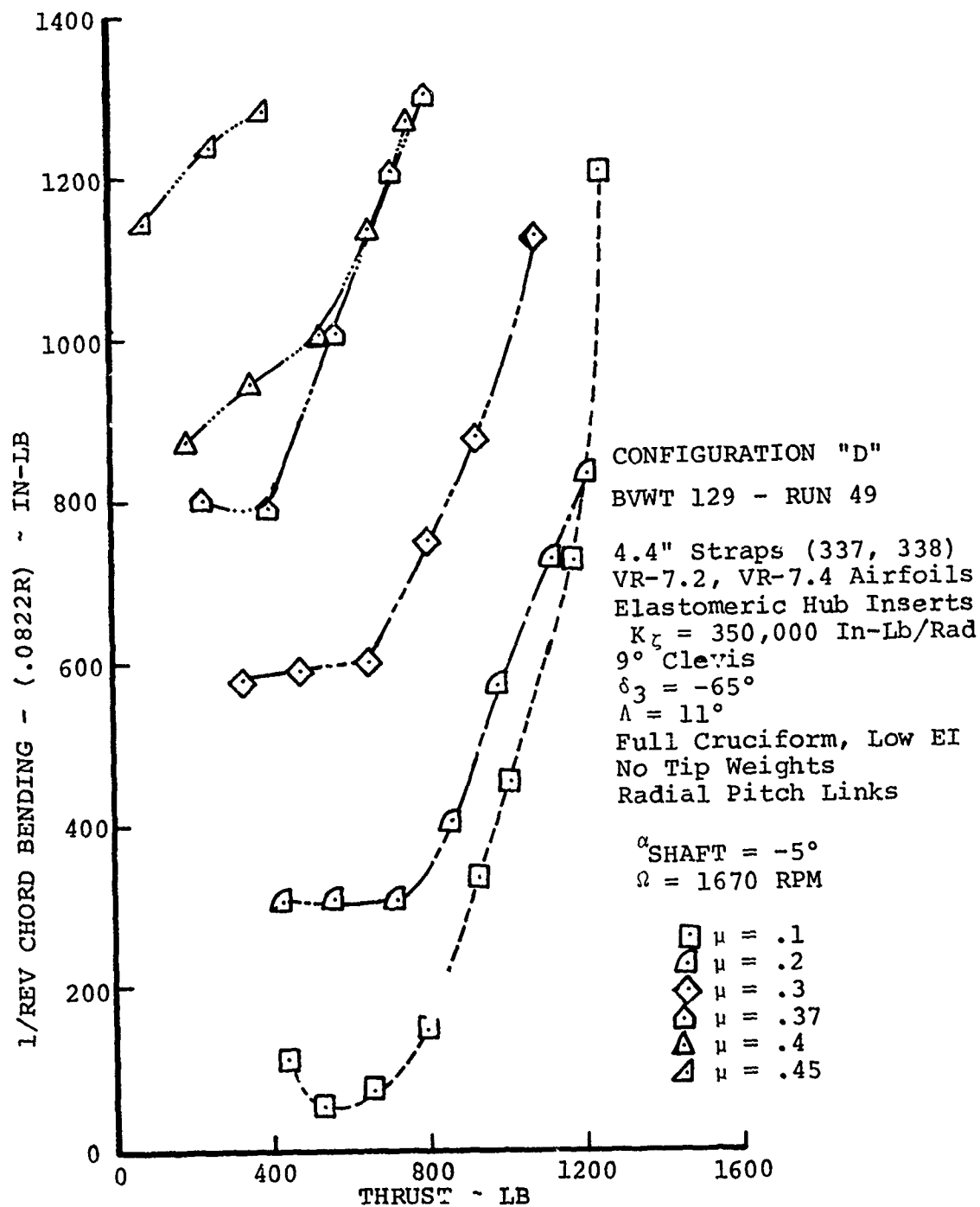
FIGURE 163   EFFECT OF ADVANCE RATIO ON FIRST-HARMONIC
CHORD BENDING LOADS FOR δ_3 = -65°

Configuration details shown on figure:

CONFIGURATION "D"

BVWT 129 – RUN 49

4.4" Straps (337, 338)
VR-7.2, VR-7.4 Airfoils
Elastomeric Hub Inserts
$K_\zeta = 350,000$ In-Lb/Rad
9° Clevis
$\delta_3 = -65°$
$\Lambda = 11°$
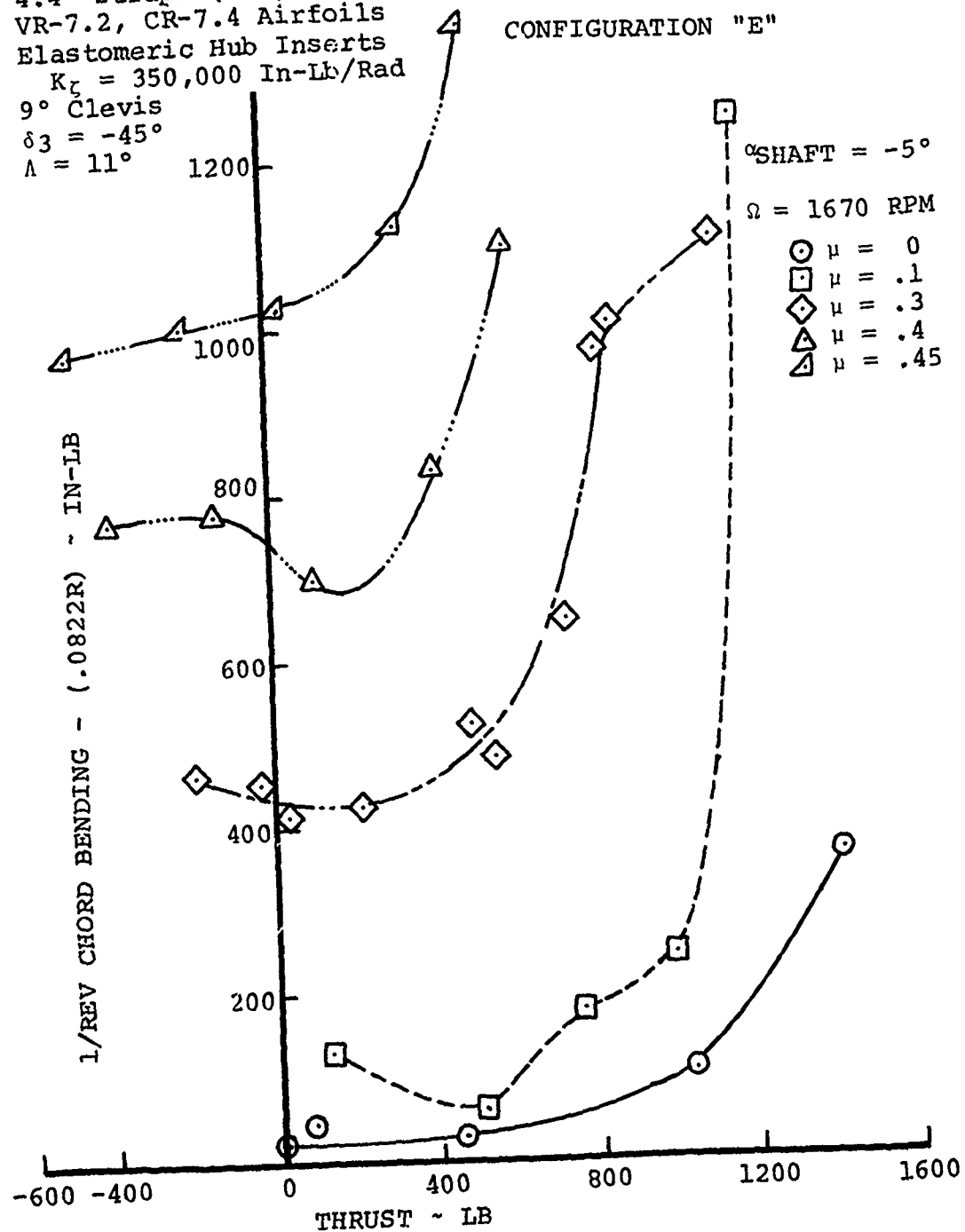Full Cruciform, Low EI
No Tip Weights
Radial Pitch Links

$\alpha_{SHAFT} = -5°$

$\Omega = 1670$ RPM

$\mu = .1$
$\mu = .2$
$\mu = .3$
$\mu = .37$
$\mu = .4$
$\mu = .45$

Y-axis: 2/REV CHORD BENDING – (.0822R) ~ IN-LB

X-axis: THRUST ~ LB
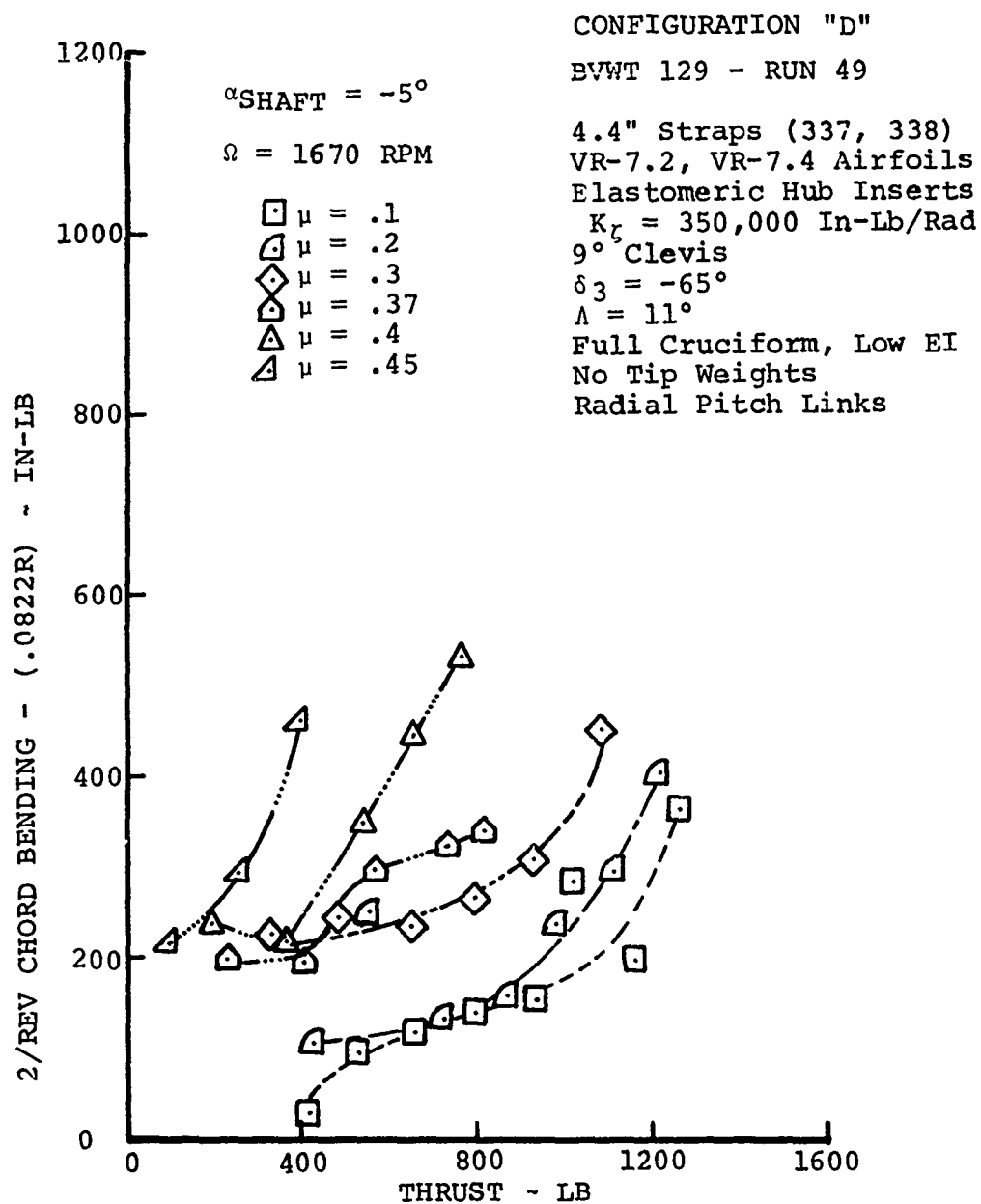
FIGURE 164   EFFECT OF ADVANCE RATIO ON SECOND-HARMONIC
CHORD BENDING LOADS FOR $\delta_3 = -65°$

235

The figure plots 3/REV CHORD BENDING − (.0822R) ~ IN-LB (vertical axis, 0 to 1200) versus THRUST ~ LB (horizontal axis, 0 to 1600).

αSHAFT = -5°

Ω = 1670 RPM

□ μ = .1
◁ μ = .2
◇ μ = .3
⊗ μ = .37
△ μ = .4
◁ μ = .45

CONFIGURATION "D"

BVWT 129 - RUN 49

4.4" Straps (337, 338)
VR-7.2, VR-7.4 Airfoils
Elastomeric Hub Inserts
K_ζ = 350,000 In-Lb/Rad
9° Clevis
δ_3 = -65°
Λ = 11°
Full Cruciform, Low EI
No Tip Weights
Radial Pitch Links
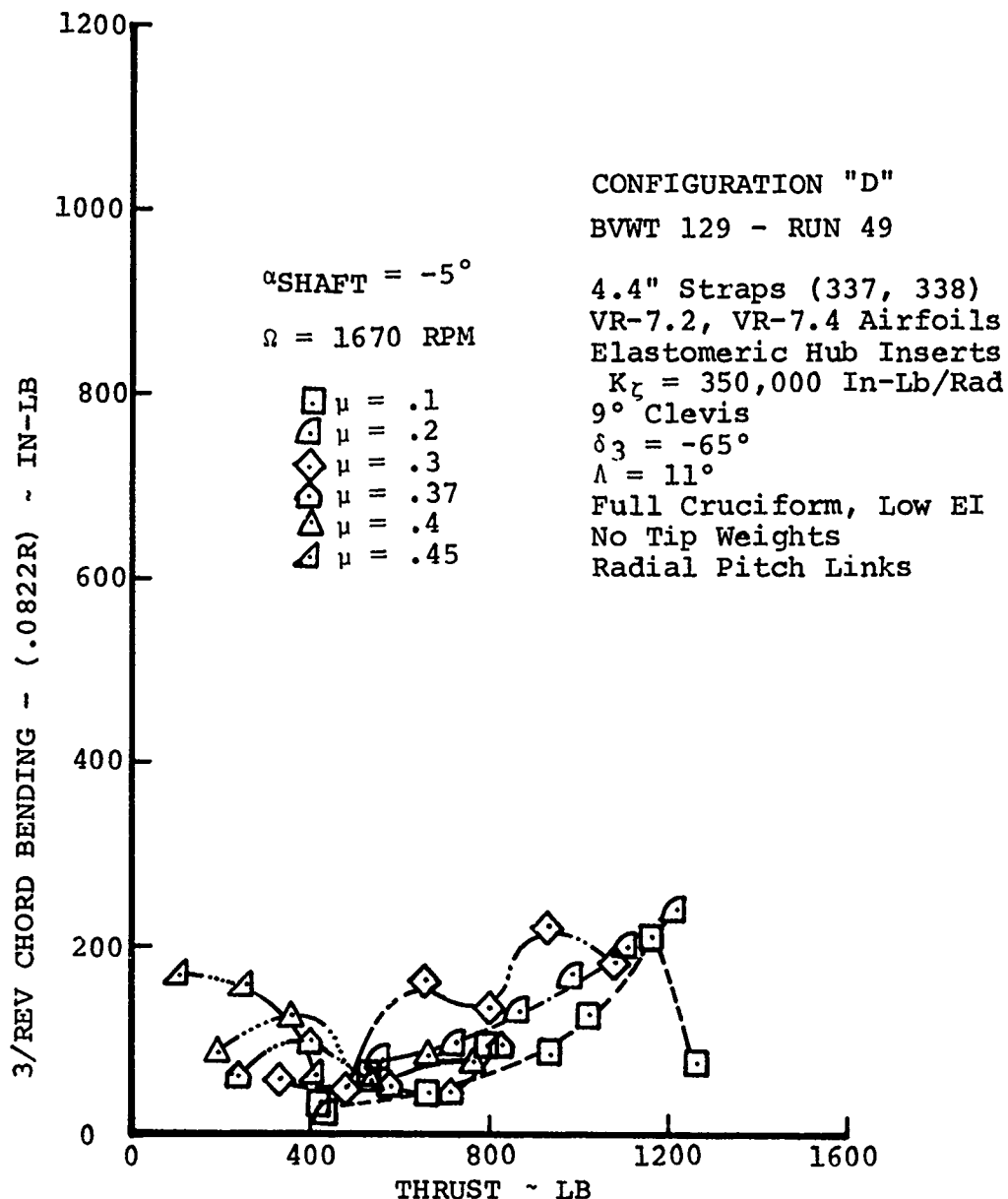
FIGURE 165   EFFECT OF ADVANCE RATIO ON THIRD-HARMONIC
CHORD BENDING LOADS FOR δ_3 = -65°

236

CONFIGURATION "D"

BVWT 129 - RUN 49

$\alpha_{SHAFT} = -5°$

$\Omega = 1670$ RPM

4.4" Straps (337, 338)
VR-7.2, VR-7.4 Airfoils
Elastomeric Hub Inserts
$K_\zeta = 350,000$ In-Lb/Rad
9° Clevis
$\delta_3 = -65°$
$\Lambda = 11°$
Full Cruciform, Low EI
No Tip Weights
Radial Pitch Links

☐ $\mu = .1$
◁ $\mu = .2$
◇ $\mu = .3$
⬡ $\mu = .37$
△ $\mu = .4$
◺ $\mu = .45$
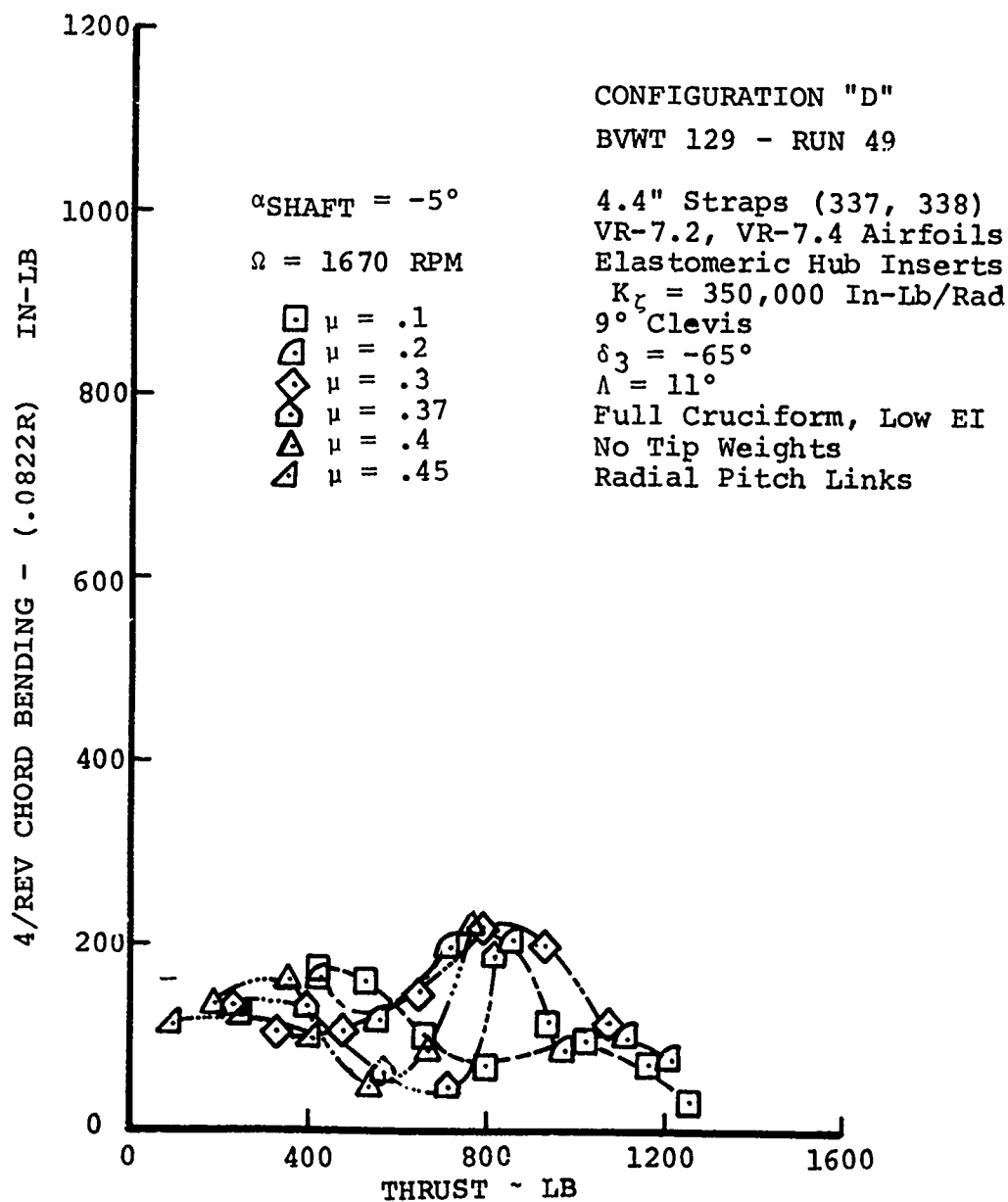
FIGURE 166   EFFECT OF ADVANCE RATIO ON FOURTH-HARMONIC
CHORD BENDING LOADS FOR $\delta_3 = -65°$

237

CONFIGURATION "D"
BVWT 129 - RUN 49

4.4" Straps (337, 338)
VR-7.2, VR-7.4 Airfoils
Elastomeric Hub Inserts
$K_\zeta = 350,000$ In-Lb/Rad
9° Clevis
$\delta_3 = -65°$
$\Lambda = 11°$
Full Cruciform, Low EI
No Tip Weights
Radial Pitch Links

$\alpha_{SHAFT} = -5°$

$\Omega = 1670$ RPM

$\mu = .1$
$\mu = .2$
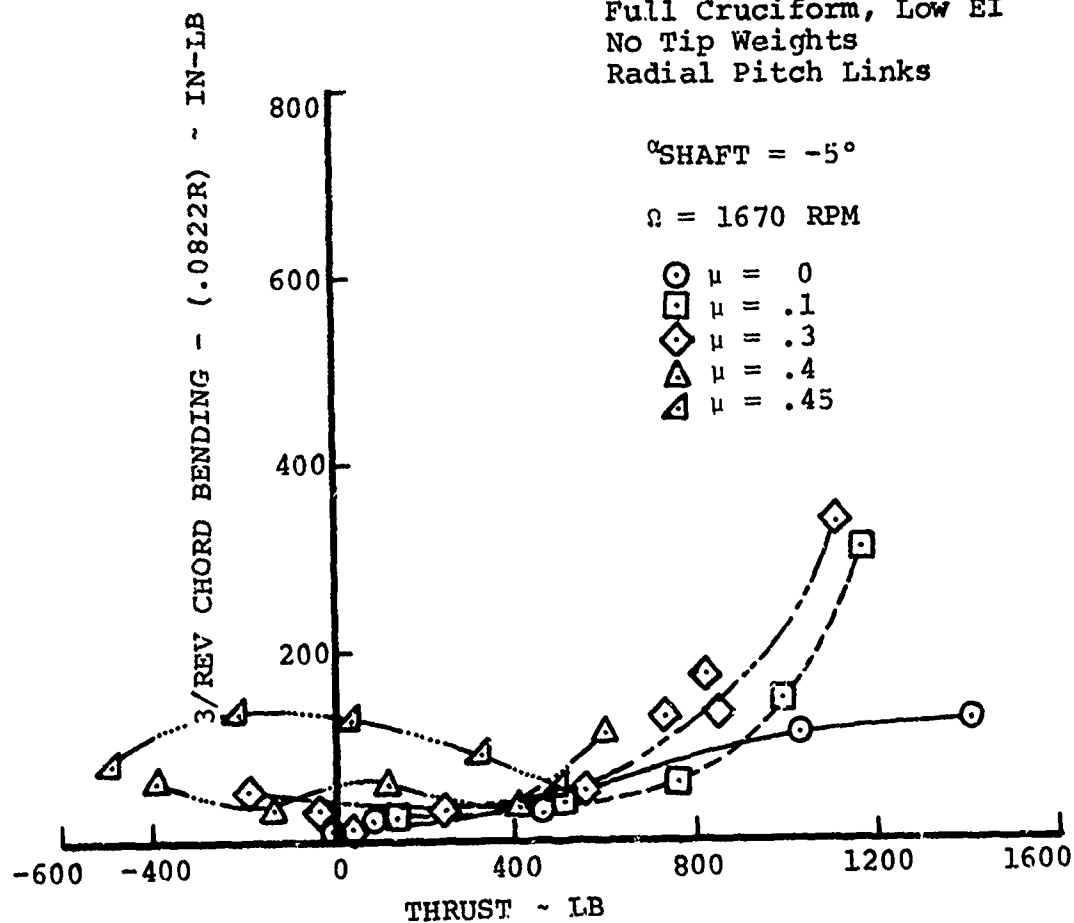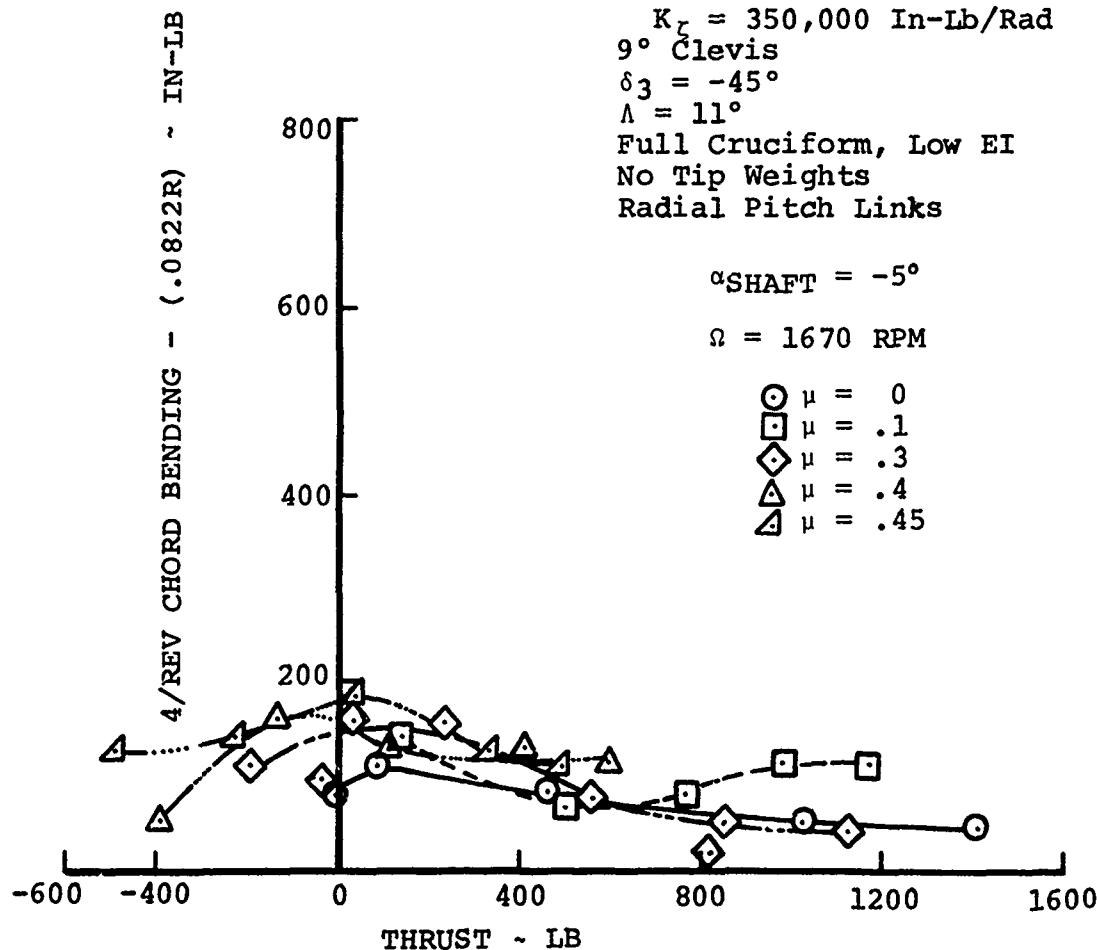$\mu = .3$
$\mu = .37$
$\mu = .4$
$\nu = .45$

FIGURE 167   EFFECT OF ADVANCE RATIO ON FIRST-HARMONIC
                TORSION BENDING LOADS FOR $\delta_3 = -65°$

238

$\alpha_{SHAFT} = -5°$

$\Omega = 1670$ RPM

□ $\mu = .1$
◁ $\mu = .2$
◇ $\mu = .3$
◈ $\mu = .37$
△ $\mu = .4$
◁ $\mu = .45$

CONFIGURATION "D"
BVWT 129 - RUN 49

4.4" Straps (337, 338)
VR-7.2, VR-7.4 Airfoils
Elastomeric Hub Inserts
$K_\zeta = 350,000$ In-Lb/Rad
9° Clevis
$\delta_3 = -65°$
$\Lambda = 11°$
Full Cruciform, Low EI
No Tip Weights
Radial Pitch Links

2/REV TORSION BENDING – (.0822R) ~ IN-LB

THRUST ~ LB
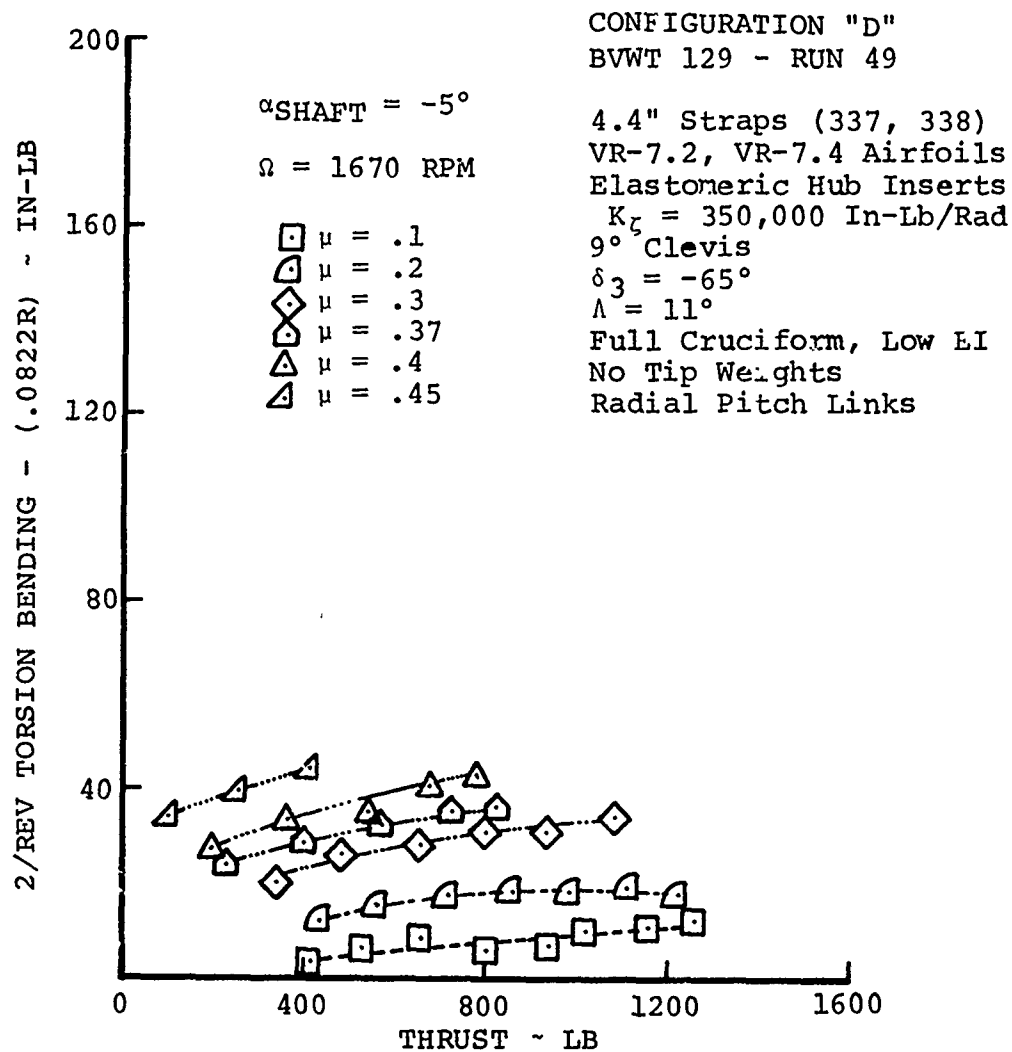
FIGURE 168   EFFECT OF ADVANCE RATIO ON SECOND-HARMONIC
                  TORSION BENDING LOADS FOR $\delta_3 = -65°$
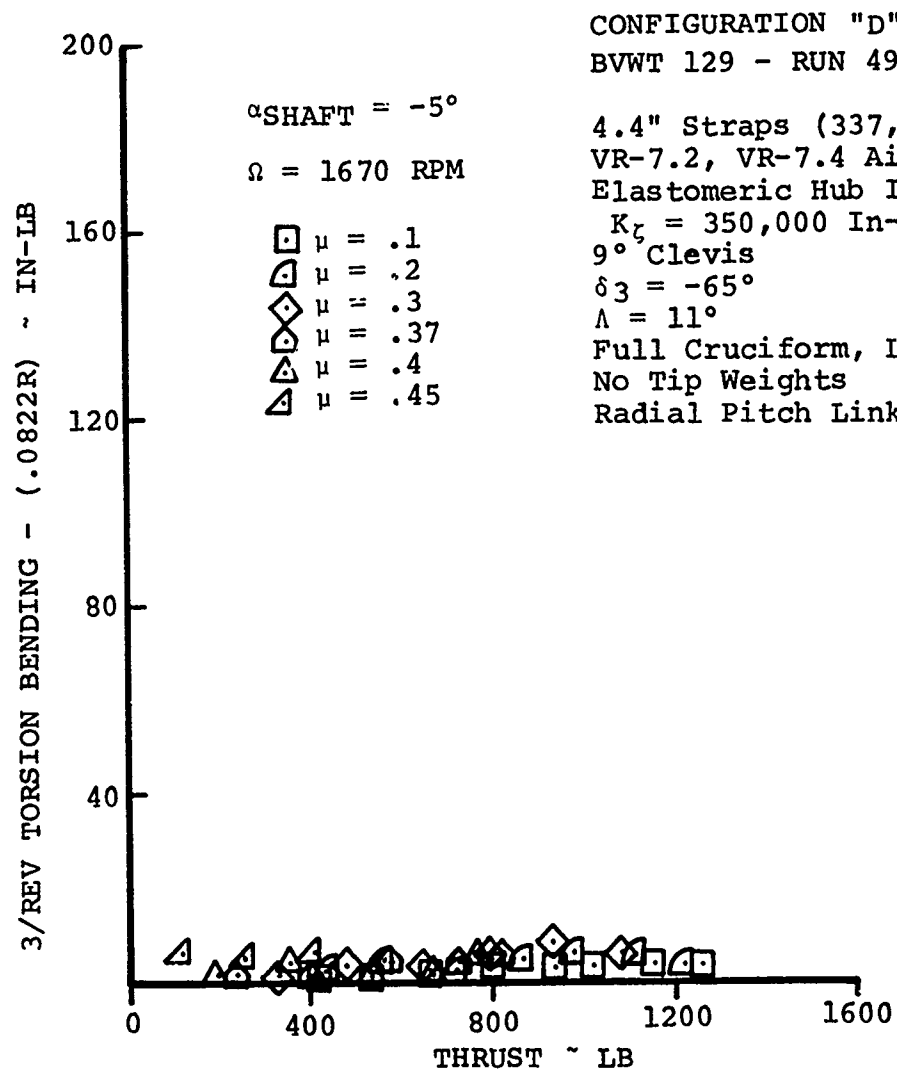
FIGURE 169 EFFECT OF ADVANCE RATIO ON THIRD-HARMONIC
TORSION BENDING LOADS FOR $\delta_3 = -65°$
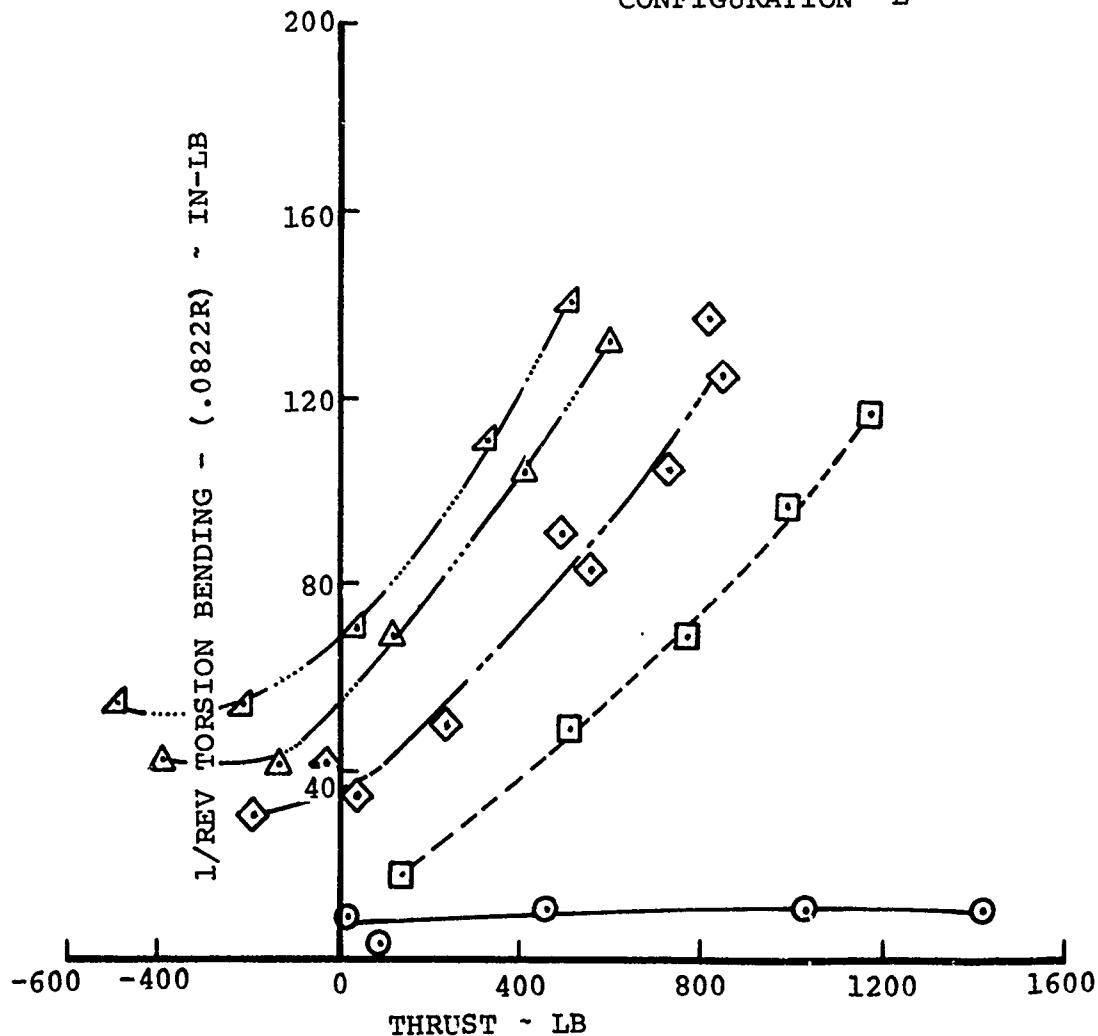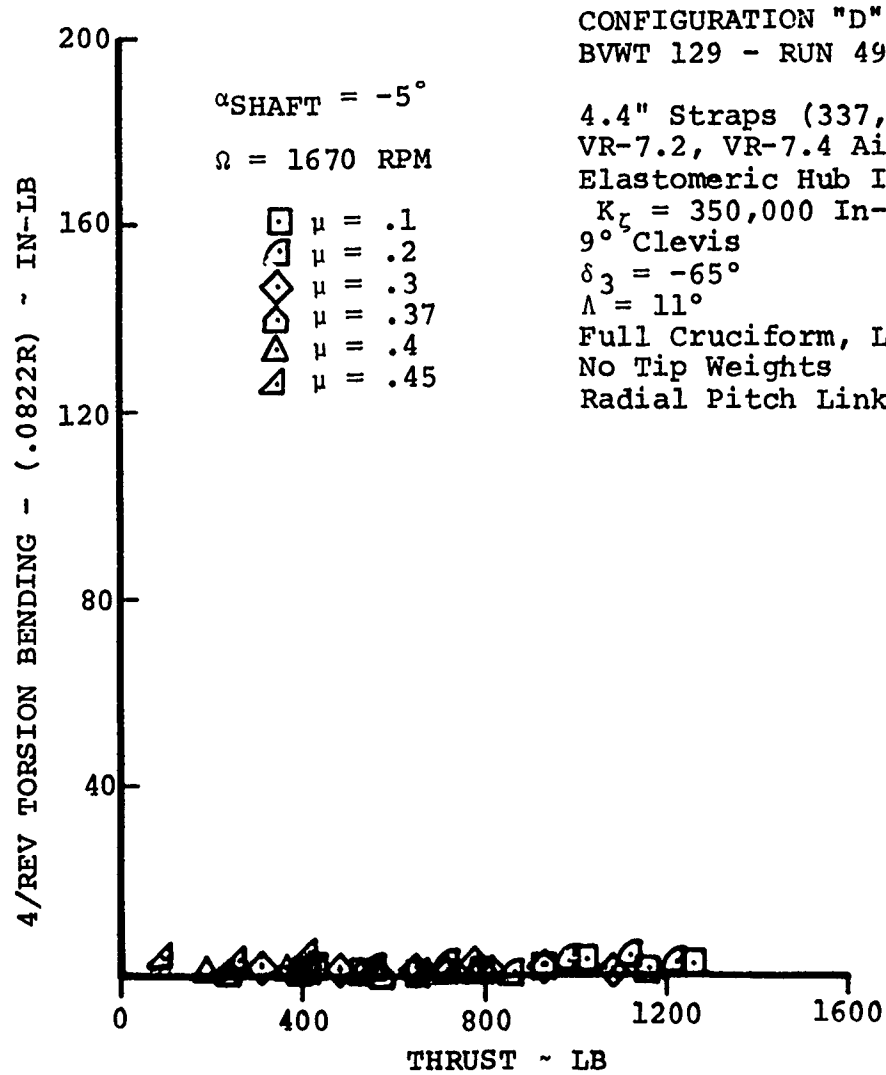
FIGURE 170   EFFECT OF ADVANCE RATIO ON FOURTH-HARMONIC
TORSION BENDING LOADS FOR $\delta_3 = -65°$

241

BVWT 129 - RUN 58

4.4" Straps (334, 337)
VR-7.2, VR-7.4 Airfoils
Elastomeric Hub Inserts
K_ζ = 350,000 In-Lb/Rad
9° Clevis
δ_3 = -45°
Λ = 11°
Full Cruciform, Low EI
No Tip Weights
Radial Pitch Links
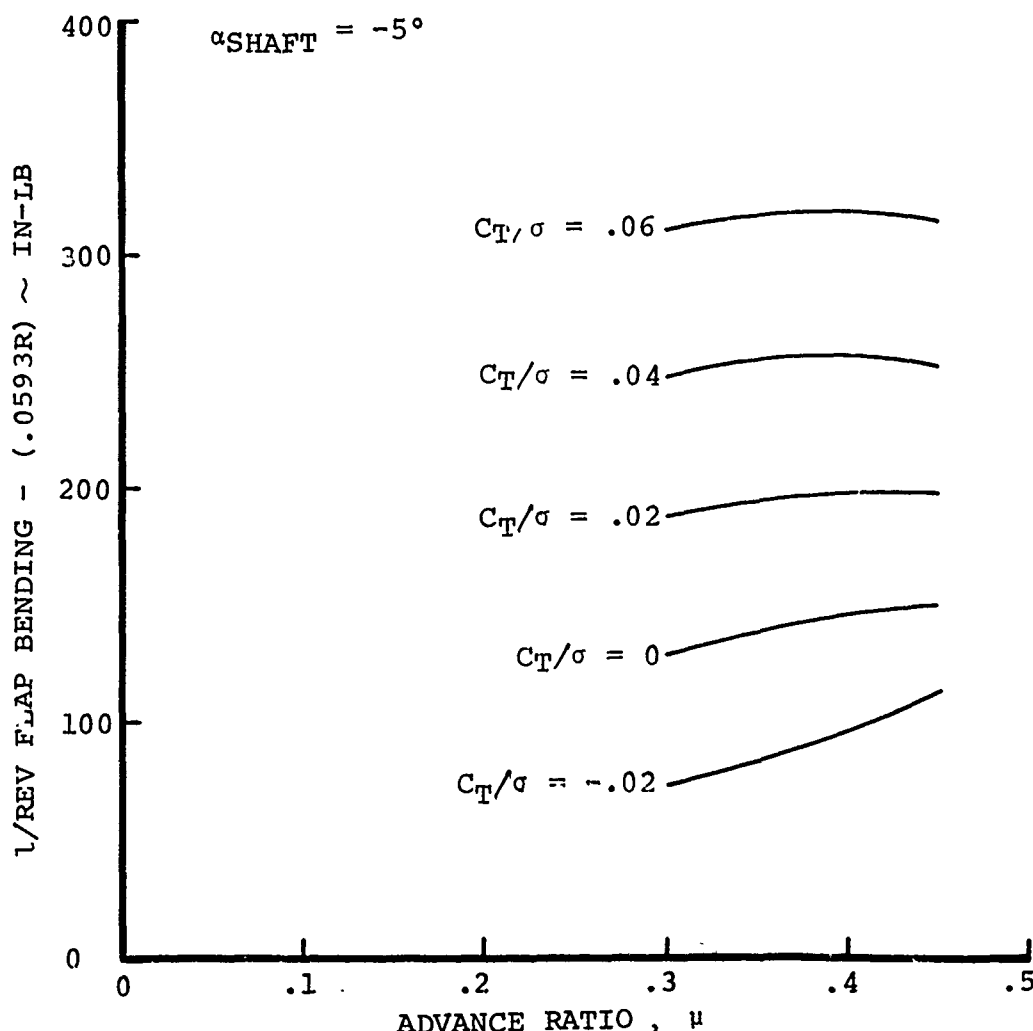
FIGURE 171   FLAP BENDING LOADS IN FORWARD FLIGHT FOR
δ_3 = -45°, CROSS-PLOTTED VS. ADVANCE RATIO

242

BVWT 129 - RUN 49

4.4" Straps (337, 338)
VR-7.2, VR-7.4 Airfoils
Elastomeric Hub Inserts
K_ζ = 350,000 In-Lb/Rad
9° Clevis
$\delta_3 = -65°$
$\Lambda = 11°$
Full Cruciform, Low EI
No Tip Weights
Radial Pitch Links
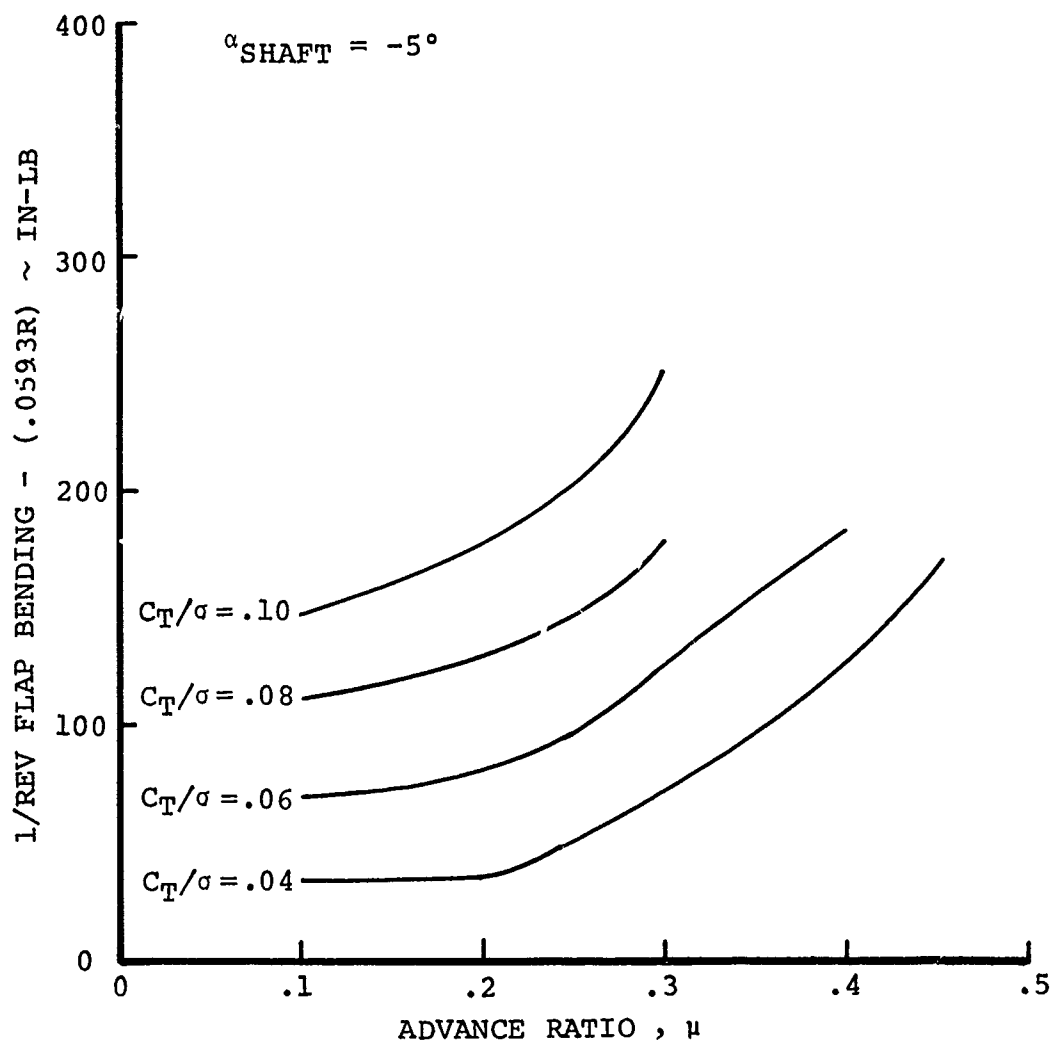
FIGURE 172   FLAP BENDING LOADS IN FORWARD FLIGHT FOR
$\delta_3 = -65°$, CROSS-PLOTTED VS. ADVANCE RATIO

243

7.0 ANALYSIS OF DATA

A limited amount of analysis was performed to determine if
the spanwise properties presented in Sections 2.0 and 3.0 of
this report can be used to predict the stability boundaries
and the associated modal frequencies and to ascertain if there
are significant problem areas that may complicate analysis of
this type. For this analytical work, the Boeing Computer Pro-
gram Y-69 and its derivative Y-71 were employed.

7.1 Description of Methodology

Y-69 - The Y-69 is a coupled blade flap/chord/torsion stability
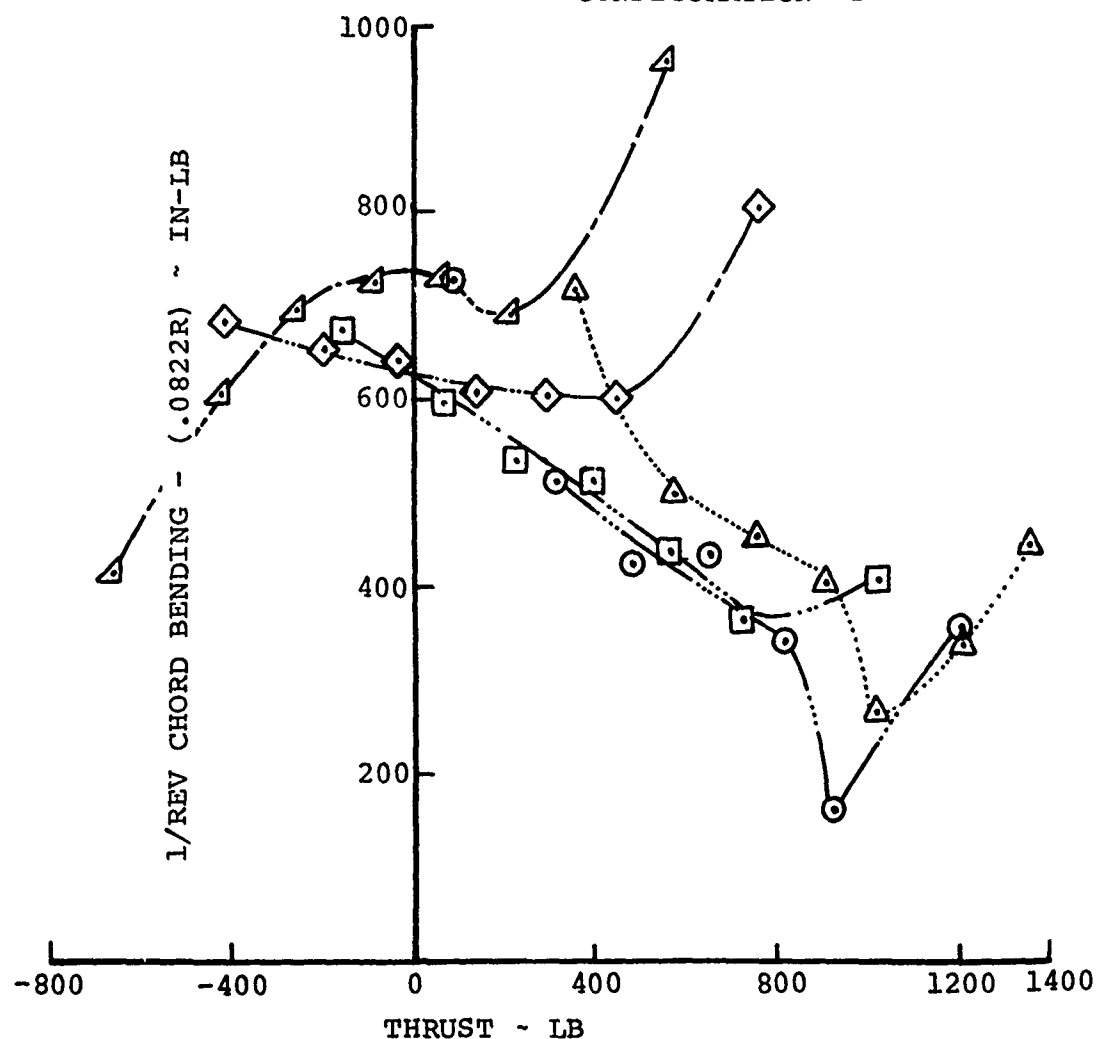analysis. It is used to predict the coupled modal frequencies
and modal damping of a low-twist helicopter blade or a highly
twisted blade for a vertical/short takeoff and landing (V/STOL)
aircraft. The method of solution for this program is a modi-
fied transfer-matrix approach. A lumped parameter approach
providing a maximum of 25 discrete sections of blade has been
adopted for the solution to represent the nonuniform distri-
bution of mass, inertia, elastic properties, and specific
geometric characteristics. The program also provide a so-
called bend matrix to account for finite deflections, a rigid
offset matrix to account for the noncoincidence of the blade
section center of mass, pitch axis, and elastic axis.

The aerodynamics for the program are designed for hover calcu-
lations only. The aerodynamic coefficients are selected by
the program through a table look-up procedure. To properly
represent the aerodynamics in flutter like conditions, Theo-
dorsen characteristic terms are also included.

Y-71 - The Y-71 coupled flap/chord/torsion blade natural fre-
quency analysis is virtually identical to the Y-69 analysis
with all aerodynamics removed. Y-71, therefore, is used to
determine the coupled natural frequencies of a rotor blade
in a vacuum.

7.2 Natural Frequency Analysis and Mode Shapes

The baseline configuration tail rotor was modeled for the Y-71
natural frequency analysis. This configuration is:

- VR-7.2 blade
- No tip weights
- Clevis angle = 9°
- No cruciform
- 4.4 inch width strap
- $\delta_3 = -65°$
- No blade sweep

244

The fully coupled mode shapes determined by this analysis for the first three modes at a rotor speed of 1700 rpm are shown in Figures 173 through 175. The first mode with a frequency of 1838 cpm, shown in Figure 173, is the first flap dominant mode. However, notice in the mode shape the large component of nose-down torsion. This large torsion component is characteristic of the pitch arm geometry which results in high flap-pitch coupling (δ_3) effects. Comparison of the flap slope at the blade three-quarter radius to the torsion angle at the same span station gives an estimate of the δ_3 effect in the configuration through the following relation,

$$\delta_3 = \tan^{-1} \left(\frac{\theta}{\beta}\right)$$

In this case for the -65° of nominal delta-3, the elastic $\delta_3 = -72.5°$. This value of δ_3 is considerably higher than the geometry of the configuration would indicate. This is due to the effect of the blade shear center offset, shown in Figure 9. As shown in Figure 73, shear center offset influences both the flap and torsion components outboard of blade station X/R = 0.6, therefore it changes the elastic δ_3 value.

The second mode, the first chord dominant mode, is shown in Figure 174. This mode is representative of the flap-lag "C" type mode recorded during the test. This is a result of the boundary conditions selected for the analytical blade retention at the root end of the flex-strap. The frequency of this mode is 2573 cpm (1.513 Ω). The mode indicates that the lead-lag motion of the blade is also strongly coupled to flap and torsion. Notice in this mode that the blade shear center outboard of X/R = 0.6 greatly influences the shape of the torsion component.

The third mode is shown in Figure 175. This mode is a highly coupled first torsion/second flap mode with 0.074 radian of noseup torsion deflection to 0.91 inch of flap up deflection. This mode, with a frequency of 3305 cpm (1.944Ω), demonstrates the stall flutter instability and limit cycles at frequencies near 2Ω.

The effect of several parameters on the frequencies of these critical modes follows so that additional insight into the behavior of the bearingless rotor may be gained.

7.2.1 Effect of Rotor Speed

The effect of rotor speed on the natural frequencies is presented in Figure 176. The plot shows the first four modes. As detailed in Section 7.2, the first three modes are the first flap, the first "C" type inplane, and the second flap/

245
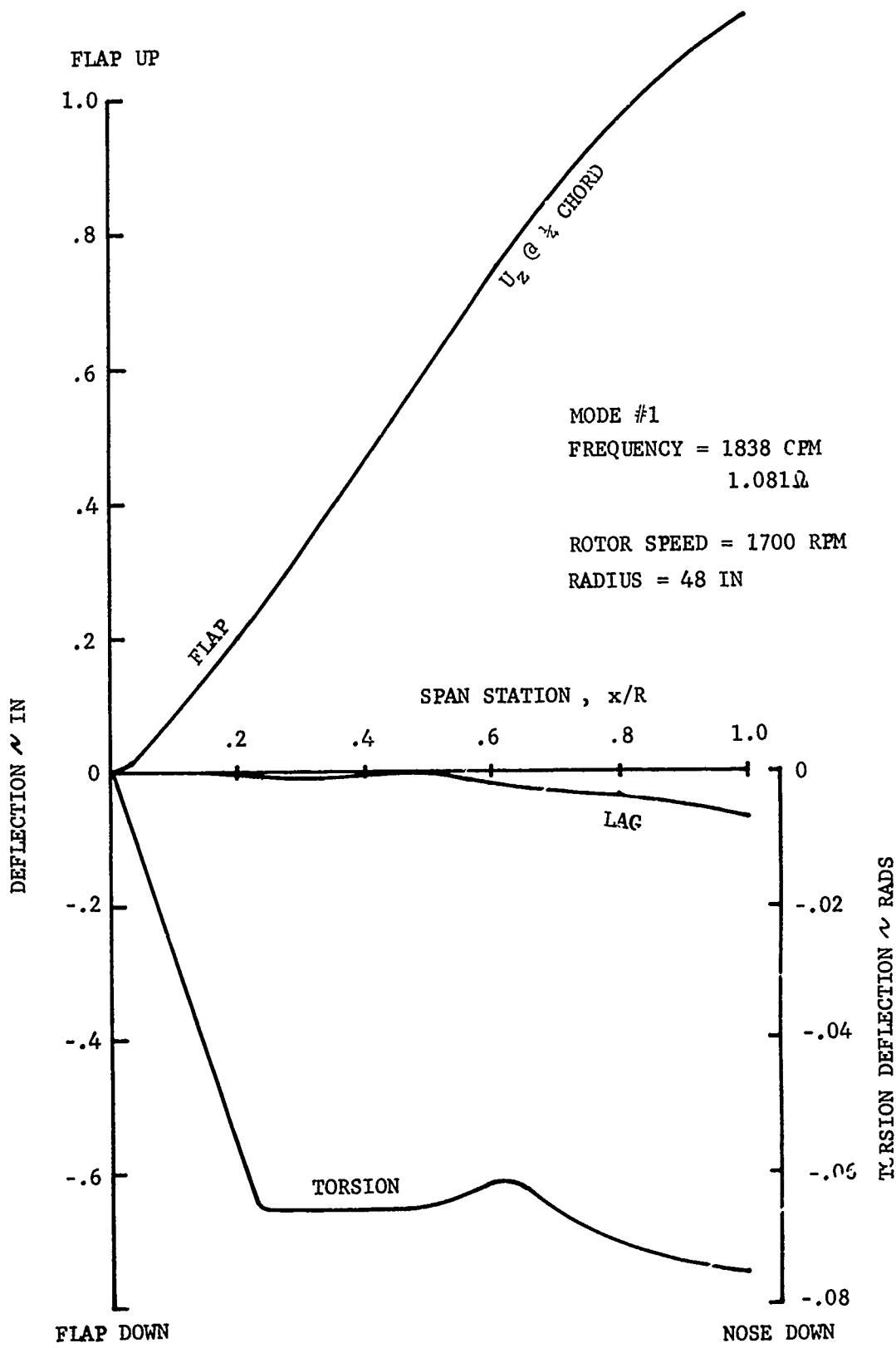
FIGURE 173   MODE SHAPE OF THE FIRST FLAP DOMINANT MODE
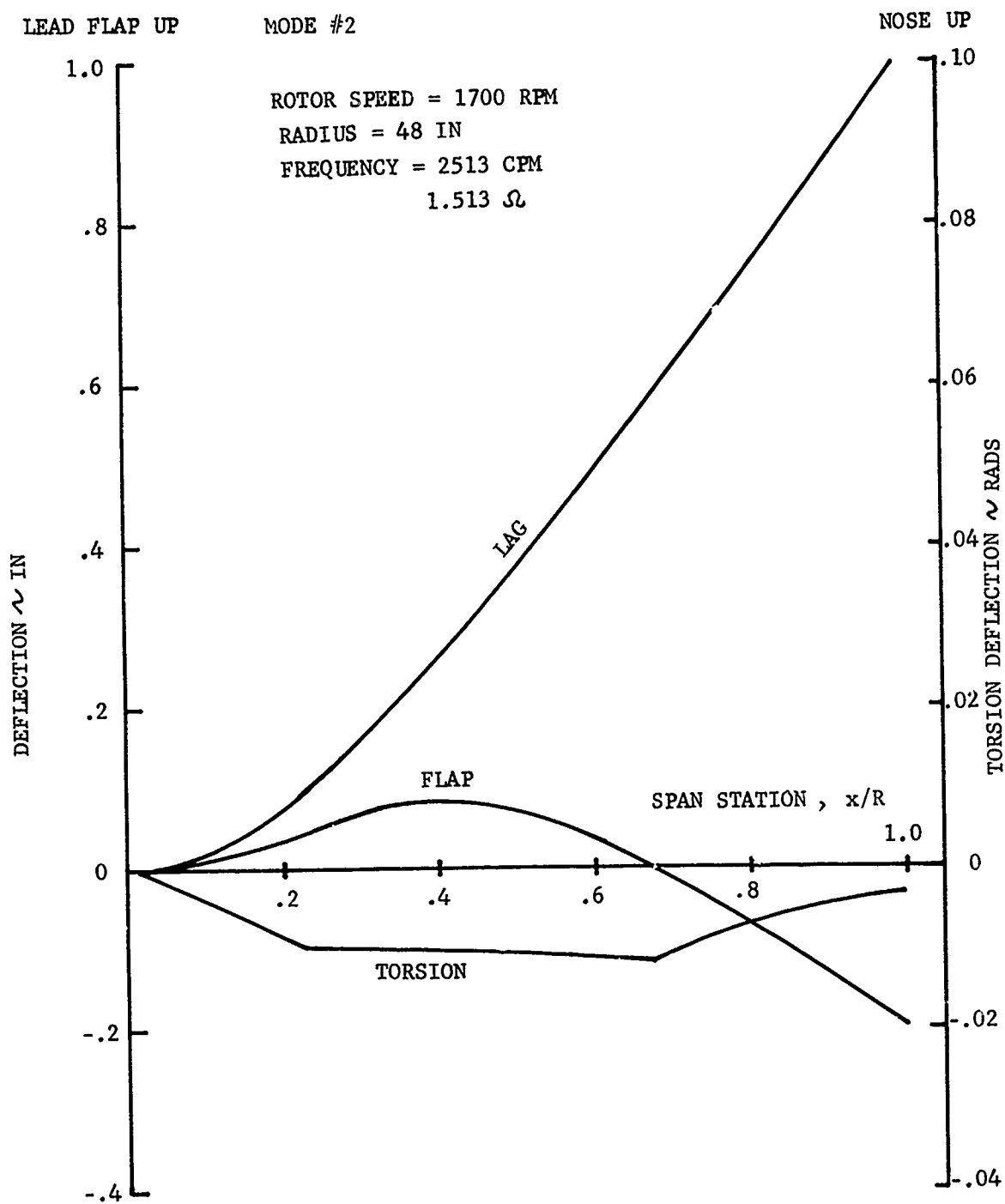
FIGURE 174   MODE SHAPE OF THE FIRST CHORD DOMINANT MODE
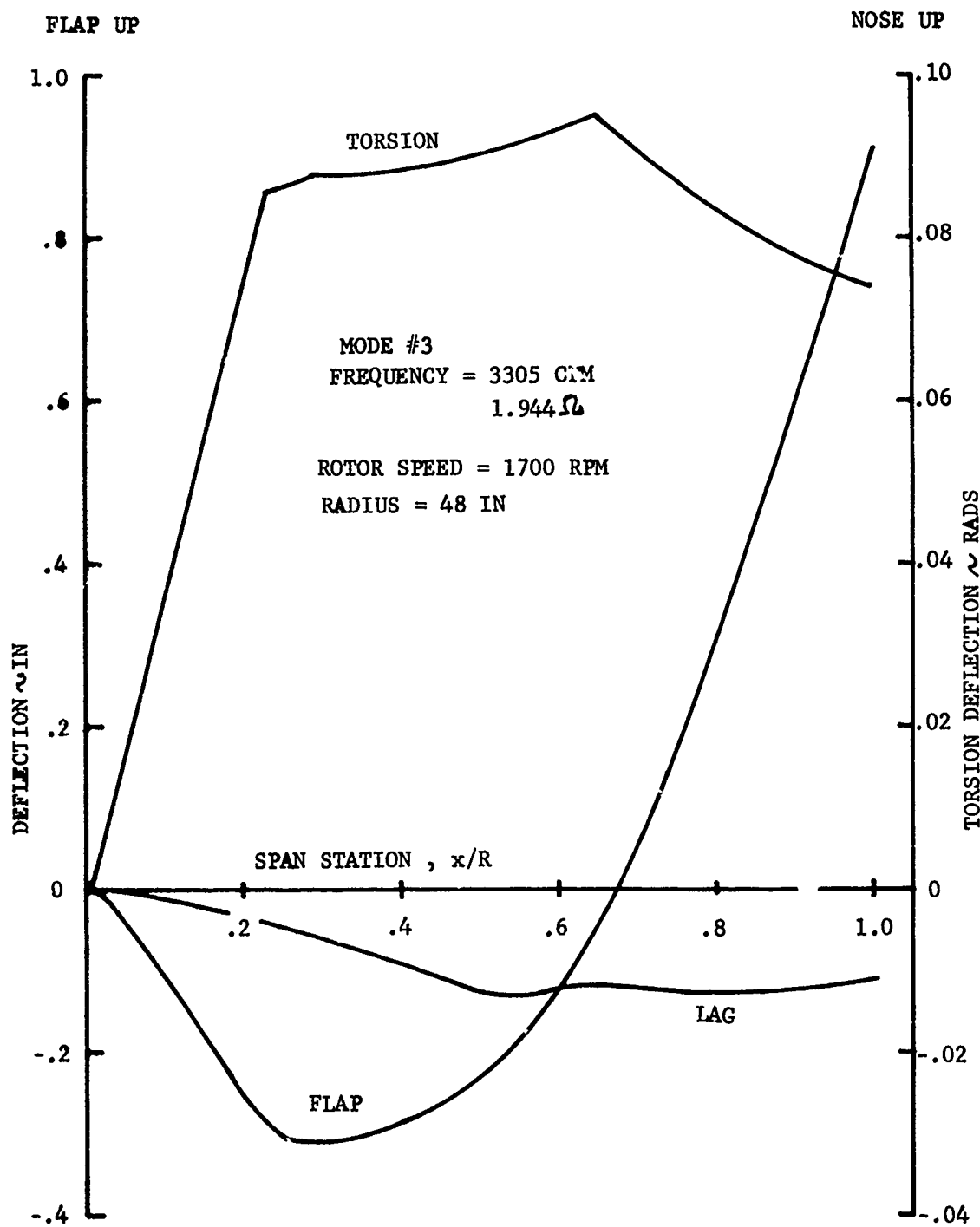
FIGURE 175   MODE SHAPE OF THE SECOND FLAP TORSION MODE
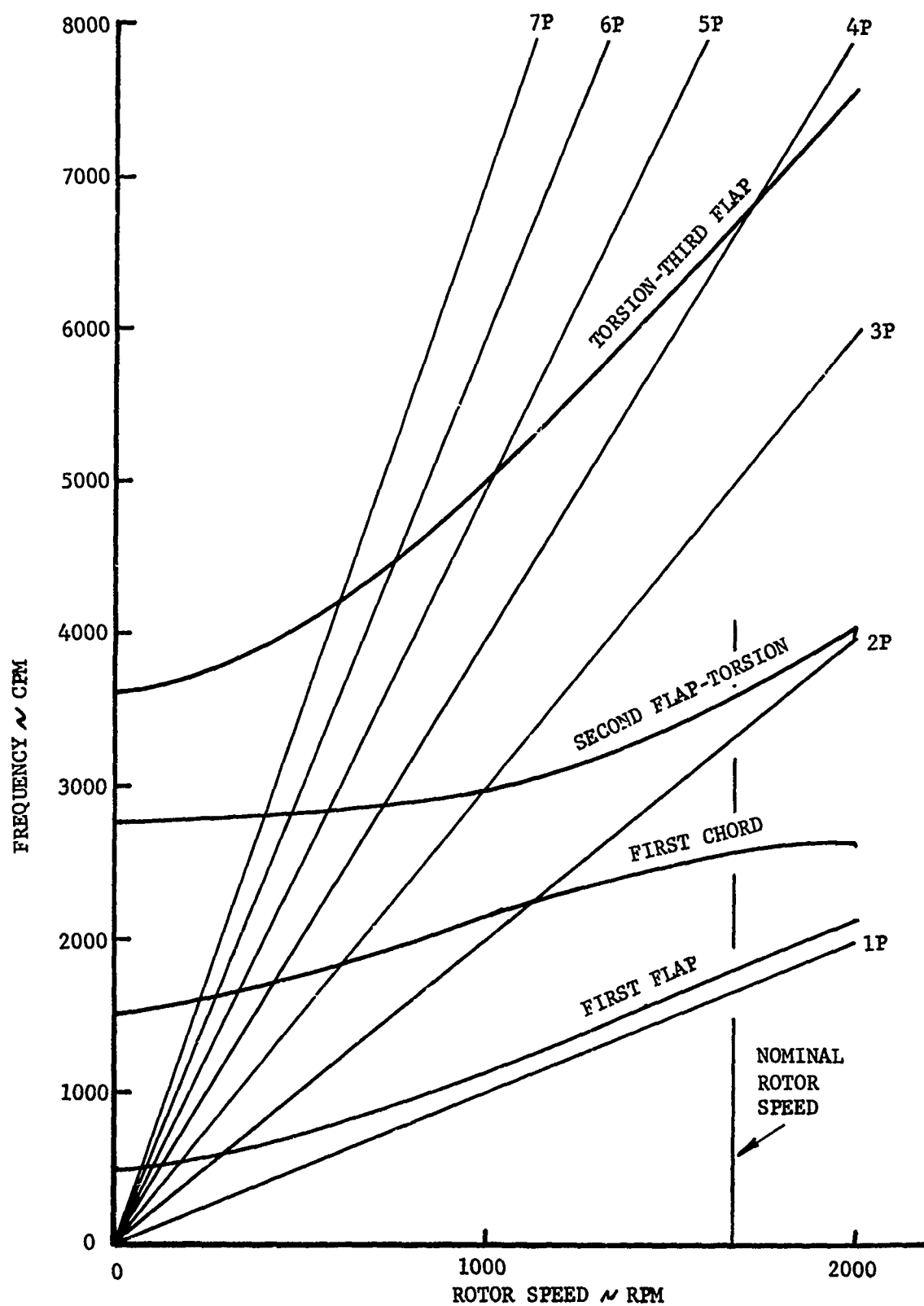
FIGURE 176   EFFECT OF ROTOR SPEED ON BLADE NATURAL FREQUENCY

249

torsion modes, respectively at 1700 rpm. The fourth mode shown is the first dominant torsion mode. The mode shapes presented in Section 7.2 describe the behavior of the model near the nominal rotor speed, 1670 rpm, which is indicated on this plot.

It is evident from Figure 176 that the first chord dominant mode is highly coupled with the second flap/torsion mode around rotor speed of 1400 rpm. In fact, at rotor speeds below 100) rpm, the second mode is the second flap/torsi⁻n modes and the third, the first chord dominant mode. At nominal rotor speed of 1670 rpm, the first chord is still coupled with the second flap/torsion. This explains why the flap component in the first chord mode, shown in Figure 174, has the second flap shape.

7.2.2 Effect of Collective Pitch

In both model testing and analysis, the effect of the collective pitch angle on the blade modal frequencies was observed; in particular, the inplane "C" mode. Plots of the variation in frequency with collective pitch angle are shown in Figures 177 and 178.

Figure 177 is a plot of he first four natural frequencies calculated by the Y-71 ar·lysis for the unswept baseline configuration near the nominal rotor speed. As shown in this figure, there is strong coupling present in the first inplane "C" mode, which produces a decrease in the frequency of the mode from a frequency of 44.5 cps at the collective corresponding to the strap flat ($\theta_{.75} = 9°$ with the 9° clevis) to a frequency of 41.5 cps at 18° of collective pitch. The coupling that produces this 3-cps decrease in frequency is an intermodal coupling primarily between the first inplane mode and the second flap/torsion mode. This is evidenced by the relatively large second flap component in the first inplane mode shape si·own in Figure 174 and discussed in Section 7.2.1.

The effect of collective pitch during model testing was recorded in test BVTC 011. This data, for a configuration different from the baseline configuration analyzed by Y-71, is shown in Figure 178. As shown in this figure, the "C" mode displays a similar decrease in frequency. Referring to the comparison of indicated and true collective pitch in Figure 95, the amount of decrease for the true collective pitch can be approximately determined. From this figure the flat strap position of 9° of collective corresponds to an indicated θ of 12°, and a $\theta_{.75}$ of 18° corresponds to an indicated value of 32°. Therefore, from Figure 178, there was a decrease of 4.5 cps between the indicated collectives of 12° and 32° at 1600 rpm.

250

BASELINE CONFIGURATION - NO SWEEP

TORSION

SECOND FLAP-TORSION

FIRST INPLANE "C" MODE

FIRST FLAP

MODAL FREQUENCY ∿ CPS

BLADE COLLECTIVE PITCH ∿ DEG
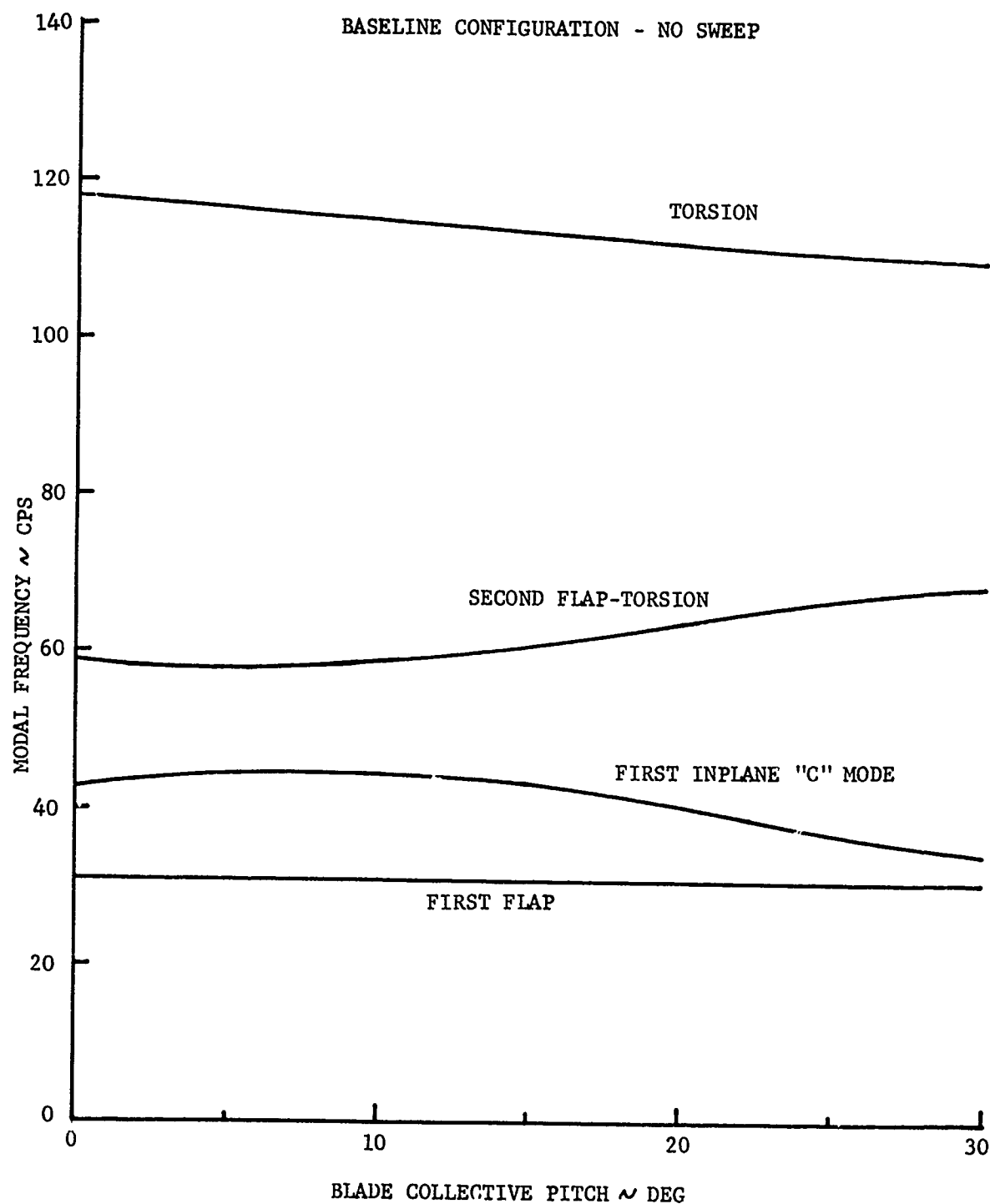
FIGURE 177   CALCULATED COLLECTIVE PITCH EFFECT ON
                  BLADE NATURAL FREQUENCY

251

BVTC 011

3.6" Straps (334, 337)
VR-7.2, VR-7.4 Airfoils
No Hub Inserts
9° Clevis
$\delta_3 = -65°$
$\Lambda = 6°$
Full Curciform, Low EI
Radial Pitch Links
Tip Weights, 88 Fwd/0 Aft

—————— ◯ 1200 RPM

——·—— △ 1400 RPM

— — — ☐ 1600 RPM

—··— ◇ 1800 RPM
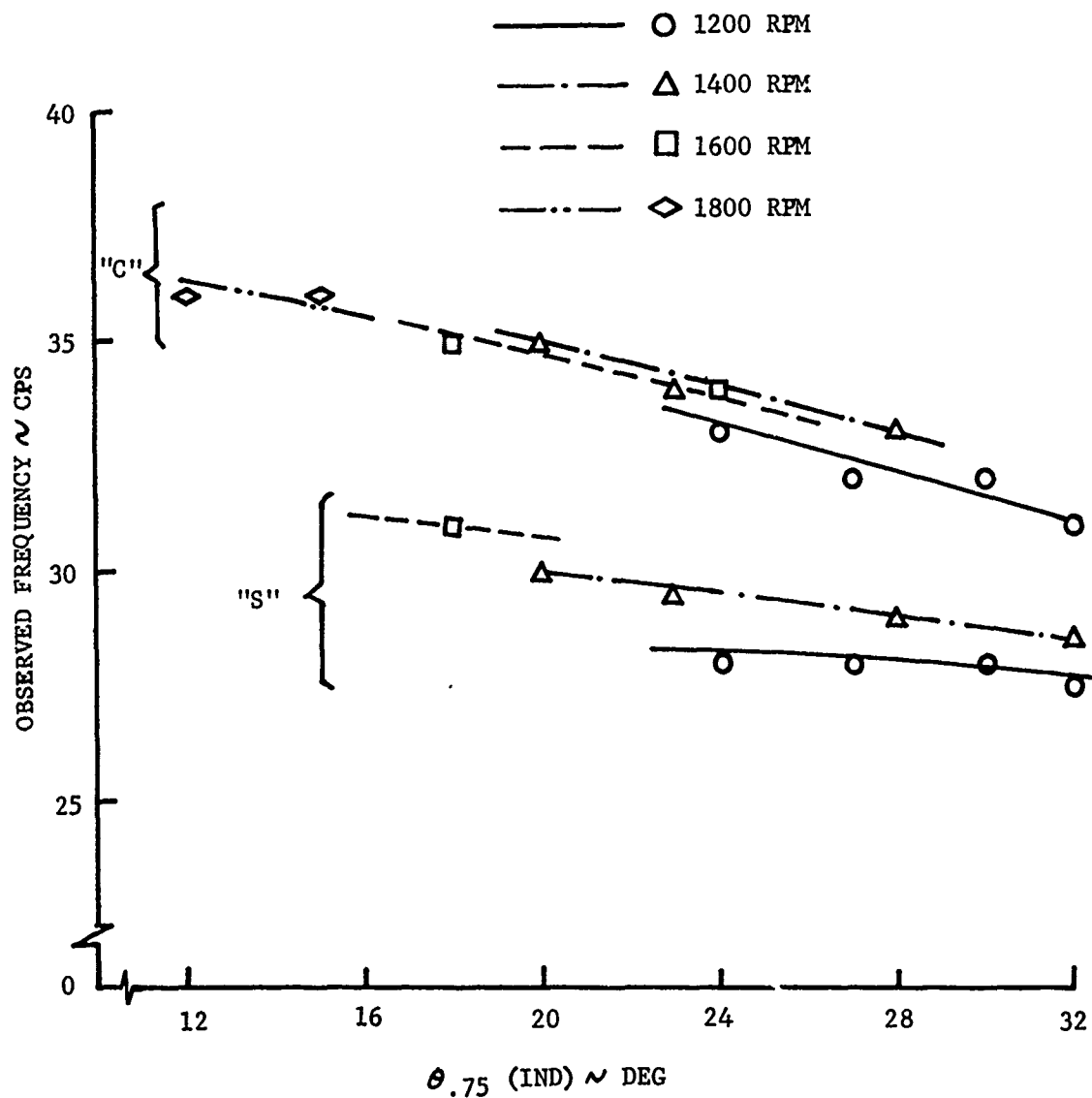
FIGURE 178   DEPENDENCE OF CHORD FREQUENCIES ON COLLECTIVE
AS DETERMINED BY SPECTRAL ANALYZER

Better correlation between test and analysis can be achieved
by better matching of the analysis to the test configuration.
For the limited analysis performed in this report, this was
not an objective. Therefore, preference was given to the
analysis of the baseline configuration.

7.2.3 Effect of Blade Sweep

The effect of blade sweep on natural frequencies was calcu-
lated using the Y-71 analysis. These results are shown in
Figure 179. In these calculations a collective of $\theta_{.75} = 9°$
and a rotor speed of 1700 rpm was used. The blade sweep angle
was input at the blade attachment point (span of 19.5 inches).
As shown in the figure, variation of this parameter produced
no significant change in the frequency of any of the first
four modes calculated.

The observed frequency in the test for swept configurations is
apparently influenced by several factors. Because sweep is a
powerfully stabilizing parameter, Section 5.2.4, which per-
mitted the model to reach high values of C_P/σ and θ, it would
be expected that the observed frequency at the boundary be
significantly lower due to the coupling effects at high
collective explained in the preceding section. Since this
is not the case, another factor must also influence frequency
tending to make it rise, thus cancelling the effect of collec-
tive. Such a factor, which gives the proper trends of sta-
bility and frequency as a function of sweep angle, appears
to be the dynamic strap shear center effect that is detailed
in Section 7.3.2.

7.3 Stability Analysis

The stability analysis of the flex-strap tail rotor was con-
ducted using Boeing Computer Program Y-69. A brief description
of the program is given in Section 7.1. This program is very
similar to the natural frequency program Y-71, which is used
to calculate the dynamic characteristics of the rotor blade-
flex-strap combination detailed in Section 7.2. The prime
difference between these two computer programs is that the
Y-71 calculates the eigen value (frequency) and eigen vectors
(mode shape) of a lumped parameter system in vacuum, while
the Y-69 calculates the same thing with hover aerodynamics.
The eigen values and eigen vectors from Y-69 are complex
numbers. The real part of the eigen value gives the informa-
tion of modal damping and the imaginary modal frequency.

7.3.1 Effect of Delta-3

The coupled flap-lag stability phenomenon of a rotating lift-
ing surface was explored in depth in Reference 3. There is a
potential instability when the first chord natural frequency

253

BASELINE CONFIGURATION

$\theta_{.75} = 9°$

$\Omega = 1700$ RPM
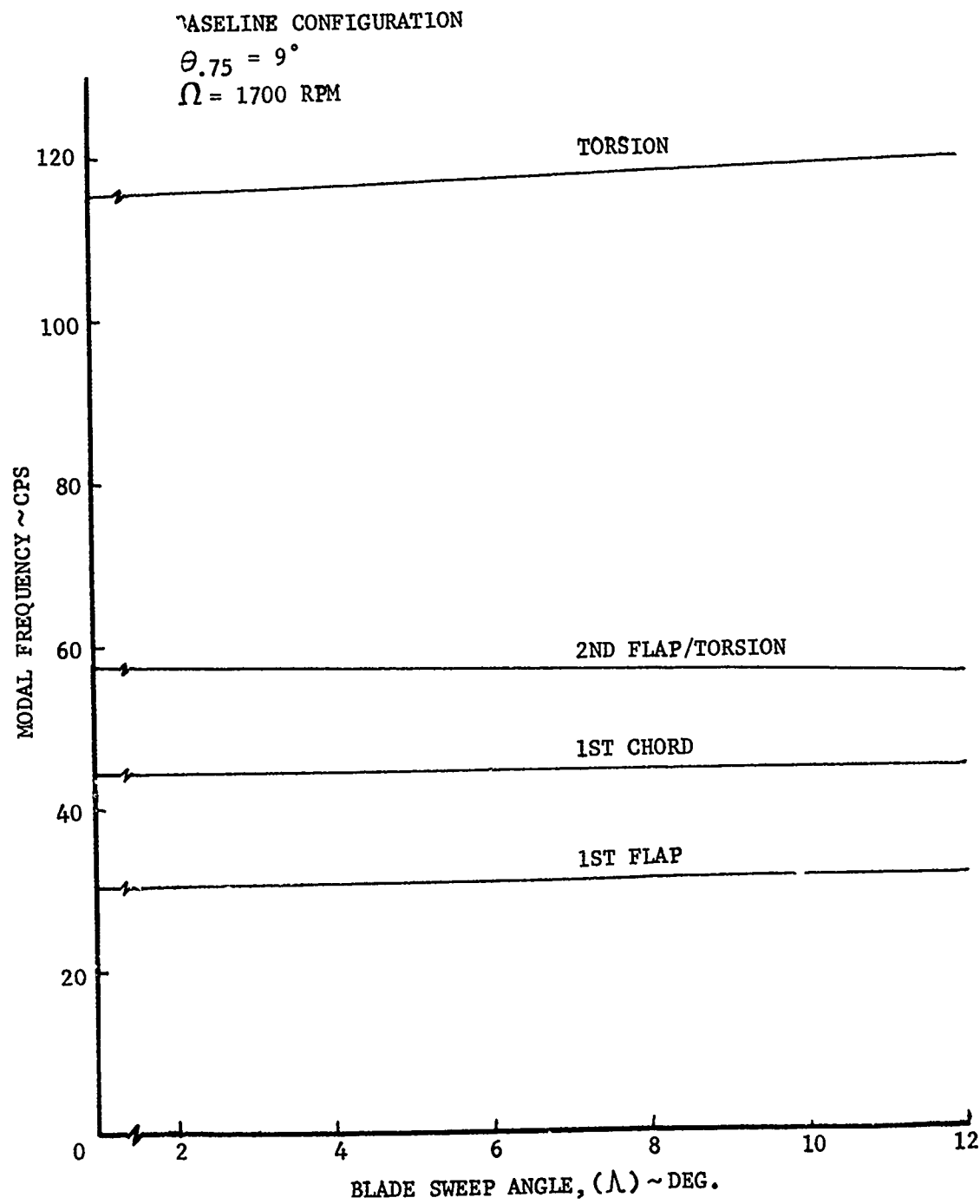
FIGURE 179   EFFECT OF SWEEP ON BLADE NATURAL FREQUENCY

coalesces with the first flap frequency. Figure 180, taken from Figure 4 of Reference 3, shows the potential instability as a function of in-plane and flap frequencies and of the collective pitch. As shown, the region of instability expands with increasing collective pitch. In other words, at higher collective pitch, there will be flap-lag instability even if the frequencies are not in exact resonance. Such is the case for the bearingless flex-strap rotor blade flap-lag stability reported herein.

As detailed in Section 7.2, the calculated first flap frequency in vacuum is 1.081/rev, and the first chord 1.513 rev for the baseline rotor blade-flex-strap configuration. However, this in-vacuum frequency difference disappears when the aerodynamics is included in the calculation as in program Y-69, in conjunction with high collective pitch. This is because of the high pitch-flap coupling, delta-3, used on this tail rotor design. The flap frequency, including the delta-3 effect, can be estimated using the following expression:

$$\frac{W_{1f}}{\Omega} = \left[\frac{W_{1fR}}{\Omega} - \frac{\gamma}{8} \tan_{\delta_3} \right]^{1/2}$$

where W_{1fR} is the in-vacuum frequency and γ is the Lock number. For the VR-7 airfoil, $\gamma = 2.39$, using the nominal $\delta_3 = -72.5°$ as indicated in Section 7.2 and $W_{1fR} = 1.081\Omega$, we have the first flap frequency in air equal to 1.42/rev close to the first chord in-vacuum frequency. As discussed in Section 7.2.2, the first chord frequency decreases with increasing collective. At collective of 20°, the first flap and first chord is in near resonance, thus the potential flap-lag instability.

Figure 181 shows the Y-69 calculated complex eigen value for the first chord mode. The solid square at (12.74 + 221.88j) is for the baseline configuration, at a high collective pitch of 20°. As shown, it is unstable. Also shown are three other eigen values for the first chord mode, which will be discussed in Section 7.3.2.

As shown in Section 5.2.3 test results, lower delta-3 improves the flap-lag stability. This is primarily due to the fact that the first flap frequency in air is much lower than the $\delta_3 = -45°$ case as compared to the -65° case and therefore is not in near resonance with the first chord mode. However, while the stability is improved with lowered δ_3, the blade bending goes up as a consequence, Section 6.2 .. As discussed in that section, a balance has to be struck between the stability and the load considerations.
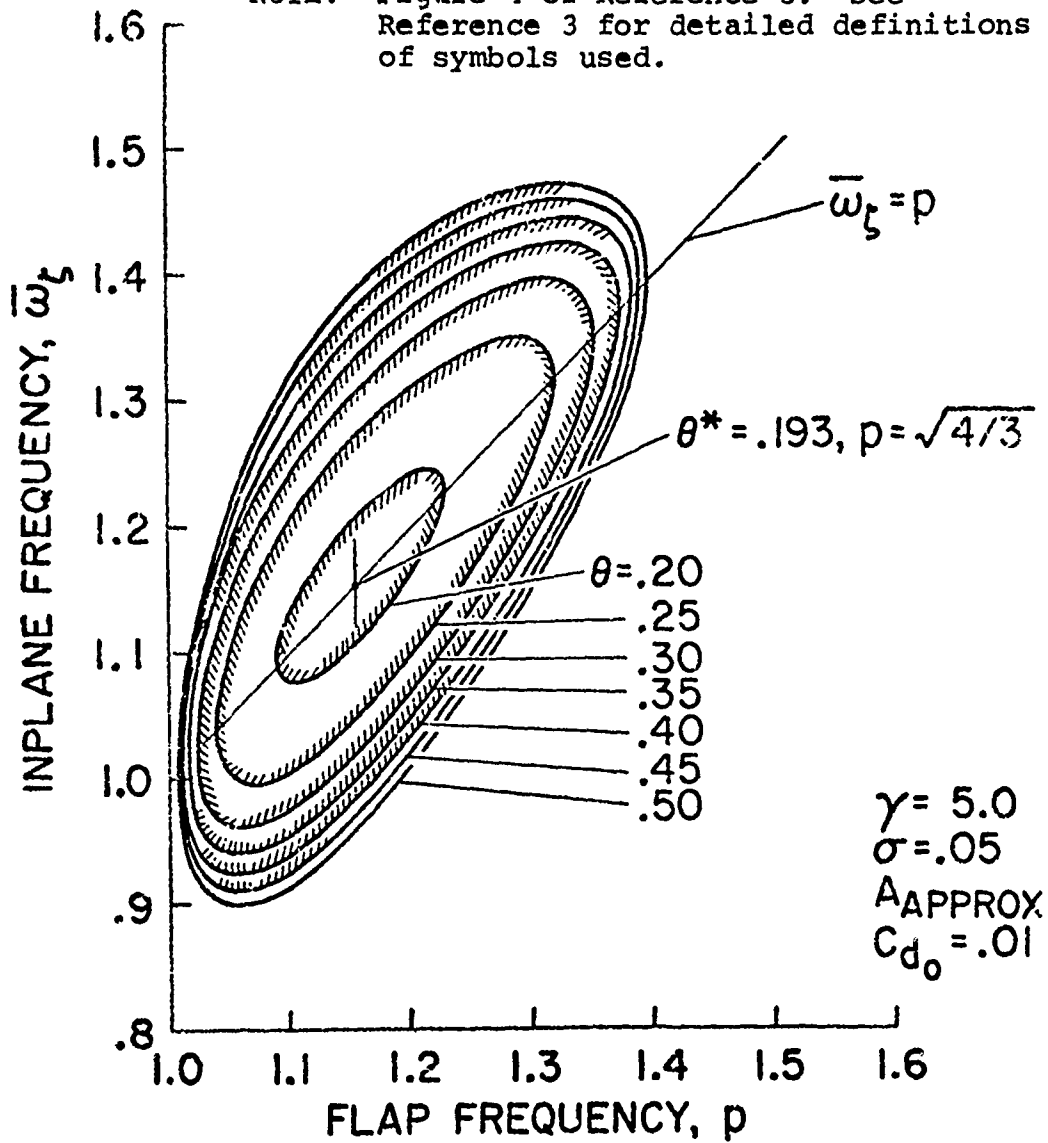
FIGURE 180   POTENTIAL FLAP-LAG INSTABILITY
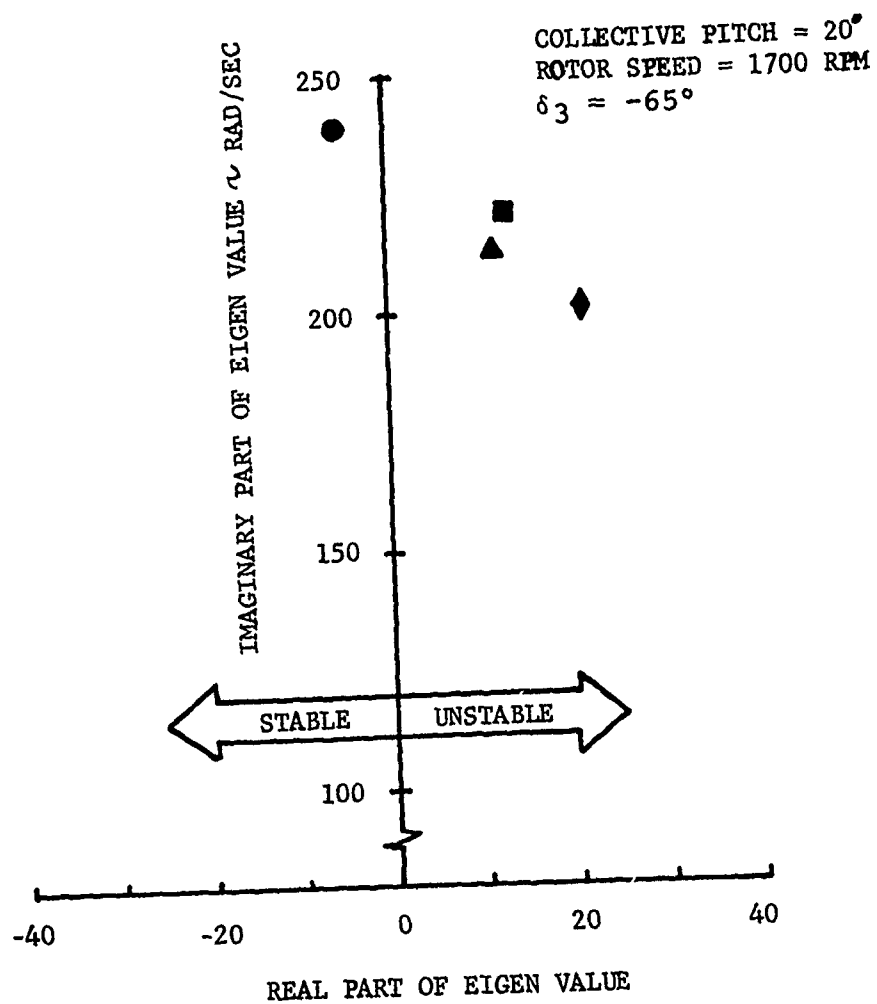
FIGURE 181   STABILITY OF FIRST CHORD DOMINANT MODE

257

A complete set of inputs to the program Y-69 for the baseline configuration is shown in Appendix B.

7.3.2   Effect of Strap Shear Center

The test results of Section 5.2.4 showed a significant stabilizing effect on the flap-lag stability by sweeping the blade aft. The Y-69 analysis was used to calculate the chord dominate mode stability with 12° of aft sweep. As shown in Figure 181 by the solid triangle, the improvement in stability, or the decreasing positive value of the real part of the eigen value, from the no sweep case, solid square, is negligible.

Knowing the importance of the shear center effect on the blade mode shape, as seen in Section 7.2, its effect on the stability of the chord dominant mode was investigated. This activity was also suggested by intuition. The flex strap is more of a plate structure than a beam. Its bending-torsion behavior in a centrifugal force field will be different from the beam. With the blade swept aft, the CF due to the blade no longer lines up with the center line of the strap, shown as the dashed line in the top sketch of Figure 182, which is also the line of chordwise symmetry and the shear center (see Figure 9). How will the shear center of the strap vary with the blade sweep? Will it incline toward the leading edge from inboard to outboard, as shown in the middle sketch of Figure 182, when the blade sweeps aft? Or, will it incline toward the trailing edge, as shown in the bottom sketch? These questions are answered in Section 7.3.3, Determination of Strap Shear Center with Centrifugal Force. For now, let us examine the effects of these shear center variations on the chord mode stability.

The eigen value of configuration #1, which has the forward inclination of shear center from inboard to outboard and no blade sweep, middle sketch of Figure 182, is shown in Figure 181 by a solid rhombus. Compared to the solid square, the deterioration in stability is rather large. With the shear center inclined aft and the blade swept aft, configuration #2 of Figure 182, the Y-69 gives a stable root for this chord dominant mode. This root is shown in Figure 181 as a solid circle. The improvement in stability, from the solid square, is significant. This improvement in stability is more like the observed stability improvement with the blade aft sweep detailed in Section 5.2.4. It seems that the aft sweep of the blade causes the shear center of the strap to have a similar aft inclination and consequently stabilizes the chord mode.

Now the question to answer is, "Does the aft sweep of the blade indeed change the effective shear center of the strap and cause it to incline aft?" This is discussed in the following section.

258

------- INDICATES MODELED SHEAR CENTER (OR PITCH AXIS)

BASELINE CONFIGURATION

LEADING EDGE

C/L

FLEX-STRAP

½ C

PITCH ARM

CLEVIS

BLADE

CONFIGURATION #1

C/L

LEADING EDGE

½ C

EFFECTIVE SHEAR CENTER

CONFIGURATION #2

C/L

LEADING EDGE

$\Lambda \approx 12°$

½ C

EFFECTIVE SHEAR CENTER
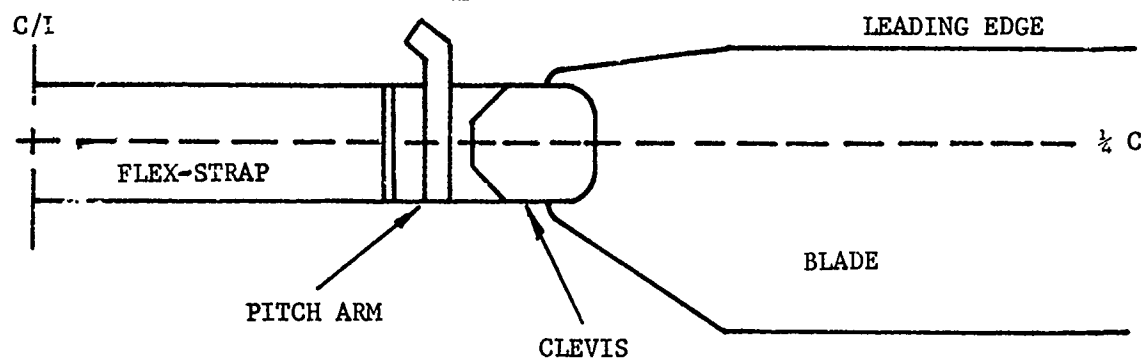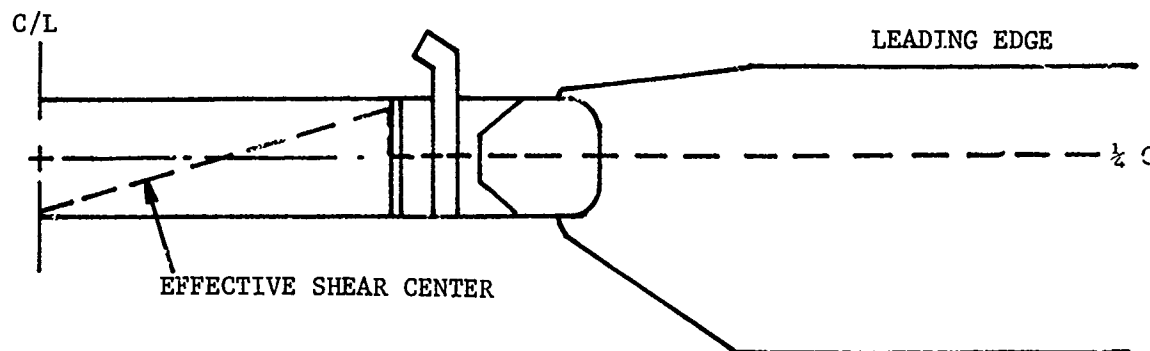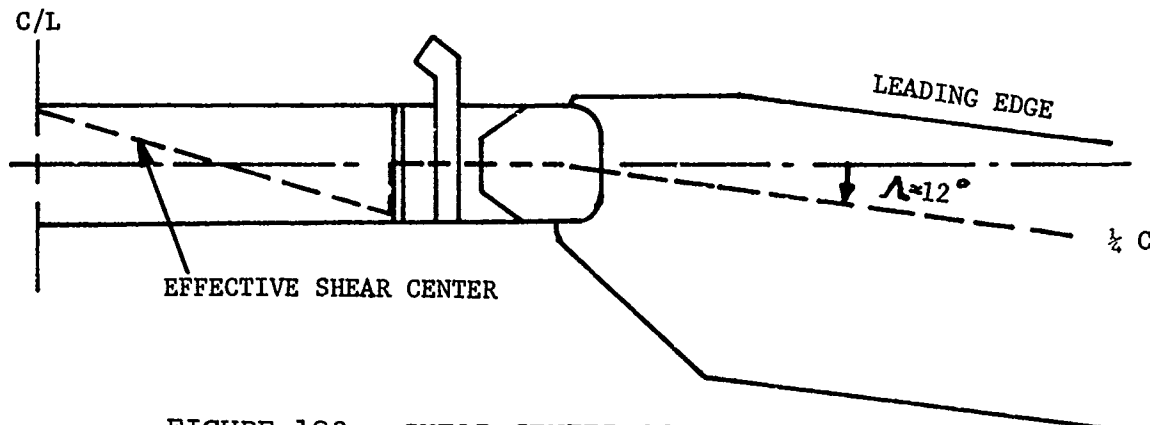
FIGURE 182   SHEAR CENTER SCHEMATICS

7.3.3 Determination of Strap Shear Center with Centrifugal Force

The flex strap and the flexure are idealized as plate elements
on the NASTRAN. Figure 183 shows the NASTRAN model of this
idealization. The strap is broken down into four lengthwise
strips and each strip is further broken down into fifteen plate
elements, which gives a plate element of approximately 1.1 inch
square. Both ends of the flexure and the end of the strap, at
the center of rotation, are fixed. The blade is idealized as
seven concentrated masses on a straight line connected to the
strap at point "A" in Figure 183.

An upward vertical force is applied at point "A" with and with-
out the blade sweep. Without blade sweep, the strap has a pure
vertical deflection; that is, the vertical deflections of the
node points on one chord line are identical from leading edge
to trailing edge, ignoring tiny differences due to plate con-
siderations. This is expected, since there is no coupling.
Also, the magnitude of the vertical displacement diminishes
when moving from point "A" to the fixed end, center of rotation.
With the blade swept aft, however, the leading edge of the strap
has more vertical deflection than the trailing edge with the same
vertical force applied at point "A". The rotations of these
chord lines are obtained from the differences of the vertical
deflections of the strap with and without the blade sweep.
These net torsional deflections along the radius of the strap
are shown in Figure 184. It is evident from these torsional
deflections that the aft sweep of the blade has shifted the
shear center of the strap aft; consequently, the upward vertical
force applied at point "A" is producing noseup pitching moments
along the strap. This moment can be calculated using the follow-
ing expression.

$$M = \frac{\Delta \Theta}{\Delta \ell} \ (GJ)_{equ.}$$

if the $(GJ)_{equ}$ is known.

Pitching a thin plate in a centrifugal force field, there exists
a centrifugal restoring moment, the so-called "trapeze" effect
(not to be confused with the so-called "tennis racquet" effect).
This CF unwinding effect produces an equivalent torsional stiff-
ness. To obtain the equivalent torsional stiffness of the strap,
a torsional moment of 10,000 in-lb is applied at point "A" with
the blade unswept. The resultant torsional deflection of the
strap, under the CF field, is shown in Figure 185. From this,
the equivalent torsional stiffness is obtained, and it is from
10 to 20 times higher than the static GJ of the strap shown in
Figure 12.

BLADE SWEEP

STRAP TO BLADE
JUNCTION

POINT "A"

PLATE ELEMENTS

STRAP

FLEXURE

CENTER OF ROTATION

FIGURE 183   NASTRAN MODEL OF STRAP

ROTOR SPEED = 1337 RPM
DIFFERENTIAL BLADE SWEEP = 12°

NET CHANGE OF TORSIONAL DEFLECTION ~ RAD

LEADING EDGE UP

STRAP RADIUS ~ IN.
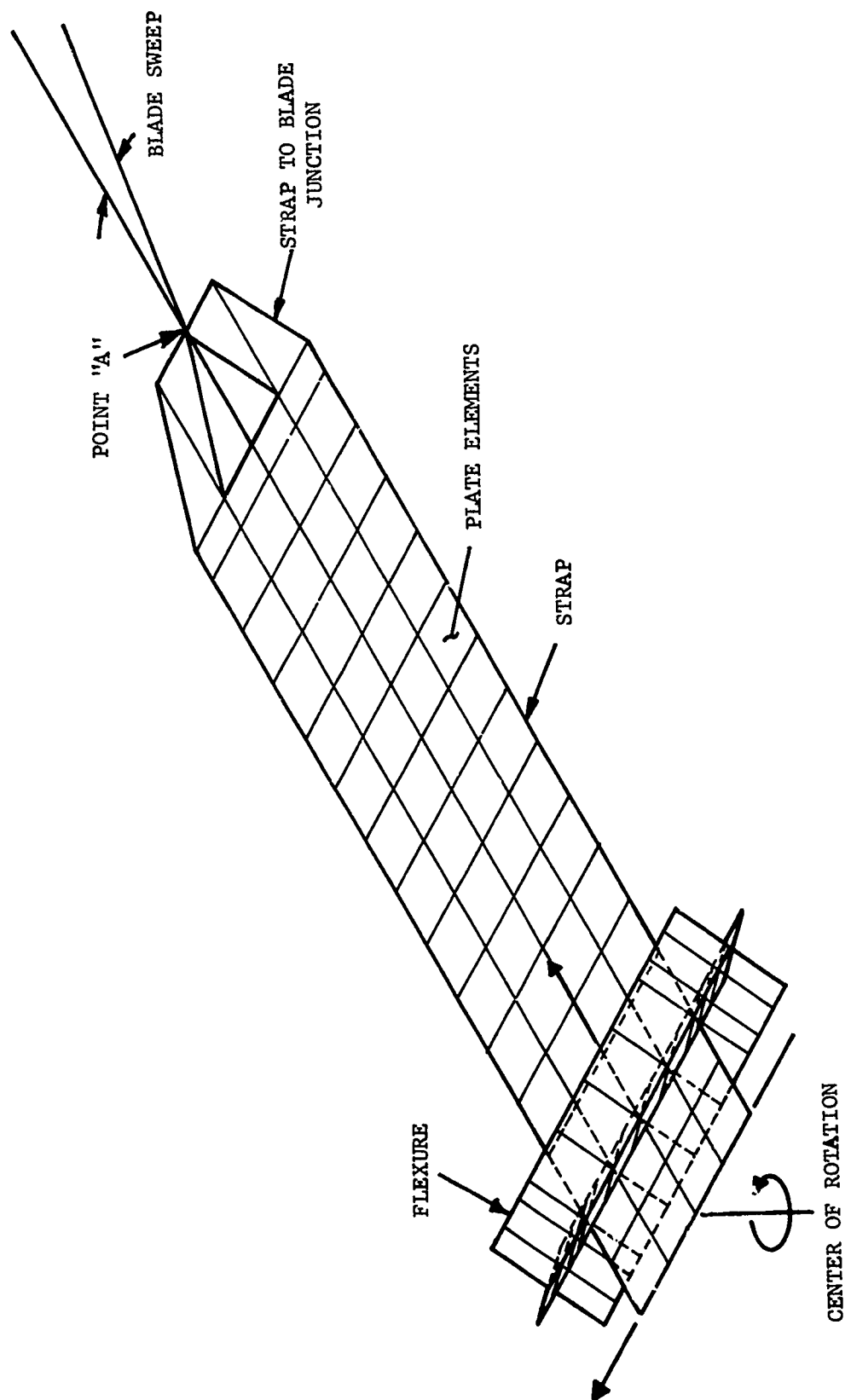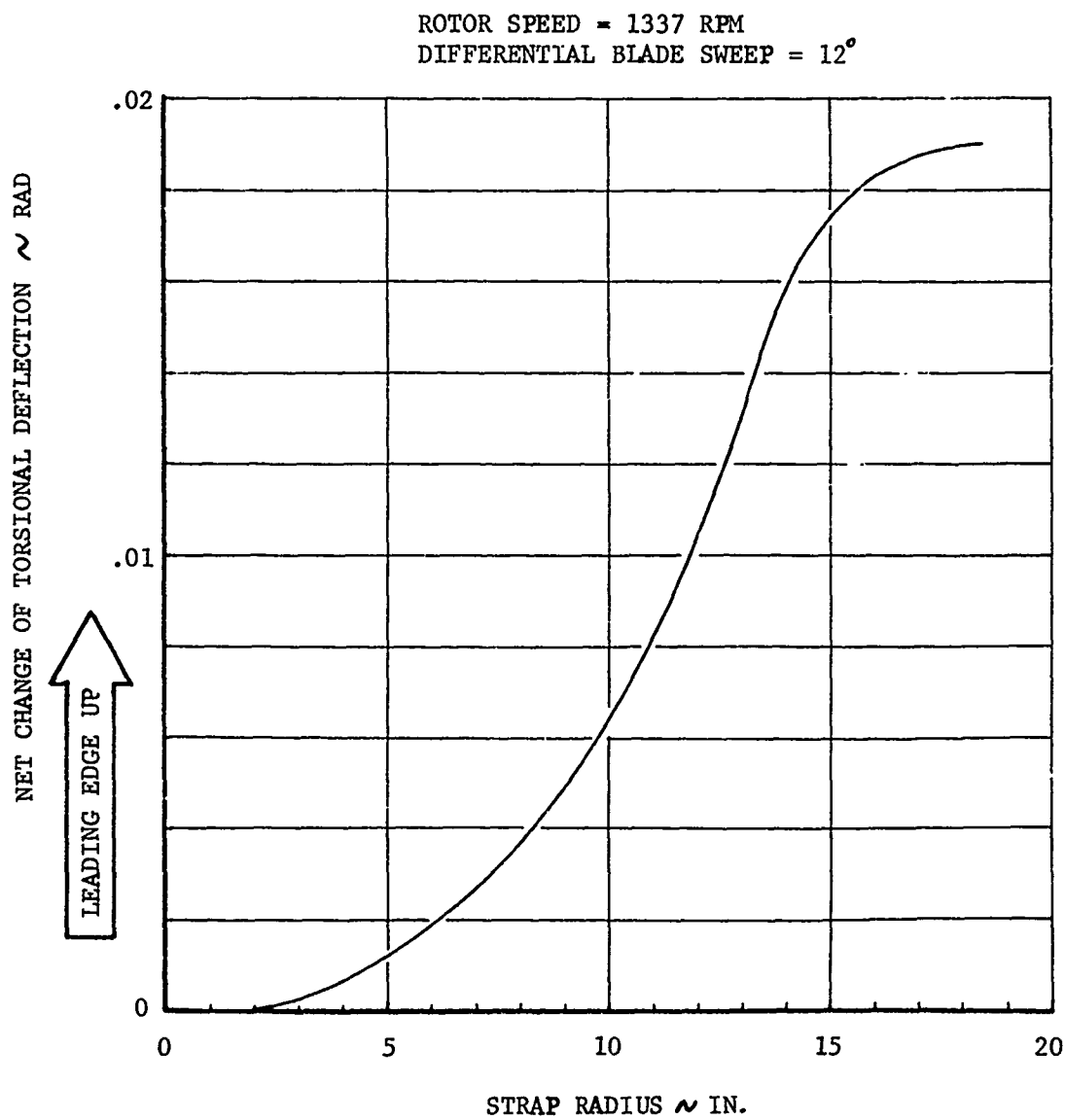
FIGURE 184   TORSIONAL DEFLECTION OF STRAP UNDER VERTICAL
LOAD WITH BLADE SWEPT AFT

ROTOR SPEED = 1337 RPM
BLADE SWEEP = 0°
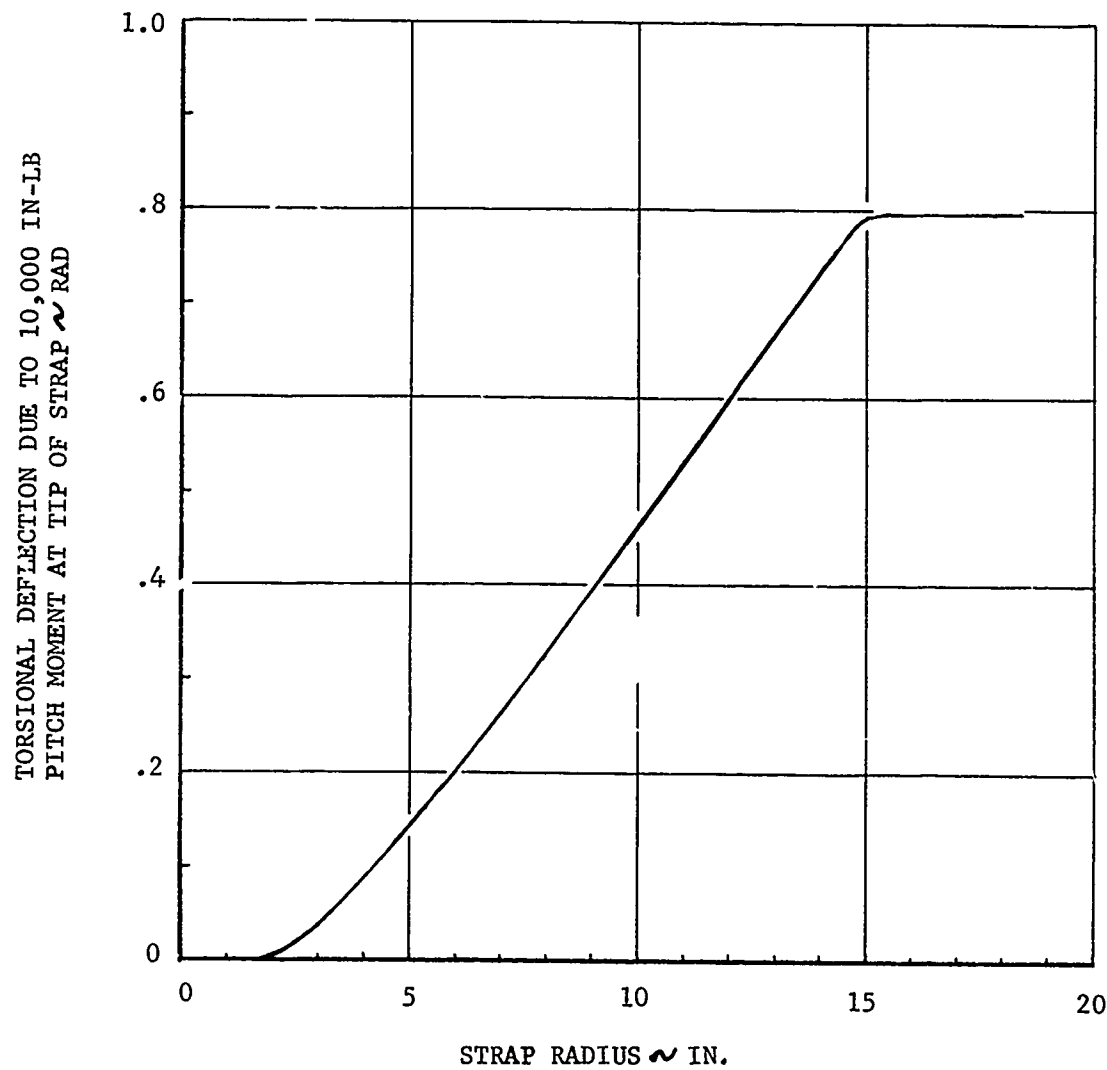
FIGURE 185   TORSIONAL DEFLECTION OF STRAP WITH CENTRIFUGAL
FORCE UNWIND EFFECT

Now that the equivalent GJ is known, we can calculate the distributed torsional moment along the strap using the expression shown above. Dividing the distributed moment by the vertical force gives the effective shear center along the strap shown in Figure 186. This dynamic strap shear center distribution is similar to the assumed shear center of configuration #2, shown in Figure 182. It can be concluded that the stabilizing effect of aft sweep on the flap-lag stability is largely the effect of the dynamic shear center variation.
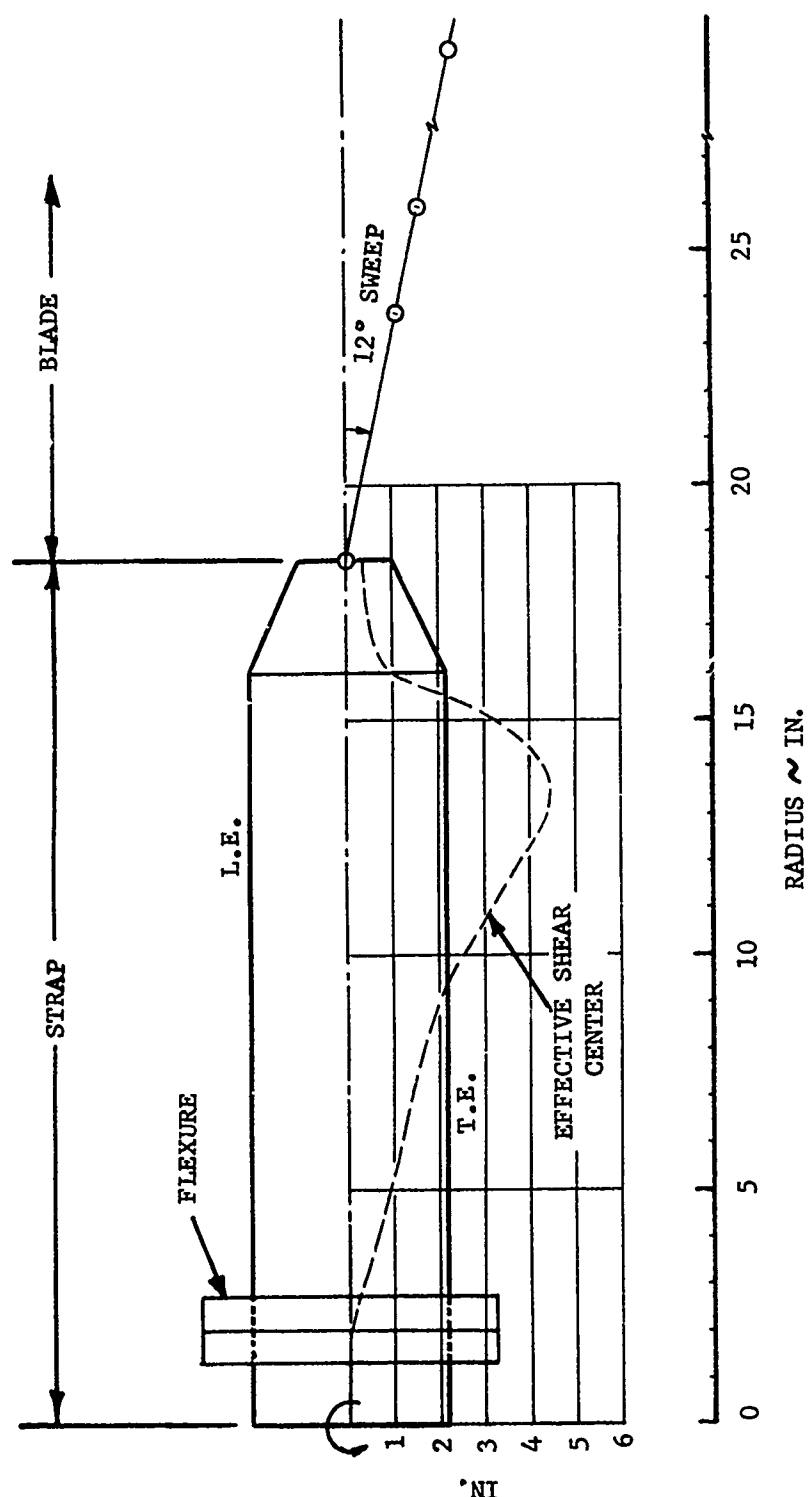
FIGURE 186   DYNAMIC STRAP SHEAR CENTER   DUE TO SWEEP

265

8.0 CONCLUSIONS

Based on the results of this effort, it can be concluded that:

1. The flex strap bearingless tail rotor model has two distinct inplane modes that have a significant effect on the behavior of this rotor system. These modes, a reactionless scissors or "S" type mode and a higher frequency "C" mode, are separated by about 200-300 cpm. The frequency separation occurs primarily because the "C" mode couples with the fixed system, whereas the scissors mode does not.

2. The scissors and the "C" mode frequencies both decrease as the straps are twisted. For the "C" mode the rate of frequency change is about -13.7 cpm per degree of blade collective pitch at 22° of indicated collective pitch. The scissors mode shows a change in frequency of about -6.1 cpm per degree at 22° of indicated collective pitch.

3. The flex strap design can experience four distinct types of aeroelastic instability, all of which are strongly affected by basic configuration parameters. The four instabilities that can occur when negative δ_3 (flap up/pitch down coupling) is used are: flap-lag instability involving either the inplane "scissors" or "C" mode, and stall flutter involving either the third flexible mode (torsion) or the fourth flexible mode (flap-torsion). All of these can occur in the same model configuration at different rpm's

4. Flap-lag instability occurs when the first flap frequency is close to either the first inplane "scissors" frequency or the first inplane "C" mode frequency, and collective is sufficiently high. The higher the collective, the less stringent is the requirement for proximity of the flap and inplane frequencies. Thus, in the rpm-collective plane, the flap-lag stability boundary is a pair of valleys witn the lowest points at the rpm's where the flap frequency crosses the inplane "scissors" and "C" modes. The "C" mode valley is observed to always be deeper and at higher rpm than the "S" mode valley.

5. The flap-lag stability boundary in the rpm-collective plane can be improved in two ways: by changing flap or inplane frequencies (and thus the rpm's where flap and inplane frequencies cross) to move the valleys out of the operating range of rpm; and by changing flap-lag coupling or damping to raise the valleys to higher collectives.

266

The stall flutter boundary in the rpm-collective plane can also be improved two ways: by changing airfoil contour to eliminate leading-edge stall and by changing the frequency or damping of the mode involved.

6. Increased clevis angle is favorable to the flap-lag stability boundary, but unfavorable to stall flutter. This change increases flap-lag stability by reducing strap twist at high collective. The lower twist has benefits: flap-lag elastic coupling is reduced, and inplane frequencies are raised (moving the valleys to higher rpm's). The destabilizing effect of increased clevis angle on stall flutter has not been explained.

7. Pitch link tilt has no significant effect on either flap-lag stability or stall flutter.

8. Reducing the magnitude of δ_3 is favorable to the flap-lag stability boundary and has little effect on stall flutter. The flap-lag stabilization is a direct result of lowered ap frequency, which moves the boundary valleys to higher rpm's. Reduced δ_3 has the serious disadvantage of increasing flapping and therefore strap loads in forward flight.

9. Increasing δ_3 coupling from -45° to -65° (flap up/nosedown) approximately halves cyclic flapping and the associated strap bending loads in forward flight. This indicates that the flapping and resulting loads vary approximately inversely with tan δ_3.

10. High-speed cyclic flapping and the associated strap loads are satisfactorily limited by δ_3 of approximately -65°. Other high-speed cyclic loads are satisfactory for either -45° or -65° of δ_3 .

11. Blade sweep has a strongly favorable effect on both flap-lag and stall flutter stability boundaries. It has little effect on the rotor speed at which flap-lag stability boundary valleys occur, since it has little effect on the modal frequencies. The means by which sweep raises the boundaries is not demonstrated by the test data, but relates to the effect of the blade centrifugal force acting through the flex strap to alter the local effective shear center along the strap. The effects of sweep are reduced at higher rotor speeds.

12. The radius of sweep point had no effect on the "C" mode flap-lag stability as recorded through testing. With respect to the "S" mode stability, this parameter

produced a measurable effect at only one rotor speed, 1450 rpm, and therefore does not significantly affect the mode throughout the speed range. No stall flutter effect was recorded for this parameter.

13. The blade chordwise position relative to the strap was investigated for two different blade sweep angles. With $\Lambda = 0$, the chordwise position did not influence the "C" mode boundary; however, the "S" mode flap-lag stability boundary is slightly more stable when the blade quarter-chord aligns directly with the strap.

With the sweep angle set to 6°, there is again little effect on the "C" mode stability boundary. The "S" mode boundary does show a rather large effect which influences the placement of the valley in the boundary. This is due to a change in the frequency of the "S" mode.

14. Tip weight improves the part of the flap-lag stability boundary produced by the scissors mode, but has little or no effect on the part produced by the "C" mode. These effects are largely independent of the chordwise position of the tip weight. Tip weight is also beneficial to the stall flutter boundary. Chordwise position of the tip weight is influential in some configurations, forward tip weight usually being superior.

Tip weight lowers the inplane frequencies, unfavorably moving the flap-lag boundary valleys to lower rpm's. At the same time, however, it raises both valleys, the scissors more than the "C". The net effect on the scissors mode valley is favorable (the boundary rises more than enough to offset the rpm shift), but the net effect on the "C" mode valley is approximately neutral. The stabilization is not attributable to decreased Lock number, and is, therefore, probably due to alteration of mode shapes. Stall flutter stabilizing effects of tip weights must be related to changes in flap-torsion coupling.

15. Inboard weight and blade lag damping had no effect on any of the several stability types. This leads to the related conclusion that the stabilizing effects of tip weights are not solely related to decreased Lock number and coning. The lack of effectiveness of lag damping to stabilize the flap-lag instability is due to the large spanwise station at which the damper was installed. If a damper was designed to act at a more inboard span station, it would be considerably more effective.

16. Increased strap width has a favorable effect on flap-lag stability boundaries, but little effect on stall flutter boundaries. This configuration change raises inplane frequencies, shifting flap-lag boundary valleys to higher rpm's. Flap-lag stability is further improved by secondary effects which are evidently related to the change in elastic coupling between flap and inplane motion.

. Elastomeric hub inserts have limited favorable effects on the flap-lag stability boundary and little effect on stall flutter. The inserts, even though their stiffness was varied over a wide range, lowered the scissors frequency only slightly and added small amounts of damping to both inplane modes. They have the additional small advantage of lowering the flap frequency slightly.

18. Cruciform strap attachments have a favorable effect on both the stall flutter and flap-lag stability boundaries. The improvement in flap-lag stability, however, results from an increase in chordwise stiffness caused by the bolt-on flanges of the attachments.

The stall flutter stabilization results from a change in the second flap mode shape. This mode shape is such that a pitch arm located for negative δ_3 produces positive δ_3 (outboard flap up/pitch up) with respect to second flap motion. Analysis shows that positive δ_3 is destabilizing at the onset of stall. Cruciform attachments minimize this effect by reducing the inboard curvature of the second flap mode.

19. Blunting the airfoil nose has a very favorable effect on stall flutter when leading-edge stall is present, but when this type of stall has been eliminated, no further benefits are gained. This change has no effect on flap-lag stability.

20. The Y-69 and Y-71 analysis methods can be used to effectively predict the occurrence of flap-lag instability. This is possible through properly representing model physical properties and the dynamic changes in the flex-strap characteristics found to exist due to centrifugal force.

9.0 RECOMMENDATIONS

During the course of this program, additional understanding into the dynamic behavior of a specific type of bearingless rotor, the stiff inplane flex strap tail rotor, was gained through the organization of test data and the description of test configuration parameters. With respect to natural frequency and stability prediction methods which employ an associated matrix type analysis, it was found that the proper representation of bearingless retention systems requires careful consideration. Because most analyses rely on these methods directly, or indirectly, for the determination of mode shapes, it is important that reliable modeling techniques be developed and proven to further bearingless rotor understanding and development.

This suggests several items which should be considered for further work. The following paragraphs list the most significant of these items.

1. The effect of the strap shear center on the stability shows the promise of understanding the dynamic behavior of the bearingless flex strap rotor system. It also points up the importance of proper analytical treatment of the flex strap as plate elements. The dynamic behavior of the strap should be further explored to further the state of the art of the bearingless rotor system.

2. The limited amount of analytical calculations shows that the Y-69 and Y-71 analyses can be used to accurately analyze this analytically complex rotor blade-flex-strap system. However, as the dynamic behavior of the strap becomes better understood and representations for this system are developed, these representations should be correlated to the test results and other information documented in this report, thereby validating the analytical tool for this type of bearingless rotor system.

3. Several other types of bearingless strap retention systems have been tested at Boeing. The effects of the configuration parameters, such as blade sweep, on the stability boundaries are not alike. It will be worthwhile to have those test results documented in the same fashion as those in this report.

10. <u>REFERENCES</u>

1. Contract DAAJ02-75-C-0017, Bearingless Tail Rotor Loads and Stability.

2. D179-10435-1, 8/10 Scale YUH-61A Flex Strap Tail Rotor Wind Tunnel Test, April 30, 1974.

3. Ormiston, R. A., and Hodges, D.H., Linear Flap-Lag Dynamics of Hingeless Helicopter Rotor Blades in Hover, Journal of American Helicopter Society, April, 1972, pp.2-14.

4. Boeing Report D301-10071-1, HLH/ATC Rotor System Two-Dimensional Airfoil Test, December 20, 1971.

5. Boeing Vertol Interoffice Memorandum 8-7445-2-115, A Contour Modification to Alter the Stall Hysteresis Characteristics of the VR-7 Airfoil, June 12, 1973.

AIRFOIL DATA

LIFT COEFFICIENTS VR-7.2

M = 0	α	0°	1.13°	12.86°	20°	340°	351.13°	360°
	C_L	.0728	.190	1.40	1.055	-1.02	-.850	-.0728
= .3	α	0°	1.14°	9.14°	11.34°	13.34°	15.34°	20°	340°
	C_L	.0778	.205	1.09	1.31	1.42	1.37	1.153	-1.035
	α	351.14°	355.14°	357.14°	360°				
	C_L	-.700	-.450	-.240	-.0778				
M = .4	α	0°	1.17°	8.568°	9.568°	11.268°	13.568°	20°	340°
	C_L	.0823	.220	1.08	1.18	1.29	1.25	1.038	-1.03
	α	351.17°	355.17°	357.17°	360°				
	C_L	-.73	-.444	-.250	.0823				
M = .505	α	0°	1.1°	7.875°	9.875°	10.875°	12.375°	20°	340°
	C_{LO}	.1125	.25	1.08	1.22	1.25	1.2	1.069	-1.035
	α	351.1°	355.1°	357.1°	360°				
	C_L	-.71	-.45	-.25	.1125				
M = .555	α	0°	1.095°	7.018°	10.018°	11.018°	12.019°	13.018°	20°
	C_L	.119	.26	1.03	1.18	1.21	1.18	1.13	1.069
	α	340°	351.095°	353.095°	355.095°	357.095°	360°		
	C_L	-1.035	-.69	-.61	-.46	-.255	.119		
M = .618	α	0°	1.094°	4.094°	6.532°	7.532°	8.532°	9.532°	10.532°
	C_L	.113	.285	.70	1.025	1.095	1.145	1.165	1.235
	α	12.532°	20°	340°	351.094°	353.094°	355.094°	357.094°	360°
	C_L	1.265	1.230	-1.04	-.67	-.62	-.47	-.27	.113
M = .680	α	0°	1.1°	3.898°	4.598°	6.898°	10.898°	14.898°	20°
	C_L	.145	.305	.72	.77	.93	1.15	1.30	1.423
	α	340°	351.1°	355.1°	356.1°	360°			
	C_L	-1.035	-.67	-.53	-.42	.145			
M = .750	α	0°	.18°	1.13°	3.13°	7.13°	11.13°	16.13°	20°
	C_L	.205	.23	.36	.56	.86	1.11	1.35	1.466
	α	340°	351.13°	353.13°	354.13°	355.13°	356.13°	357.13°	360°
	C_L	-1.035	-.70	-.67	-.67	-.61	-.49	-.35	.205
M = .820	α	0°	.646°	1.646°	2.646°	6.646°	8.646°	15.646°	20°
	C_L	.06125	.160	.30	.40	.79	.97	1.40	1.539
	α	340°	350.646°	354.646°	356.046°	357.446°	360°		
	C_L	-1.021	-.680	-.44	-.19	-.33	.06125		
M = 1.0°	α	0°	20°	350°	360°				
	C_L	0.0	2.50	-2.50	0.0				

DRAG COEFFICIENT VR-7.2

α								
α = 0°	M	0.0	.500	.675	.702	.750	.850	1.00
	C_D	.0105	.0095	.011	.0125	.0176	.0794	.210
α = 1°	M	0.0	.500	.610	.680	.750	.100	
	C_D	.010	.0095	.010	.0111	.031	.210	
α = 2'	M	0.0	.40	.620	.680	.750	1.00	
	C_D	.0105	.0095	.010	.011	.045	.240	
α = 3°	M	0.0	.400	.500	.635	.680	.750	1.00
	C_D	.011	.0096	.0095	.0109	.018	.065	.250
α = 4°	M	0.0	.575	.615	.638	.680	.750	1.00
	C_D	.011	.0098	.0107	.0125	.037	.095	.260
α = 6°	M	0.0	.300	.525	.570	.620	.700	1.00
	C_D	.011	.0108	.0105	.0135	.025	.100	.300
α = 8°	M	0.0	.300	.400	.535	.563	.620	1.00
	C_D	.012	.012	.013	.01575	.0275	.076	.340
α = 10°	M	0.0	.300	.400	.507	.540	.570	1.00
	C_D	.0145	.0145	.026	.045	.060	.080	.350
α = 12°	M	0.0	.300	.400	.550	.720	1.00	
	C_D	.013	.024	.035	.1218	.265	.350	
α = 14°	M	0.0	.300	.400	.500	1.00		
	C_D	.030	.030	.080	.130	.350		
α = 354°	M	0.0	.300	.500	.610	.750	1.00	
	C_D	.013	.013	.023	.058	.085	.250	
α = 356°	M	0.0	.300	.400	.500	.630	1.00	
	C_D	.0125	.0115	.014	.019	.050	.200	
α = 358°	M	0.0	.400	.680	.750	1.00		
	C_D	.0115	.0098	.0155	.030	.180		
α = 359°	M	0.0	.400	.500	.610	.703	1.00	
	C_D	.0105	.0095	.0105	.011	.013	.180	
α = 360°	M	0.0	.500	.675	.702	.750	.850	1.00
	C_D	.0105	.0095	.011	.0125	.0176	.0794	.210

MOMENT COEFFICIENT VR-7.2

α =0°	M	0.	.3	.4	.5	.61	.74	.82
	C_M	-.001	-.001	-.0015	-.004	-.007	-.025	-.092
	M	.92	1.0					
	C_M	-.103	-.103					
α =2°	M	0.	.4	.5	.61	.74	.82	.92
	C_M	-.007	-.007	-.0115	-.0125	-.0665	-.100	-.146
	M	1.0						
	C_M	-.146						
α =4°	M	0.	.3	.4	.5	.61	.74	.82
	C_M	-.0135	-.0135	-.013	-.0165	-.017	-.079	-.115
	M	.92	1.0					
	C_M	-.175	-.175					
α =6°	M	0.	.3	.4	.5	.61	.74	.82
	C_M	-.021	-.021	-.0185	-.0195	-.020	-.094	-.137
	M	.92	1.0					
	C_M	-.175	-.175					
α =8°	M	0.	.3	.4	.5	.61	.74	.82
	C_M	-.027	-.027	-.024	-.024	-.0375	-.111	-.163
	M	.92	1.0					
	C_M	-.175	-.175					
α =10°	M	0.	.3	.4	.5	.61	.74	.82
	C_M	-.032	-.032	-.028	-.022	-.062	-.127	-.175
	M	1.0						
	C_M	-.175						
α =11°	M	0.	.3	.4	.5	.61	.74	.82
	C_M	-.034	-.134	-.029	-.015	-.06775	-.1375	-.175
	M	1.0						
	C_M	-.175						
α =11.4°	M	0.	.3	.4	.5	.61	.74	.82
	C_M	-.035	-.035	-.0295	-.022	-.0601	-.1417	-.175
	M	1.0						
	C_M	-.175						
α =13.4°	M	0.	.3	.4	.5	.61	.74	.82
	C_M	-.038	-.038	-.0575	-.053	-.0829	-.1669	-.175
	M	1.0						
	C_M	-.175						
α =15.9°	M	0.	.3	.4	.5	.61	.74	1.0
	C_M	-.079	-.079	-.068	-.091	-.109	-.175	-.175
α =16°	M	0.	1.0					
	C_M	-.109	-.109					

MOMENT COEFFICIENT VR-7.2

α								
α =344.°	M	0.	1.0					
	C$_M$	.113	.113					
α =344.1°	M	0.	.3	.4	.5	.61	.74	.82
	C$_M$	.092	.092	.095	.106	.113	.125	.105
	M	.92	1.0					
	C$_M$	.177	.177					
α =346.°	M	0.	.3	.4	.5	.61	.74	.82
	C$_M$	.078	.078	.083	.097	.106	.123	.095
	M	.92	1.0					
	C$_M$	.177	.177					
α = 348.°	M	0.	.3	.4	.5	.61	.74	.82
	C$_M$	.064	.064	.071	.088	.099	.121	.085
	M	.92	1.0					
	C$_M$	.170	.170					
α =350.°	M	0.	.3	.4	.5	.61	.74	.82
	C$_M$	.05	.05	.059	.079	.092	.119	.075
	M	.92	1.0					
	C$_M$	.130	.130					
α =352.°	M	0.	.3	.4	.5	.61	.74	.82
	C$_M$	.0165	.0165	.019	.033	.045	.071	.030
	M	.92	1.0					
	C$_M$	.084	.084					
α =354.°	M	0.	.3	.4	.5	.61	.74	.82
	C$_M$	.003	.003	0.	0.	.007	.023	-.015
	M	.92	1.0					
	C$_M$	.0375	.0375					
α =356.°	M	0.	.3	.4	.5	.61	.74	.82
	C$_M$	.0065	.0065	.007	-.003	-.006	-.011	-.0595
	M	.92	1.0					
	C$_M$	-.008	-.008					
α =358.°	M	0.	.3	.4	.5	.61	.74	.82
	C$_M$	.0035	.0035	.0045	.0	-.002	-.0125	-.029
	M	.92	1.0					
	C$_M$	-.055	-.055					
α =360.°	M	0.	.3	.4	.5	.61	.74	.82
	C$_M$	-.001	-.001	-.0015	-.004	-.007	-.025	-.092
	M	.92	1.0					
	C$_M$	-.103	-.103					

APPENDIX B

ANALYTICAL REPRESENTATION OF TAIL ROTOR

COMPLEX ROTOR/ELASTIC STRUCTURE AEROELASTIC STABILITY ANALYSIS

ROTOR SPEED	=	.178CE 03	COLL. ANG.	=	.0000E 00	NS	=	24.0	ITDET	=	1.0	AERODYNAMICS	YES
SOUND	=	.1340E 05	ROTOR RAD	=	.4800E 02	NCON	=	26.0	NREMS	=	1.0	D/DT TERMS	NO
AIR DENSITY	=	.1150E-06	LAG OFFSET	=	.0000E 00	NFFA	=	26.0	NFX	=	6.0	LOCAL OUTPUT	YES
CRAFT VEL.	=	.0000E 00	THMC	=	.1000E 01	NSS	=	1.0	NORM	=	5.0	DISC OUTPUT	YES
ROTOR ANG.	=	.0000E 00	THXX	=	.1000E 01	MEAN	=	0.	IG	=	0.	C-39 CALCULAT	NO
GRAV. ACC.	=	.3864E 03	THXY	=	.1000E 01	NFGNS	=	3.0	IF	=	0.	TAPE FOR C-39	NO
CYC. ANGLE	=	.0000E 00	THXZ	=	.1000E 01	NPRCNT	=	100.0	MXERUR	=	9.0	FREQ. SEARCH	NO
CYC. AMPL.	=	.0000E 00	STG	=	.0000E 00	MXITER	=	10.0					
1/KC	=	.0000E 00	GTF	=	.0000E 00							

EIGENVALUE 1 = -20.0 , 179.

EIGENVALUE 2 = .000 , 274.

EIGENVALUE 3 = -20.0 , 419.

276

STRUCTURAL DATA

SECTION	M1	M2	M3	M4	M5	M6	M7	M	X	TY	TZ
1	1.0	.0	.0	.0	.0	.0	.0	1.0125E-05	2.5100E-05	.0000E 00	2.5100E-05
2	1.0	1.0	.0	.0	.0	.0	.0	3.9485E-04	9.7910E-04	.0000E 00	9.7910E-04
3	1.0	1.0	1.0	.0	.0	.0	.0	4.0497E-04	1.0042E-03	.0000E 00	1.0042E-03
4	1.0	1.0	1.0	1.0	.0	.0	.0	2.2251E-04	7.1380E-04	.0000E 00	7.1380E-04
5	1.0	1.0	1.0	1.0	.0	.0	.0	4.0447E-04	1.3632E-03	.0000E 00	1.3632E-03
6	1.0	1.0	1.0	1.0	.0	.0	.0	5.0559E-04	1.7040E-03	.0000E 00	1.7040E-03
7	1.0	1.0	1.0	1.0	.0	.0	.0	5.0559E-04	1.7040E-03	.0000E 00	1.7040E-03
8	1.0	1.0	1.0	1.0	.0	.0	.0	1.0112E-03	3.4080E-03	.0000E 00	3.4080E-03
9	1.0	1.0	1.0	1.0	.0	.0	.0	1.0772E-03	3.6754E-03	.0000E 00	3.6754E-03
10	1.0	1.0	1.0	1.0	1.0	.0	.0	1.3X96E-03	4.4315E-03	.0000E 00	4.4316E-03
11	1.0	1.0	1.0	1.0	1.0	.0	.0	7.2638E-04	1.5200E-03	.0000E 00	1.5200E-03
12	1.0	1.0	1.0	1.0	1.0	.0	.0	2.1673E-03	5.7700E-03	.0000E 00	5.7700E-03
13	1.0	1.0	1.0	1.0	1.0	.0	.0	5.8266E-03	1.2950E-02	.0000E 00	1.2950E-02
14	1.0	1.0	1.0	1.0	.0	.0	.0	2.0194E-03	2.7284E-03	.0000E 00	2.7284E-03
15	1.0	1.0	1.0	1.0	.0	.0	.0	1.2313E-03	4.0754E-03	.0000E 00	4.0754E-03
16	1.0	1.0	1.0	1.0	.0	.0	.0	1.4050E-03	6.0540E-03	.0000E 00	6.0540E-03
17	1.0	1.0	1.0	1.0	.0	.0	1.0	.0000E 00	.0000E 00	.0000E 00	.0000E 00
18	1.0	1.0	1.0	1.0	.0	.0	.0	4.4849E-04	1.6355E-0.	.0000E 00	1.6355E-03
19	1.0	1.0	1.0	1.0	.0	.0	.0	2.9714E-04	4.7810E-04	.0000E 00	4.7810E-04
20	1.0	1.0	1.0	1.0	.0	.0	.0	2.9714E-04	4.7810E-04	.0000E 00	4.7X10E-04
21	1.0	1.0	1.0	1.0	.0	.0	.0	2.2286E-04	3.5860E-04	.0000E 00	3.5860E-04
22	1.0	1.0	1.0	1.0	.0	.0	.0	2.2246E-04	3.5860E-04	.0000E 00	3.5860E-04
23	1.0	1.0	1.0	1.0	.0	.0	.0	2.2286E-04	3.5860E-04	.0000E 00	3.5860E-04
24	1.0	1.0	1.0	1.0	.0	.0	.0	2.2266E-04	3.5860E-04	.0000E 00	3.5860E-04
25	1.0	1.0	1.0	1.0	.0	.0	.0	7.3540E-05	1.1830E-04	.0000E 00	1.1830E-04

◆TIP

◆ROOT

277

STRUCTURAL DATA

SECTION	ERY	MRX	ARY	L	GJ	IZ	FTY	FTYY
	-1.420	47.93	.0000	.0000	0.000	.000	.0000	.0000
2	-1.420	47.51	.0000	.4820	1.4400E 05	1.4330E 05	8.4560E 06	.0000
3	-1.420	46.55	.0000	.9460	1.4400E 05	1.4330E 05	8.4560E 06	.0000
4	-1.420	45.66	.0000	1.000	1.4400E 05	1.4330E 05	8.4560E 06	.0000
5	-1.420	44.10	.0000	1.400	1.4400E 05	1.4330E 05	8.4560E 06	.0000
6	-1.420	42.00	.0000	2.160	1.4400E 05	1.4330E 05	8.4560E 06	.0000
7	-1.420	39.50	.0000	2.400	1.4400E 05	1.4330E 05	8.4560E 06	.0000
8	-1.420	36.00	.0000	2.400	1.4400E 05	1.4644E 05	8.6148E 06	.0000
9	-.3400	31.20	.0000	3.600	2.5400E 05	2.1423E 06	1.4167E 07	.0000
10	.7500	26.40	.0000	4.800	3.5400E 05	3.7633E 06	2.0879E 07	.0000
11	.2250	22.80	.0000	4.800	3.5400E 05	4.4209E 05	1.5049E 07	.0000
12	.0000	20.40	.0000	3.600	1.1352E 06	1.0897E 06	1.9961E 07	.0000
13	.0000	18.00	.0000	2.400	2.9543E 06	8.4935E 06	3.0265E 07	.0000
14	.0000	15.60	.0000	2.400	8.7270E 05	2.3360E 05	1.7606E 07	.0000
15	.0000	13.50	.0000	1.500	8.7270E 05	2.7380E 05	1.5602E 07	.0000
16	.0000	12.60	.0000	1.200	.0100	.0000	.0000	1.5000E 07
17	.0000	.000	.0000	.0000	4.1300E 04	3.8652E 05	1.0155E 07	.0000
18	.0000	11.40	.0000	1.540	4.0000E 04	1.4500E 04	7.4600E 06	.0000
19	.0000	9.120	.0000	1.920	4.0000E 04	1.4500E 04	7.4600E 06	.0000
20	.0000	7.200	.0000	1.920	4.0000E 04	1.4500E 04	7.4600E 06	.0000
21	.0000	5.520	.0000	1.650	4.0000E 04	1.4500E 04	7.4600E 06	.0000
22	.0000	4.080	.0000	1.440	4.0000E 04	1.4500E 04	7.4600E 06	.0000
23	.0000	2.870	.0000	1.440	4.0000E 04	1.4500E 04	7.4600E 06	.0000
24	.0000	1.200	.0000	1.440	4.0000E 04	1.4500E 04	7.4600E 06	.0000
25	.0000	.2424	.0000	.9576				

278

STRUCTURAL DATA

SECTION	PHI	THETA	PSI	1/KX	1/KY	1/KZ	K	CENTRIFUGAL FORCE, # PT
1	.0000	-1.7450E-02	.3373	.0000	.0000	.0000	.0000	.0000
2	.0000	-1.7450E-02	.3673	.0000	.0000	.0000	.0000	15.40
3	.0000	-1.7450E-02	.3645	.0000	.0000	.0000	.0000	609.9
4	.0000	-1.7450E-02	.3649	.0000	.0000	.0000	.0000	1207.
5	.0000	-1.7450E-02	.3821	.0000	.0000	.0000	.0000	1529.
6	.0000	-1.7450E-02	.3761	.0000	.0000	.0000	.0000	2095.
7	.0000	-1.7450E-02	.3505	.0000	.0000	.0000	.0000	2768.
8	.0000	-1.7450E-02	.3505	.0000	.0000	.0000	.0000	3402.
9	.0000	-1.7450E-02	.3203	.0000	.0000	.0000	.0000	4556.
10	.0000	-1.7450E-02	.3269	.0000	.0000	.0000	.0000	5621.
11	.0000	-1.7450E-02	.3365	.0000	.0000	.0000	.0000	6776.
12	.0000	-1.7450E-02	.3373	.0000	.0000	.0000	.0000	7301.
13	.0000	-1.7450E-02	.3375	.0000	.0000	.0000	.0000	8704.
14	.0000	-1.7450E-02	.3375	.0000	.0000	.0000	.0000	1.0887E 04
15	.0000	-1.7450E-02	.3375	.0000	.0000	.0000	.0000	1.1880E 04
16	.0000	-1.7450E-02	.3375	.0000	.0000	.0000	.0000	1.2419E 04
17	.0000	.0000	.3376	.0000	.0000	.0000	.0000	.0000
18	.0000	-1.7450E-02	.3327	.0000	.0000	.0000	.0000	1.3060E 04
19	.0000	-1.7450E-02	.2736	.0000	.0000	.0000	.0000	1.3274E 04
20	.0000	-1.7450E-02	.2145	.0000	.0000	.0000	.0000	1.3310E 04
21	.0000	-1.7450E-02	.1027	.0000	.0000	.0000	.0000	1.3376E 04
22	.0000	-1.7450E-02	.1163	.0000	.0000	.0000	.0000	1.3417E 04
23	.0000	.0000	7.340CE-02	.0000	.0000	.0000	.0000	1.3445E 04
24	.0000	.0000	2.950CE-02	.0000	.0000	.0000	.0000	1.3464E 04
25	.0000	.0000	.0000	.0000	.0000	.0000	.0000	1.3472E 04

STRUCTURAL DATA

SECTION	TAU X	TAU Y	TAU Z	DELTA X	DELTA Y	DELTA Z	LX	LY
1	.0000	.0000	.0000	.0000	.0000	.0000	.0000	.0000
2	.0000	.0000	.0000	.0000	.0000	.0000	.0000	.0000
3	.0000	.0000	.0000	.0000	.0000	.0000	.0000	.0000
4	.0000	.0000	.0000	.0000	.0000	.0000	.0000	.0000
5	.0000	.0000	.0000	.0000	.0000	.0000	.0000	.0000
6	.0000	.0000	.0000	.0000	.0000	.0000	.0000	.0000
7	.0000	.0000	.0000	.0000	.0000	.0000	.0000	.0000
8	.0000	.0000	.0000	.0000	.0000	.0000	.0000	.0000
9	.0000	.0000	.0000	.0000	.0000	.0000	.0000	.0000
10	.0000	.0000	.0000	.0000	1.760	.0000	.0000	.0000
11	.0000	.0000	.0000	.0000	.4200	.0000	.0000	.0000
12	.0000	.0000	.0000	.0000	.5400	.0000	.0000	.0000
13	.0000	.0000	.0000	.0000	-.2200	.0000	.0000	.0000
14	.0000	.0000	.0000	.0000	.0000	.0000	.0000	.0000
15	.0000	.0000	.0000	.0000	.0000	.0000	.0000	.0000
16	.0000	.0000	.0000	.0000	.0000	.0000	.0000	.0000
17	.0000	.0000	.0000	.0000	.0000	.0000	.0000	.0000
18	.0000	.0000	.0000	.0000	.0000	.0000	.0000	.0000
19	.0000	.0000	.0000	.0000	.0000	.0000	.0000	.0000
20	.0000	.0000	.0000	.0000	.0000	.0000	1.540	3.500
21	.0000	.0000	.0000	.0000	.0000	.0000	.0000	.0000
22	.0000	.0000	.0000	.0000	.0000	.0000	.0000	.0000
23	.0000	.0000	.0000	.0000	.0000	.0000	.0000	.0000
24	.0000	.0000	.0000	.0000	.0000	.0000	.0000	.0000
25	.0000	.0000	.0000	.0000	.0000	.0000	.0000	.0000

+TIP

+ROOT

STRUCTURAL DATA

SECTION	L	DEL	CHORD	IND. VEL	XXXX	UY	UZ
1	.0000	.0000	.0000	.0000	.0000	.000	.0000
2	.0000	.0000	7.080	.0000	.0000	.0000	.0000
3	1.320	1.770	.0000	2340.	46.56	.0000	.0000
4	.0000	.0000	7.080	.0000	.0000	.0000	.0000
5	2.420	1.770	7.080	1800.	44.16	.0000	.0000
6	2.420	1.770	7.080	1550.	42.00	.0000	.0000
7	4.200	1.770	7.080	1440.	39.60	.0000	.0000
8	4.300	1.770	7.080	1300.	36.00	.0000	.0000
9	4.300	1.770	7.080	1160.	31.20	.0000	.0000
10	7.120	1.770	7.080	1002.	26.40	.0000	.0000
11	7.120	1.770	7.080	840.0	22.80	.0000	.0000
12	7.120	1.770	7.080	680.0	20.40	.0000	.0000
13	.0000	.0000	.0000	.0000	.0000	.0000	.0000
14	.0000	.0000	.0000	.0000	.0000	.0000	.0000
15	.0000	.0000	.0000	.0000	.0000	.0000	.0000
16	.0000	.0000	.0000	.0000	.0000	.0000	.0000
17	.0000	.0000	.0000	.0000	.0000	.0000	.0000
18	.0000	.0000	.0000	.0000	.0000	.0000	.0000
19	.0000	.0000	.0000	.0000	.0000	.0000	.0000
20	.0000	.0000	.0000	.0000	.0000	.0000	.0000
21	.0000	.0000	.0000	.0000	.0000	.0000	.0000
22	.0000	.0000	.0000	.0000	.0000	.0000	.0000
23	.0000	.0000	.0000	.0000	.0000	.0000	.0000
24	.0000	.0000	.0000	.0000	.0000	.0000	.0000
25	.0000	.0000	.0000	.0000	.0000	.0000	.0000

+TIP

+ROOT

PHOTOGRAPHS OF SEVERAL CONFIGURATION PARAMETERS (BVTC 009)

BVTC 009 RUN 12 FULL CRUCIFORM

BVTC 009 RUN 13 FULL CRUCIFORM
HALVES DISCONNECTED

BVTC 009 RUN 14 NARROW CRUCIFORM

BVTC 009 RUN 18 L.E. TIP WEIGHTS

282
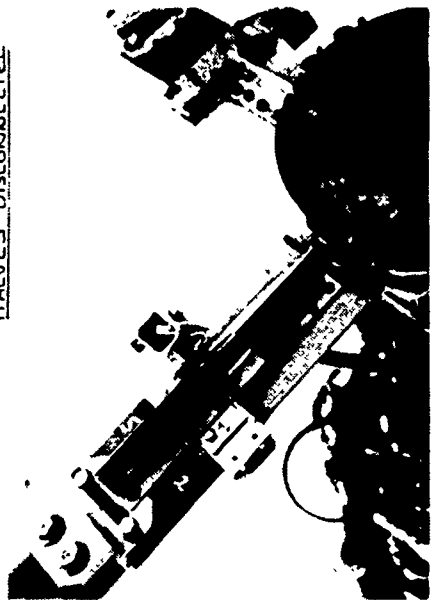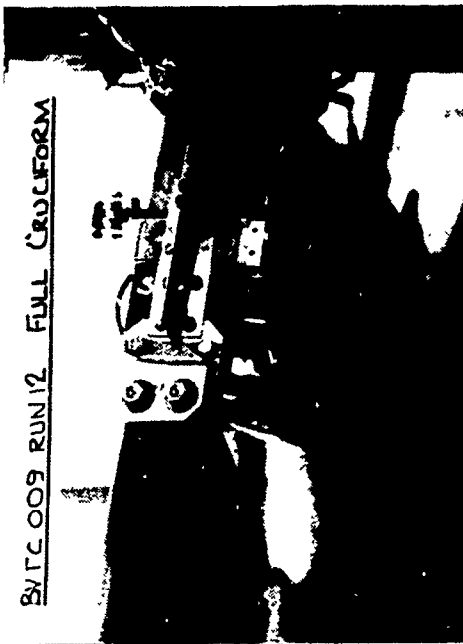
BVTC 009 RUN 26   TEST CELL GENERAL
ARRANGEMENT SHOWING HOLE
IN WALL.
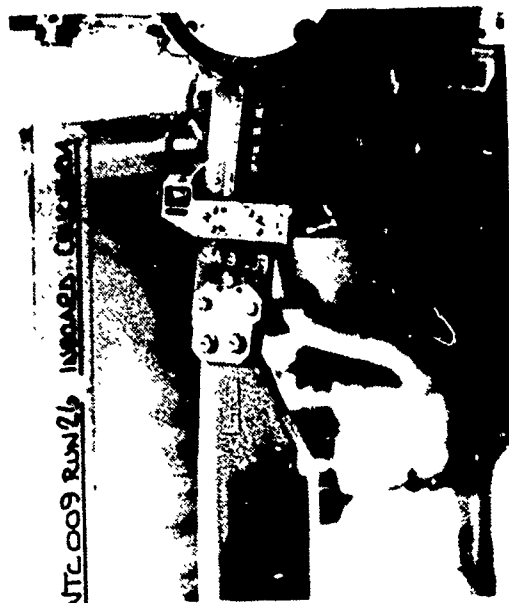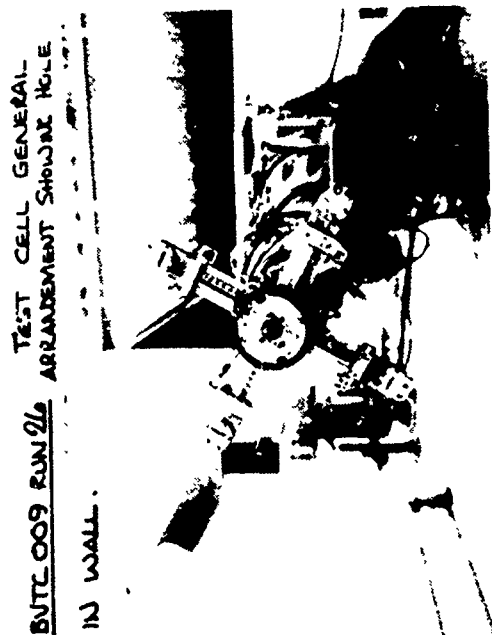
BVTC 009 RUN 42   88 GM. TIP WEIGHTS ON FWD
& AFT TIP LOCATIONS

VTC 009 RUN 26   INBOARD CRUCIFORM

BVTC 009 RUN 27   2 BLADES + INBD.
CRUCIFORMS

BVTC 009 CANTED PITCH LINKS
RUN 110.

BVTC 009 7.5# MASS ON CLEVIS TO
SIMULATE ELASTOMERIC DAMPER
RUN 142.

BVTC 009 CANTED PITCH LINKS
RUN 157.

BVTC 009 CANTED PITCH LINKS
REAMED EI OUTB'D CRACKING.
RUN 160.

BVTC 009. 7.5° MASS ON CLEVIS TO SIMULATE ELASTOMERIC DAMPER.
RUN 162.

7.5° MASS ON CLEVIS TO SIMULATE ELASTOMERIC DAMPER.
BVTC 009. RUN 162.

LORD ELASTOMERIC BLADE DAMPER.
BVTC 009. RUN 165.

LORD ELASTOMERIC BLADE DAMPER.
BVTC 009. RUN 165.

13773-77